Abstract

Shaping Brillouin Dynamics for Silicon Photonic Device Physics

Nils Thomas Otterstrom

2020

Leveraging mature silicon fabrication processes to create sophisticated optical circuitry, the field of silicon photonics is poised to revolutionize a range of photonic applications, from high-speed communications to state-of-the-art quantum information processing. Historically, however, silicon photonics has lacked a number of silicon-based technologies for crucial photonic components, including lasers, amplifiers, and non-reciprocal devices. Thus, as the field expands in scope, there is a pressing need to develop silicon-based device physics to shape, amplify, and route light on-chip.

As a strong and highly tailorable optical nonlinearity, stimulated Brillouin scattering is uniquely suited to these emerging chip-scale technologies. Only through the recent development of suspended optomechanical silicon waveguides, which simultaneously guide both light and elastic waves, has it been possible to achieve stimulated Brillouin scattering (SBS) utilizing a process called forward SBS. However, new strategies are necessary to adapt the nontrivial dynamics of forward SBS—which intrinsically couples Stokes and anti-Stokes processes—to laser, amplifier, and non-reciprocal device physics.

In this dissertation, we manipulate the dynamics of the forward Brillouin process by engineering elastic-wave-mediated coupling between distinct optical spatial modes, in a process called stimulated inter-modal Brillouin scattering. Due to distinct phase-matching conditions that arise from two spatial modes, inter-modal Brillouin scattering yields a form of phase-matching-induced symmetry breaking that intrinsically decouples the red-shifting Stokes (phonon creation) process from the blue-shifting anti-Stokes (phonon annihilation) process, resulting in single-sideband gain. Through the development of high-Q (2.5×10^6) multimode racetrack resonators, we harness inter-modal SBS to demonstrate Brillouin lasing in silicon for the first time. This flexible inter-modal Brillouin laser concept avoids the need

for on-chip isolators and circulators, offers control over cascading dynamics, and enables size and frequency scalability in ways that are not possible with traditional backward-Brillouin lasers. We also show that this laser exhibits an unusual combination of spatial and temporal dynamics, in which optical self-oscillation produces acoustic linewidth narrowing.

Using this device concept, we also demonstrate resonantly enhanced Brillouin amplification, yielding record-high Brillouin gain and amplification in a silicon photonic circuit. By operating just below the laser threshold, we are able to transform the modest gains ($\sim$ 3.5 dB) possible in linear waveguide systems into more than 30 dB of Brillouin gain in silicon. Moreover, we show that due to phase matching, the Brillouin gain is inherently unidirectional, yielding $\sim$ 30 dB of non-reciprocity without insertion loss in an all-silicon device. Operating this system above the laser threshold, we demonstrate high-coherence injection locking dynamics in a Brillouin laser. This system permits lock ranges up to 1.8 MHz while simultaneously reducing low-frequency phase noise by $\sim$ 70 dB. We find that injection locking in this system is also intrinsically unidirectional, demonstrating that the laser emission is distinctly impervious to unwanted back-scatter. We demonstrate this physics with devices fabricated using both academic electron-beam lithography and CMOS-foundry photolithography using the MESA facilities at Sandia National Laboratories. These results pave the way toward mass-manufacturable Brillouin-based technologies in silicon photonics.

Using Hamiltonian-based models in conjunction with the fluctuation-dissipation theorem, we analyze the spatio-temporal dynamics of these Brillouin systems and identify important performance metrics for new technologies. We find that the noise figure and linewidth of Brillouin-based amplifiers and lasers are fundamentally determined by the phonon occupation of the system. In this context, the ability to cool traveling-wave phonons that mediate these Brillouin processes is essential to control noise and dissipation within Brillouin-based technologies.

Here, we experimentally demonstrate such optomechanical cooling in a continuous system for the first time through the phase-matching-induced symmetry breaking of spontaneous inter-modal Brillouin scattering. Within these silicon optomechanical waveguides, we show that this form of cooling is possible without the use of an optical cavity or discrete acoustic modes. Due to the wavevector-selective nature of this process, we show that

this form of cooling is orders of magnitude stronger than previously predicted, allowing us to reduce the temperature of traveling-wave phonons by more than 30 degrees from room temperature. This physics opens the door to strategies for controlling noise and dissipation within a range of important Brillouin-based systems.

Looking forward, we show how these Brillouin-based technologies could be further enhanced and manipulated by operating at mid-infrared wavelengths (> 2.1 μm), where both two-photon absorption (TPA) and TPA-induced free-carrier absorption vanish. The favorable loss properties in this wavelength range may permit orders of magnitude larger Brillouin couplings, admitting new regimes of laser, amplifier, and optomechanical cooling dynamics. We report our progress towards this nonlinear optical physics, both in terms of the devices and experimental apparatus, and show that many of these demonstrations are now within reach.

Shaping Brillouin Dynamics for Silicon Photonic Device Physics

A Dissertation
Presented to the Faculty of the Graduate School
of
Yale University
in Candidacy for the Degree of
Doctor of Philosophy

by
Nils Thomas Otterstrom

Dissertation Director: Prof. Peter Rakich

December 2020

Contents

Acknowledgments

I owe a great debt of gratitude to my advisor, Prof. Peter Rakich, for a PhD experience that has surpassed all of my greatest expectations. I really can't imagine a more dedicated, talented, enthusiastic, and considerate mentor to have during these formative years of my scientific career. I am so grateful for how he invested in me personally: for the opportunities to expand my scientific horizons, for the countless brainstorming sessions, and for all his input and feedback in writing and presenting the material contained in this dissertation.

I also wish to express my gratitude to my other committee members, Prof. Douglas Stone and Prof. Hui Cao. I extend these thanks as well to Prof. Owen Miller, who has graciously been willing to serve as the external reader. Thank you all so much for your time, input, and support through this process.

I would be remiss if I did not mention the incredible support from my undergraduate advisers and research mentors, Prof. Dallin Durfee, Dr. Benjamin Lawrie, Dr. Raphael Pooser, Dr. Chris Erickson, Dr. John Burke, and Dr. Nathan Lemke. Their support and encouragement played a vital role in preparing me for and making my graduate career possible.

I would like to acknowledge the generous funding from the Packard Fellowship and NSF graduate research fellowship,[1] as well as support from DARPA and Sandia National Laboratories.[2]

1. Grant No. DGE1122492

2. Sandia National Laboratories is a multi-program laboratory managed and operated by National Technology and Engineering Solutions of Sandia, LLC., a wholly owned subsidiary of Honeywell International, Inc., for the U.S. Department of Energy's National Nuclear Security Administration under contract DE-NA-0003525. This dissertation describes objective technical results and analysis. Any subjective views or opinions that might be expressed in the dissertation do not necessarily represent the views of the U.S. Department of Energy, the National Science Foundation, or the United States Government.

I wouldn't be at this point without the contributions and tremendous support of my colleagues and collaborators. In particular, I am so grateful for the incredible people I've been able to work with as part of the Rakich Lab: Eric Kittlaus, Ryan Behunin, Shai Gertler, Prashanta Kharel, Will Renninger, Yishu Zhou, Margaret Pavlovich, Freek Ruesink, David Mason, Taekwan Yoon, Vijay Jay, Ruoping Li, Yizhi Luo, Naijin Jin, Yanni Dahmani, and Haotian Cheng. I especially want to thank: Eric, for the many hours in the lab, cleanroom, and office we spent working together to bring many of these projects to fruition and for so freely sharing his knowledge and skills; Ryan, for teaching and working with me on many of the theoretical aspects of this dissertation and for his constant mentorship and his example of generous collaboration; Shai, for being an incredible teammate, insightful collaborator, and dependable support; Prash, being so inclusive and for buoying me up with his contagious enthusiasm for research; Will, for his wise advice and perspective how to approach research as a scientist; Yishu, for her example of grit and for her important contributions to the injection-locking theory; Maggie, for her can-do attitude and for working with me to push forward the mid-infrared research effort in the group.

I also owe a great deal of gratitude to our exceptional collaborators Dr. Tony Lentine, Dr. Michael Gehl, and Prof. Zheng Wang. In particular, it has been tremendously rewarding to work with Tony, Mike, and the Sandia fabrication team to make CMOS-foundry Brillouin devices possible.

There are countless others who I can thank for making my experience wonderful in practically every way. A big thank you to Giselle, Maria, Nuch, Terri, and Alex for making the Applied Physics department feel like home. I want to also thank to the cleanroom and YINQE staff, especially Dr. Michael Rooks, Dr. Yong Sun, Sean Rinehart, Kelly Woods, Michael Powers, Chris Tillinghast, and for providing world-class facilities and for so freely sharing their expertise with us. I also wish to thank Prof. Dan Prober for his mentorship and sharing his passion for teaching as I worked with him as a teaching fellow.

Finally, I would not be here without the people who have loved me and shaped who I am. My Mom and Dad have been a constant source of inspiration and support. Thank you for showing me what truly matters in life and for being right there when the going gets tough. And to my wonderful wife Jessica, I cannot thank you enough for embarking on this

life-changing adventure with me. Your support, patience, constant love, and encouragement mean the world to me. To my children, thank you for being my purest and greatest source of motivation and joy.

List of Figures

8.5 (A) Experimental setup for wavevector-resolved phonon spectroscopy involving two, tunable CW lasers–labeled the probe laser (indexed by superscript $^{(1)}$) and the pump laser (indexed by superscript $^{(2)}$). The probe laser is used to measure the dynamics of the acoustic states that satisfy the phase-matching condition given by the probe wavelength, while the pump laser is used to modify the phonon dynamics. Here, we again use an optical local oscillator discriminate between the spontaneous sidebands of the probe and the pump, as shown in Panels (Ai-ii). Since the optical LO (blue-shifted 44 MHz by the AOM) is synthesized from the probe source, the heterodyne Stokes and anti-Stokes signals centered at ($\Omega_B + \Delta$ MHz and $\Omega_B - \Delta$ MHz, respectively) originate entirely from the spontaneously scattered probe light. EDFA: erbium-doped fiber amplifier; AOM: acousto-optic modulator; PD: photo-detector. (B) Difference in Stokes and anti-Stokes phonon dissipation rates (spectral widths of the Stokes and anti-Stokes sidebands produced by the probe laser) as a function of probe wavelength while the pump wavelength remains fixed at $\lambda_p^{(2)} = 1535.6$ nm. Each data point represents the difference between Stokes and anti-Stokes dissipation rates at a pump power ($P_p^{(2)}$) of 30 mW, obtained by fitting the measured spectral widths over a series of 10 different pump powers. The theoretical trend obtained from Eq. 8.28 is superimposed. The phonon wavevector is calculated from the effective phase and group indices of the two optical spatial modes supported by the silicon waveguide, and the anti-Stokes phonon occupation is estimated by a comparison with the spatio-temporal theory. (Bi) Example spectra (of the probe sidebands) when the probe wave is not phase-matched to the same acoustic states as the pump wave. In this case, the dissipation rates for the Stokes and anti-Stokes phonons remain constant as the pump power increases. (Bii) Example spectra (of the probe sidebands) when the probe wave is phase-matched to the same group of phonons as the pump wave. Here, increasing the pump power enhances the dissipation rate asymmetry (see also Appendix D). These data reveal that the pump wave reduces the phonon occupation over a narrow band of phonon wavevectors, with a bandwidth given by $\Delta q = 2.78/L$. Adapted from Ref. [99]. Copyright (2018) by APS. 190

List of Tables

Chapter 1

Introduction

1.1 Silicon photonics

In the same way that integrated circuits have revolutionized the field of electronics and information processing, the ability to fabricate integrated systems of optical components has already begun to transform the field of optics, both from a scientific and technological standpoint [1–3]. What was once only possible with an optics table full of expensive and complex free-space or fiber-optic systems is now readily available within robust, cm-scale chips. These systems offer tremendous advantages in terms of scalability, cost, and adaptability to a range of new technologies [2]. From a scientific standpoint, the nano-scale waveguides that enable such photonic circuits also permit strong light-matter interactions that can be used to explore regimes of nonlinear optical physics [4].

Among the integrated photonics platforms, silicon photonics is a clear leader thanks to the (1) intrinsic compatibility with mature fabrication infrastructure, (2) ability to monolithically integrate optics and electronics, and (3) superb light guidance properties of silicon (i.e., high index of refraction). First, silicon photonics stands on the shoulders of giants—the microelectronic industry—which has collectively invested 100s of Billions in refining and developing precise and reproducible silicon-based circuits [2]. This infrastructure also provides a natural interface between photonic and electronic components, allowing us to synergistically combine the capabilities of both systems [5]. Finally, due to its large index of refraction, silicon is amenable to compact waveguide geometries for dense layouts and

routing, enabling space-efficient footprints [5].

From both a device and systems perspective, silicon photonic technologies have developed at an accelerated pace. For instance, new high-speed detectors and traveling-wave modulators have enabled 100 Gb/s data communications systems [6] and high-performance RF-photonic links [7]. Low-loss serpentine waveguides and high-Q silicon photonic resonators have enabled new precision chemical [8], optical [9], and biological sensors [10]. Recently, the use of trimmable Mach-Zehnder arrays have become the basis for quantum-photonic circuits that have demonstrated first steps towards quantum simulations [11]. However, not all device physics is readily accessible in silicon-based systems. In particular, it has been challenging to develop new lasers, amplifiers, and non-reciprocal devices in silicon—essential components for fully equipped silicon photonic circuits. As we will explore in this dissertation, the ability to shape and manipulate light by harnessing optical nonlinearities is a powerful and effective strategy to develop these and other essential photonic technologies [4].

1.1.1 Optical nonlinearities

In linear optical media, light transmitted through the system is simply proportional to the input. This property can be observed in the polarization field, which is the material response to an applied field, given by

$$P(t) = \epsilon_0 \chi^{(1)} E_{\text{in}}(t), \tag{1.1}$$

where $\chi^{(1)}$ is the linear optical susceptibility. Here and below we assume no dispersion for simplicity.[1] In the case of linear optical media, the light retains its spectral properties. It may be refracted, reflected, or scattered, but its frequency remains unchanged.

By contrast, in nonlinear optical media, light exiting the material can be nonlinearly proportional to the input. In this case, the polarization field is given by

$$P(t) = \epsilon_0 \left[\chi^{(1)} E_{\text{in}}(t) + \chi^{(2)} E_{\text{in}}^2(t) + \chi^{(3)} E_{\text{in}}^3(t) + \chi^{(4)} E_{\text{in}}^4(t) + ...\right]. \tag{1.2}$$

1. Otherwise the polarization field is given by the convolution of the field with the susceptibility.

A

$$E_{out}(t) \propto \chi^{(1)} E_{in}(t)$$

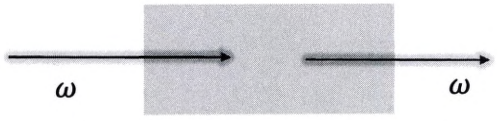

Output field is proportional

B

$$E_{out}(t) \propto \chi^{(1)} E_{in}(t) + \epsilon_0 \chi^{(2)} E_{in}^2(t) + \epsilon_0 \chi^{(3)} E_{in}^3(t) + \cdots$$

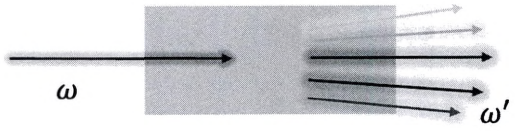

Generates new frequencies

Figure 1.1: (A) Linear optical medium. The output electromagnetic field is proportional to the input. (B) Nonlinear optical medium. The output field can be nonlinearly proportional to the input, enabling frequency mixing and new colors of light. In both (A) and (B) we assume no dispersion for conceptual simplicity.

As shown in Eq. 1.2, the polarization current can be proportional to any power of the electric field, allowing the optical fields to nonlinearly mix. This polarization field can subsequently source an electric field with a frequency given by a sum, difference, or combination of sum and difference frequencies. Thus, nonlinear optical systems change the spectral content of the light, and as such, can be a powerful tool to shape and manipulate light for a varied array of on-chip technologies.

1.1.2 Nonlinear optical technologies in silicon

As a material, silicon's crystal structure possesses inversion symmetry, and consequently it has no intrinsic $\chi^{(2)}$ nonlinearity. As such, appreciable nonlinear interactions arise only through $\chi^{(3)}$ nonlinearities, such as Raman or Kerr interactions [12, 13]. Raman processes arise due to the interaction of light with optical phonons within a solid-state system. Due to higher order dispersion,[2] spontaneous inelastic scattering can become a stimulated process, leading to exponential amplification of the Stokes wave. This gain mechanism has been used to create low-noise amplifiers and lasers in silicon [14]. Kerr interactions, by contrast, are electronic in nature, and are characterized by how the index of material changes in the presence of high optical intensities [12]. These interactions have been used within resonant systems to create frequency combs [15] for applications in sensing and time-keeping [16]. Kerr nonlinearities have also been used in the context of quantum photonics for heralded single-photon generation [17, 18] and quantum frequency conversion [19].

Another powerful $\chi^{(3)}$ nonlinearity, termed stimulated Brillouin scattering, arises from the interaction of light with acoustic phonons. As we discuss below, this highly flexible interaction gives rise to a range of unique and powerful dynamics for new silicon photonic applications.

2. Even with modest group-velocity dispersion, the large frequency shifts ($\sim$ THz) typical of Raman processes produce a phase-mismatch that decouples the Stokes (amplification) process from the anti-Stokes (attenuation) process.

1.2 Stimulated Brillouin scattering

Stimulated Brillouin scattering is a $\chi^{(3)}$ nonlinearity arising from the interaction of 3 waves—two optical and one elastic. As such, stimulated Brillouin scattering gives us access to the distinct and complementary properties of acoustic phonons. This coupling is made possible through a combination of optical forces and the photoelastic response of the material. Given that the sound velocity is typically many orders of magnitude ($\sim 10^5$) slower than that of light, traveling elastic waves with optical-scale wavelengths oscillate in the GHz rather than the 100s of THz regime [12]. As a result, Brillouin scattering provides a natural interface between optical and microwave frequency scales that can be leveraged for new signal processing schemes in microwave photonic applications [20, 21]. In addition, the relatively slow speed of sound permits compact optomechanical geometries that can support long-lived acoustic excitations, enabling high-performance filtering or delay functionalities [22].

The distinct optical and mechanical properties of materials, in conjunction with the ability to precisely fashion device geometries through microfabrication, allows us to independently control light and sound as we so desire [23]. This extra degree of freedom is the basis for interesting non-local phenomena, where acoustic waves can be exploited to sense or transduce information that light cannot 'see' [24–28]. At the same time, the ability to independently control the optical and acoustic fields through both material and structural engineering allows us to shape the Brillouin dynamics in ways that otherwise might not be possible with all-optical nonlinearities [29]. For instance, various key properties, including the Brillouin frequency, dissipation rate, and Brillouin coupling strength can readily be tuned through geometry [29, 30]. Moreover, propagating sound waves possess a natural directionality that can be harnessed for non-reciprocal modulation and control of light propagation [31–33].

Brillouin interactions are also compelling because they are (1) found in practically any transparent medium and (2) intrinsically strong relative to other nonlinearities. For instance, silica-based fiber optic systems are one of the most nonlinear optical systems, and yet Brillouin interactions exceed all other nonlinearities by factor of > 100 [13]. The strength

of this nonlinear coupling can therefore be a resource for low-threshold nonlinear-based technologies such as amplifiers and lasers [34]. Moreover, the intrinsic strength of this coupling can be used to sense minute changes in temperature or strain over large distances and with high resolution [35]. Thus, considering both the strength and overall tailorability of these processes, Brillouin interactions are one of the most versatile and useful nonlinearities to harness for new integrated photonic technologies.

1.2.1 Brief historical context

The discovery and development of stimulated Brillouin scattering is closely tied with the history of its sister scattering processes, such as Rayleigh and Raman scattering, which goes back to the late 19th century [36]. In particular, the collective work of John Tyndale and John William Strutt (Lord Rayleigh) was the first significant step [37, 38], detailing how light scatters from wavelength-scale particles in a process that we now refer to as Rayleigh scattering. This early work set the stage for hypotheses of Joseph Larmor that, if the nano-scale particles producing such scattering were in motion, the Doppler effect could change the frequency of the scattered light [39]. This idea was subsequently extended to solid-state systems by C V Raman in 1919, who predicted that inelastic interactions with molecular vibrations would also produce distinct frequency shifts corresponding to the natural oscillation of what we now call optical phonons [40]. However, it was Léon Brillouin was first to recognize in 1922 (at least in the published record) that this type of inelastic scattering could also be produced by periodic density fluctuations arising from propagation of acoustic phonons [41].

Eight years after the theoretical predictions of Brillouin, the spontaneous version of this scattering process was first observed by Federovich Gross in 1930 [42]. Using a bright mercury lamp and high-resolution echelon grating, he measured the spontaneous scattering produced by thermal acoustic fluctuations of various liquids, in convincing agreement with calculations based on Brillouin's early work. Similar spontaneous Brillouin measurements were subsequently used to measure the elastic constants of various materials [43]. However, it wasn't until the advent of the optical laser [44], which could provide an intense source of spatially and temporally coherent light, that the stimulated version of this process was first

observed by Chiao, Townes, and Stoicheff in 1964 [45]. In this seminal work, Chiao et al. focused high power ruby laser light ($\sim$ 50 MW) within Quartz and Sapphire crystals and observed the stimulated emission of back-propagating Stokes radiation [45]. Bright Brillouin spectrograms obtained from Fabry-Perot interferometers revealed that intensities met the required threshold condition for stimulated scattering and amplification of hypersonic waves.

Since this first demonstration, stimulated Brillouin scattering phenomena have been observed in a variety of solid, liquid, and gas media [46–51]. Importantly, it was shown that by providing optical feedback within a resonant geometry, the required threshold power for stimulated scattering could be significantly reduced, thereby introducing the concept of a Brillouin laser [52]. Additionally, Brillouin scattering-based physics became significantly more accessible with the invention of optical fiber systems [53]. In fact, the Brillouin threshold was quickly recognized as a clear limiting factor when considering the power capacity of fiber-optic systems [54]. As such, stimulated Brillouin scattering has often been viewed as an unwanted effect in high-power applications. On the other hand, the intrinsically large nonlinear SBS coupling opened the door to various high-performance laser [55], amplifier [56], and sensing technologies [57]. Such interactions have been enhanced by using photonic-crystal fiber systems [58] and other glass-waveguide systems for non-reciprocal devices [31], Brillouin gyroscopes [59, 60], and microwave generators [61, 62]. With the emergence of integrated photonic systems, the ability to precisely engineer the optical and mechanical properties of devices through micro-fabrication opens the door a new landscape of high-performance Brillouin-based technologies [2, 63].

1.2.2 Challenges in adapting Brillouin technologies to silicon photonics

As discussed earlier, silicon photonic systems hold tremendous promise for the next generation of signal processing and sensing technologies, as well as new explorations of fundamental science [2]. In this context, Brillouin interactions are uniquely adapted to many of the most pressing needs within the field. The tight optical confinement provided by nano- and micro-scale silicon waveguides enable radically enhanced Raman and Kerr nonlinearities [14, 64–68]. Surprisingly, Brillouin interactions have been markedly absent from conventional silicon photonics, despite the potential to harness large optical forces to trans-

duce mechanical motion [69].

Silicon's elastic and photo-elastic properties present a unique landscape for Brillouin-based device physics [69]. Importantly, the component of the photo-elastic tensor p_{12}, which is the dominant source of coupling in conventional backward stimulated Brillouin scattering (BSBS), is unusually small, preventing direct adaption of mature fiber-optic or bulk stimulated Brillouin scattering technologies. By contrast, the component of the photo-elastic tensor that couples optical and acoustic fields of the same polarization, p_{11}, is significantly larger ($p_{11}^2/p_{12}^2 > 30$) [70]. This particular form of optomechanical coupling is ideally suited to a process called intra-modal forward stimulated Brillouin scattering (FSBS), in which cut-off phonons—with characteristic breathing-mode-like behavior—mediate coupling between co-propagating optical fields propagating in the same spatial mode [71, 72]. Such forward scattering processes offer the most promising path to high-performance Brillouin-based devices in silicon photonics.

While possessing great potential, this non-standard scattering process poses two significant challenges in the context of silicon photonic device technologies. First, while standard silicon-on-insulator waveguides provide optical confinement through total internal reflection, they do not support long-lived acoustic modes; since the sound velocity of silica is lower than that of silicon, the oxide undercladding quickly draws away the elastic energy necessary to sustain appreciable interactions [69]. Only through a new class of suspended optomechanical structures that provide confinement for both optical and elastic waves, have large Brillouin nonlinearities become possible in silicon ($\sim 10^4 \times$ larger than in silica fiber) [30,73], yielding optical gain that can outpace linear and nonlinear propagation losses [23,74]. Second, due to phase matching, the dynamics of FSBS are fundamentally distinct from those of BSBS (see Fig. 1.3) [13], making these interactions nontrivial to adapt to new amplifier, laser, and non-reciprocal technologies.

In what follows, we will examine the dynamics of backward and forward stimulated Brillouin scattering using a Hamiltonian-based theoretical framework, leveraging many of the results presented in Ref. [75]. We show that backward stimulated Brillouin scattering fundamentally decouples the Stokes from the anti-Stokes process through phase-matching, producing single-sideband gain. By contrast, the Stokes and anti-Stokes processes are in-

trinsically coupled in forward intra-modal Brillouin scattering, preventing stimulated gain from spontaneous scattering. We show how the introduction of multiple spatial modes in a forward Brillouin scattering allows us to fundamentally manipulate the dynamics, allowing us to combine the strong elasto-optic couplings of forward SBS with the single-sideband dynamics of backward Brillouin scattering.

1.3 Brillouin processes and dynamics

To describe the coupled spatio-temporal dynamics produced by stimulated Brillouin scattering (SBS), we use a Hamiltonian formalism [75] that builds upon prior traveling-wave quantum optics [76] and optomechanical frameworks [77]. This analysis offers a complementary approach to traditional formulations for SBS based on Maxwell's equations and the acoustic wave equation [12]. It also provides a clear connection to the growing body of literature surrounding cavity optomechanical systems [78] and a natural extension to scenarios in which the quantum nature of light becomes relevant [76, 79]. As outlined in Ref. [75], the generalizable Hamiltonian that captures the traveling-wave dynamics of Brillouin interactions in continuous systems is given by

$$H = H^{\text{optical}} + H^{\text{phonon}} + H^{\text{int}}, \tag{1.3}$$

where H^{phonon}, H^{optical}, and H^{int} are the Hamiltonians describing the optical field, the phonon field, and the optomechanical interaction.

We begin by describing the uncoupled dynamics of the optical and phonon fields. In a continuous system, the total mechanical energy (excluding vacuum fluctuations) is given by a sum over a continuum of phonon modes indexed by wavevector q', such that

$$H^{\text{phonon}} = \int dq' \hbar\Omega(q') b^{\dagger}_{q'} b_{q'}. \tag{1.4}$$

Here, $\Omega(q)$ is the acoustic dispersion relation. Through a Fourier transform, we can re-express this Hamiltonian in the spatial domain as

$$H^{\text{phonon}} = \int dz' \hbar B^{\dagger}(z) \hat{\Omega}_z B(z) \tag{1.5}$$

where the dispersion operator is given by the Taylor expansion

$$\hat{\Omega}_z = \sum_{n=0}^{\infty} \frac{1}{n!} \frac{\partial^n \Omega}{\partial q^n}\bigg|_{q_0} \left(-i \frac{\partial}{\partial z} \right)^n, \tag{1.6}$$

and the phonon mode envelope operator $B(z) = (2\pi)^{(-1/2)} \int dq' b_{q'} \exp[i(q' - q_0)]$, such that the phonon field is described by a sharply peaked distribution of acoustic wavevectors centered around q_0.[3] We note that, according to this definition, $B^{\dagger}(z)B(z)$ represents a number density such that Number $= \int dz' B^{\dagger}(z')B(z')$. In a similar fashion, we can express the Hamiltonian for the optical fields as

$$H^{\text{optical}} = \sum_{\nu} \int dk' \hbar \omega_{\nu}(k') a^{\dagger}_{\nu,k'} a_{\nu,k'}, \tag{1.7}$$

which, transformed into the spatial domain, becomes

$$H^{\text{optical}} = \sum_{\nu} \int dz' \hbar A^{\dagger}_{\nu}(z') \hat{\omega}_{\nu,z'} A_{\nu}(z'). \tag{1.8}$$

Here, $A_{\nu}(z) = (2\pi)^{(-1/2)} \int dk' a_{k'} \exp[i(k' - k_{\nu})]$ and ν indexes the fields and dispersion relations pertaining to the pump, Stokes, and anti-Stokes fields. The dispersion operator $\hat{\omega}_{\nu,z'}$ is described by a Taylor expansion of $\omega_{\nu}(k)$ much like its acoustic counterpart (Eq. 1.6).

Having distilled the traveling-wave Hamiltonian for the uncoupled phonon and optical fields, we derive their spatio-temporal dynamics using the Heisenberg equations of motion. The dynamics of the phonon field are given by

$$\begin{aligned} \frac{\partial B(z,t)}{\partial t} &= -\frac{i}{\hbar}\left[B(z,t), H^{\text{phonon}}\right] \\ &= -i \int dz' \left[B(z,t), B^{\dagger}(z',t)\right] \hat{\Omega}_{z'} B(z',t) \\ &= -i\hat{\Omega}_z B(z,t), \end{aligned} \tag{1.9}$$

3. To simplify the analysis, we factor out the phase associated with the center wavevector q_0.

where we have used the commutator $[B(z,t), B^{\dagger}(z',t)] = \delta(z-z')$.

To first order (i.e., neglecting higher order dispersion), Eq. 1.9 becomes

$$\frac{\partial B(z,t)}{\partial t} \approx -i\Omega(q_0)B(z,t) - v_{\mathrm{b}}\frac{\partial B(z,t)}{\partial z} \tag{1.10}$$

where the acoustic group velocity is given by $v_b = \Omega'(q_0)$.

Now, following the same steps with the optical fields, we have

$$\begin{aligned}\frac{\partial A_\nu(z,t)}{\partial t} &= -\frac{i}{\hbar}\left[A_\nu(z,t), H^{,\mathrm{optical}}\right] \\ &= -i\hat{\omega}_{\nu,z}A_\nu(z,t) \\ &\approx -i\omega(k_\nu)A_\nu(z,t) - v_\nu\frac{\partial A_\nu(z,t)}{\partial z},\end{aligned} \tag{1.11}$$

where again we have neglected higher-order dispersion terms, which is a good approximation for the systems described in this dissertation.

1.3.1 Optomechanical Brillouin coupling

We now consider the case when the relevant optical and phonon fields are coupled together optomechanically through Brillouin scattering. This coupling is captured by the interaction Hamiltonian

$$\begin{aligned}H^{\mathrm{int}} = \hbar\int dz'\Big(&g_{\mathrm{s,p}}A_{\mathrm{p}}^{\dagger}(z')A_{\mathrm{s}}(z')B(z')e^{i(q_0-k_{\mathrm{p}}+k_{\mathrm{s}})} \\ &+g_{\mathrm{p,as}}A_{\mathrm{as}}^{\dagger}(z')A_{\mathrm{p}}(z')B(z')e^{i(q_0-k_{\mathrm{as}}+k_{\mathrm{p}})z}\Big) + h.c..\end{aligned} \tag{1.12}$$

Here $g_{\mathrm{s,p}}$ and $g_{\mathrm{p,as}}$ are the elasto-optic coupling coefficients corresponding to the Stokes and anti-Stokes processes that arise from the interplay between optical forces (both electrostriction and radiation pressure) and the photo-elastic response of the material. The total elasto-optic coupling is given by

$$g_{\nu,\nu'} = g_{\nu,\nu'}^{\mathrm{es}} + g_{\nu,\nu'}^{\mathrm{rp}}, \tag{1.13}$$

where the electrostrictive $g_{\nu,\nu'}^{\mathrm{es}}$ and radiation pressure coupling $g_{\nu,\nu'}^{\mathrm{rp}}$ are given by

$$
\begin{aligned}
g^{\mathrm{es}}_{\nu,\nu'} &= \kappa \sum_{i,j,k,l} \int dr_\perp (D^i_\nu(r_\perp))^* (D^j_{\nu'}(r_\perp)) p^{ijkl}(r_\perp) \frac{\partial u^k(r_\perp)}{\delta r^l} \\
g^{\mathrm{rp}}_{\nu,\nu'} &= \kappa \int dr_\perp \left[\epsilon_0^2 (E^{\parallel}_\nu)^* \cdot (E^{\parallel}_{\gamma'}) \nabla(\epsilon(r_\perp)) - (D^{\perp}_\nu) \cdot (D^{\perp}_{\nu'}) \nabla\left(\frac{1}{\epsilon(r_\perp)}\right) \right] u(r_\perp),
\end{aligned}
\tag{1.14}
$$

where $\kappa = 2^{-3/2}\epsilon_0^{-1}(\hbar\omega_\nu\omega_{\nu'}\Omega_0)^{1/2}$. Here, we use $r_\perp$ to denote the 2-D space that is perpendicular to the direction of light propagation and that spans the cross-section of the waveguide system. We also note that we sum i, j, k, and l over each orthogonal direction. $D^i_\nu(r_\perp)$ is the spatial profile of the ith polarization displacement field of optical mode γ; $p^{ijkl}(r_\perp)$ is the photo-elastic tensor; $u(r_\perp)$ is the elastic displacement profile and $\frac{\partial u^k(r_\perp)}{\delta r^l}$ is the 2-D strain profile; $E^{\parallel}_{\gamma'}$ ($D^{\perp}_{\nu'}$) is the component of the electric (displacement) field profile that is parallel (perpendicular) to the boundary; $\epsilon(r_\perp)$ is the dielectric spatial profile of the waveguide. Notice that we have separated the parallel and perpendicular field components such that the field values are well-defined at the boundaries—an important consideration in high-index dielectric waveguides [80].

To consider the Stokes or anti-Stokes process, we will replace the central wavevector q_0 with q_{s} or q_{as} such that the phase-matching condition is satisfied for the first or second term, respectively. Finally, we note that the case of a backward propagating wave will reverse the sign of the relevant wavevectors.

1.3.2 Backward stimulated Brillouin scattering

For a backward stimulated Brillouin scattering (Stokes) process, we consider a traveling phonon field with a central wavevector of $q_0 \rightarrow q_{\mathrm{s}} = k_{\mathrm{p}} + k_{\mathrm{s}} \approx 2k_{\mathrm{p}}$ such that the phase-matching condition is satisfied for a forward propagating pump wave and backward-propagating Stokes wave. In this case, the interaction Hamiltonian takes the form

$$
\begin{aligned}
H^{\mathrm{int}} &= \hbar \int dz' \left(g_{\mathrm{s,p}} A^\dagger_{\mathrm{p}}(z') A_{\mathrm{s}}(z') B(z') + g_{\mathrm{p,as}} A^\dagger_{\mathrm{as}}(z') A_{\mathrm{p}}(z') B(z') e^{-i(2k_{\mathrm{p}}+k_{\mathrm{s}}+k_{\mathrm{as}})z} \right) + h.c.. \\
&\approx \int dz' g_{\mathrm{s,p}} A^\dagger_{\mathrm{p}}(z') A_{\mathrm{s}}(z') B(z') + h.c.,
\end{aligned}
\tag{1.15}
$$

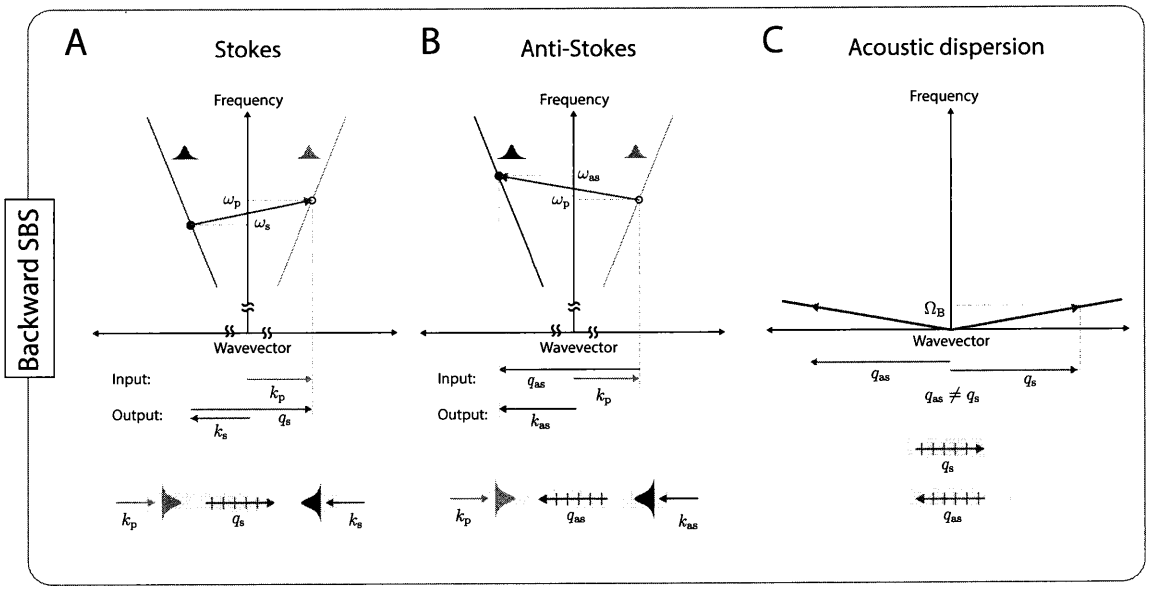

Figure 1.2: Phase-matching and energy conservation conditions for backward SBS, illustrated by the optical and acoustic dispersion relations. Together, these conditions require that the wavevector (x-axis) and frequency (y-axis) of the Brillouin-active phonon connect the initial (open circle) and final (closed circle) optical states. (A) The BSBS Stokes process requires a forward-propagating phonon with $q_s \approx 2k_p$ and $\Omega_s = \Omega_B = 2\omega_p v_p / v_b$. (B) By contrast, the anti-Stokes process is mediated by a backward-propagating phonon of approximately the same magnitude of wavevector and frequency. (C) Because the Stokes and anti-Stokes processes are mediated by distinct phonons, these two processes are intrinsically decoupled; this we refer to as phase-matching-induced or dispersive symmetry breaking.

Here, we have used the fact that the phonon wavevector that satisfies the phase-matching condition for the Stokes process does not satisfy the anti-Stokes process (i.e., $k_{\mathrm{s}} \neq k_{\mathrm{as}}$). As such, the second term is highly oscillatory and, for system lengths $L \gg 1/(4k_{\mathrm{p}})$, becomes vanishingly small under the integration. As a result, the Stokes process is completely decoupled from the anti-Stokes process. Such dispersive symmetry breaking, as we call it, can be understood diagrammatically, as presented in Fig. 1.2. We observe that, for phase matching to be satisfied, the Stokes process must be mediated by a forward-propagating phonon ($+z$). By contrast, the anti-Stokes process requires a backward-traveling phonon ($-z$).

This interaction Hamiltonian, in conjunction with the traveling-wave optical and phonon Hamiltonians, can then be used derive the coupled Heisenberg equations of motion for the pump, Stokes, and phonon fields, yielding

$$\begin{aligned}
\frac{\partial B}{\partial t} &= -i\Omega_{\mathrm{s}} B - v_{\mathrm{b}} \frac{\partial B}{\partial z} - i g_{\mathrm{s,p}}^{*} A_{\mathrm{s}}^{\dagger} A_{\mathrm{p}} \\
\frac{\partial A_{\mathrm{p}}}{\partial t} &= -i\omega_{\mathrm{p}} A_{\mathrm{p}} - v_{\mathrm{p}} \frac{\partial A_{\mathrm{p}}}{\partial z} - i g_{\mathrm{s,p}} A_{\mathrm{s}} B \\
\frac{\partial A_{\mathrm{s}}}{\partial t} &= -i\omega_{\mathrm{s}} A_{\mathrm{p}} + v_{\mathrm{s}} \frac{\partial A_{\mathrm{s}}}{\partial z} - i g_{\mathrm{s,p}}^{*} A_{\mathrm{p}} B^{\dagger}
\end{aligned} \tag{1.16}$$

For simplicity we move these fields to the rotating frame in time, such that $B(z,t) = \bar{B}(z,t)\exp(-i\Omega t)$, $A_{\mathrm{p}}(z,t) = \bar{A}_{\mathrm{p}}(z,t)\exp(-i\omega_{\mathrm{p}} t)$, and $A_{\mathrm{s}}(z,t) = \bar{A}_{\mathrm{s}}(z,t)\exp(-i\omega_{\mathrm{s}} t)$, where $\Omega = \omega_{\mathrm{p}} - \omega_{\mathrm{s}}$. We also introduce loss for each field and corresponding Langevin terms, representing the thermal and quantum fluctuations that maintain detailed balance (i.e., thermal equilibrium). Under these conditions the equations of motion become

$$\begin{aligned}
\frac{\partial \bar{B}}{\partial t} &= -i(\Omega_{\mathrm{s}} - \Omega)\bar{B} - \frac{\Gamma}{2}\bar{B} - v_{\mathrm{b}} \frac{\partial \bar{B}}{\partial z} - i g_{\mathrm{s,p}}^{*} \bar{A}_{\mathrm{s}}^{\dagger} \bar{A}_{\mathrm{p}} + \eta \\
\frac{\partial \bar{A}_{\mathrm{p}}}{\partial t} &= -\frac{\gamma_{\mathrm{p}}}{2}\bar{A}_{\mathrm{p}} - v_{\mathrm{p}} \frac{\partial \bar{A}_{\mathrm{p}}}{\partial z} - i g_{\mathrm{s,p}} \bar{A}_{\mathrm{s}} \bar{B} + \xi_{\mathrm{p}} \\
\frac{\partial \bar{A}_{\mathrm{s}}}{\partial t} &= -\frac{\gamma_{\mathrm{s}}}{2}\bar{A}_{\mathrm{s}} + v_{\mathrm{s}} \frac{\partial \bar{A}_{\mathrm{s}}}{\partial z} - i g_{\mathrm{s,p}}^{*} \bar{A}_{\mathrm{p}} \bar{B}^{\dagger} + \xi_{\mathrm{s}}
\end{aligned} \tag{1.17}$$

where Γ, γ_{p}, γ_{s} and η, ξ_{p}, ξ_{s} are the dissipation rates and Langevin terms for the phonon, Stokes, and pump fields, respectively.

For the purposes of this section, we will momentarily ignore the stochastic Langevin terms, but note that they will play an important role in Chapters 3, 6-8. To understand

the power dynamics of the system, we analyze the steady-state equations of motion

$$\begin{aligned} v_{\mathrm{b}}\frac{\partial \bar{B}}{\partial z} &= -i(\Omega_{\mathrm{s}}-\Omega)\bar{B} - \frac{\Gamma}{2}\bar{B} - ig^{*}_{\mathrm{s,p}}\bar{A}^{\dagger}_{\mathrm{s}}\bar{A}_{\mathrm{p}} \\ v_{\mathrm{p}}\frac{\partial \bar{A}_{\mathrm{p}}}{\partial z} &= -\frac{\gamma_{\mathrm{p}}}{2}\bar{A}_{\mathrm{p}} - ig_{\mathrm{s,p}}\bar{A}_{\mathrm{s}}\bar{B} \\ -v_{\mathrm{s}}\frac{\partial \bar{A}_{\mathrm{s}}}{\partial z} &= -\frac{\gamma_{\mathrm{s}}}{2}\bar{A}_{\mathrm{s}} - ig^{*}_{\mathrm{s,p}}\bar{A}_{\mathrm{p}}\bar{B}^{\dagger}, \end{aligned} \tag{1.18}$$

where we note that the sign of the optical Stokes field velocity indicates the backward direction of propagation. Given the typically rapid spatial decay of acoustic waves at room temperature (with attenuation lengths of order 100 μm), we can adiabatically eliminate[4] the spatial phonon dynamics such that, to an excellent approximation, the phonon field can be expressed as the local beat-note between the Stokes and pump fields [12]. Specifically, under this approximation, the phonon field can be written as

$$\bar{B}(z) = -ig^{*}_{\mathrm{s,p}}\chi_{\mathrm{b}}(\Omega)\bar{A}_{\mathrm{p}}(z)\bar{A}^{\dagger}_{\mathrm{s}}(z), \tag{1.19}$$

where the phonon susceptibility $\chi_{\mathrm{b}}(\Omega) = (i(\Omega_{\mathrm{s}}-\Omega)+\frac{\Gamma}{2})^{-1}$. As such, for most Brillouin systems, the phonon field is given by the local pump-Stokes beat note. Substituting this expression into the steady-state dynamics of the pump and Stokes fields yields

$$\begin{aligned} \frac{\partial \bar{A}_{\mathrm{p}}}{\partial z} &= -\frac{\alpha_{\mathrm{p}}}{2}\bar{A}_{\mathrm{p}} - \frac{|g_{\mathrm{s,p}}|^2|\bar{A}_{\mathrm{s}}|^2}{v_{\mathrm{p}}}\chi_{\mathrm{b}}(\Omega)\bar{A}_{\mathrm{p}} \\ \frac{\partial \bar{A}_{\mathrm{s}}}{\partial z} &= \frac{\alpha_{\mathrm{s}}}{2}\bar{A}_{\mathrm{s}} - \frac{|g_{\mathrm{s,p}}|^2|\bar{A}_{\mathrm{p}}|^2}{v_{\mathrm{s}}}\chi^{*}_{\mathrm{b}}(\Omega)\bar{A}_{\mathrm{s}}. \end{aligned} \tag{1.20}$$

where α_{p} and α_{s} are the spatial decay rates for the pump and Stokes fields defined by $\alpha_{\mathrm{p}} = \gamma_{\mathrm{p}}/v_{\mathrm{p}}$ and $\alpha_{\mathrm{s}} = \gamma_{\mathrm{s}}/v_{\mathrm{s}}$. In single-mode systems, these two loss rates are typically equal. We make a quick observation that linear loss for the backward-propagating Stokes

4. In cases with well-resolved decay rates, adiabatic elimination allows us to greatly simplify the equations of motion. We begin with the integral solution for the phonon field in Eq. 1.18 given by $\bar{B}(z) = (-ig^{*}_{\mathrm{s,p}})/v_{\mathrm{b}}\int_0^z dz'\bar{A}_{\mathrm{p}}(z')\bar{A}^{\dagger}_{\mathrm{s}}(z')\exp\big(-(z-z')/(\chi_{\mathrm{b}}(\Omega)v_{\mathrm{b}})\big)$, where $\chi_{\mathrm{b}}(\Omega) = (i(\Omega_{\mathrm{s}}-\Omega)+\frac{\Gamma}{2})^{-1}$. Next, recognizing that the attenuation length for the optical fields is far larger than for the phonon field, we can use the Markov, or two-scale approximation to pull the optical fields out of the integral, yielding $\bar{B}(z) = -ig^{*}_{\mathrm{s,p}}\chi_{\mathrm{b}}(\Omega)\bar{A}_{\mathrm{p}}(z)\bar{A}^{\dagger}_{\mathrm{s}}(z)\big(1-\exp\big(-z/(\chi_{\mathrm{b}}(\Omega)v_{\mathrm{b}})\big)\big)$. Noting that the device lengths are typically much longer than the phonon attenuation length (i.e., $L \gg v_{\mathrm{b}}\chi_{\mathrm{b}}(0)/2$), the phonon field can be expressed, to an excellent approximation, as $\bar{B}(z) = -ig^{*}_{\mathrm{s,p}}\chi_{\mathrm{b}}(\Omega)\bar{A}_{\mathrm{p}}(z)\bar{A}^{\dagger}_{\mathrm{s}}(z)$. Alternatively, one can arrive at the same adiabatically eliminated form by solving for the steady state spatial dynamics (i.e., $v_{\mathrm{b}}\frac{\partial \bar{B}}{\partial z} = 0$). Given appropriate separation of scales, adiabatic elimination can be used in both space and time domains, as we show in Chapter 3.

dynamics takes the form of exponential gain in the forward direction. Conversely, exponential gain from stimulated Brillouin scattering appears as a loss term in the forward direction. Equation 1.20 can be rewritten in terms of the optical powers by noting that $P_{(\mathrm{p,s})} \cong \hbar\omega_{\mathrm{p}} v_{\mathrm{p}} A^{\dagger}_{(\mathrm{p,s})} A_{(\mathrm{p,s})}$ (and $A_\nu(z,t)$ has units of [number][Length]$^{-(1/2)}$),[5] which yields

$$\begin{aligned} \frac{dP_{\mathrm{p}}}{dz} &= -\alpha_{\mathrm{p}} P_{\mathrm{p}} - G_{\mathrm{B}}(\Omega) P_{\mathrm{s}} P_{\mathrm{p}} \\ \frac{dP_{\mathrm{s}}}{dz} &= \alpha_{\mathrm{s}} P_{\mathrm{s}} - G_{\mathrm{B}}(\Omega) P_{\mathrm{p}} P_{\mathrm{s}}, \end{aligned} \tag{1.21}$$

where the frequency-dependent Brillouin gain coefficient is given by

$$G_{\mathrm{B}}(\Omega) = G_{\mathrm{B}} \frac{(\Gamma/2)^2}{(\Omega - \Omega_{\mathrm{s}})^2 + (\Gamma/2)^2}, \tag{1.22}$$

with $G_{\mathrm{B}} = 4|g_{\mathrm{s,p}}|^2/(\hbar\omega_{\mathrm{p}}\Gamma v_{\mathrm{s}} v_{\mathrm{p}})$.[6]

In the case of an undepleted pump wave, the optical Stokes power as a function of space is given by

$$P_{\mathrm{s}}(z) = P_{\mathrm{s}}(L) e^{(-G_{\mathrm{B}}(\Omega) P_{\mathrm{p}} + \alpha_{\mathrm{s}})(z-L)}. \tag{1.23}$$

From Eq. 1.23, we see that backward stimulated Brillouin scattering yields exponential backward amplification for the Stokes wave when the Brillouin gain exceeds the propagation loss. Such amplification is also evident in the phonon field power. Since the phonon field is proportional to the optical Stokes field (see Eq. 1.19), we find that the phonon power is

$$P_{\mathrm{b}}(z) = \hbar\Omega_{\mathrm{s}} v_{\mathrm{b}} \bar{B}^{\dagger}(z) \bar{B}(z) \propto P_{\mathrm{s}}(L) e^{(-G_{\mathrm{B}}(\Omega) P_{\mathrm{p}} + \alpha_{\mathrm{s}})(z-L)}. \tag{1.24}$$

Thus, given a injected Stokes or spontaneous fluctuation, backward Brillouin amplification produces exponential amplification. This form of amplification is the basis for low-noise Brillouin lasers [81–84], high-gain amplifiers [85], distributed fiber sensors [86,87], and narrowband optical and RF-photonic filters [88,89].

5. Approximately true for fields possessing a narrow spectrum, and exactly true in the case of a monochromatic source.

6. We can reparameterize the Brillouin gain by noting that $P_{\mathrm{p}} = \hbar\omega_{\mathrm{p}} v_{\mathrm{p}} |\bar{A}_{\mathrm{p}}|^2$ such that $G_{\mathrm{B}} = 4|g_{\mathrm{s,p}}|^2 |A_{\mathrm{p}}|^2 / P_{\mathrm{p}} \Gamma v_{\mathrm{s}}$.

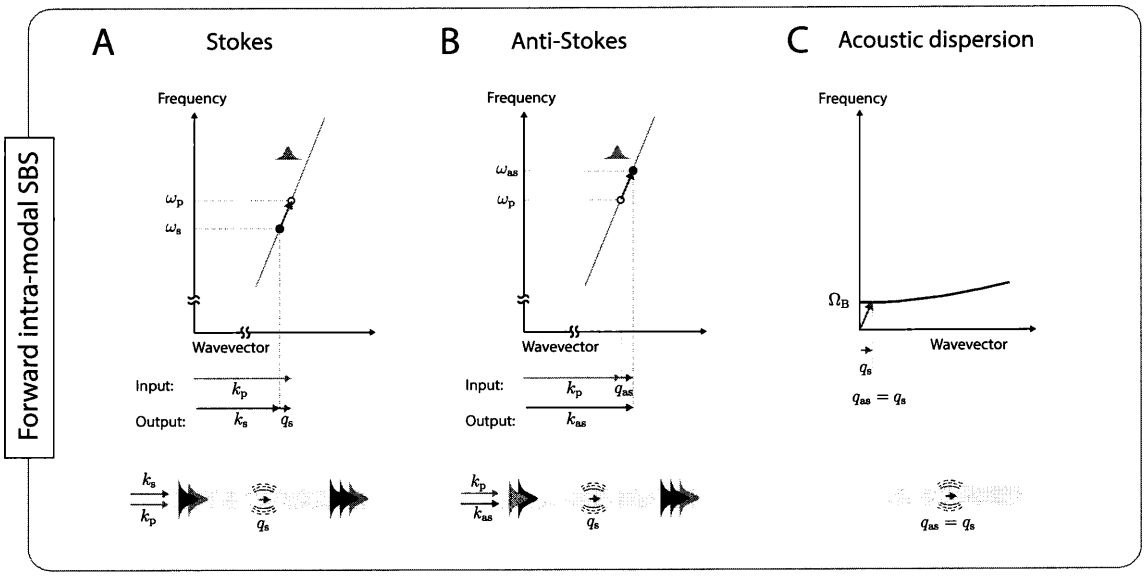

Figure 1.3: 2-D representation of phase-matching and energy conservation conditions for forward intra-modal Brillouin scattering. Together, these conditions require that the wavevector (x-axis) and frequency (y-axis) of the Brillouin-active phonon connect the initial (open circle) and final (closed circle) optical states. (A) In this forward intra-modal SBS Stokes process, this means that the a forward-propagating cut-off Brillouin-active phonon of frequency $\Omega_s = \Omega_B$, the phonon wavevector $q_s = v_p^{-1}\Omega_B$ where v_p is the optical pump group velocity. (B) The anti-Stokes process is mediated by the same phonon. (C) As such, the Stokes and anti-Stokes processes are intrinsically coupled, yielding dual-sideband gain.

1.3.3 Forward intra-modal Brillouin scattering

As we have discussed, the dominant scattering process possible in silicon waveguides is forward intra-modal stimulated Brillouin scattering. In this case, the dynamics are quite different from those of backward stimulated Brillouin scattering.

We begin with the interaction Hamiltonian of the system given by

$$\begin{aligned} H^{\text{int}} = \hbar \int dz' \Big(& g_{\text{s,p}} A_{\text{p}}^{\dagger}(z') A_{\text{s}}(z') B(z') e^{i(q_0 - k_{\text{p}} + k_{\text{s}})} \\ & + g_{\text{p,as}} A_{\text{as}}^{\dagger}(z') A_{\text{p}}(z') B(z') e^{i(q_0 - k_{\text{as}} + k_{\text{p}})z} \Big) + h.c.. \end{aligned} \tag{1.25}$$

In the case of forward Brillouin scattering, the relevant central wavevector the phonon field becomes $q_0 \rightarrow q_{\text{s}} = k_{\text{p}} - k_{\text{s}}$, approximately identical to the anti-Stokes phonon $q_{\text{as}} = k_{\text{as}} - k_{\text{s}}$ such that $q_0 \rightarrow q_{\text{s}} \cong q_{\text{as}}$. Specifically, the phonon that phase-matches to the Stokes process also satisfies the phase-matching condition of the anti-Stokes process, as illustrated by Fig. 1.3. This intrinsic coupling is in sharp contrast to dynamics of backward stimulated Brillouin scattering (see Section 1.3.2). Given these properties, the interaction Hamiltonian becomes

$$\begin{aligned} H^{\text{int}} = \hbar \int dz' \Big(& g_{\text{s,p}} A_{\text{p}}^{\dagger}(z') A_{\text{s}}(z') B(z') \\ & + g_{\text{p,as}} A_{\text{as}}^{\dagger}(z') A_{\text{p}}(z') B(z') \Big) + h.c., \end{aligned} \tag{1.26}$$

and the resulting coupled-wave dynamics are given by

$$\begin{aligned} \frac{\partial B}{\partial t} &= -i\Omega_{\text{s}} B - v_{\text{b}} \frac{\partial B}{\partial z} - i g_{\text{s,p}}^{*} A_{\text{s}}^{\dagger} A_{\text{p}} - i g_{\text{p,as}}^{*} A_{\text{p}}^{\dagger} A_{\text{as}} \\ \frac{\partial A_{\text{p}}}{\partial t} &= -i\omega_{\text{p}} A_{\text{p}} - v_{\text{p}} \frac{\partial A_{\text{p}}}{\partial z} - i g_{\text{s,p}} A_{\text{s}} B - i g_{\text{p,as}}^{*} B^{\dagger} A_{\text{as}} \\ \frac{\partial A_{\text{s}}}{\partial t} &= -i\omega_{\text{s}} A_{\text{p}} - v_{\text{s}} \frac{\partial A_{\text{s}}}{\partial z} - i g_{\text{p,s}}^{*} A_{\text{p}} B^{\dagger} \\ \frac{\partial A_{\text{as}}}{\partial t} &= -i\omega_{\text{as}} A_{\text{as}} - v_{\text{as}} \frac{\partial A_{\text{as}}}{\partial z} - i g_{\text{p,as}} A_{\text{p}} B. \end{aligned} \tag{1.27}$$

From Eq. 1.27, we observe that, due to phase-matching, the Stokes and anti-Stokes processes are intrinsically coupled. This means that phonons generated through a Stokes process can be annihilated by the anti-Stokes process with nearly equal probability (i.e., $g_{\text{s,p}} \approx g_{\text{p,as}}$). In this way, spontaneous forward Brillouin scattering does not lead to stimu-

lated amplification (see Ref. [75]), in contrast to the case of backward Brillouin scattering. This is evident by solving for the steady-state equations of motion under the rotating wave and stiff pump approximations, which yields

$$\begin{aligned}
\bar{B}(z) &= \chi_{\mathrm{b}}(\Omega)\big(-ig^{*}_{\mathrm{s,p}}\bar{A}^{\dagger}_{\mathrm{s}}\bar{A}_{\mathrm{p}} - ig^{*}_{\mathrm{p,as}}\bar{A}^{\dagger}_{\mathrm{p}}\bar{A}_{\mathrm{as}}\big) \\
\frac{\partial \bar{A}_{\mathrm{s}}}{\partial z} &= \frac{-ig^{*}_{\mathrm{s,p}}\bar{A}_{\mathrm{p}}\bar{B}^{\dagger}}{v_{\mathrm{s}}} \\
\frac{\partial \bar{A}_{\mathrm{as}}}{\partial z} &= \frac{-ig_{\mathrm{p,as}}\bar{A}_{\mathrm{p}}\bar{B}}{v_{\mathrm{as}}},
\end{aligned} \tag{1.28}$$

where as before, $\bar{B}$, $\bar{A}_{\mathrm{p}}$, $\bar{A}_{\mathrm{s}}$ are the slowly-varying envelopes in the rotating frame.

These coupled equations allow us to analyze the spatial dynamics of the phonon field, yielding

$$\begin{aligned}
\frac{\partial \bar{B}}{\partial z} &= -i\chi_{\mathrm{b}}(\Omega)\Bigg(\underbrace{g^{*}_{\mathrm{s,p}}\left(\frac{\partial \bar{A}^{\dagger}_{\mathrm{s}}}{\partial z}\right)\bar{A}_{\mathrm{p}}}_{\text{Generation rate}} + \underbrace{g^{*}_{\mathrm{p,as}}\bar{A}^{\dagger}_{\mathrm{p}}\left(\frac{\partial \bar{A}_{\mathrm{as}}}{\partial z}\right)}_{\text{Annihilation rate}}\Bigg) \\
&= -i\chi_{\mathrm{b}}(\Omega)\Bigg[g^{*}_{\mathrm{s,p}}\Bigg[\frac{ig_{\mathrm{p,s}}\bar{A}^{\dagger}_{\mathrm{p}}\chi_{\mathrm{b}}(\Omega)}{v_{\mathrm{s}}}\big(-ig^{*}_{\mathrm{s,p}}\bar{A}^{\dagger}_{\mathrm{s}}\bar{A}_{\mathrm{p}} - ig^{*}_{\mathrm{p,as}}\bar{A}^{\dagger}_{\mathrm{p}}\bar{A}_{\mathrm{as}}\big)\Bigg]\bar{A}_{\mathrm{p}} \\
&\quad + g^{*}_{\mathrm{p,as}}\bar{A}^{\dagger}_{\mathrm{p}}\Bigg[\frac{-ig_{\mathrm{p,as}}\bar{A}_{\mathrm{p}}\chi_{\mathrm{b}}(\Omega)}{v_{\mathrm{as}}}\big(-ig^{*}_{\mathrm{s,p}}\bar{A}^{\dagger}_{\mathrm{s}}\bar{A}_{\mathrm{p}} - ig^{*}_{\mathrm{p,as}}\bar{A}^{\dagger}_{\mathrm{p}}\bar{A}_{\mathrm{as}}\big)\Bigg]\Bigg] \\
&\approx 0.
\end{aligned} \tag{1.29}$$

The final line takes the case of $g_{\mathrm{p,as}} = g_{\mathrm{s,p}}$ and $v_{\mathrm{as}} = v_{\mathrm{s}}$, which are excellent approximations in practically all forward intra-modal systems since the Brillouin frequencies are many orders of magnitude smaller than the relevant optical frequencies [75].

Thus, the spatial growth of the phonon field depends on the relative Stokes (generation) and anti-Stokes (annihilation) rates. A stimulated process requires that the Stokes process (which generates phonons and Stokes photons) outpace the anti-Stokes process (which annihilates phonons). From Eq. 1.29, we find that these two counteracting processes are balanced, resulting in no net growth of the phonon field—in sharp contrast to the case of backward SBS. These dynamics arise due to the fundamental coupling between Stokes and anti-Stokes processes, which prevents stimulated gain from spontaneous scattering [75]. Consequently, it is nontrivial to adapt these forward Brillouin dynamics to new laser de-

signs.[7]

1.3.4 Forward inter-modal Brillouin scattering

By expanding these concepts to systems that support multiple optical spatial modes, however, we are able to manipulate the dynamics of these forward Brillouin processes in profound ways. In particular, by precisely engineering the spatial character of the optical and phonon modes within a multimode optomechanical waveguide, an elastic wave of the appropriate symmetry can mediate coupling between light waves propagating in distinct optical spatial modes in a process termed stimulated inter-modal Brillouin scattering [91–94].

Through phase-matching, forward inter-modal Brillouin scattering combines many of the compelling features of both backward and forward SBS. In the case where the pump propagates in the fundamental optical spatial waveguide mode (of wavevector $k_1(\omega)$) and the Stokes and anti-Stokes waves propagate in the first excited mode (of wavevector $k_1(\omega)$), phase matching requires that $q_s = k_1(\omega_p) - k_2(\omega_s)$ for the Stokes process and $q_{as} = k_2(\omega_{as}) - k_1(\omega_{as})$. As shown in Fig. 1.4, these conditions demand that the Stokes process be mediated by a forward-propagating phonon while the anti-Stokes process must be mediated by a backward-propagating phonon. This fundamental decoupling of Stokes and anti-Stokes processes, which we refer to as dispersive symmetry breaking, profoundly changes the interaction Hamiltonian (Eq. 1.26). For the Stokes process, $q_0 \rightarrow q_s = k_1(\omega_p) - k_2(\omega_s)$ and the interaction Hamiltonian becomes

7. The Stokes ("Phonon generation") and anti-Stokes ("Phonon annihilation") interactions are counteracting processes. This means that, in contrast to BSBS, stimulated Brillouin processes cannot initiate from noise [90]. Furthermore, in a standard cavity system (with equally spaced modes), any gain provided by the Stokes process will be negated by the anti-Stokes process, preventing a forward Brillouin-based system from reaching the laser threshold.

$$
\begin{aligned}
H^{\text{int}} &= \hbar \int dz' \Big(g_{\text{s,p}} A_{\text{p}}^{\dagger}(z') A_{\text{s}}(z') B(z') e^{i(q_{\text{s}} - k_1(\omega_{\text{p}}) + k_2(\omega_{\text{s}}))} \\
&\quad + g_{\text{p,as}} A_{\text{as}}^{\dagger}(z') A_{\text{p}}(z') B(z') e^{i(q_{\text{s}} - k_2(\omega_{\text{as}}) + k_1(\omega_{\text{p}}))z} \Big) + h.c. \\
&= \hbar \int dz' \Big(g_{\text{s,p}} A_{\text{p}}^{\dagger}(z') A_{\text{s}}(z') B(z') \\
&\quad + g_{\text{p,as}} A_{\text{as}}^{\dagger}(z') A_{\text{p}}(z') B(z') e^{i(2k_1(\omega_{\text{p}}) - k_2(\omega_{\text{s}}) - k_2(\omega_{\text{as}}))z} \Big) + h.c. \\
&\approx \hbar \int dz' g_{\text{s,p}} A_{\text{p}}^{\dagger}(z') A_{\text{s}}(z') B(z') + h.c.
\end{aligned}
\tag{1.30}
$$

As shown in the second line, the phase mismatch for the anti-Stokes process is $2k_1(\omega_{\text{p}}) - k_2(\omega_{\text{s}}) - k_2(\omega_{\text{as}})) \approx 2\Delta n_{12}(\omega_{\text{p}})\omega_{\text{p}}/c$, where $\Delta n_{12}(\omega)$ denotes the effective index difference between mode 1 and mode 2. Thus, for device lengths that exceed the spatial beat length of the two modes ($L \gg c/(4\Delta n_{12}(\omega_{\text{p}})\omega_{\text{p}})$), the second term (of line 2) is again highly oscillator over the domain and integrates away.[8] As a consequence, we recover the dispersive symmetry breaking and single-sideband gain associated with backward Brillouin scattering (see Fig. 1.2), but in a forward scattering geometry.

From here, we derive the equations of motion for forward inter-modal Brillouin scattering, which yield

$$
\begin{aligned}
\frac{\partial B}{\partial t} &= -i\Omega_{\text{s}} B - v_{\text{b}} \frac{\partial B}{\partial z} - i g_{\text{s,p}}^{*} A_{\text{s}}^{\dagger} A_{\text{p}} \\
\frac{\partial A_{\text{p}}}{\partial t} &= -i\omega_{\text{p}} A_{\text{p}} - v_{\text{g,1}} \frac{\partial A_{\text{p}}}{\partial z} - i g_{\text{s,p}} A_{\text{s}} B \\
\frac{\partial A_{\text{s}}}{\partial t} &= -i\omega_{\text{s}} A_{\text{s}} - v_{\text{g,2}} \frac{\partial A_{\text{s}}}{\partial z} - i g_{\text{s,p}}^{*} A_{\text{p}} B^{\dagger},
\end{aligned}
\tag{1.31}
$$

where $v_{\text{g,1}}$ and $v_{\text{g,2}}$ are the group velocities of the pump and Stokes waves propagating in the waveguide mode 1 and 2, respectively. We now transform these equations to the rotating frame and add linear damping and noise terms consistent with the fluctuation-dissipation theorem, as we did with the BSBS equations of motion (see Eq. 1.17). These steps yield

8. For typical multimode silicon waveguide, the spatial beat length is typically 10-100 μm.

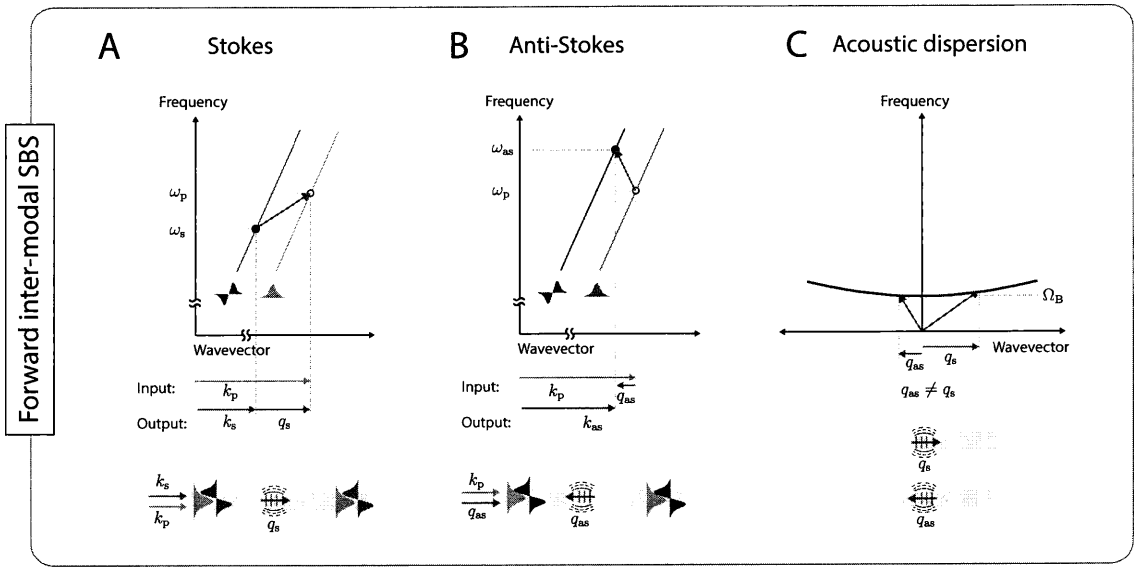

Figure 1.4: Phase-matching and energy conservation conditions for forward inter-modal stimulated Brillouin scattering. Together, these conditions require that the wavevector (x-axis) and frequency (y-axis) of the Brillouin-active phonon connect the initial (open circle) and final (closed circle) optical states. (A) In a forward inter-modal Stokes process, this means that the a forward-propagating phonon with $q_s = k_1(\omega_p) - k_2(\omega_s) \approx 2\pi\Delta n_{12}\omega_p/c$, where Δn_{12} denotes the effective index mismatch between mode 1 and mode 2 of the waveguide. (B) By contrast, the anti-Stokes process is mediated by a backward-propagating phonon of approximately the same wavenumber and frequency. (C) Because the Stokes and anti-Stokes processes are mediated by distinct phonons, forward stimulated inter-modal Brillouin scattering dynamics exhibit dispersive symmetry breaking much like that produced in backward stimulated Brillouin scattering.

$$\begin{aligned}
\frac{\partial \bar{B}}{\partial t} &= -i(\Omega_{\mathrm{s}} - \Omega)\bar{B} - \frac{\Gamma}{2}\bar{B} - v_{\mathrm{b}}\frac{\partial \bar{B}}{\partial z} - ig^{*}_{\mathrm{s,p}}\bar{A}^{\dagger}_{\mathrm{s}}\bar{A}_{\mathrm{p}} + \eta \\
\frac{\partial \bar{A}_{\mathrm{p}}}{\partial t} &= -\frac{\gamma_{\mathrm{p}}}{2}\bar{A}_{\mathrm{p}} - v_{\mathrm{g,1}}\frac{\partial \bar{A}_{\mathrm{p}}}{\partial z} - ig_{\mathrm{s,p}}\bar{A}_{\mathrm{s}}\bar{B} + \xi_{\mathrm{p}} \\
\frac{\partial \bar{A}_{\mathrm{s}}}{\partial t} &= -\frac{\gamma_{\mathrm{s}}}{2}\bar{A}_{\mathrm{s}} - v_{\mathrm{g,2}}\frac{\partial \bar{A}_{\mathrm{s}}}{\partial z} - ig^{*}_{\mathrm{s,p}}\bar{A}_{\mathrm{p}}\bar{B}^{\dagger} + \xi_{\mathrm{s}},
\end{aligned} \tag{1.32}$$

where we note that the existence of two spatial modes can yield two distinct optical dissipation rates γ_{p} and γ_{s}. These coupled inter-modal equations form the basis for the dynamics we will study in Chapters 3, 4, 6, and 7. To analyze the power dynamics of the system, we seek the steady state equations of motion of the pump and Stokes waves. Again, we adiabatically eliminate the spatial phonon dynamics of the phonon (i.e., $\bar{B}(z) = -ig^{*}_{\mathrm{s,p}}\chi_{\mathrm{b}}(\Omega)\bar{A}_{\mathrm{s}}(z)\bar{A}_{\mathrm{p}}(z)$). Through these steps, we obtain

$$\begin{aligned}
\frac{\partial \bar{A}_{\mathrm{p}}}{\partial z} &= -\frac{\alpha_1}{2}\bar{A}_{\mathrm{p}} - \frac{|g_{\mathrm{s,p}}|^2|\bar{A}_{\mathrm{s}}|^2}{v_{\mathrm{p}}}\chi_{\mathrm{b}}(\Omega)\bar{A}_{\mathrm{p}} \\
\frac{\partial \bar{A}_{\mathrm{s}}}{\partial z} &= -\frac{\alpha_2}{2}\bar{A}_{\mathrm{s}} + \frac{|g_{\mathrm{s,p}}|^2|\bar{A}_{\mathrm{p}}|^2}{v_{\mathrm{s}}}\chi^{*}_{\mathrm{b}}(\Omega)\bar{A}_{\mathrm{s}}.
\end{aligned} \tag{1.33}$$

where α_{p} and α_{s} are the spatial decay rates for the pump and Stokes fields and the phonon susceptibility is given by $\chi_{\mathrm{b}}(\Omega) = (i(\Omega_{\mathrm{s}} - \Omega) + \frac{\Gamma}{2})^{-1}$. We again transform these equations into power (see Section 1.3.2), yielding

$$\begin{aligned}
\frac{dP_{\mathrm{p}}}{dz} &= -\alpha_{\mathrm{p}}P_{\mathrm{p}} - G_{\mathrm{B}}(\Omega)P_{\mathrm{s}}P_{\mathrm{p}} \\
\frac{dP_{\mathrm{s}}}{dz} &= -\alpha_{\mathrm{s}}P_{\mathrm{s}} + G_{\mathrm{B}}(\Omega)P_{\mathrm{p}}P_{\mathrm{s}}.
\end{aligned} \tag{1.34}$$

Considering the case of an small signal and undepleted pump (i.e., $P_{\mathrm{p}}(z) = P_{\mathrm{p}}$), the solution to Eq. 1.34 is

$$P_{\mathrm{s}}(z) = P_{\mathrm{s}}(0)e^{(G_{\mathrm{B}}(\Omega)P_{\mathrm{p}} - \alpha_{\mathrm{s}})z}. \tag{1.35}$$

Thus, single-sideband gain from stimulated inter-modal Brillouin scattering can lead to exponential amplification of the Stokes wave if the Brillouin gain exceeds the propagation loss. In like manner, the phonon field also experiences exponential growth since it is proportional to the Stokes field.

$$P_{\mathrm{b}}(z) \propto P_{\mathrm{s}}(0) e^{(G_{\mathrm{B}}(\Omega) P_{\mathrm{p}} - \alpha_{\mathrm{s}}) z}. \tag{1.36}$$

Thus, as in the case of backward SBS, stimulated optical gain can result in the case of either an injected Stokes signal or the presence of thermal-mechanical noise. In this way, inter-modal Brillouin scattering allows us to combine powerful BSBS-like dynamics with large FSBS-like coupling strengths for a range of silicon-photonic amplifier, laser, and non-reciprocal technologies. In what follows, we demonstrate, utilize, and control this device physics for emerging integrated photonic technologies.

1.4 Summary of dissertation

In this dissertation, we will explore new ways to manipulate and control Brillouin interactions to develop flexible and useful silicon photonic technologies. Below is a summary of the content of each chapter.

- In Chapter 2, we fundamentally change the dynamics of forward Brillouin scattering in silicon by engineering Brillouin coupling between distinct optical spatial modes. To demonstrate this physics, we develop an all-silicon optomechanical waveguide that supports (1) low-loss TE-like symmetric and antisymmetric optical waveguide modes and (2) an antisymmetric elastic wave that is designed to yield maximal acousto-optic overlap. We also design, optimize, and fabricate low-crosstalk integrated mode-multiplexers, which allow us to access each optical spatial mode independently. In this way, we inject pump and signal waves into distinct optical spatial modes for highly controlled inter-modal Brillouin spectroscopy. Harnessing the dispersive symmetry breaking made possible through inter-modal couplings, we demonstrate 3.5 dB of single-sideband gain in a cm-scale device, corresponding to more than 2 dB of net amplification. This chapter is based on Ref. [29]:

  [29] E.A. Kittlaus, N.T. Otterstrom, and P.T. Rakich, "On-chip inter-modal Brillouin Scattering." *Nature Communications* **8**, 15819 (2017).

- In Chapter 3, we develop a high-Q multimode resonator system that harnesses the

single-sideband gain produced by stimulated inter-modal Brillouin scattering to achieve Brillouin lasing for the first time in silicon. Thanks to the new modal degrees of freedom, the inter-modal laser concept we demonstrate allows us to manipulate and control the laser emission in a number of ways. In particular, this system offers unprecedented size and frequency scalability, avoids the need for isolators and circulators, allows independent control of pump and Stokes emission, and permits controllable energy transfer dynamics. We also develop new experimental and theoretical tools to analyze the unique spatio-temporal dynamics of the system, revealing that optical self-oscillation produces an intriguing form of acoustic linewidth narrowing. We show that these 3-wave laser dynamics are analogous to an extreme limit of optical parametric oscillator physics and are made possible by the unusually large Brillouin coupling and unique elasto-optic properties of our system. We also highlight how, building on this work, the introduction of optical feedback lays the groundwork for powerful amplifier and non-reciprocal technologies. Content for this Chapter has been adapted and partially reproduced from Ref. [95]:

[96] N.T. Otterstrom, R.O. Behunin, E.A. Kittlaus, Z. Wang, and P.T. Rakich, "A silicon Brillouin laser." *Science* **360**, 6393, 1113-1116 (2018). (see also arXiv:1705.05813v4)

- In Chapter 4, we leverage a resonant Brillouin geometry to manipulate and profoundly enhance the Brillouin amplification dynamics produced by stimulated inter-modal Brillouin scattering. Within this resonant system, we show that when Brillouin gain exceeds the internal losses of the cavity, but not the total losses of the system, we can achieve large degrees of amplification without producing self-oscillation (below the laser threshold). This strategy allows us to sidestep major challenges stemming from nonlinear loss and geometric broadening to transform the modest gain possible in a linear waveguide (3.5 dB) into more than 30 dB of on-off Brillouin gain in silicon. We also show that, due to the phase-matching conditions of this inter-modal Brillouin process, Brillouin amplification in this system is intrinsically unidirectional, yielding large degrees of isolation without insertion loss in an all-silicon system. We further highlight how this powerful device physics may be used for narrowband optical and

RF-photonic filters and integrated non-reciprocal technologies. Content for this chapter has been adapted and partially reproduced from Ref. [97] (copyright 2019 by the Optical Society of America):

[97] N.T. Otterstrom, E.A. Kittlaus, S. Gertler, R.O. Behunin, A.L. Lentine, and P.T. Rakich, "Resonantly enhanced nonreciprocal silicon Brilouin amplifier." *Optica* **6**, 9, 1117–1123 (2019).

- In Chapter 5, we develop new strategies for co-integration of Brillouin photonic technologies with CMOS-foundry silicon photonic circuits to (1) improve Brillouin device performance, (2) add new degrees of control, and (3) introduce Brillouin technologies to important integrated photonic applications. In collaboration with Sandia National Laboratories, we design and fabricate a range of Brillouin-active amplifier, laser, and filter technologies using a variant of standard CMOS-foundry fabrication. We characterize these devices through various forms of nonlinear laser spectroscopy and show that Brillouin-photonic devices exhibit exceptional performance relative to those fabricated with our standard academic electron-beam lithography. These results open the door to co-integration of Brillouin devices within active silicon photonic circuits. Building on this progress, we design and fabricate Brillouin-enabled silicon photonic circuits that leverage new degrees of active thermal and electrical control and interface with silicon-photonic modulator technologies. These results provide a powerful new framework to shape dynamics of Brillouin-photonic systems in a dynamical fashion and introduce powerful Brillouin-based device physics into mainstream silicon photonics.

- In Chapter 6, we harness the nonlinear dynamics of synchronization to achieve injection-locked operation of a silicon Brillouin laser and demonstrate its back-scatter immune properties. Building on the resonantly enhanced amplifier results of Chapter 5, we develop high-performance mode-selective couplers to individually address cavity modes produced by the symmetric and antisymmetric optical spatial mode. These couplers allow us to inject a seed into a self-oscillating symmetric cavity mode. When the seed frequency is in sufficient proximity of the natural Brillouin laser frequency, the

Brillouin laser will spontaneously synchronize to the input source. Through this form of injection locking, we are able to control the laser emission with Hz-level precision and dramatically improve the exhibited phase-noise properties of the system. We also study the unidirectional nature of the injection locking dynamics and show that this system permits an intriguing form of back-scatter immunity. Content for this chapter has been adapted and partially reproduced from Ref. [98] (copyright 2020 by the American Physical Society):

[98] N.T. Otterstrom, S. Gertler, Y. Zhou, E.A. Kittlaus, R.O. Behunin, M. Gehl, A.L. Starbuck, C.M. Dallo, A.T. Pomerene, D.C. Trotter, A.L. Lentine, and P.T. Rakich, "Backscatter-Immune Injection-Locked Brillouin Laser in Silicon." *Physical Review Applied* **14**, 044042 (2020).

- In Chapter 7, we theoretically explore the fundamental noise processes that influence the performance of Brillouin amplifiers. Based on these noise mechanisms, we develop a well-defined formulation for the optical noise figure of Brillouin amplifiers in both resonant and non-resonant configurations. We also explore the out-of-band noise properties of these systems and characterize the performance within RF-photonic links. From these calculations, we find that the noise figure of these systems depends critically on the thermal occupation of the phonons, and we discuss strategies for noise-conscious design of Brillouin-based systems. Content for this chapter is adapted and partially reproduced from:

  N.T. Otterstrom, S. Gertler, R.O. Behunin, Y. Zhou, E.A. Kittlaus, A.L. Lentine, and P.T. Rakich, "The optical noise figure of Brillouin amplifiers." *In preparation*

- In Chapter 8, we demonstrate a new form of optomechanical cooling that allows us to reduce the occupation of thermal phonons in continuous Brillouin-photonic systems. This powerful form of optomechanical control is enabled by the well-resolved phase-matching conditions of spontaneous inter-modal Brillouin scattering; we show that these conditions (1) decouple the anti-Stokes (cooling) from the Stokes (heating) process and (2) allow us to reduce the thermal occupation of traveling elastic waves among a continuum of acoustic states in a wavevector selective fashion. To under-

stand these dynamics, we develop Hamiltonian-based theoretical models and a new form of phonon-resolved wavevector spectroscopy. We also discuss how this new form of optomechanical control allows us to manipulate noise and dissipation for improved performance in a range of Brillouin-photonic systems. Content from this chapter has been adapted and partially reproduced from Ref. [99] (copyright 2018 by the American Physical Society):

[99] N.T. Otterstrom, R.O. Behunin, E.A. Kittlaus, and P.T. Rakich, "Optomechanical Cooling in a Continuous System." *Physical Review X* **8**, 041034 (2018).

- In Chapter 9, we explore new strategies to radically enhance the nonlinear Brillouin strength through high-power mid-infrared nonlinear silicon photonics. We discuss the both the opportunities and experimental challenges presented by this spectral region. We also outline our experimental scheme to generate, route, and detect mid-infrared light, which leverages nonlinear wave mixing to seamlessly convert between telecom and mid-infrared wavelengths. We report our progress on the development of the experimental apparatus and silicon photonic devices. Finally, we show how the unusually large nonlinear couplings strengths made possible by this mid-infrared spectral region allow us to control, shape, and enhance nonlinear optical phenomena for a range of powerful new silicon photonic device physics.

Chapter 2

Stimulated inter-modal Brillouin scattering in silicon

2.1 Introduction

As we explored in Chapter 1, silicon's unique photo-elastic properties make it well suited to Brillouin processes in which pump and Stokes waves co-propagate in a forward scattering geometry. While these interactions can be strong, the phase-matching conditions fundamentally couple the Stokes and anti-Stokes processes in ways that require new strategies to adapt to laser and amplifier technologies. For example, as we derived, engineering Brillouin coupling between distinct optical spatial modes through inter-modal Brillouin scattering changes the dynamics profoundly, yielding single-sideband gain similar to conventional backward stimulated Brillouin scattering. This device physics is within reach if we can develop (1) silicon-based optomechanical waveguides that support large inter-modal couplings and (2) robust mode multiplexers to individually address each optical spatial mode.

Here we demonstrate stimulated inter-modal Brillouin scattering on-chip for the first time. Our monolithic silicon system consists of a multimode optomechanical waveguide that is interfaced with two integrated mode multiplexers. As illustrated by Fig. 2.1B-C, these multiplexers permit efficient and low-crosstalk coupling of pump (ω_p) and signal waves

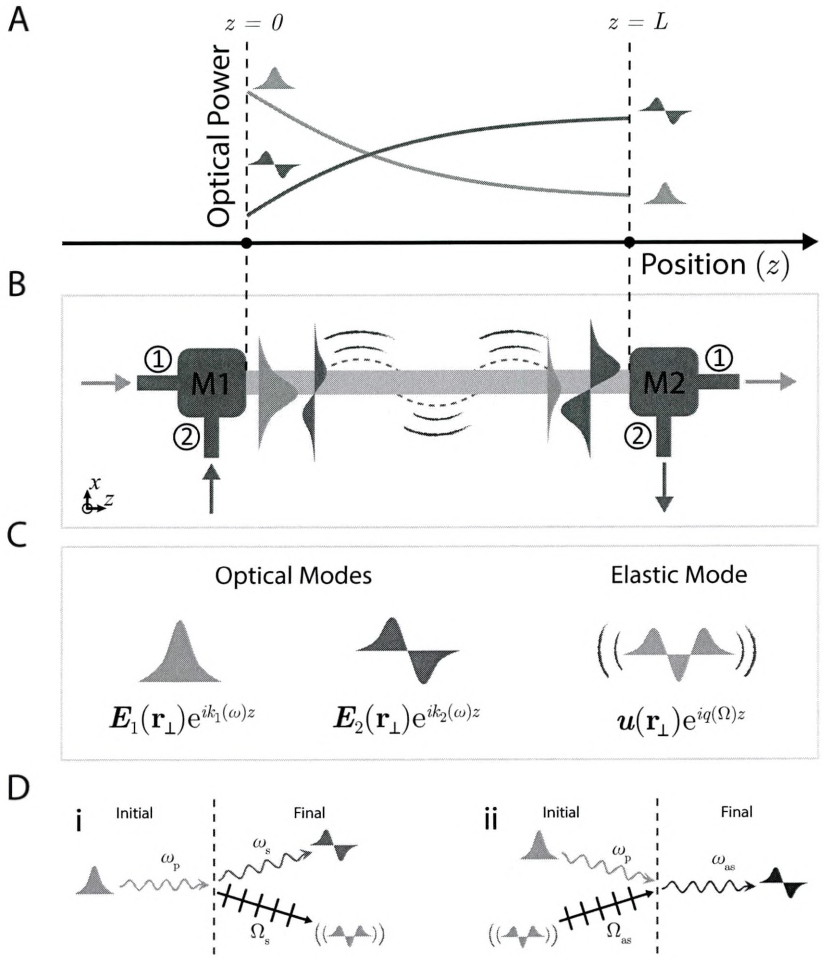

Figure 2.1: (A)-(B) Device concept and operation. Pump (blue) and signal (red) waves are injected into and out of the symmetric and antisymmetric spatial mode, respectively, via integrated mode multiplexers M1 and M2. (A) Nonlinear energy transfer from the pump to the signal wave occurs when the Brillouin condition is satisfied. (C) Diagrammatic representations of the TE-like symmetric and antisymmetric optical spatial modes, as well as the Lamb-like elastic wave. (D) Feynman-like diagrams emphasizing the dynamics of the (Di) Stokes and (Dii) anti-Stokes processes. The inter-modal Stokes process transforms a pump photon in the symmetric mode into a phonon and a red-shifted Stokes photon in the antisymmetric mode. The anti-Stokes process combines the energy of the phonon with the pump photon to produce a blue-shifted anti-Stokes photon propagating in the antisymmetric spatial mode. Adapted from Ref. [29].

(ω_s) into the TE-like symmetric ($\mathbf{E}_1(\mathbf{r}_\perp)e^{ik_1(\omega)z}$) and antisymmetric ($\mathbf{E}_2(\mathbf{r}_\perp)e^{ik_2(\omega)z}$) optical spatial modes of the multimode optomechanical waveguide, respectively. This Brillouin-active segment of the device is also designed to support a Lamb-like elastic wave $\mathbf{u}(\mathbf{r}_\perp)e^{iq(\Omega)z}$ that produces large opto-acoustic overlap. When energy conservation is satisfied (i.e., $\omega_p = \omega_s + \Omega_B$), this traveling elastic wave mediates large inter-modal Brillouin coupling, resulting in significant energy transfer from the pump to signal wave (see Fig. 2.1A).

In what follows, we detail important considerations for (1) the integrated mode multiplexers and (2) the multimode Brillouin-active waveguide.

2.1.1 Integrated mode multiplexers

We employ mode-selective directional couplers to multiplex light into two distinct spatial modes of the multimode optomechanical waveguide [100, 101]. Our design consists of a multimode waveguide of width w_1 and a single-mode bus waveguide of width w_2 that are permitted to couple over a region of length L_c. As illustrated by Fig. 2.2a, light propagating in the single-mode bus waveguide (port 2) is converted into the antisymmetric spatial mode of the multimode waveguide while light injected in the symmetric spatial mode of the multimode waveguide (port 1) remains in the same spatial mode. With proper design parameters, these couplers yield minimal crosstalk due to phase matching. From spatial coupled mode theory [101], we can show that the fraction of light coupled (C) into the higher order mode is given by

$$C = \frac{\kappa_{12}}{k_0} \sin k_0 \tag{2.1}$$

where k_0 is defined by $k_0 = (\kappa_{12}\kappa_{21} + (k_1(\omega) - k_2(\omega))^2/2)^{1/2}$. Here the subscripts 1 and 2 denote the symmetric mode of the bus waveguide and antisymmetric mode of the multimode waveguide, κ_{12} and κ_{21} are the evanescent coupling rates, and $k_1(\omega)$ and $k_2(\omega)$ are the propagation constants of the modes of interest. Eq. 2.1 predicts maximal (unity) coupling when $k_1(\omega) = k_2(\omega)$, a condition that is satisfied when the effective optical indices of the bus and desired mode of the multimode waveguide are equal. It also highlights that both the magnitude and phase of the coupling vary dramatically with effective index mismatch,

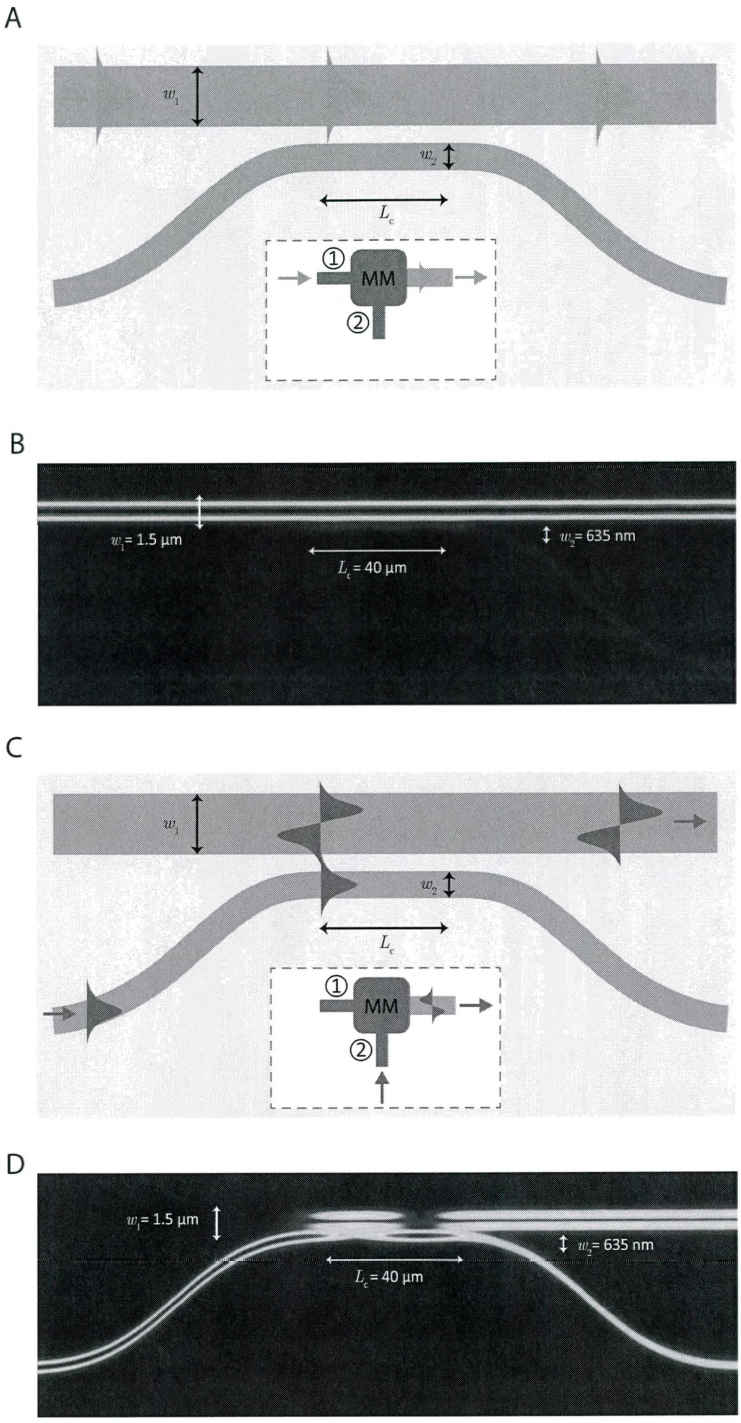

Figure 2.2: Schematic of the mode selective directional coupler (mode multiplexer: MM) when light is injected in (A) port 1 and (C) port 2. 2.5D FDTD simulation of the electric field amplitude, obtained by injecting light into (B) port 1 and (D) port 2, with $> 95\%$ and 78% simulated conversion efficiency, respectively.

permitting large coupling into the desired mode with little crosstalk to other spatial modes. Thus, for high-fidelity mode multiplexers, we seek to simultaneously (1) match the effective index of the single-mode bus waveguide to the effective index of the antisymmetric waveguide mode and (2) create a large index mismatch to prevent undesired coupling to other modes.

We optimize our device parameters through a combination of FDTD simulations (Lumerical 2.5D FDTD) and fabrication splits. Before the mode multiplexer, each port (see insets of Fig. 2.3A,C) begins as a single-mode (450 nm wide) ridge waveguide. To illustrate, we give typical design parameters that yield good performance. The upper waveguide (port 1) is tapered to a multimode width of 1.5 μm while the lower bus waveguide (port 2) is tapered to a width 635 nm such that its effective index closely matches that of the antisymmetric mode of the 1.5 μm waveguide. Using the process outlined in Appendix A, we fabricate the mode multiplexers on a silicon on insulator (SOI) platform using standard SOI techniques. In practice, these directional couplers optimally produce approximately 80% coupling from the bus to the antisymmetric waveguide mode.

Each multiplexer is paired with an identical coupler that demultiplexes the two modes into two spatially separated single-mode waveguides. Through use of a spatial mode filter, any residual light in the antisymmetric waveguide mode that has not been demultiplexed is radiated away at the output (labelled O-1 in Fig. 2.3). Ideally, each port of the multiplexer couples uniquely to its respective mode. In practice, some small amount of light is multiplexed (demultiplexed) into the incorrect mode (port). Figure 2.3A shows a schematic for the crosstalk measurement and the crosstalk for a typical mode multiplexer and demultiplexer in series. These devices admit typical < -15 dB of crosstalk per coupler over large bandwidths, allowing us to address each optical spatial mode of the multimode optomechanical waveguide with high fidelity.

2.1.2 Multimode optomechanical waveguide for stimulated inter-modal Brillouin scattering

Our multimode Brillouin-active waveguide consists of a 1.5 μm ridge waveguide atop a 2.85 μm suspended acoustic membrane (see Fig. 2.4A-D). This optomechanical structure guides low-loss TE-like symmetric and antisymmetric spatial modes, with effective phase indices

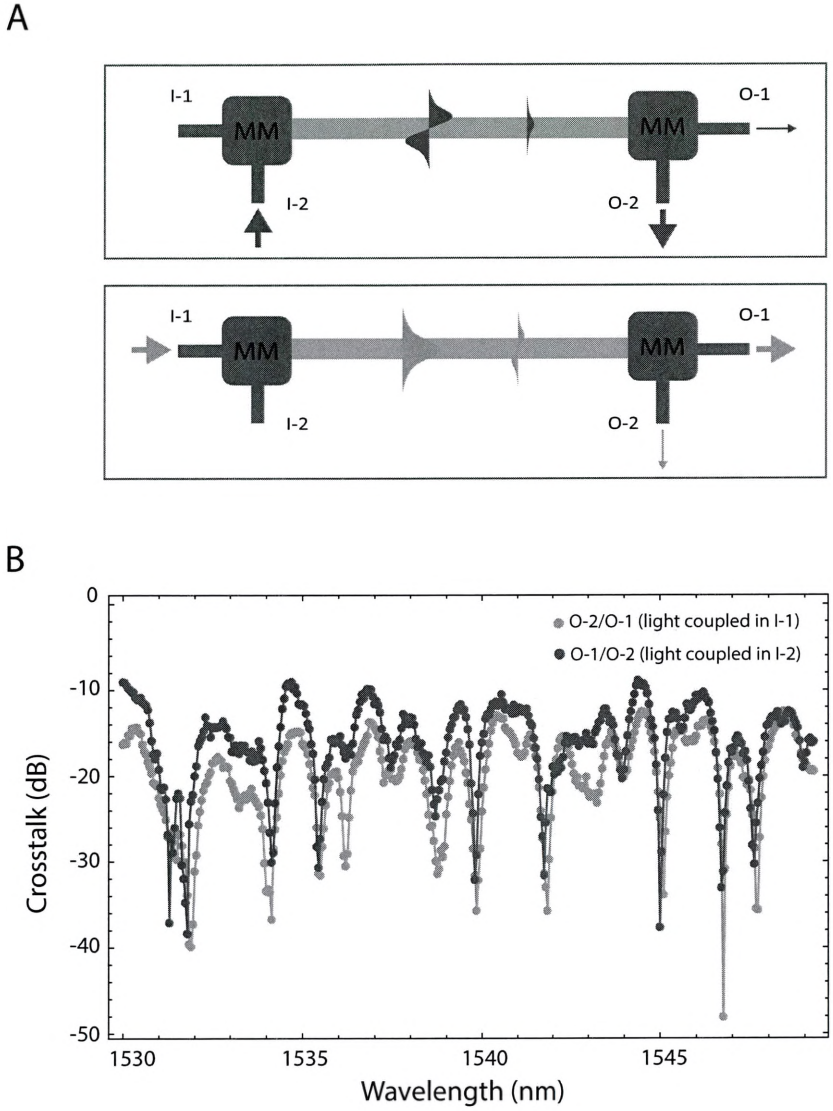

Figure 2.3: (A) Schematic for crosstalk measurement. Light injected into input port (I-1) of the mode multiplexer (MM) is coupled into the fundamental mode with a small amount of light in the first excited mode. Light coupled into input port (I-2) is converted into the first excited mode with some residual light in the fundamental. (B) Typical crosstalk of a multiplexer and demultiplexer in series. Crosstalk is calculated by dividing optical powers at the two output ports (O-1 and O-2). Adapted from Ref. [29].

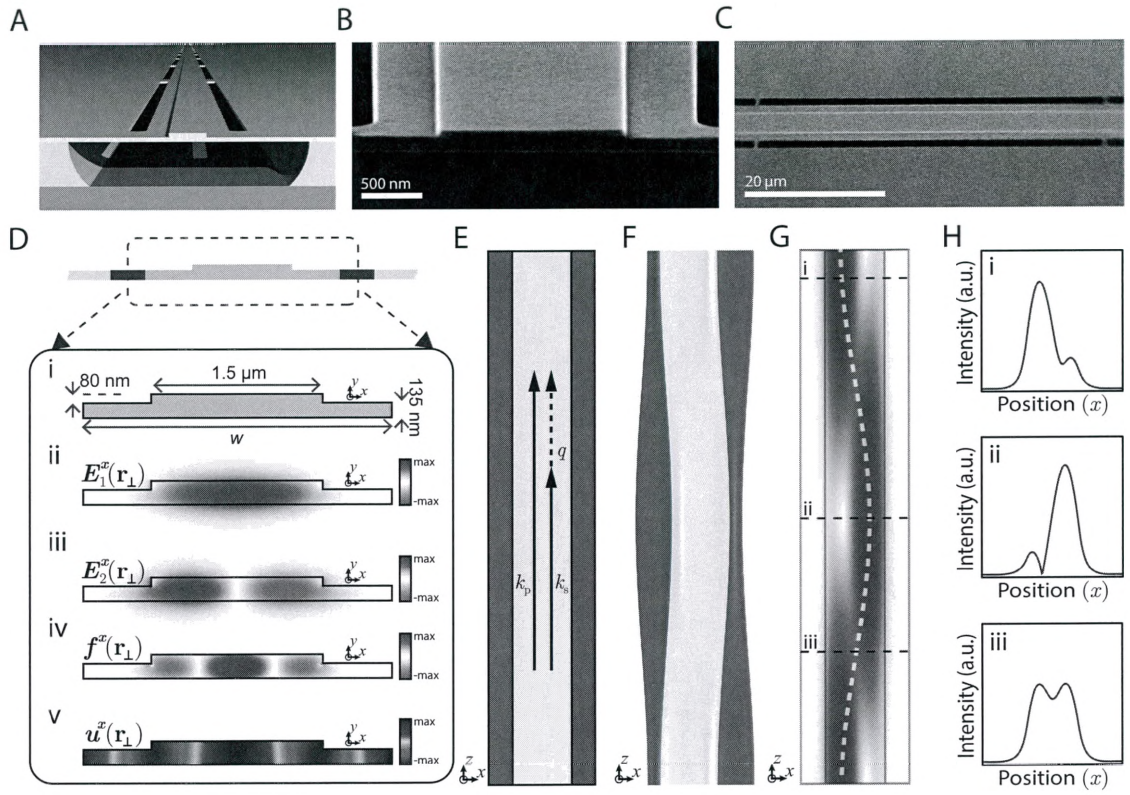

Figure 2.4: (A) Artistic representation of the suspended Brillouin-active waveguide. Scanning electron micrographs of (B) the waveguide cross-section and (C) a top-down view of the suspended waveguide segments. (Di) Waveguide dimensions, supported TE-like (Dii) symmetric and (Diii) antisymmetric optical modes, optical force profile (Div), and (Dv) displacement field of the 6-GHz Brillouin-active elastic mode. (E) Diagram illustrating phase-matching along the propagation direction. (F) Simulated elastic displacement and corresponding (G) optical intensity beat pattern. (H) Intensity profile at three distinct points. Reproduced from Ref. [29].

of 2.8 and 2.7. Simulated electric field profiles for these two fields are displayed in Fig. 2.4Dii-iii.

Pump and signal waves in the symmetric and antisymmetric spatial modes, respectively, produce a time-modulated force profile plotted in Fig. 2.4Div, which drives a Brillouin-active 6-GHz Lamb-like elastic wave with excellent spatial overlap (compare Fig. 2.4Div with Fig. 2.4Dv). Since this is a phase-matched process, the phonon wavelength also matches the characteristic optical beat length, as illustrated by Fig. 2.4E-G. Through the self-reinforcing stimulated process, this system supports large ($G_{\mathrm{B}} = 430 \pm 70$ $\mathrm{W^{-1}m^{-1}}$, simulated) inter-modal Brillouin coupling.

We fabricate devices from a single-crystal silicon-on-insulator (SOI) wafer through a two-step electron-beam lithography process followed by a HF wet etch release (see Appendix A for more details). The Brillouin-active segment is 2.3 cm-long and is comprised of 436 suspended segments supported by an array of nano-scale tethers placed every 50 μm.

2.1.3 Experimental characterization

We characterize inter-modal Brillouin scattering within our waveguide system using heterodyne-based Brillouin spectroscopy, as diagrammed in Fig. 2.5A. All experiments are performed at atmospheric pressure and room temperature. In this system, pump and signal waves are synthesized from the same continuous wave telecom source of frequency ω_{p}; pump light is amplified to a desired power level using an erbium-doped fiber amplifier and variable optical attenuator, while signal light is generated from an intensity modulator sideband of frequency $\omega_{\mathrm{p}} - \Omega$, where Ω is the microwave-frequency drive. Pump and signal waves are subsequently coupled on-chip through distinct grating couplers, which channel light into the respective symmetric and antisymmetric spatial modes of the Brillouin-active waveguide through integrated mode multiplexers. Transmitted signal light is coupled off-chip and combined with a blue-shifted local oscillator ($\Delta = 2\pi \times 44$ MHz) and detected on a high-speed photo-receiver. We sweep the microwave drive frequency Ω and synchronously detect at $\Omega + \Delta$ using a spectrum analyzer, allowing us to characterize Brillouin gain spectrum with Hz-level resolution.

Figure 2.5B plots the stimulated inter-modal Brillouin gain spectrum taken over a 9-GHz

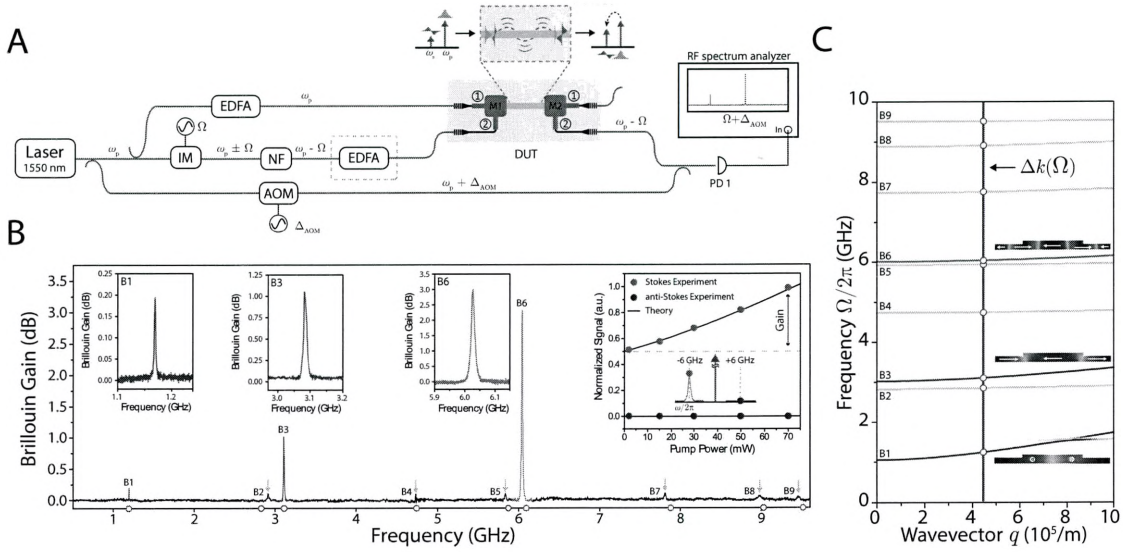

Figure 2.5: (A) Experimental setup for inter-modal Brillouin spectroscopy. A telecom laser is split along three paths to generate (1) an amplified pump using an erbium-doped fiber amplifier (EDFA), (2) a tunable, redshifted signal wave using an intensity modulator (IM) and filter (NF), and (3) a blue-shifted optical local oscillator (LO) using an acousto-optic modulator (AOM) oscillating at $\Delta = 2\pi \times 44$ MHz. The pump and signal waves are injected into the symmetric and antisymmetric waveguide modes of the device under test (DUT). Signal light exiting the chip is combined with the optical LO and detected through heterodyne spectroscopy using a high-speed photo-receiver labelled PD 1. (B) As we sweep the signal-wave frequency, we observe characteristic Brillouin gain spectra from at least 9 Brillouin-active modes. Inset, the signal wave experiences single-sideband gain characteristic of stimulated inter-modal Brillouin scattering. (C) The frequencies of these modes (red circles) agree well with our finite-element simulations. Adapted from Ref. [29].

range. A number of Brillouin-active modes (labelled B1-B9) with distinct flexural, longitudinal, and shear character are observed, each with varying degrees of Brillouin coupling. Consistent with our multi-physics simulations, the elastic mode centered at 6.03 GHz yields the largest Brillouin gain. For the remainder of this section, we focus our characterization on this high-gain Brillouin-active mode.

Due to the dispersive symmetry breaking produced through phase matching, inter-modal Brillouin scattering produces single-sideband gain—in sharp contrast with the dual-sideband dynamics of forward intra-modal Brillouin scattering. We verify this property by analyzing light both at the red and blue-shifted frequencies as we tune the signal frequency through the Brillouin resonance condition. As we increase the pump power, we observe that, while the red-shifted signal wave is amplified, the blue-shifted light does not experience gain, revealing the characteristic single-sideband nature of this process.

We next characterize the power-dependent Brillouin gain and net amplification provided by stimulated inter-modal Brillouin scattering. We perform nonlinear laser spectroscopy on the 6-GHz Brillouin resonance as we increase the pump power over a range of values (see Fig. 2.6B). Figure 2.6Ai-iii plot 3 such spectra with pump powers of 11 mW, 43 mW, and 88 mW, respectively. These spectra reveal a resonance full-width half-maximum (FWHM) of 13 MHz, corresponding to an acoustic quality factor of $Q = \Omega_B/\Delta\Omega = 460$. At a maximum on-chip power of 88 mW, we observe a peak gain of more than 3.5 dB.

To determine the degree of net amplification (i.e., gain relative to total loss), we perform a series of linear and nonlinear loss measurements. Length-dependent passive ring resonator measurements reveal linear propagation losses of 0.24 ± 0.02 dB/cm and 0.3 ± 0.12 dB/cm for the symmetric and antisymmetric spatial modes, respectively. Nonlinear losses—arising primarily from two-photon-absorption (TPA) and TPA-induced free carrier absorption—are determined from a combination of finite-element simulations and power-dependent intra- and inter-modal transmission measurements. Figure 2.6C incorporates these loss mechanisms to calculate the overall amplification of the signal wave. At the highest pump powers, a maximum 3.5 dB of Brillouin gain translates into more than 2.3 dB of net amplification. These measurements, together with our comprehensive loss model, reveal a Brillouin gain coefficient of $G_B = 470 \pm 30$ W^{-1}m^{-1}, in good agreement with our multi-physics simulations

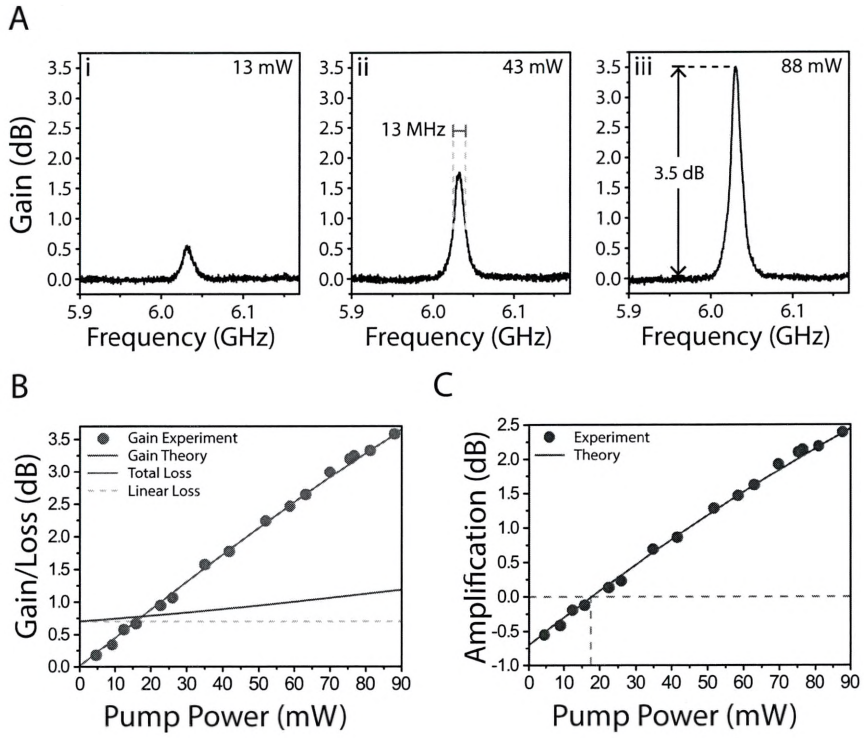

Figure 2.6: (A) Experimental inter-modal Brillouin gain spectra at three distinct optical powers. At a maximum on-chip pump power of 88 mW, we achieve more than 3.5 dB of gain. (B) Peak gain and total loss as a function of pump power. (C) Net amplification as a function of pump power, taking into consideration both linear and nonlinear loss. A peak gain of 3.5 dB corresponds to a net amplification of 2.3 dB. Adapted from Ref. [29].

($G_B = 430 \pm 70$ W^{-1}m^{-1}).

2.2 Outlook: inter-modal Brillouin scattering in silicon

In this chapter, we have demonstrated stimulated inter-modal Brillouin scattering for the first time on chip [29] and harness this interaction to achieve more than 3.5 dB of gain and 2.3 dB of net amplification within an all-silicon waveguide. More generally, we show that inter-modal interactions allow us to shape the Brillouin dynamics as the basis for new silicon-based photonic systems. Here, through a form of dispersive symmetry breaking, we are able to decouple the Stokes from the anti-Stokes process, permitting single-sideband Brillouin gain for the first time in silicon photonics.

These inter-modal nonlinearities open the door to powerful new silicon photonic amplifier technologies. The inherent single sideband nature of this process produces no spurious sidebands that would otherwise encumber amplifiers based on forward intra-modal stimulated Brillouin scattering [23, 72]. Moreover, the new modal degrees of freedom allow us to individually address and independently route pump and signal waves. Using integrated mode multiplexers, the residual pump can be suppressed by more than 25 dB, highlighting the potential for straightforward and modular implementation within integrated silicon photonic circuits.

As we will see in Chapter 3, this interaction is an important step towards the first generation of silicon-based Brillouin lasers. The intrinsic single-sideband gain provided by stimulated inter-modal Brillouin scattering avoids the need for exotic optical resonator geometries that would otherwise be necessary to reach the laser threshold condition with intra-modal forward Brillouin scattering. Moreover, the inter-modal nature of the interactions opens the door to a range of flexible device concepts that leverage mode-specific control, allowing us to tailor the laser dynamics in new and powerful ways.

This new on-chip scattering process is also an essential resource for the development of non-reciprocal optical technologies in silicon. Recent proposals based on time-modulation have suggested the use of phase-matched inter-modal nonlinearities to break reciprocity [32,102], with the potential for ultra-wide non-reciprocal bandwidths [32,102]. To this end,

stimulated inter-modal Brillouin scattering can be viewed as a form of unidirectional mode conversion with an asymmetric scattering matrix [31]. Together with high-performance mode multiplexers, this new scattering process is a crucial step towards isolators and circulators in silicon photonics.

Our ability to translate this device physics into useful Brillouin-photonic technologies will depend upon the extent to which we can control and manipulate these inter-modal interactions. In subsequent chapters, we will develop a variety of strategies to design these Brillouin dynamics according to the desired application. We will use optical feedback to achieve laser oscillation and enhanced amplification (Chapters 3, 4 and 6), design active silicon photonic devices that permit dynamical control of phase and nonlinear loss (Chapters 5), harness spontaneous anti-Stokes processes to engineer noise and dissipation (Chapter 8), and explore mid-infrared wavelengths to radically enhance the available nonlinear coupling strengths (Chapter 9). Together, these new degrees of freedom lay the groundwork for a new range of powerful, CMOS-compatible, Brillouin-based technologies.

Chapter 3

Brillouin lasing in silicon

3.1 Introduction

The use of optical nonlinearities as laser gain media has given rise to a varied array of optically pumped laser oscillators [12], from tunable optical parametric oscillators (OPOs) [103] to femtosecond laser sources [104]. Within the context of photonic technologies, these diverse laser systems—each with unique properties and use cases—have become a key resource to tailor the spectral and coherence properties of light for applications ranging from precision spectroscopy [16, 105, 106] to time-keeping [107].

Among nonlinear-based laser oscillators, Brillouin lasers offer a range of flexible, high-performance dynamics, from frequency-tunable laser emission [52] to mode-locked pulsed operation [108]. In particular, one of the most widely-used characteristics of Brillouin-based laser systems is their ultra-low-noise properties, with intrinsic linewidths that can approach the Schawlow-Townes limit [81, 109, 110]. As discussed in Chapter 2, however, the prospect of silicon-based Brillouin lasers has been out of reach due to two major challenges: (1) substrate induced acoustic dissipation that prevents appreciable Brillouin couplings in conventional silicon photonic waveguides and (2) intrinsic coupling between Stokes and anti-Stokes processes in forward intra-modal SBS that make it nontrivial to reach the laser threshold.

In this Chapter, we overcome these challenges by leveraging the large coupling strengths and single-sideband dynamics of stimulated inter-modal Brillouin scattering (SIMS), de-

scribed in Chapter 2, to demonstrate Brillouin lasing in silicon. Combining the dispersive symmetry breaking provided by SIMS with high-Q multimode racetrack resonators, we are able to achieve large Brillouin gains with low-loss, enabling laser thresholds as low as 11 mW. Moreover, the single-sideband gain and new modal degrees of freedom allow us to develop a robust and highly engineerable Brillouin laser concept that is well-adapted to scalable integration within complex silicon photonic circuits. We also explore in depth the unique and unusual spatio-temporal dynamics of the system, which reveal a form of optical self-oscillation that produces phonon linewidth narrowing—in close analogy with an unusual limit of OPO physics. We will see that this unconventional behavior is made possible by the exceedingly large Brillouin gain and the disparate velocities of light and sound in the system.

3.2 Inter-modal Brillouin laser concept and basic operation

We first describe the essential device concept and operation of our silicon Brillouin laser. The racetrack laser cavity shown in Fig. 3.1A is formed from a multimode waveguide that supports low-loss guidance of both symmetric (red) and antisymmetric (blue) TE-like spatial modes. In this resonant geometry, these two spatial modes yield two corresponding distinct sets of high quality-factor cavity modes. The Brillouin-active regions (dark gray) along the racetrack straights allow the two optical spatial modes to nonlinearly couple through stimulated inter-modal Brillouin scattering (SIMS), as described in Chapter 2. When the Brillouin gain from SIMS is able to compensate for the round-trip optical loss, Brillouin laser oscillation occurs, yielding coherent laser emission at the Stokes frequency ω_s. In the following, we give more details on the Brillouin-gain regions and the multimode resonator properties.

3.2.1 Single-sideband gain through inter-modal Brillouin scattering

As mentioned, optical gain required for laser oscillation is supplied by stimulated inter-modal Brillouin scattering within the the Brillouin-active segments (dark gray) of the racetrack

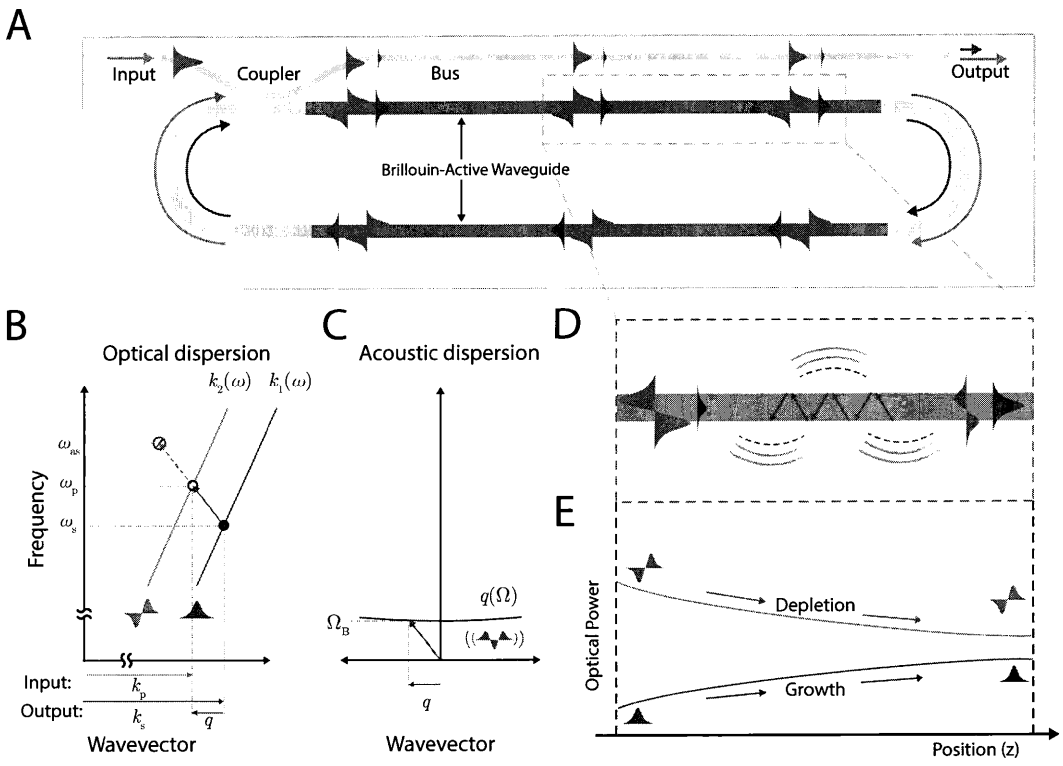

Figure 3.1: Inter-modal Brillouin laser device concept and operation scheme. (A) Diagram of laser cavity (not to scale) with pump and Stokes waves indicated diagrammatically. The Brillouin laser geometry is comprised of a multimode racetrack cavity with two Brillouin-active regions (dark gray). Pump light (blue) is coupled into the antisymmetric spatial mode of the racetrack resonator via a single-mode bus waveguide (directional coupler). Within the racetrack straights, a SIMS-active phonon mediates energy transfer from the pump wave (antisymmetric waveguide mode) to the Stokes wave (symmetric waveguide mode). (B) Idealized dispersion relations for the two optical modes and (C) the Brillouin-active elastic mode of the waveguide. This system supports a phase-matched interaction in which pump light with frequency ω_p and wavevector k_p (plotted as an open circle to indicate initial state) scatters to the Stokes wave with frequency ω_s and wavevector k_s (final state indicated by a closed circle). Here, the Brillouin-active phonon vector defined by $(q(\Omega), \Omega)$ must connect the initial and final optical state coordinates. As highlighted by the red no symbol, this phonon, once excited cannot mediate the anti-Stokes process as there is no optical dispersion relation that can satisfy phase matching. (D) and (E) illustrate SIMS energy transfer in the Brillouin-active racetrack straight where an acoustic phonon mediates pump depletion and Stokes growth. Reproduced from Ref. [96].

resonator (Fig. 3.1D). In the standard mode of operation, a pump wave traveling in the antisymmetric mode (ω_p) produces amplification of the Stokes wave propagating in the symmetric mode (ω_s) (see Figs. 3.1D-E). This particular configuration is chosen such that the Stokes wave propagates in the waveguide mode with the least propagation loss. Note that while opposite of the configuration described in Chapter 2, the dispersive symmetry breaking and single-sideband dynamics are functionally equivalent, as we will see below.

Nonlinear coupling from stimulated inter-modal Brillouin scattering is conditioned on both the energy conservation ($\omega_p = \omega_s + \Omega_B$) and phase-matching conditions ($k_2(\omega_p) = k_1(\omega_s) + q(\Omega_B)$). Combining these two requirements yields

$$k_2(\omega_p) = k_1(\omega_p - \Omega_B) + q(\Omega_B). \tag{3.1}$$

As discussed in Chapter 1, these conditions can be succinctly represented using the 2-dimensional diagram shown in shown in Fig. 3.1B-C. The acoustic phonons that mediate stimulated inter-modal Brillouin scattering must belong to the acoustic dispersion curve, $q(\Omega)$, (Fig. 3.1C) and bridge the frequency and wavevector gap between the initial (open circle; $(k_2(\omega_p), \omega_p)$) and final (solid circle; $(k_2(\omega_p), \omega_p)$) optical states that lie on the dispersion curves for the antisymmetric and symmetric optical spatial modes, respectively. Since the effective optical index of refraction is larger for the symmetric spatial mode, this means that the Brillouin-active phonon in this configuration must be backward propagating. Note that this phonon cannot mediate the anti-Stokes process (for further discussion, see Chapter 1), which would require a forward-propagating phonon.

3.2.2 Multimode racetrack resonator properties

We next detail the linear optical properties of our racetrack system. Here, the two different propagation constants of the symmetric ($k_1(\omega)$) and antisymmetric ($k_2(\omega)$) spatial modes yield two distinct sets of resonance conditions within a cavity of circumference L, namely

$$\begin{aligned} k_1(\omega_1^n)L &= 2\pi n \\ k_2(\omega_2^m)L &= 2\pi m, \end{aligned} \tag{3.2}$$

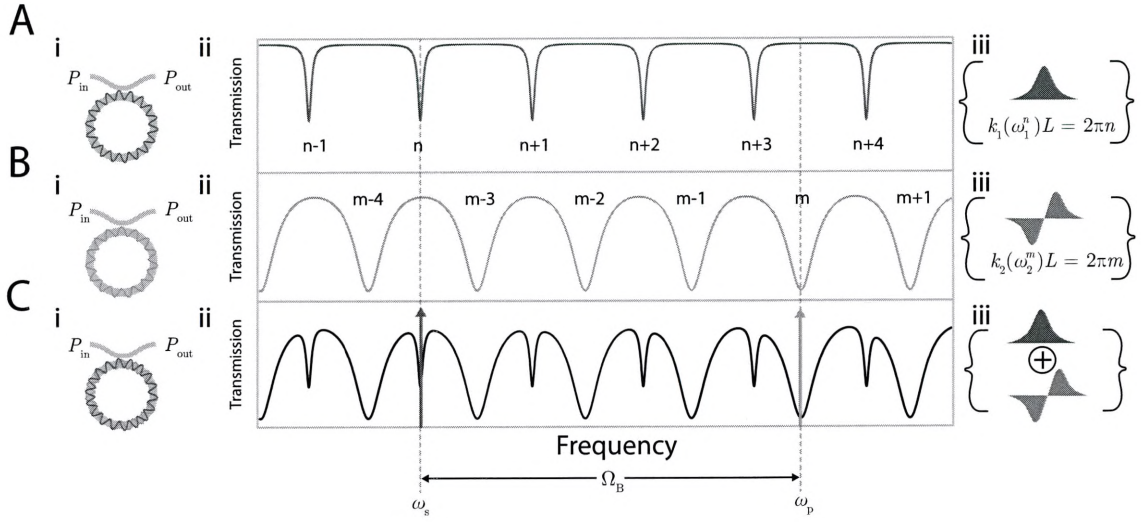

Figure 3.2: Passive optical properties of multimode silicon resonator. (A-C) Idealized transmission spectrum for the multimode ring cavity in the case when (A) $\mu_2 = 0$, (B) $\mu_1 = 0$, and (C) $\mu_2 > \mu_1 > 0$. (A) Transmission spectrum produced by the symmetric waveguide mode (Ai). Cavity resonances are indexed by the letter n (Aii), according to the resonance condition (Aiii). (B) Transmission spectrum produced by the antisymmetric mode (Bi), with cavity resonances indexed by m (Bii). The resonance condition for this mode is given in (Biii). (C) Idealized transmission spectrum in the case of non-zero coupling to both waveguide modes. Due to the different loss rates of the two optical spatial modes, broader (narrower) resonant features correspond to the antisymmetric (symmetric) resonances of the racetrack system. (Cii) Brillouin lasing requirements are met by injecting pump light (of power P_p) into an antisymmetric cavity mode that is separated in frequency from a symmetric cavity mode by the Brillouin frequency (i.e., $\omega_2^m - \omega_1^n = \Omega_B$). Adapted from Ref. [96].

where $\{\omega_1^n\}$ and $\{\omega_1^m\}$ are the resonant frequencies of the cavity modes produced by the symmetric and antisymmetric optical spatial modes of the waveguide. Fig. 3.2A-B depicts the distinct resonance conditions and idealized transmission spectrum for each transverse spatial mode. The directional coupler depicted in Fig. 3.1A provides evanescent coupling to both spatial waveguide modes.[1] Thus, sweeping the optical frequency yields a characteristic multimode spectrum of the type illustrated in Fig. 3.2C.

3.2.3 Condition for laser oscillation

As we discuss in Section 3.4.1, the conditions for laser oscillation are met when the Brillouin gain supplied through stimulated inter-modal Brillouin scattering matches the round-trip loss for the Stokes wave. Within this inter-modal system, we inject pump light (of power P_p) into an antisymmetric cavity mode (ω_2^n) that is separated in frequency from a symmetric cavity mode (ω_1^m) by the Brillouin frequency (i.e., $\omega_2^m - \omega_1^n = \Omega_\mathrm{B}$). Above the laser threshold, laser oscillation of the Stokes wave is initiated by thermal-mechanical fluctuations. Stokes radiation is then emitted from the cavity through the directional coupler.

3.2.4 Advantages relative to conventional BSBS lasers

We pause here to discuss the unique properties and fundamental distinctions of this Brillouin laser design relative to prior Brillouin laser systems. As described above, this silicon Brillouin laser is based on a forward inter-modal Brillouin process, yielding Stokes emission in the forward direction. This is entirely different from conventional Brillouin lasers based on backward SBS, which produce Stokes laser emission in the backward direction. When assessing the prospect of integration on-chip, this conventional backward propagating operation presents a significant challenge; such Brillouin lasers would likely require on-chip circulators and isolators—components that are not widely available in integrated photonics—to protect the pump laser from unwanted feedback. In this context, the forward-scattering geometry enabled by this new inter-modal Brillouin laser concept avoids the need for isolators or circulators, making integration practical and feasible for the first time.

1. The design and coupling rates are similar to those of the mode multiplexer presented in Section 2.1.1.

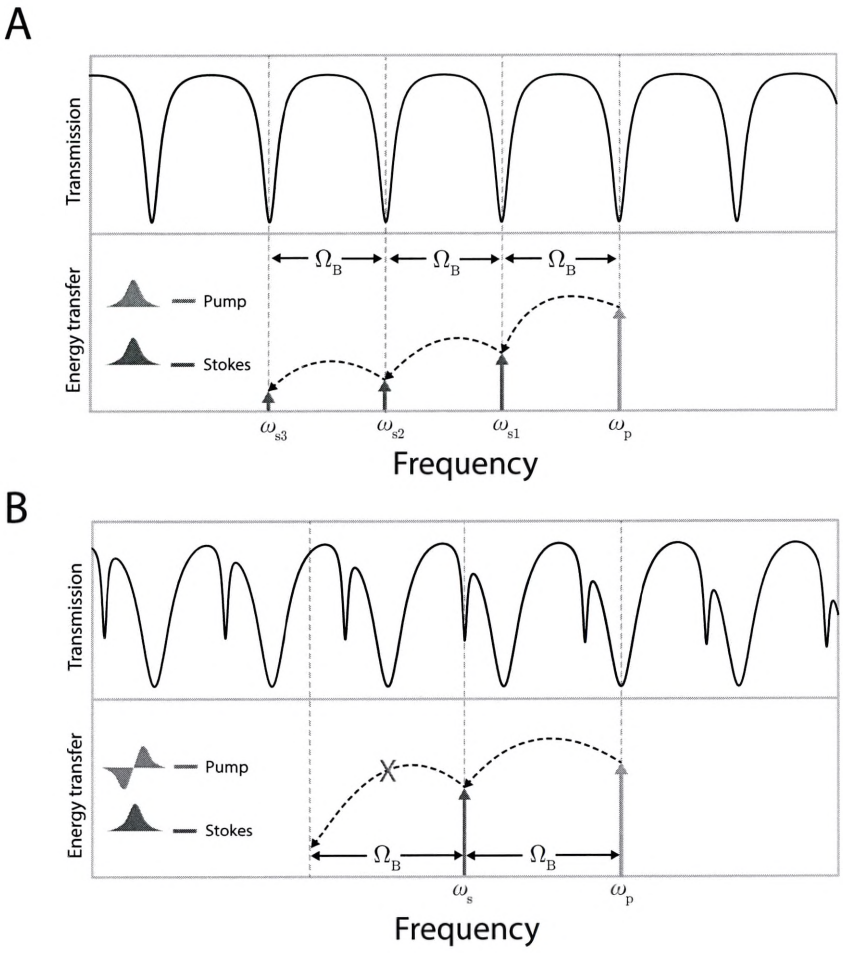

Figure 3.3: (A) Cascading dynamics of a conventional backward Brillouin laser, where pump and Stokes fields counter-propagate within the same optical spatial mode of the resonator waveguide. Except in the case of large higher-order dispersion, meeting the Brillouin condition with one pair of optical resonances implies that the Brillouin condition is also satisfied for successively redshifted resonances. Thus, above a certain threshold condition, BSBS lasers will produce cascaded energy transfer to many Stokes sidebands. By contrast, our inter-modal Brillouin laser concept (B) allows us to control and suppress unwanted cascaded through multimode engineering. Here, the second Stokes order is not supported by a cavity mode, preventing cascaded energy transfer.

Furthermore, this inter-modal Brillouin laser offers new degrees of design and control that are not possible with conventional Brillouin lasers based on BSBS. In particular, the multimode nature of the inter-modal Brillouin design gives us the potential to independently access the pump and Stokes modes; we utilize these new degrees of freedom in Chapters 4-6. Additionally, this multimode geometry allows us to independently control the dissipation rates of and relative spacing between pump and Stokes modes. This is in stark contrast to traditional BSBS lasers, where the pump and Stokes circulate within cavity modes produced by the same spatial waveguide mode, and as such, there is little control over the relative dissipation rates. In this BSBS case, the pump and Stokes waves have near-identical dissipation rates, as shown in Fig. 3.3A, which can actually limit performance. For instance, if the Stokes wave becomes strong enough in conventional systems, it can reach the lasing threshold to produce cascaded energy transfer to successive Stokes orders (see Fig. 3.3A). In contrast, this inter-modal system allows us to precisely control the degree to which cascading can or cannot occur. For example, by tailoring the Q-factor of the pump wave, we can precisely engineer the Stokes-power threshold required for cascaded energy transfer. Alternatively, we can completely suppress cascading by engineering the mode spectrum such that the 2^{nd} Stokes order wave is not supported by a cavity mode, as shown in Fig. 3.3B. In this way, we are able to completely suppress cascading in our system.

This inter-modal laser concept also offers flexibility in design and performance that would otherwise be difficult to achieve with conventional Brillouin lasers based on BSBS. In particular, since amplification in this laser system is produced through a form of guided-wave form of Brillouin scattering, it is quite straightforward to change the resonance frequency, Brillouin coupling, and even acoustic dissipation rate through geometry [30, 111]. Additionally, the multimode nature of this inter-modal Brillouin interaction permits remarkable flexibility in the laser cavity design relative to BSBS systems. In conventional lasers based on BSBS, the Brillouin frequency must equal an integer number of the FSR of the cavity, constraining the cavity length to $L = 2\pi n v_{\text{g}}/\Omega_{\text{B}}$, where n is an integer. By contrast, this new inter-modal Brillouin laser concept permits a cavity length that is entirely unconstrained; since the group velocities of the symmetric and antisymmetric spatial modes are distinct, the spacing between modes changes with frequency. As a result, there will always

exist a pair of modes that satisfies the Brillouin condition regardless of the cavity length. This new degree of freedom gives us great flexibility in the laser design. For example, by reducing the footprint and increasing the cavity finesse, we can significantly increase the resonant pump-power enhancement, thereby dramatically lowering the laser threshold.

3.3 Results: Laser characterization

We fabricate silicon-based inter-modal Brillouin laser devices using a standard silicon-on-insulator (SOI) process (see Fig. 3.4A and Fig. 3.5; also Appendix A). The laser cavity is formed from a multimode waveguide that is fashioned into a racetrack geometry. Through total internal reflection, this silicon waveguide supports low-loss propagation of TE-like symmetric and antisymmetric spatial modes. Within the Brillouin-active regions of the device (Fig. 3.4B), the oxide undercladding is removed such that the optomechanical structure also guides a 6-GHz elastic wave that mediates large Brillouin coupling. This waveguide is mechanically supported by an array of nano-scale tethers, as shown in Fig. 3.4A, and the cross-sectional geometry is chosen after the same design described in Chapter 2, yielding a Brillouin gain of $G_{\mathrm{B}} \cong 470\ \mathrm{W}^{-1}\mathrm{m}^{-1}$ with a bandwidth (acoustic linewidth) of approximately 13 MHz.

3.3.1 Passive optical properties

The design of the silicon laser resonator (diagrammed in Fig. 3.4A) (1) yields numerous pairs of modes that satisfy the Brillouin condition and (2) maximizes the Brillouin gain while minimizing the optical loss. The experimental parameters for this system are contained in Appendix B. In particular, the device we characterize in this Chapter has a circumference of 4.576 cm (see Fig. 3.5), yielding cavity free spectral ranges (FSRs) of 1.614 GHz and 1.570 GHz for the symmetric and antisymmetric modes, respectively. Thus, since the group velocities and FSRs differ by 3.1%, pairs of symmetric and antisymmetric cavity modes that satisfy the Brillouin condition occur every 0.4 nm. Of the entire device circumference, more than 97% is suspended in order to maximize the Brillouin gain supplied by stimulated inter-modal Brillouin scattering. In addition, the aforementioned directional coupler is designed

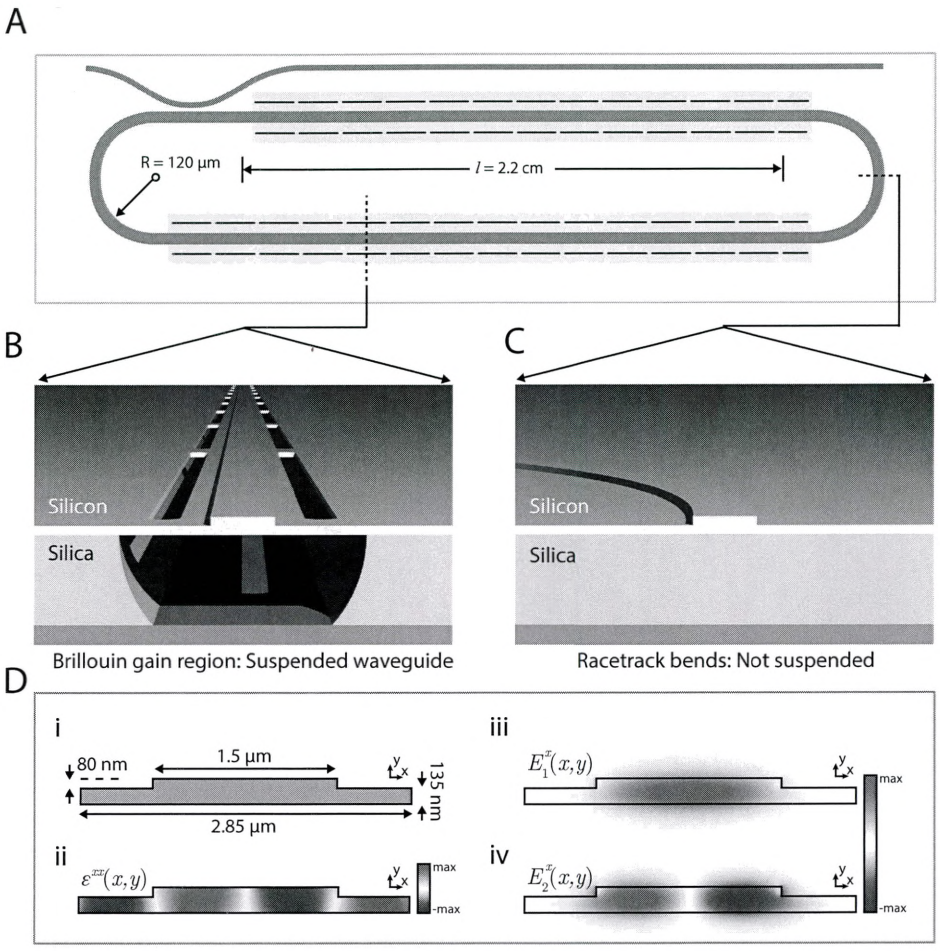

Figure 3.4: (A) Diagram of the silicon Brillouin laser cavity with relevant dimensions (not to scale). As diagrammed, the Brillouin-active regions are composed of continuously-suspended photonic-phononic waveguides supported by an array of nano-scale tethers (see slotted waveguide sections). Panel (B) shows a cross-section of the suspended Brillouin-active waveguide segment while (C) plots the laser cross-section near the racetrack bends (where the multimode waveguide is not suspended). The presence of the oxide under-cladding has negligible impact on the guidance of the optical modes, but does not permit phononic guidance around the bends. (Di) Dimensions of the suspended Brillouin-active waveguide. (Dii) Strain profile $\epsilon^{xx}(x, y)$ of the 6 GHz Lamb-like acoustic mode that mediates the inter-modal Brillouin scattering process. (Giii) and (Giv) plot the x-directed electric field profiles (E^x) of the TE-like symmetric and antisymmetric optical modes, respectively. Adapted from Ref. [96].

to preferentially couple to the antisymmetric spatial mode. This design ensures that we can readily couple the pump wave into an antisymmetric cavity mode while only nominally increasing the symmetric mode loss rate, keeping the laser threshold within reach.

We determine both the linear losses and the directional coupler properties from passive transmission spectra in conjunction with our theoretical model (see Supplementary Materials Section 3 of Ref. [96]). Through these measurements, we identify optical Q-factors for the cavity modes produced by the symmetric and antisymmetric waveguide modes of 2.4×10^6 and (4×10^5), respectively. Fitting the transmission spectra also reveals bus-ring coupling of $\mu_1^2 = 0.06$ ($\mu_2^2 = 0.71$) and linear loss rates of 0.26 dB cm^{-1} (0.69 dB cm^{-1}) for the symmetric (antisymmetric) mode. Taking into consideration the Brillouin gain of the system (see Chapter 2), we estimate a threshold pump power as low as 9 mW (18 mW intracavity).

3.3.2 Laser threshold, slope efficiency, and spectrum

A characteristic laser chip under test is shown in Fig. 3.5. Experiments are conducted at room temperature using the apparatus in Fig. 3.6A. A continuous-wave (CW) pump wave (ω_p) is generated by a tunable external cavity laser (Agilent 81600B) around a vacuum wavelength (λ_p) of 1535 nm. The pump power is controlled by an erbium-doped fiber amplifier (EDFA) and a variable optical attenuator. To initiate laser oscillation, the pump wave is coupled into an antisymmetric cavity mode that is separated in frequency from a symmetric cavity mode by the Brillouin frequency. As the pump wave power is increased, spontaneous Stokes scattering from thermal-mechanical noise becomes coherent laser oscillation above the laser threshold. The Stokes radiation is then emitted from the cavity through the directional coupler, and subsequently routed off-chip for heterodyne spectral analysis.

Fig. 3.6A diagrams the experimental apparatus used for high-resolution spectral analysis of the emitted Stokes light. We use a frequency-shifted reference ($\omega_\mathrm{p} + 2\pi \times 44$ MHz) as an optical local oscillator (LO) for heterodyne spectroscopy. Using a high-speed detector and radio-frequency spectrum analyzer, this approach allows us to measure both the spectrum and total power of the emitted Stokes light in the microwave domain.

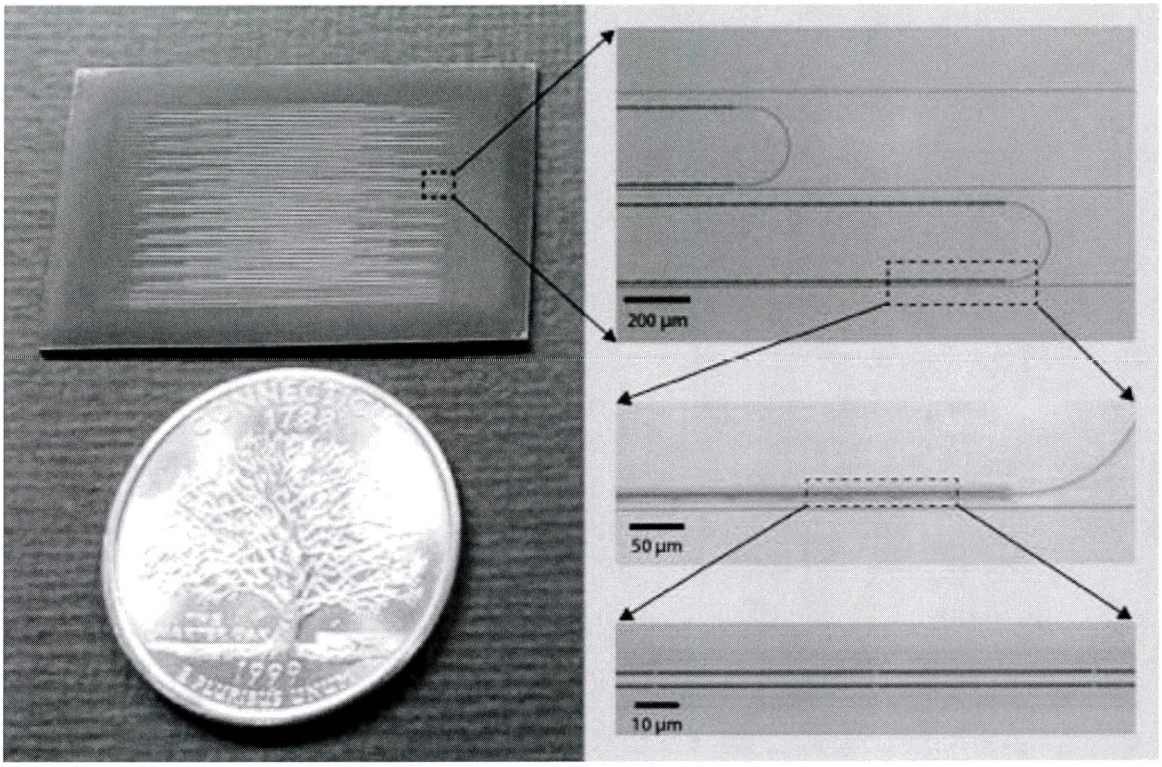

Figure 3.5: (Left) Image of typical Brillouin laser chip. Brillouin laser devices are fabricated on standard single-crystal silicon-on-insulator wafers. Coin juxtaposed to show scale. (Right) Series of optical micrographs with different magnifications, highlighting the large range of scales of this system. The total resonator dimensions in this system can exceed 4 cm, in contrast to the micron-scale Brillouin-active waveguide. Note that the slight contrast in coloration reveals the suspended regions of the device.

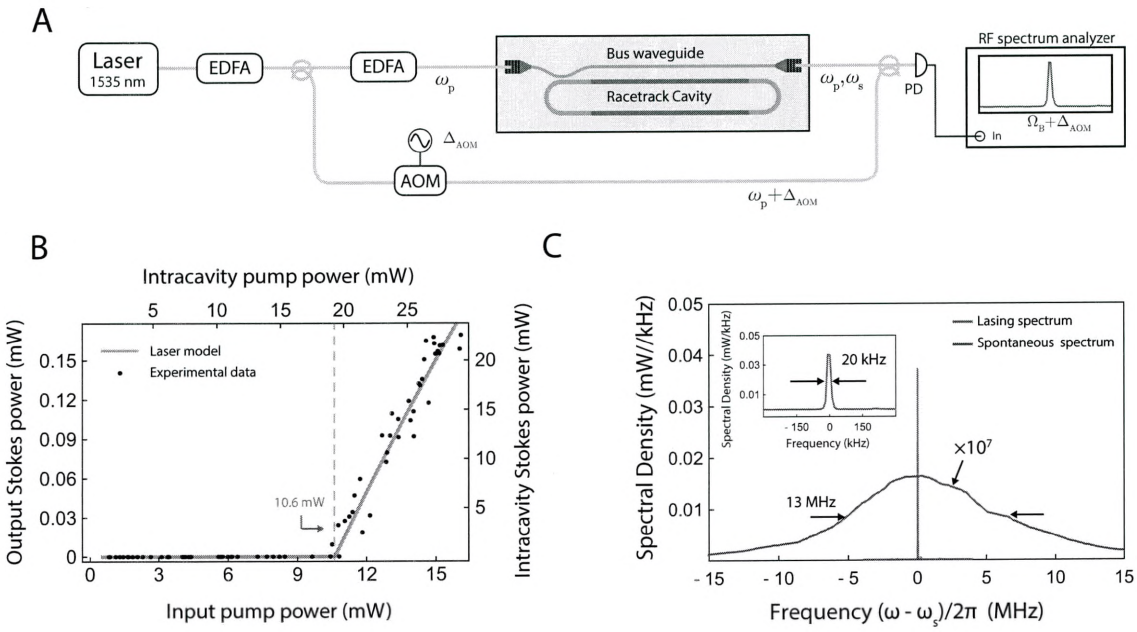

Figure 3.6: (A) Heterodyne apparatus used for laser spectroscopy. Continuous-wave pump light (Agilent 81600B, linewidth = 13 kHz) is (1) amplified and coupled on-chip to initiate Brillouin lasing and (2) and used to create a frequency-shifted (+44 MHz) local oscillator (LO) using an acousto-optic modulator (AOM). The optical beat note between the emitted Stokes light and optical LO is detected by a fast photodiode, and its spectrum is recorded by a radio frequency spectrum analyzer. EDFA: erbium doped fiber amplifier; PD: photodetector. Panel (B) plots theory and experiment for the output laser power vs. input pump power, with a clear laser threshold of 10.6 mW. Intracavity pump powers are estimated using the transmitted pump power and the detuning from resonance (ω_2^n), while intracavity Stokes power is determined from the measured bus Stokes power and comparison with the theoretical model. (C) Heterodyne spectra the linewidth-narrowed intracavity laser emission above threshold compared with the spontaneous Brillouin scattering spectrum (multiplied by 10^7), demonstrating a linewidth narrowing factor of approximately 10^3. The spontaneous spectrum determines the intrinsic Brillouin gain bandwidth (13.1 MHz) and is obtained from the linear waveguide of the same cross section as the laser waveguide. From Ref. [96]. Reprinted with permission from AAAS.

We use this heterodyne scheme to perform power and linewidth measurements of the output Stokes wave as a function of injected pump power. Figure 3.6C plots the emitted Stokes-wave power as the pump-wave power is increased. This slope efficiency data exhibits a threshold value of 10.6 mW (19 mW intracavity) and a slope efficiency of 3%. We also observe dramatic spectral narrowing of the heterodyne spectrum above the laser threshold, compressing a 13 MHz spontaneous spectrum to a resolution-bandwidth limited value of 20 kHz (3.6B).

3.4 Spatio-temporal dynamics

We next present an analytical framework to capture the spatio-temporal dynamics of this system. We first explore the spatial dynamics of this Brillouin laser through a steady-state analysis. This approach allows us to identify the origin of laser oscillation in this system and derive the threshold condition. We also show that the spatial behavior of this system is characteristic of other Brillouin lasers. Following our investigation of the spatial dynamics, we make a series of approximations to develop a mean-field model of the laser physics — a reduction that is sufficient to capture the salient temporal dynamics and linewidth narrowing properties. In particular, we show that in contrast to the temporal dynamics conventionally exhibited in Brillouin lasers, optical self-oscillation in this system yields phonon linewidth narrowing.

3.4.1 Spatial dynamics

In virtually all Brillouin systems, the phonon field decays rapidly in space ($\sim$ 100 μm) relative to the optical fields (see also Chapter 1). As such, the phonon field can be adiabatically eliminated in space; to an excellent approximation, the phonon field can be described by local optical beat note between pump and Stokes fields (see also Section 1.3.2). These dynamics naturally result in exponential spatial amplification for the Stokes field [12,13]. In the following, we show that the spatial dynamics of this silicon Brillouin laser are consistent with other Brillouin lasers. We also derive the threshold condition and show that laser oscillation occurs when round-trip optical Brillouin gain balances round-trip optical loss of

the Stokes wave.

We begin our analysis with the envelope equations of motion [75,77] described in Chapter 1, given by

$$\dot{A}_{\mathrm{p}} + i\omega_{\mathrm{p}}A_{\mathrm{p}} + v_{\mathrm{g,p}}A'_{\mathrm{p}} + \frac{1}{2}v_{\mathrm{g,p}}\alpha_{\mathrm{p}}A_{\mathrm{p}} = -ig_{\mathrm{s,p}}A_{\mathrm{s}}B \tag{3.3}$$

$$\dot{A}_{\mathrm{s}} + i\omega_{\mathrm{s}}A_{\mathrm{s}} + v_{\mathrm{g,s}}A'_{\mathrm{s}} + \frac{1}{2}v_{\mathrm{g,s}}\alpha_{\mathrm{s}}A_{\mathrm{s}} = -ig^{*}_{\mathrm{s,p}}A_{\mathrm{p}}B^{\dagger} \tag{3.4}$$

$$\dot{B} + (i\Omega_{\mathrm{B}} + \frac{1}{2}\Gamma)B - v_{\mathrm{g,b}}B' = -ig^{*}_{\mathrm{s,p}}A_{\mathrm{p}}A^{\dagger}_{\mathrm{s}}, \tag{3.5}$$

where $(\,)'$ denotes the partial spatial derivation $\partial/\partial z$; A_{p}, A_{s}, and B describe the spatio-temporal dynamics of the pump, Stokes, and phonon fields (without explicit reference to the arguments (z,t)), each with natural frequencies ω_{p}, ω_{s}, and Ω_{B}, respectively. $g_{\mathrm{s,p}}$ is the traveling-wave elasto-optic coupling rate, $v_{\mathrm{g,p}}$ ($v_{\mathrm{g,s}}$) is the group velocity of the pump (Stokes) field, $v_{\mathrm{g,b}}$ is the group velocity of the phonon field, and α_{p} (α_{s}) is the spatial decay rate of the pump (Stokes) field in the inter-modal waveguide. For the moment, we neglect noise to simplify our analysis of the laser threshold condition. We return to the noise dynamics for our mean-field analysis of the temporal dynamics in Section 3.4.2.

We derive the steady-state spatial dynamics of the Brillouin laser system by moving to the rotating frame such that

$$A_{\mathrm{p}}(z,t) \equiv \bar{A}_{\mathrm{p}}(z,t)\exp\left(-i\omega_{\mathrm{s}}t\right) \tag{3.6}$$

$$A_{\mathrm{s}}(z,t) \equiv \bar{A}_{\mathrm{s}}(t)\exp\left(-i\omega_{\mathrm{p}}t\right) \tag{3.7}$$

$$B(z,t) \equiv \bar{B}(z,t)\exp\left(-i\Omega_{\mathrm{B}}t\right), \tag{3.8}$$

where $\bar{A}_{\mathrm{p}}(z,t)$, $\bar{A}_{\mathrm{s}}(z,t)$, $\bar{B}(z,t)$ are now the slowly varying envelopes in space and time.[2] For simplicity, we next assume that the resonant Brillouin condition is satisfied (i.e., $\omega_{\mathrm{p}} = \omega_{\mathrm{s}} + \Omega_{\mathrm{B}}$) and that the pump remains undepleted below the laser threshold (i.e., $\bar{A}_{\mathrm{p}}(z,t) = A_{\mathrm{p}}$). Analyzing the system in its steady state yields

2. We remind the reader that, as in Chapter 1, we have factored out the phase associated with the central wavevector of each field.

$$v_{\mathrm{g,s}}\bar{A}_{\mathrm{s}}' = -ig_{\mathrm{s,p}}^{*}A_{\mathrm{p}}\bar{B}^{\dagger} - \frac{1}{2}v_{\mathrm{g,s}}\alpha_{\mathrm{s}}\bar{A}_{\mathrm{s}} \tag{3.9}$$

$$-v_{\mathrm{g,b}}\bar{B}' = -ig_{\mathrm{s,p}}^{*}A_{\mathrm{p}}\bar{A}_{\mathrm{s}}^{\dagger} - \frac{1}{2}\Gamma\bar{B}. \tag{3.10}$$

From these governing equations, the integral solution $\bar{B}(z)$ is given by

$$\bar{B}(z) = \frac{-ig_{\mathrm{s,p}}^{*}A_{\mathrm{p}}}{v_{\mathrm{g,b}}}\int_{z}^{L} dz'\bar{A}_{\mathrm{s}}^{\dagger}(z')e^{\frac{\Gamma(z-z')}{2v_{\mathrm{g,b}}}}. \tag{3.11}$$

By recognizing that the Stokes wave varies very slowly compared to the spatial decay length of the phonon field, we are able to pull the Stokes envelope out of the integral under the Markov (two-scale) approximation, resulting in a simple spatial solution of the phonon field:

$$\bar{B}(z) \cong \frac{-2ig_{\mathrm{s,p}}^{*}}{\Gamma}A_{\mathrm{p}}\bar{A}_{\mathrm{s}}^{\dagger}(z)(1 - e^{\frac{-\Gamma(L-z)}{2v_{\mathrm{g,b}}}}). \tag{3.12}$$

In the case that the device length far exceeds the phonon coherence length (i.e., $(L-z) \gg \frac{v_{\mathrm{g,b}}}{\Gamma}$, well-satisfied in the present system), we can approximate the phonon field as

$$\bar{B}(z) \cong \frac{-2ig_{\mathrm{s,p}}^{*}}{\Gamma}A_{\mathrm{p}}\bar{A}_{\mathrm{s}}^{\dagger}(z). \tag{3.13}$$

Equation 3.13 reveals that the phonon field strength at z ($B(z)$) is given by the local pump-Stokes beat note $A_{\mathrm{p}}\bar{A}_{\mathrm{s}}^{\dagger}(z)$. These spatial dynamics are common to practically all Brillouin systems, as discussed in standard nonlinear optics textbooks (see [12, 13]). We can now insert our solution for $\bar{B}(z)$ into the equation of motion for the Stokes field, which becomes

$$\bar{A}_{\mathrm{s}}' = \frac{2|g_{\mathrm{s,p}}|^2|A_{\mathrm{p}}|^2}{v_{\mathrm{g,s}}\Gamma}\bar{A}_{\mathrm{s}} - \frac{\alpha_{\mathrm{s}}}{2}\bar{A}_{\mathrm{s}}. \tag{3.14}$$

We recast Eq. 3.14 in terms of the Brillouin gain coefficient defined by $G_{\mathrm{B}} = 4|g_{\mathrm{s,p}}|^2 /(\hbar\omega_{\mathrm{p}}\Gamma v_{\mathrm{g},1}v_{\mathrm{g},2})$.[3] With this substitution, the solution to Eq. 3.14 is given by

$$\bar{A}_{\mathrm{s}} = C_1 e^{(\frac{G_{\mathrm{B}}P_{\mathrm{P}}}{2} - \frac{\alpha_{\mathrm{s}}}{2})z}, \tag{3.15}$$

where the boundary conditions determine the value of C_1. The Stokes cavity is formed by fashioning a multimode waveguide into a racetrack ring configuration with an input/output coupler. Consistent with the physical parameters of the device under study, here we apply no acoustic feedback.[4] The boundary condition is therefore expressed as

$$\bar{A}_{\mathrm{s}}(0) = -i\mu A_{\mathrm{s,in}} + r\bar{A}_{\mathrm{s}}(L). \tag{3.16}$$

Here, μ^2 represents the coupling into/out of the ring and r parameterizes the fraction of light that feeds back into the ring after the coupler ($r = \sqrt{1-\mu^2}$). In our laser, there is no input Stokes light, and thus in this simple analysis, $A_{\mathrm{s,in}}$ is a proxy for the noise that initiates laser oscillation. Applying this boundary condition, we find that the solution for the Stokes field envelope is given by

$$\bar{A}_{\mathrm{s}}(z) = \frac{-i\mu A_{\mathrm{s,in}}}{1 - re^{\frac{(G_{\mathrm{B}}P_{\mathrm{P}} - \alpha_{\mathrm{s}})L}{2}}} e^{\frac{(G_{\mathrm{B}}P_{\mathrm{P}} - \alpha_{\mathrm{s}})z}{2}}. \tag{3.17}$$

This is the main result of this section. Here we wish to make a couple of important

3. We can reparameterize the Brillouin gain by noting that $P_{\mathrm{p}} = \hbar\omega_{\mathrm{p}}v_{\mathrm{g},2}|\bar{A}_{\mathrm{p}}|^2$ such that $G_{\mathrm{B}} = 4|g_{\mathrm{s,p}}|^2|A_{\mathrm{p}}|^2/P_{\mathrm{p}}\Gamma v_{\mathrm{g},1}$.

4. Given the racetrack bends are not suspended (i.e., do not support long-lived traveling elastic waves), the total round-trip acoustic attenuation is in excess of 10,000 dB.

observations. From Eq. 3.17, we see that the field diverges when $G_{\mathrm{B}}P_{\mathrm{P}} = \alpha_{\mathrm{s}} + \frac{2}{L}\log\frac{1}{r}$. In other words, the Stokes field experiences a pole on the real axis (a lossless state) when round-trip Brillouin gain matches the optical round-trip loss [112]; a condition that pushes the system into optical self-oscillation. This is the threshold condition for Brillouin lasing [13].

From Eq. 3.13, we note that above threshold, optical self-oscillation also dramatically increases the phonon field strength. Since the phonon field is spatially heavily damped, the spatial dynamics are determined by the local optical driving force ($\propto \bar{A}_{\mathrm{p}}(z)\bar{A}_{\mathrm{s}}^{\dagger}(z)$, which radically increases in magnitude above threshold. Thus, because the phonon field mediates coupling between the pump and Stokes waves, phonon emission can be viewed as a byproduct of Stokes laser-oscillation (much like the idler in a singly-resonant OPO). Thus, in general, Brillouin lasers require only an optical cavity for the Stokes field; no phonon feedback is necessary for laser oscillation to occur.

3.4.2 Mean-field analysis

We next develop a time-dependent mean-field model to analyze the temporal dynamics of the system. This approach adapts well-known techniques in solid-state physics [113–115] to simplify the coupled Brillouin equations by averaging the field values over the spatial degrees of freedom [116, 117]. This model can be derived by again starting from the slowly-varying envelope dynamics of these fields [75, 77] given by

$$\dot{A}_{\mathrm{p}} + i\omega_{\mathrm{p}}A_{\mathrm{p}} + v_{\mathrm{g,p}}A_{\mathrm{p}}' + \frac{1}{2}v_{\mathrm{g,p}}\alpha_{\mathrm{p}}A_{\mathrm{p}} = -ig_{\mathrm{s,p}}A_{\mathrm{s}}B + \frac{1}{\sqrt{L}}\xi_{\mathrm{p}}(z,t) \tag{3.18}$$

$$\dot{A}_{\mathrm{s}} + i\omega_{\mathrm{s}}A_{\mathrm{s}} + v_{\mathrm{g,s}}A_{\mathrm{s}}' + \frac{1}{2}v_{\mathrm{g,s}}\alpha_{\mathrm{s}}A_{\mathrm{s}} = -ig_{\mathrm{s,p}}^{*}A_{\mathrm{p}}B^{\dagger} + \frac{1}{\sqrt{L}}\xi_{\mathrm{s}}(z,t) \tag{3.19}$$

$$\dot{B} + (i\Omega_{\mathrm{B}} + \frac{1}{2}\Gamma)B + v_{\mathrm{g,b}}B' = -ig_{\mathrm{s,p}}^{*}A_{\mathrm{p}}A_{\mathrm{s}}^{\dagger} + \frac{1}{\sqrt{L}}\eta(z,t). \tag{3.20}$$

Here, we introduce Langevin forces $\xi_{\mathrm{p}}(z,t)$, $\xi_{\mathrm{s}}(z,t)$, and $\eta(z,t)$ that represent the thermal and vacuum fluctuations of the pump, Stokes, and phonon fields. These Stochastic terms are locally correlated in both space and time, such that $\langle\eta^{\dagger}(t,z)\eta(t',z')\rangle = L\Gamma n_{\mathrm{B}}^{\mathrm{th}}\delta(t-t')\delta(z-z')$.

Under the mean-field approximation, we eliminate the spatial dependence of the fields by averaging over the spatial extent of the racetrack resonator. In the case of the pump,

the mean-field value is given by

$$\underline{A}_{\mathrm{p}}(t) \equiv \frac{1}{L}\int_0^L dz\ A_{\mathrm{p}}(z,t). \tag{3.21}$$

Now, we use the same approach to simplify the equation of motion for the pump wave, yielding

$$\dot{\underline{A}}_{\mathrm{p}} + i\omega_{\mathrm{p}}\underline{A}_{\mathrm{p}} + \frac{v_{\mathrm{g,p}}}{L}(A_{\mathrm{p}}(L) - A_{\mathrm{p}}(0)) + \frac{1}{2}v_{\mathrm{g,p}}\alpha_{\mathrm{p}}\underline{A}_{\mathrm{p}} = -ig_{\mathrm{s,p}}\underline{A_{\mathrm{s}}B} + \frac{1}{\sqrt{L}}\underline{\xi}_{\mathrm{p}}. \tag{3.22}$$

If we assume that the field envelopes change minimally over the length of the device, we can apply the following boundary condition $A_{\mathrm{p}}(0) = r_{\mathrm{p}}A_{\mathrm{p}}(L) - i\mu_{\mathrm{p}}A_{\mathrm{ext}}$, where μ_{p} is the bus ring coupling and r_{p} is defined by $r_{\mathrm{p}} = \sqrt{1-\mu_{\mathrm{p}}^2}$. Here, A_{ext} represents the mode envelope of the injected pump. When the fields are simultaneously resonant, we find

$$\underline{A_{\mathrm{s}}B} \approx \underline{A}_{\mathrm{s}}\underline{B} \tag{3.23}$$

$$A_{\mathrm{p}}(L) - A_{\mathrm{p}}(0) \approx i\mu_{\mathrm{p}}A_{\mathrm{ext}} + (1-r_{\mathrm{p}})A_{\mathrm{p}}(L). \tag{3.24}$$

where the first line assumes the Stokes and phonon amplitudes are nearly constant in space. The second line is approximately true in the case of low optical propagation loss.

We further simplify these equations by approximating $r_{\mathrm{p}} - 1$ as $\ln r_{\mathrm{p}}$ and taking $A_{\mathrm{p}}(L) \approx \underline{A}_{\mathrm{p}}$.

$$A_{\mathrm{p}}(L) - A_{\mathrm{p}}(0) \approx i\mu_{\mathrm{p}}A_{\mathrm{ext}} - \ln r_{\mathrm{p}}\underline{A}_{\mathrm{p}}. \tag{3.25}$$

These substitutions allow us to group together the intrinsic propagation losses and external coupling losses. We apply this same treatment to the Stokes and phonon fields, yielding the coupled mean-field equations

$$\dot{\underline{A}}_{\mathrm{p}} + \frac{1}{2} v_{\mathrm{g,p}} (\alpha_{\mathrm{p}} - \frac{2}{L} \ln r_{\mathrm{p}}) \underline{A}_{\mathrm{p}} = -i g_{\mathrm{s,p}} \underline{A}_{\mathrm{s}} \underline{B} - i \frac{v_{\mathrm{g,p}}}{L} \mu_{\mathrm{p}} A_{\mathrm{ext}} + \frac{1}{\sqrt{L}} \underline{\xi}_{\mathrm{p}} \tag{3.26}$$

$$\dot{\underline{A}}_{\mathrm{s}} + \frac{1}{2} v_{\mathrm{g,s}} (\alpha_{\mathrm{s}} - \frac{2}{L} \ln r_{\mathrm{s}}) \underline{A}_{\mathrm{s}} = -i g^{*}_{\mathrm{s,p}} \underline{A}_{\mathrm{p}} \underline{B}^{\dagger} + \frac{1}{\sqrt{L}} \underline{\xi}_{\mathrm{s}} \tag{3.27}$$

$$\dot{\underline{B}} + (i\Omega_{\mathrm{B}} + \frac{1}{2}\Gamma) \underline{B} = -i \tilde{g}^{*} \underline{A}_{\mathrm{p}} \underline{A}^{\dagger}_{\mathrm{s}} + \frac{1}{\sqrt{L}} \underline{\eta}. \tag{3.28}$$

From here, it is straightforward to re-write these expressions as the Langevin equations produced by coupling of normal modes.

We first find the correlation function of the mean-field Langevin force $\underline{\eta}(t)$

$$\langle \underline{\eta}^{\dagger}(t) \underline{\eta}(t') \rangle = \frac{1}{L^2} \int_0^L dz \int_0^L dz' \ \langle \eta^{\dagger}(t,z) \eta(t',z') \rangle \tag{3.29}$$

$$= \frac{1}{L} \int_0^L dz \int_0^L dz' \ \Gamma n_{\mathrm{B}}^{\mathrm{th}} \delta(t-t') \delta(z-z') \tag{3.30}$$

$$= \Gamma n_{\mathrm{B}}^{\mathrm{th}} \delta(t-t'). \tag{3.31}$$

Next, we define $a_{\mathrm{p}} \equiv \sqrt{L} \underline{A}_{\mathrm{p}}$ (and similarly for the other fields). We also note that the total decay rates of the optical modes are given by $\gamma_{\mathrm{p}} = v_{\mathrm{g,p}} (\alpha_{\mathrm{p}} - \frac{2}{L} \ln r_{\mathrm{p}})$ and $\gamma_{\mathrm{s}} = v_{\mathrm{g,s}} (\alpha_{\mathrm{s}} - \frac{2}{L} \ln r_{\mathrm{s}})$. These notational simplifications lead to the coupled mean-field equations of motion, upon which we base our model of the temporal dynamics of laser oscillation. These equations are given by

$$\text{Mean-field equations of motion} = \begin{cases} \dot{a}_{\mathrm{p}} = -\left(i\omega_{\mathrm{p}} + \gamma_{\mathrm{p}}/2\right) a_{\mathrm{p}} - i g a_{\mathrm{s}} b + \gamma_{\mathrm{p}} a_{\mathrm{p}}^{\mathrm{ext}}/2 + \xi_{\mathrm{p}} \\ \dot{a}_{\mathrm{s}} = -\left(i\omega_{\mathrm{s}} + \gamma_{\mathrm{s}}/2\right) a_{\mathrm{s}} - i g^{*} a_{\mathrm{p}} b^{\dagger} + \xi_{\mathrm{s}} \\ \dot{b} = -\left(i\Omega_{\mathrm{B}} + \Gamma/2\right) b - i g a_{\mathrm{p}} a_{\mathrm{s}}^{\dagger} + \eta, \end{cases} \tag{3.32}$$

where $g = g_{\mathrm{s,p}}/\sqrt{L}$ is the distributed optomechanical coupling and $a_{\mathrm{p}}^{\mathrm{ext}}$ is the externally sourced pump field. The lumped-element noise terms ξ_{p}, ξ_{s}, and η are zero-mean Gaussian random variables that represent thermal and quantum fluctuations of each field (we have

dropped the underline for simplicity of notation). These Langevin terms have correlation properties given by

$$\left\langle \xi_{\mathrm{p}}^{\dagger}(t)\xi_{\mathrm{p}}(t')\right\rangle = \gamma_{\mathrm{p}} n_{\mathrm{p}}^{\mathrm{th}} \delta(t-t') \tag{3.33}$$

$$\left\langle \xi_{\mathrm{s}}^{\dagger}(t)\xi_{\mathrm{s}}(t')\right\rangle = \gamma_{\mathrm{s}} n_{\mathrm{s}}^{\mathrm{th}} \delta(t-t') \tag{3.34}$$

$$\left\langle \eta^{\dagger}(t)\eta(t')\right\rangle = \Gamma n_{\mathrm{B}}^{\mathrm{th}} \delta(t-t'), \tag{3.35}$$

where $n_{\mathrm{p}}^{\mathrm{th}}$, $n_{\mathrm{s}}^{\mathrm{th}}$, and $n_{\mathrm{B}}^{\mathrm{th}}$ are the thermal occupation number given by the Bose distribution, in accordance with the fluctuation-dissipation theorem.

Assumptions of the mean-field model

We pause here to discuss the assumptions implicit in this mean-field approximation. First, this mean-field approach requires that the coherence length of the optical fields extend beyond the total circumference of the resonator. In this inter-modal silicon Brillouin laser, this condition is easily met by the high-Q symmetric cavity mode (Stokes) and approximately satisfied by the pump mode.

These same conditions must hold for the phonon field. However, the intrinsic spatial coherence length of the phonon ($\sim$ 60 μm) is much smaller than the circumference of the cavity ($\sim$ 4.6 cm). In this context, it may be surprising that this mean-field model can capture the physics adequately. However, due to this short coherence length, the spatial character of the phonon field is actually given by the local pump-Stokes beat-note, as we derived in Section 3.4.1. Therefore, if the pump and Stokes fields adequately satisfy the mean-field conditions, the phonon field will as well. In this way, we are able to model pump, Stokes, and phonon fields as lumped-element modes with distributed Brillouin coupling.

3.4.3 Temporal dynamics

We next use this mean-field treatment to calculate the steady-state laser power, threshold, slope efficiency, and power spectrum of our inter-modal Brillouin laser. We find that, in contrast to the temporal dissipation hierarchy in conventional Brillouin lasers (i.e., $\Gamma \gg$

γ_p, γ_s), this laser operates in a regime where the acoustic dissipation rate is much smaller than that of the optical fields. This allows us to adiabatically eliminate the time dynamics of the light fields as we discuss below.

In this system, the temporal dissipation rate associated with pump field far exceeds that of the Stokes field, phonon field, and decoherence rate of the pump laser. Due to this separation of time scales, we can treat the pump field as a steady state quantity that depends on the dynamics of the Stokes and phonon fields. Through this form of adiabatic elimination, we find

$$a_p \approx -i\frac{g a_s b}{i(\Omega_B - \Omega) + \gamma_p/2} + a_p^{ext} \equiv -ig\chi_p(\Omega) a_s b + a_p^{ext}, \tag{3.36}$$

where $\Omega = \omega_p - \omega_s$ and $\chi_p(\Omega)$ is the SBS-induced pump susceptibility. Inserting Eq. 3.36 into the equations for the Stokes and the phonon fields yields

$$\dot{a}_s = -\left(i\omega_s + \gamma_s/2\right) a_s - |g|^2 \chi_p(\Omega)|b|^2 a_s + \xi_s - ig^* a_p^{ext} b^\dagger \tag{3.37}$$

$$\dot{b} = -\left(i\Omega_B + \Gamma/2\right) b - |g|^2 \chi_p(\Omega)|a_s|^2 b + \eta - ig^* a_p^{ext} a_s^\dagger. \tag{3.38}$$

Following the natural dissipation hierarchy,[5] we solve for the Stokes-mode amplitude, yielding

$$\begin{aligned} a_s(t) &= \int_{-\infty}^{t} d\tau\; e^{-[(i\omega_s + \frac{1}{2}\gamma_s)(t-\tau) + |g|^2 \chi_p(\Omega) \int_\tau^t dt'\; |b(t')|^2]} \left[\xi_s(\tau) - ig^* a_p^{ext}(\tau) b^\dagger(\tau)\right] \\ &= \hat{a}_s(t) - ig^* \int_{-\infty}^{t} d\tau\; e^{-[(i\omega_s + \frac{1}{2}\gamma_s)(t-\tau) + |g|^2 \chi_p(\Omega) \int_\tau^t dt'\; |b(t')|^2]}\; a_p^{ext}(\tau) b^\dagger(\tau), \end{aligned} \tag{3.39}$$

where the dressed operator $\hat{a}_s$,[6] produced by the intrinsic optical fluctuations, is given by

5. In the case of our silicon Brillouin laser, the phonon decay rate Γ is much smaller than the Stokes decay rate γ_s, which in turn is much smaller than the pump decay rate γ_p.

6. Here we use the symbol $\hat{()}$ to indicate a dressed operator.

$$\hat{a}_{\rm s}(t) = \int_{-\infty}^{t} d\tau \; e^{-[(i\omega_{\rm s}+\frac{1}{2}\gamma_{\rm s})(t-\tau)+|g|^2\chi_{\rm p}(\Omega)\int_{\tau}^{t} dt' \; |b(t')|^2]} \; \xi_{\rm s}(\tau). \tag{3.40}$$

This expression can be simplified by again noting the separation of time scales. Since the pump phase-noise and phonon fields vary slowly compared to the Stokes field,[7] we can approximate $\int_{\tau}^{t} dt' \; |b(t')|^2 \approx |b(t)|^2(t-\tau)$,[8] allowing us to simplify as follows.

$$\begin{aligned} a_{\rm s}(t) &\approx \hat{a}_{\rm s}(t) - ig^* a_{\rm p}^{\rm ext}(t) b^\dagger(t) \int_{-\infty}^{t} d\tau \; e^{-[i(\omega_{\rm s}-\omega_{\rm p}+\Omega_{\rm B})+\frac{1}{2}\gamma_{\rm s}+|g|^2\chi_{\rm p}(\Omega)|b(t)|^2](t-\tau)} \\ &\approx \hat{a}_{\rm s}(t) - \frac{ig^* a_{\rm p}^{\rm ext}(t) b^\dagger(t)}{i(\Omega_{\rm B}-\Omega)+\frac{1}{2}\gamma_{\rm s}+|g|^2\chi_{\rm p}(\Omega)|b(t)|^2} \equiv \hat{a}_{\rm s}(t) - ig^*\chi_{\rm s}(\Omega) a_{\rm p}^{\rm ext}(t) b^\dagger(t), \end{aligned} \tag{3.41}$$

where $\chi_{\rm s}(\Omega)$ is the Stokes susceptibility arising from these coupled-mode dynamics.

The dynamics derived above allow us to draw some important insights about our heterodyne measurements. In particular, we note that the heterodyne beat-note results from the interference between the Stokes and an optical local oscillator, which is derived from the pump laser. If we neglect the quantum fluctuations of the Stokes field, the heterodyne beat-note can be expressed as

$$a_{\rm ext}(t) a_{\rm s}^\dagger(t) = ig\chi_{\rm s}^*(\Omega) |a_{\rm p}^{\rm ext}(t)|^2 b(t). \tag{3.42}$$

Thus, since the pump laser is phase-noise dominated,[9] a heterodyne beat-note reveals the heterodyne measurement reveals the underlying dynamics of the phonon field.

Again following the well-defined separation of time scales (i.e., $\Gamma \ll \gamma_{\rm s}$), we seek to elucidate the phonon dynamics. By inserting the approximate solution for the Stokes field

7. The effective decay rate associated with the non-zero pump phase noise in our experiments is 15 kHz. This is much smaller than the decay rate of the Stokes field, which is of order 100 MHz.

8. We can approximate $|b(t)|^2$ as constant over the duration of the Stokes field decay.

9. In the case of a phase-noise dominated source, the pump field can be expressed as $a_{\rm p}^{\rm ext}(t) = a^{\rm ext} \exp(i\phi(t))$, where $\phi(t)$ is a stochastic variable. As such, $|a_{\rm p}^{\rm ext}(t)|^2 = |a_{\rm p}^{\rm ext}|^2$ is a time-independent quantity, and the heterodyne beat-note provides a window into the phonon dynamics.

into Eq. 3.38, we find

$$\dot{b} = -\left(i\Omega_{\mathrm{B}} + \Gamma/2\right) b + |g|^2 |\chi_{\mathrm{s}}(\Omega)|^2 (i(\Omega_{\mathrm{B}} - \Omega) + \gamma_{\mathrm{s}}/2) |a_{\mathrm{p}}^{\mathrm{ext}}|^2 b + \eta - i g^* a_{\mathrm{p}}^{\mathrm{ext}} \hat{a}_{\mathrm{s}}^{\dagger}. \tag{3.43}$$

To proceed, we consider in the following the case in which all three fields are simultaneously resonant ($\Omega = \Omega_{\mathrm{B}}$, $\chi_{\mathrm{p}}(\Omega_{\mathrm{B}}) = 2/\gamma_{\mathrm{p}}$) such that the effective nonlinear dynamics of the phonon field can be expressed as

$$\dot{b} = -\left(i\Omega_{\mathrm{B}} + \Gamma/2\right) b + \frac{\gamma_{\mathrm{s}}}{2} \frac{|g|^2 |a_{\mathrm{p}}^{\mathrm{ext}}|^2}{(\frac{1}{2}\gamma_{\mathrm{s}} + \frac{2}{\gamma_{\mathrm{p}}} |g|^2 |b|^2)^2} b + \zeta, \tag{3.44}$$

where $\zeta \equiv \eta - i g^* a_{\mathrm{p}}^{\mathrm{ext}} \hat{a}_{\mathrm{s}}^{\dagger}$ captures all relevant quantum, optomechanical, and phase-noise-induced fluctuations.

Threshold behavior, lasing, and steady-state phonon amplitude

Equation 3.44 captures the basic lasing behavior and noise properties of the 3-wave system. When the pump power is large enough to satisfy

$$\frac{2}{\gamma_{\mathrm{s}}} |g|^2 |a_{\mathrm{p}}^{\mathrm{ext}}|^2 > \Gamma/2, \tag{3.45}$$

the mean-field phonon amplitude exhibits a dramatic increase in strength. From this analysis, we see that the threshold pump amplitude predicted by our mean-field treatment is

$$|a_{\mathrm{p,th}}^{\mathrm{ext}}|^2 \sim \frac{\Gamma \gamma_{\mathrm{s}}}{4|g|^2}. \tag{3.46}$$

Converting this threshold photon number to optical power using the relation $P = \hbar \omega v_g |a|^2 / L$, we obtain a threshold power of

$$P_{\mathrm{th}} \sim \frac{\hbar \omega_{g,\mathrm{p}} v_{\mathrm{g,p}} \Gamma \gamma_{\mathrm{s}}}{4|g|^2 L} = \frac{\gamma_{\mathrm{s}}}{G_{\mathrm{B}} v_{\mathrm{g,s}}} = \frac{1}{G_{\mathrm{B}}} (\alpha_s - \frac{2}{L} \ln(r_{\mathrm{s}})). \tag{3.47}$$

From Eq. 3.47, we see that the mean-field prediction is consistent with the threshold pump power required for the round-trip optical SBS gain for the Stokes field to match the round-

trip optical loss (See Eq. 3.17). We note here that because the phonon field mediates coupling between pump and Stokes wave, the coherent growth of the mean phonon field is simply a byproduct of the optical self-oscillation of the Stokes field. However, we will see in Section 3.4.4 that due to the temporal dissipation hierarchy exhibited by our Brillouin laser, the phonon field plays a dominant role in the linewidth narrowing dynamics.

Slope efficiency

Next, we examine the theoretical efficiency limits of this silicon Brillouin laser. Starting from Eq. 3.44, we relate the inject pump power to the coherent phonon number by expressing the phonon field in terms of the time-averaged amplitude β, such that $b = \beta e^{-i\Omega_B t}$. Assuming the threshold condition (Eq. 3.47) is met, we obtain

$$0 = -\left[\Gamma/2 - \frac{\gamma_s}{2}\frac{|g|^2|a_p^{ext}|^2}{(\frac{1}{2}\gamma_s + \frac{2}{\gamma_p}|g|^2|\beta|^2)^2}\right]. \tag{3.48}$$

Using the steady-state phonon amplitude and its relationship to the that of the external pump (as expressed by Eq. 3.48), we can estimate the optical laser efficiency just above the laser threshold. Here, we assume that the coherent amplitude $4|g|^2|\beta|^2/(\gamma_s\gamma_p) \ll 1$. In this limit, we can Taylor expand Eq. 3.48 to first order, yielding

$$\frac{\gamma_s^2\Gamma}{8|g|^2|a_p^{ext}|^2} = 1 - \frac{8|g|^2\beta^2}{\gamma_p\gamma_s} \tag{3.49}$$

To draw a clear connection with our experiments, we express the intracavity Stokes (P_s), pump (P_{ext}), and threshold (P_{th}) powers as

$$P_s = \frac{\hbar\omega_s|a_s|^2 v_{g,s}}{L} = \frac{\hbar\omega_s v_{g,s}}{L}\left((\frac{2}{\gamma_s})^2|g|^2|a_p^{ext}|^2\beta^2\right) \tag{3.50}$$

$$P_p = \frac{\hbar\omega_s|a_s|^2 v_{g,s}}{L} \tag{3.51}$$

$$P_{th} = \frac{\hbar\omega_p v_{g,p}}{L}\left(\frac{\Gamma\gamma_s^2}{8|g|^2}\right), \tag{3.52}$$

where we have used Eq. 3.41 on resonance in the first line. These expressions allows us to derive the power dynamics of the Stokes emission P_{s} relative to the external source laser power P_{ext}, yielding

$$P_{\mathrm{s}} \approx \frac{\gamma_{\mathrm{p}}\omega_{\mathrm{s}}v_{\mathrm{g,s}}}{2\gamma_{\mathrm{s}}\omega_{\mathrm{p}}v_{\mathrm{g,p}}}(P_{\mathrm{ext}} - P_{\mathrm{th}}). \tag{3.53}$$

Using the parameters obtained by our passive transmission measurements (see Supplementary Materials of Ref. [95]), we estimate an on-chip slope efficiency of $\sim 4\%$, close to the measured value of 3%.

3.4.4 Phonon power spectrum above threshold

Phase and residual intensity noise

The laser threshold is characterized by a phase-like transition [118] in which the expectation value of the phonon and Stokes amplitudes become non-zero. In this limit, both the amplitude and phase-noise properties change dramatically. We examine this physics by expressing the phonon field in terms of its coherent and fluctuating amplitude and phase, such that

$$b = (\beta + \delta\beta)e^{-i\Omega_{\mathrm{B}}t + i\varphi}, \tag{3.54}$$

where the real-valued $\delta\beta$ and φ represent the zero-mean amplitude and phase fluctuations. We calculate the dynamics of the amplitude and phase noise by inserting this expression into the nonlinear laser dynamics of Eq. 3.44 and separating into real and imaginary parts, which yields

$$\dot{\delta\beta} \approx -\frac{1}{2}\Gamma_{\mathrm{RIN}}\delta\beta + \tilde{\zeta}_r \tag{3.55}$$

$$\dot{\varphi} \approx \frac{1}{\beta}\tilde{\zeta}_i, \tag{3.56}$$

where we have taken the case of small amplitude fluctuations (i.e., $|\beta| \gg |\delta\beta|$), and where the real and imaginary Langevin terms are given by $\tilde{\zeta}_r(t) \equiv \mathrm{Re}[\zeta(t)\exp\{i\Omega_\mathrm{B}t - i\varphi(t)\}]$ and $\tilde{\zeta}_i(t) \equiv \mathrm{Im}[\zeta(t)\exp\{i\Omega_\mathrm{B}t - i\varphi(t)\}]$.

Linearizing the nonlinear denominator of Eq. 3.44, we find that the effective decay rate for the amplitude fluctuations (or relative intensity fluctuations (RIN)) is given by

$$\Gamma_\mathrm{RIN} \equiv \frac{8}{\gamma_\mathrm{p}} \frac{\gamma_\mathrm{s}|g|^4|a_\mathrm{p}^\mathrm{ext}|^2\beta^2}{(\frac{1}{2}\gamma_\mathrm{s} + \frac{2}{\gamma_\mathrm{p}}|g|^2\beta^2)^3} \tag{3.57}$$

$$= \frac{8}{\gamma_\mathrm{p}} \frac{\Gamma|g|^2\beta^2}{(\frac{1}{2}\gamma_\mathrm{s} + \frac{2}{\gamma_\mathrm{p}}|g|^2\beta^2)}. \tag{3.58}$$

Noise correlation properties

We now examine the correlation properties of the total Langevin force $\tilde{\zeta} \equiv \tilde{\zeta}_r + i\tilde{\zeta}_i$, which yields

$$\begin{aligned}
\langle\tilde{\zeta}^\dagger(t)\tilde{\zeta}(t')\rangle &= \langle\zeta^\dagger(t)e^{-i\varphi(t)}e^{i\varphi(t')}\zeta(t')\rangle e^{-i\Omega_\mathrm{B}(t-t')} \\
&= \Big[\langle\eta^\dagger(t)e^{-i\varphi(t)}e^{i\varphi(t')}\eta(t')\rangle \\
&\quad + |g|^2\langle[a_\mathrm{p}^\mathrm{ext}(t)\hat{a}_\mathrm{s}^\dagger(t)]^\dagger e^{-i\varphi(t)}e^{i\varphi(t')}[a_\mathrm{p}^\mathrm{ext}(t')\hat{a}_\mathrm{s}^\dagger(t')]\rangle\Big] e^{-i\Omega_\mathrm{B}(t-t')} \\
&\approx \Gamma n_\mathrm{B}^\mathrm{th}\delta(t-t') + |g|^2|a_\mathrm{p}^\mathrm{ext}|^2 e^{i(\omega_\mathrm{p}-\Omega_\mathrm{B})(t-t')}\langle\hat{a}_\mathrm{s}(t)\hat{a}_\mathrm{s}^\dagger(t')\rangle \\
&\approx \Gamma n_\mathrm{B}^\mathrm{th}\delta(t-t') + \frac{\gamma_\mathrm{s}|g|^2|a_\mathrm{p}^\mathrm{ext}|^2}{\gamma_\mathrm{s} + 4|g|^2\beta^2/\gamma_\mathrm{p}}(n_\mathrm{s}^\mathrm{th}+1)e^{-\frac{1}{2}(\gamma_\mathrm{s}+4|g|^2\beta^2/\gamma_\mathrm{p})|t-t'|} \\
&\approx \left[\Gamma n_\mathrm{B}^\mathrm{th} + 4\frac{\gamma_\mathrm{s}|g|^2|a_\mathrm{p}^\mathrm{ext}|^2}{(\gamma_\mathrm{s} + 4|g|^2\beta^2/\gamma_\mathrm{p})^2}(n_\mathrm{s}^\mathrm{th}+1)\right]\delta(t-t') \\
&\approx \Gamma(n_\mathrm{B}^\mathrm{th} + n_\mathrm{s}^\mathrm{th} + 1)\delta(t-t').
\end{aligned} \tag{3.59}$$

Since the correlation time for the Stokes field ($\gamma_\mathrm{s}/(2\pi) \sim 100$ MHz) is much shorter than that of the phonon ($\Gamma/(2\pi) \sim 13$ MHz) and the effective correlation time associated with the external pump phase noise ($\gamma_\mathrm{s}/(2\pi) \sim 13$ kHz), we are able to make 2 key approximations: (1) we neglect pump and phonon phase noise (third line of Eq. 3.59) and (2) we treat the Stokes correlation function as local in time (fifth line of Eq. 3.59). We have also used the relation between the steady-state phonon amplitude and the phonon decay rate, given by

Eq. 3.48, in the final line.

Having derived the correlation function for $\tilde{\zeta}$, we can compute the correlation functions for its real ($\tilde{\zeta}_r$) and imaginary parts ($\tilde{\zeta}_i$), yielding

$$\langle \tilde{\zeta}_r(t)\tilde{\zeta}_r(t')\rangle = \frac{1}{2}\Gamma(n_{\mathrm{B}}^{\mathrm{th}} + n_{\mathrm{s}}^{\mathrm{th}} + 1)\delta(t-t') \tag{3.60}$$

$$\langle \tilde{\zeta}_i(t)\tilde{\zeta}_i(t')\rangle = \frac{1}{2}\Gamma(n_{\mathrm{B}}^{\mathrm{th}} + n_{\mathrm{s}}^{\mathrm{th}} + 1)\delta(t-t') \tag{3.61}$$

$$\langle \tilde{\zeta}_r(t)\tilde{\zeta}_i(t')\rangle = 0. \tag{3.62}$$

Laser power spectra

Equipped with the correlation properties of the Langevin force, we derive the complete power spectrum of the phonon field. We use the fact that for stochastic variable $\varphi(t)$ exhibits random Gaussian statistics in time such that $\langle e^{i(\varphi(t+\tau)-\varphi(t))}\rangle = e^{-\frac{\langle(\varphi(t+\tau)-\varphi(t))^2\rangle}{2}}$ [119].[10] This relation, in conjunction with Eq. 3.56, allows us to calculate the phase noise correlation function

$$\langle e^{i(\varphi(t+\tau)-\varphi(t))}\rangle = e^{-\frac{1}{4\beta^2}\Gamma(n_{\mathrm{B}}^{\mathrm{th}}+n_{\mathrm{s}}^{\mathrm{th}}+1)|\tau|}. \tag{3.63}$$

We also compute the correlation function associated with the amplitude fluctuations $\delta\beta(t)$ using Eq. 3.55, yielding

$$\langle \delta\beta(t+\tau)\delta\beta(t)\rangle = \frac{\Gamma(n_{\mathrm{B}}^{\mathrm{th}} + n_{\mathrm{s}}^{\mathrm{th}} + 1)}{2\Gamma_{\mathrm{RIN}}} e^{-\frac{1}{2}\Gamma_{\mathrm{RIN}}|\tau|}. \tag{3.64}$$

We can now use Eqs. 3.63 and 3.64 to find the two-time correlation function for the

10. This relationship is stated as fact in Ref. [119]. It can be derived by analyzing the expectation value $\langle \exp(ix)\rangle = \int_{-\infty}^{\infty} dx p(x) \exp(ix)$, assuming the probability distribution is Gaussian (i.e., $p(x) = (2\pi\sigma^2)^{-1/2}\exp(-x^2/(2\sigma^2))$). The author would like to thank Shai Gertler for this helpful insight.

phonon field

$$\begin{aligned}\langle b(t+\tau)b^{\dagger}(t)\rangle &= [\beta^2 + \langle\delta\beta(t+\tau)\delta\beta(t)\rangle]\langle e^{-i(\varphi(t+\tau)-\varphi(t))}\rangle e^{-i\Omega_{\mathrm{B}}\tau} \\ &= \left[\beta^2 + \frac{\Gamma(n_{\mathrm{B}}^{\mathrm{th}}+n_{\mathrm{s}}^{\mathrm{th}}+1)}{2\Gamma_{\mathrm{RIN}}}e^{-\frac{1}{2}\Gamma_{\mathrm{RIN}}|\tau|}\right]e^{-\frac{1}{4\beta^2}\Gamma(n_{\mathrm{B}}^{\mathrm{th}}+n_{\mathrm{s}}^{\mathrm{th}}+1)|\tau|}e^{-i\Omega_{\mathrm{B}}\tau} \\ &\approx \Bigg[\underbrace{\beta^2 e^{-\frac{1}{4\beta^2}\Gamma(n_{\mathrm{B}}^{\mathrm{th}}+n_{\mathrm{s}}^{\mathrm{th}}+1)|\tau|}}_{\text{phase noise}} + \underbrace{\frac{\Gamma(n_{\mathrm{B}}^{\mathrm{th}}+n_{\mathrm{s}}^{\mathrm{th}}+1)}{2\Gamma_{\mathrm{RIN}}}e^{-\frac{1}{2}\Gamma_{\mathrm{RIN}}|\tau|}}_{\text{RIN}}\Bigg]e^{-i\Omega_{\mathrm{B}}\tau}.\end{aligned} \tag{3.65}$$

Equation 3.65 allows us to compute the two-sided power spectral density using the Wiener-Khinchin theorem (i.e., $\mathfrak{S}_b[\omega] = \hbar\Omega_{\mathrm{B}}\Gamma\int_{-\infty}^{\infty} d\tau\langle b(t+\tau)b^{\dagger}(t)\rangle\exp(i\omega\tau)$), yielding

$$\mathfrak{S}_b[\omega] = \hbar\Omega_{\mathrm{B}}\Gamma\Bigg[\underbrace{\beta^2\left[\frac{2\pi\Delta\nu_{\mathrm{b}}}{(\pi\Delta\nu_{\mathrm{b}}/2)^2+\omega^2}\right]}_{\text{phase noise}} + \underbrace{\frac{\Gamma(n_{\mathrm{B}}^{\mathrm{th}}+n_{\mathrm{s}}^{\mathrm{th}}+1)}{2\Gamma_{\mathrm{RIN}}}\left[\frac{\Gamma_{\mathrm{RIN}}}{(\Gamma_{\mathrm{RIN}}/2)^2+\omega^2}\right]}_{\text{RIN}}\Bigg], \tag{3.66}$$

where the quantity $(\Delta\nu_{\mathrm{b}})$ is given by

$$\Delta\nu_{\mathrm{b}} = \frac{\Gamma}{4\pi\beta^2}(n_{\mathrm{B}}^{\mathrm{th}}+n_{\mathrm{s}}^{\mathrm{th}}+1), \tag{3.67}$$

which can be interpreted as the Schawlow-Townes linewidth associated with the phonon field. Notice that when $\beta \gg 1$, the power spectrum is phase noise dominated and exhibits the characteristic Schawlow-Townes linewidth narrowing. Thus, above threshold, the mean-field model predicts phonon linewidth narrowing that is reminiscent of that produced in cavity-optomechanical systems [120].

3.5 Experimental characterization of laser coherence

3.5.1 Standard heterodyne spectroscopy

We characterize the laser coherence properties experimentally using two complementary measurement techniques, as shown in Fig. 3.7A-B. First, as discussed in Section 3.4.3, standard heterodyne spectroscopy naturally reveals the underlying phonon dynamics. We

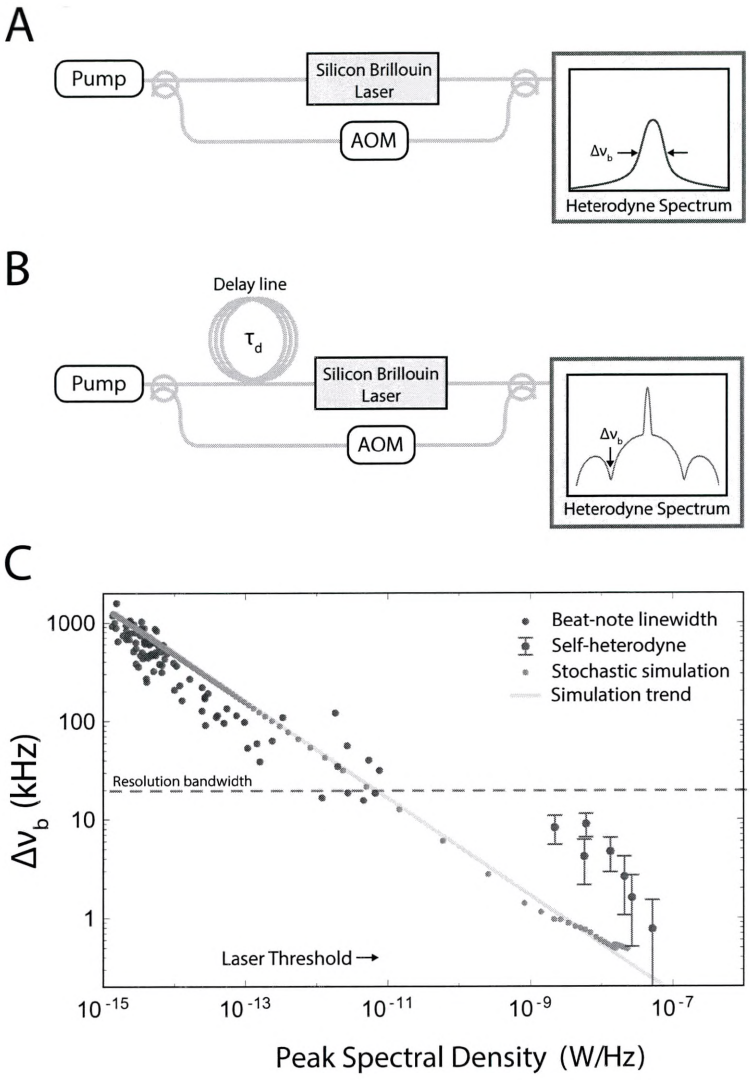

Figure 3.7: Two methods used to measure the phonon linewidth. (A) Diagrams the standard heterodyne spectroscopy apparatus to measure the phonon linewidth, where the linewidth given by the FWHM of the heterodyne spectrum. (B) Subcoherence self-heterodyne apparatus used to probe the phonon dynamics at higher output Stokes powers (see Section 3.5). The phonon linewidth is determined by measuring the fringe contrast or coherence between output Stokes and pump waves, yielding the blue data points in panel (C). (C) Experimental and theoretical comparison of pump-Stokes beat note (or phonon) linewidth as a function of peak Stokes spectral density. Below threshold we use the standard heterodyne spectroscopy (dark red data points). At higher powers, this measurement becomes resolution bandwidth limited. For this reason, we use the sub-coherence self-heterodyne technique which yields the blue data points (error bars represent the 95% confidence interval). Using this method, we measure a minimum phonon linewidth of $\sim$ 800 Hz (See Section 3.5). From Ref. [96]. Reprinted with permission from AAAS.

use this method to measure the laser coherence down a resolution-bandwidth limited value of 20 kHz. The resolution bandwidth is limited by the acquisition time ($\sim$ 30 milliseconds) required to avoid distortions from low-frequency variations in the pump wavelength. With this limitation, standard heterodyne spectroscopy does not permit a direct measurement of phonon linewidth narrowing below the original pump linewidth ($\sim$ 15 kHz).

3.5.2 Sub-coherence self-heterodyne interferometry

To sidestep the resolution limitation posed by standard heterodyne spectroscopy, we develop a separate sub-coherence delayed self-heterodyne measurement technique, which allows us to measure the phonon coherence well above the laser threshold. This method is based on a form of delayed interferometry that allows us to determine the relative coherence between pump and Stokes waves. We use this technique to measure the phonon linewidth at high powers, which yields the blue data points presented in Fig. 3.7E. These measurements demonstrate (1) the pump-Stokes phase coherence unique to this limit of Brillouin dynamics and (2) phonon linewidth narrowing far below the linewidth of the pump laser ($\sim$ 13 kHz), in good agreement with the theoretical trend obtained from stochastic simulations (see Section 6.3.1 and Supplementary Materials of Ref. [95] for more details). Using this technique, we observe a minimum phonon linewidth of $\sim$ 800 Hz, corresponding to a compression factor of $\sim 10^4$ relative to the spontaneous Brillouin linewidth.

In what follows, we describe the sub-coherence self-heterodyne method and derive its theoretical response. This method allows us to determine the intrinsic laser linewidth (and resulting phonon dynamics) despite the slow center-frequency hops induced by the pump laser [121, 122]. This technique employs an unbalanced Mach-Zehnder interferometer that possesses both a sub-coherence delay arm and a frequency shifted reference arm (See Fig. 3.8). With sub-coherence delay times, the measured spectral density is composed of a delta function and a sinc-like background. By comparing the relative magnitude of each component, one can determine the coherence time of the laser. Using this sub-coherence technique, we measure the linewidth of the pump laser and show that the silicon Brillouin laser behaves analogously to a self-driven acousto-optic frequency shifter.[11]

11. With excess phase noise that becomes negligible in the limit as $\beta^2 \to \infty$.

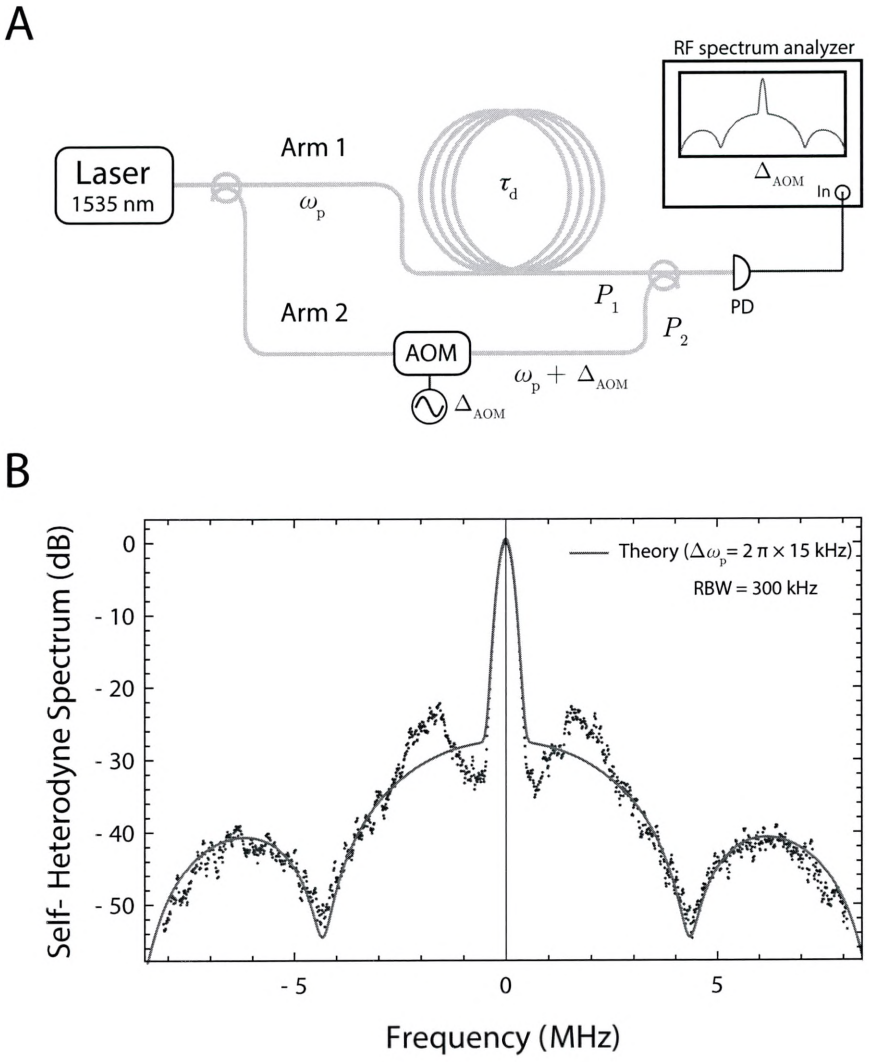

Figure 3.8: (A) Diagram of self-heterodyne interferometer. The first arm of the interferometer provides a delay (of time τ_d) while the second arm frequency shifts the light using an acousto-optic frequency shifter (AOM). The two waves are combined and the beat note is detected with a fast photodiode (PD). (B) Self-heterodyne spectrum of the Agilent 81600B diode laser with a delay length of 48.25 m, revealing a linewidth of 15 kHz. From Ref. [96]. Reprinted with permission from AAAS.

3.5.3 Traditional self-heterodyne interferometry

In this section, we discuss the essential elements of the sub-coherence self-heterodyne measurement. Figure 3.8A depicts a typical self-heterodyne interferometer. For an arbitrary delay length associated with a time delay τ_{d}, the self-heterodyne spectral density is given by [121]

$$\mathfrak{S}[\omega] \propto P_1 P_2 \Bigg[\pi e^{-\Delta\omega_{\mathrm{p}}\tau_{\mathrm{d}}} \delta(\omega - \Delta_{\mathrm{AOM}}) + \frac{\Delta\omega_{\mathrm{p}}}{(\omega - \Delta_{\mathrm{AOM}})^2 + \Delta\omega_{\mathrm{p}}^2} (1 - e^{-\Delta\omega_{\mathrm{p}}\tau_{\mathrm{d}}} (\cos((\omega - \Delta_{\mathrm{AOM}})\tau_{\mathrm{d}}) + \frac{\sin((\omega - \Delta_{\mathrm{AOM}})\tau_{\mathrm{d}})\Delta\omega_{\mathrm{p}}}{\omega - \Delta_{\mathrm{AOM}}})) \Bigg]. \tag{3.68}$$

Here, P_1 and P_2 are the powers in arm 1 and arm 2 of the self-heterodyne interferometer, $\Delta\omega_{\mathrm{p}}$ is the linewidth of the laser in units of angular frequency, and Δ_{AOM} is the driving frequency of the acousto-optic modulator.

Note that in the limit that $\tau_{\mathrm{d}} \gg 1/\Delta\omega_{\mathrm{p}}$, the spectrum becomes a simple Lorentzian with a half width at half maximum (HWHM) of the intrinsic laser linewidth. For this reason, the self-heterodyne technique typically involves a delay line that far exceeds the expected coherence time. However, as with other external cavity diode lasers, the low frequency fluctuations of the center laser frequency of the Agilent 81600B obscure the traditional measurement [122]. For this reason, we employ a sub-coherence delay arm to measure the linewidth of the pump laser. Figure 3.8B shows a comparison of a typical self-heterodyne spectrum of the pump laser (Agilent 81600B) with the theoretical spectral density of a laser with a linewidth of 15 kHz.

3.5.4 Sub-coherence self-heterodyne measurement using a silicon Brillouin laser

We next generalize this form of self-heterodyne sub-coherence spectroscopy to the case in which the frequency shifter is a silicon Brillouin laser, as depicted in Fig. 3.7B. This technique, which we develop for the first time, allows us to (1) determine the relative coherence between Stokes and pump (i.e., phonon linewidth $\Delta\nu_b$) with improved resolution

(down to 1 kHz) and (2) verify the new regime of spatio-temporal dynamics through clear spectral signatures.

In the discussion that follows we present a simple model that captures the effect of a non-zero phonon linewidth in the self-heterodyne technique diagrammed in Fig. 3.7B. Using the Wiener-Khinchin theorem and assuming stationarity, the spectral density of a heterodyne beat note can be written as

$$\mathfrak{S}[\omega] = \frac{1}{2\pi}\int_{-\infty}^{\infty} d\tau\ e^{i\omega\tau}\langle E_{\mathrm{LO}}(\tau)E_{\mathrm{s}}^{*}(\tau)E_{\mathrm{LO}}^{*}(0)E_{\mathrm{s}}(0)\rangle, \tag{3.69}$$

where E_{s} and E_{LO} represent the signal and local oscillator waves, respectively. Applying Eq. 3.69 to the measurement presented in Fig. 3.7B, the spectral density becomes

$$\mathfrak{S}[\omega] = \frac{1}{2\pi}\int_{-\infty}^{\infty} d\tau\ e^{i\omega\tau}\langle \tilde{a}_{\mathrm{p}}(\tau+\tau_{\mathrm{d}})a_{\mathrm{s}}^{\dagger}(\tau)\tilde{a}_{\mathrm{p}}^{\dagger}(\tau_{\mathrm{d}})a_{\mathrm{s}}(0)\rangle, \tag{3.70}$$

where a_{s}, a_{p}, and $\tilde{a}_{\mathrm{p}}$ will denote the Stokes, input pump, and AOM-shifted pump waves, respectively, and τ_{d} represents the transit time of the delay arm. As we saw in Section 3.4.3, separation of time scales allows us to approximate the resonant Stokes field as

$$a_{\mathrm{s}} = \frac{-2ig^{*}a_{\mathrm{p}}b^{\dagger}}{\gamma_{\mathrm{s}}(1+\frac{4|g|^{2}|\beta|^{2}}{\gamma_{\mathrm{s}}\gamma_{\mathrm{p}}})}, \tag{3.71}$$

Hence, the spectral density becomes

$$\mathfrak{S}[\omega] = \frac{2|g|^{2}}{\pi(\gamma_{\mathrm{s}}(1+\frac{4|g|^{2}|\beta|^{2}}{\gamma_{\mathrm{s}}\gamma_{\mathrm{p}}}))^{2}}\int_{-\infty}^{\infty} d\tau\ e^{i\omega\tau}\langle \tilde{a}_{\mathrm{p}}(\tau+\tau_{\mathrm{d}})a_{\mathrm{p}}^{\dagger}(\tau)b(\tau)\tilde{a}_{\mathrm{p}}^{\dagger}(\tau_{\mathrm{d}})a_{\mathrm{p}}(0)b^{\dagger}(0)\rangle. \tag{3.72}$$

Due to the separation of time scales, the phonon and pump fields are uncorrelated. Therefore the expectation value in Eq. 3.72 simplifies to

$$\mathfrak{S}[\omega] = \frac{2|g|^{2}}{\pi(\gamma_{\mathrm{s}}(1+\frac{4|g|^{2}|\beta|^{2}}{\gamma_{\mathrm{s}}\gamma_{\mathrm{p}}}))^{2}}\int_{-\infty}^{\infty} d\tau\ e^{i\omega\tau}\langle \tilde{a}_{\mathrm{p}}(\tau+\tau_{\mathrm{d}})a_{\mathrm{p}}^{\dagger}(\tau)\tilde{a}_{\mathrm{p}}^{\dagger}(\tau_{\mathrm{d}})a_{\mathrm{p}}(0)\rangle\langle b(\tau)b^{\dagger}(0)\rangle. \tag{3.73}$$

We will now focus on the first expectation value $\langle \tilde{a}_{\mathrm{p}}(\tau+\tau_{\mathrm{d}})a_{\mathrm{p}}^{\dagger}(\tau)\tilde{a}_{\mathrm{p}}^{\dagger}(\tau_{\mathrm{d}})a_{\mathrm{p}}(0)\rangle$. For simplicity, we assume that the pump fields (as well as the Stokes and phonon fields) are

phase noise dominated. As such, we express the pump and optical as $a_{\mathrm{p}} = \alpha_p \exp(\phi(t))$ and $\tilde{a}_{\mathrm{p}} = \tilde{\alpha}_p \exp(\tilde{\phi}(t))$, with phases $\phi(t)$ and $\tilde{\phi}(t)$ defined as

$$\begin{aligned} \phi(t) &= -i\omega_{\mathrm{p}} t + i\phi_{\mathrm{n}}(t) \\ \tilde{\phi}(t) &= -i(\omega_{\mathrm{p}} + \Delta_{\mathrm{AOM}})t + i\phi_{\mathrm{n}}(t), \end{aligned} \tag{3.74}$$

where $\phi_{\mathrm{n}}(t)$ represents the zero-mean phase fluctuations.

We model the dynamics of these phase fluctuations with the phase diffusion equation such that

$$\dot{\phi}_{\mathrm{n}}(t) = \eta(t) \tag{3.75}$$

where $\eta(t)$ is a Langevin force with a two-time correlation function $\langle \eta(t)\eta(t') \rangle = \Delta\omega_{\mathrm{p}} \delta(t-t')$.

Applying Eq. 3.74 to the first expectation value in Eq. 3.73, we find

$$\begin{aligned} \langle \tilde{a}_{\mathrm{p}}(\tau+\tau_{\mathrm{d}}) a_{\mathrm{p}}^{\dagger}(\tau) \tilde{a}_{\mathrm{p}}^{\dagger}(\tau_{\mathrm{d}}) a_{\mathrm{p}}(0) \rangle &= |\alpha_{\mathrm{p}}|^2 |\tilde{\alpha}_{\mathrm{p}}|^2 \langle e^{i\Delta\phi_{\mathrm{n}}(\tau,\tau_{\mathrm{d}})} \rangle e^{-i\Delta_{\mathrm{AOM}}\tau} \\ \Delta\phi_{\mathrm{n}}(\tau,\tau_{\mathrm{d}}) &= \phi_{\mathrm{n}}(\tau+\tau_{\mathrm{d}}) - \phi_{\mathrm{n}}(\tau) - \phi_{\mathrm{n}}(\tau_{\mathrm{d}}) + \phi_{\mathrm{n}}(0). \end{aligned} \tag{3.76}$$

By direct integration, we compute $\Delta\phi_{\mathrm{n}}(\tau,\tau_{\mathrm{d}})$:

$$\Delta\phi_{\mathrm{n}}(\tau,\tau_{\mathrm{d}}) = \int_{\tau}^{\tau+\tau_{\mathrm{d}}} dt'\ \eta(t') - \int_{0}^{\tau_{\mathrm{d}}} dt'\ \eta(t'). \tag{3.77}$$

As $\Delta\phi_{\mathrm{n}}(\tau,\tau_{\mathrm{d}})$ can be described by Gaussian statistics, we can rewrite the expectation value for $\langle e^{i\Delta\phi_{\mathrm{n}}(\tau,\tau_{\mathrm{d}})} \rangle$ as we did in Section 3.4.4 [119], yielding

$$\langle e^{i\Delta\phi_{\mathrm{n}}(\tau,\tau_{\mathrm{d}})} \rangle = e^{\frac{-\langle [\Delta\phi_{\mathrm{n}}(\tau,\tau_{\mathrm{d}})]^2 \rangle}{2}}. \tag{3.78}$$

Evaluating Eq. 3.78, the spectral density becomes

$$\mathfrak{S}[\omega] = \frac{2|g|^2|\alpha_{\mathrm{p}}|^2|\tilde{\alpha}_{\mathrm{p}}|^2}{\pi(\gamma_{\mathrm{s}}(1+\frac{4|g|^2|b|^2}{\gamma_{\mathrm{s}}\gamma_{\mathrm{p}}}))^2} \int_{-\infty}^{\infty} d\tau e^{i(\omega-\Delta_{\mathrm{AOM}})\tau} e^{-\Delta\omega_{\mathrm{p}}(\tau_{\mathrm{d}}-(\tau_{\mathrm{d}}-|\tau|)\theta(\tau_{\mathrm{d}}-|\tau|))} \langle b(\tau) b^{\dagger}(0) \rangle, \tag{3.79}$$

where $\theta(t)$ is a step function such that $\theta(t>0) = 1$ and $\theta(t \leq 0) = 0$.

We derived the remaining phonon correlation function in Section 3.4.4. As discussed, when $\beta \gg 1$, the phonon correlation function is phase-noise dominated and can be expressed

as

$$\langle b(\tau)b^{\dagger}(0)\rangle \approx \beta^2 e^{-\pi\Delta\nu_b|\tau|}. \tag{3.80}$$

Inserting the phonon correlation function into Eq. 3.79 yields

$$\mathfrak{S}[\omega] = \frac{2|g|^2|\alpha_{\mathrm{p}}|^2|\tilde{\alpha}_{\mathrm{p}}|^2\beta^2}{\pi(\gamma_{\mathrm{s}}(1+\frac{4|g|^2|\beta|^2}{\gamma_{\mathrm{s}}\gamma_{\mathrm{p}}}))^2}\int_{-\infty}^{\infty} d\tau e^{i(\omega-\Delta_{\mathrm{AOM}}-\Omega_b)\tau}e^{-\Delta\omega_{\mathrm{p}}(\tau_{\mathrm{d}}-(\tau_{\mathrm{d}}-|\tau|)\theta(\tau_{\mathrm{d}}-|\tau|))-\pi\Delta\nu_b|\tau|}. \tag{3.81}$$

Note that in the limit that $\tau_{\mathrm{d}} \to 0$, standard heterodyne detection directly measures the phonon power spectrum. In this case, the spectral density can be calculated as

$$\mathfrak{S}[\omega] = \frac{2|g|^2|\alpha_{\mathrm{p}}|^2|\tilde{\alpha}_{\mathrm{p}}|^2|\beta|^2}{\pi(\gamma_{\mathrm{s}}(1+\frac{4|g|^2|\beta|^2}{\gamma_{\mathrm{s}}\gamma_{\mathrm{p}}}))^2}\int_{-\infty}^{\infty} d\tau e^{i(\omega-\Delta_{\mathrm{AOM}}-\Omega_b)\tau}e^{-\pi\Delta\nu_b|\tau|}, \tag{3.82}$$

which is proportional to the phonon power spectrum Eq. 3.66, as expected.

To calculate the sub-coherence self-heterodyne spectrum, we instead take the limit of a significant time delay τ_{d}, such that integration of Eq. 3.81 yields

$$\begin{aligned}\mathfrak{S}[\omega] =& \frac{2|g|^2|\alpha_{\mathrm{p}}|^2|\tilde{\alpha}_{\mathrm{p}}|^2\beta^2}{\pi(\gamma_{\mathrm{s}}(1+\frac{4|g|^2\beta^2}{\gamma_{\mathrm{s}}\gamma_{\mathrm{p}}}))^2}\Bigg[\frac{4\left(2\pi\Delta\nu_b+2\Delta\omega_{\mathrm{p}}\right)}{\left(2\pi\Delta\nu_b+2\Delta\omega_{\mathrm{p}}\right)^2+4w^2} \\ &- \frac{32w\Delta\omega_{\mathrm{p}}\left(2\pi\Delta\nu_b+\Delta\omega_{\mathrm{p}}\right)\sin\left(w\tau_{\mathrm{d}}\right)e^{-\tau_{\mathrm{d}}(\pi\Delta\nu_b+\Delta\omega_{\mathrm{p}})}}{\left((2\pi\Delta\nu_b)^2+4w^2\right)\left(\left(2\pi\Delta\nu_b+2\Delta\omega_{\mathrm{p}}\right)^2+4w^2\right)} \\ &+ \frac{8\Delta\omega_{\mathrm{p}}\left((2\pi\Delta\nu_b)^2+4\pi\Delta\nu_b\Delta\omega_{\mathrm{p}}-4w^2\right)\cos\left(w\tau_{\mathrm{d}}\right)e^{-\tau_{\mathrm{d}}(\pi\Delta\nu_b+\Delta\omega_{\mathrm{p}})}}{\left((2\pi\Delta\nu_b)^2+4w^2\right)\left(\left(2\pi\Delta\nu_b+2\Delta\omega_{\mathrm{p}}\right)^2+4w^2\right)}\Bigg],\end{aligned} \tag{3.83}$$

which is the main result of this section. Here, $w \equiv \omega - \Delta_{\mathrm{AOM}} - \Omega_{\mathrm{B}}$. If we instead evaluate Eq. (3.81) with $\Delta\nu_b = 0$ (zero phonon phase noise), the spectrum matches that of the simple sub-coherence self-heterodyne measurement (refer to Eq. (3.68)), as given by

$$\begin{aligned}\mathfrak{S}[\omega] &= \frac{2|g|^2|a_{\mathrm{p}}|^2|\tilde{a}_{\mathrm{p}}|^2\beta^2}{\pi(\gamma_{\mathrm{s}}(1+\frac{4|g|^2\beta^2}{\gamma_{\mathrm{s}}\gamma_{\mathrm{p}}}))^2}\Bigg[2\pi e^{-\Delta\omega_{\mathrm{p}}\tau_{\mathrm{d}}}\delta(w) \\ &+ \frac{2\Delta\omega_{\mathrm{p}}}{w^2+\Delta\omega_{\mathrm{p}}^2}(1-e^{-\Delta\omega_{\mathrm{p}}\tau_{\mathrm{d}}}(\cos(w\tau_{\mathrm{d}})+\frac{\sin(w\tau_{\mathrm{d}})\Delta\omega_{\mathrm{p}}}{w}))\Bigg] \\ &\propto P_1P_2\Bigg[\pi e^{-\Delta\omega_{\mathrm{p}}\tau_{\mathrm{d}}}\delta(w)+\frac{\Delta\omega_{\mathrm{p}}}{w^2+\Delta\omega_{\mathrm{p}}^2}(1-e^{-\Delta\omega_{\mathrm{p}}\tau_{\mathrm{d}}}(\cos(w\tau_{\mathrm{d}})+\frac{\sin(w\tau_{\mathrm{d}})\Delta\omega_{\mathrm{p}}}{w}))\Bigg].\end{aligned} \tag{3.84}$$

Here P_1 and P_2 are the powers in arm 1 and arm 2 of the self-heterodyne interferometer. Figure 3.9A plots Eq. 3.83 with a 15 kHz linewidth pump and various phonon linewidths. Note that as the phonon linewidth increases, the interference fringes wash out and the pedestal becomes more Lorentzian-like.

Using the experimental setup depicted in Fig. 3.7B, we measure the sub-coherence self-heterodyne spectrum with the silicon Brillouin laser as the frequency-shifter and compare it to that of the traditional measurement using an acoustic-optic frequency shifter. Fig. 3.9B shows the two spectra superimposed. Strong qualitative agreement between the two experimental spectra demonstrates that the SBS laser behaves analogously to a self-driven acousto-optic frequency shifter. More specifically, the emitted Stokes light from this silicon Brillouin laser is a frequency-shifted copy of the pump light with a small degree of phase noise imparted by the phonon field. Fig. 3.9C shows the range of the spectrum that is most sensitive to the phonon linewidth and the theoretical comparison. The spectrum plotted (Stokes power of 0.025 mW) in Fig. 3.9C shows good agreement with the theoretical spectrum with a phonon linewidth of 3 kHz.

Spectral characteristics conventionally exhibited by Brillouin lasers

The self-heterodyne measurement performed with the silicon Brillouin laser demonstrates the unique phonon linewidth narrowing characteristics of this device. By contrast, in the dissipation hierarchy conventionally realized in silica Brillouin lasers— that is, $\Gamma \gg \gamma_{\mathrm{p}}, \gamma_{\mathrm{s}}$ — the predicted spectrum is very different from both Eq. 3.83 and the experimentally measured spectrum of this silicon Brillouin laser. In this more widely studied regime, the Stokes field experiences Schawlow-Townes narrowing, resulting in a narrow linewidth Stokes

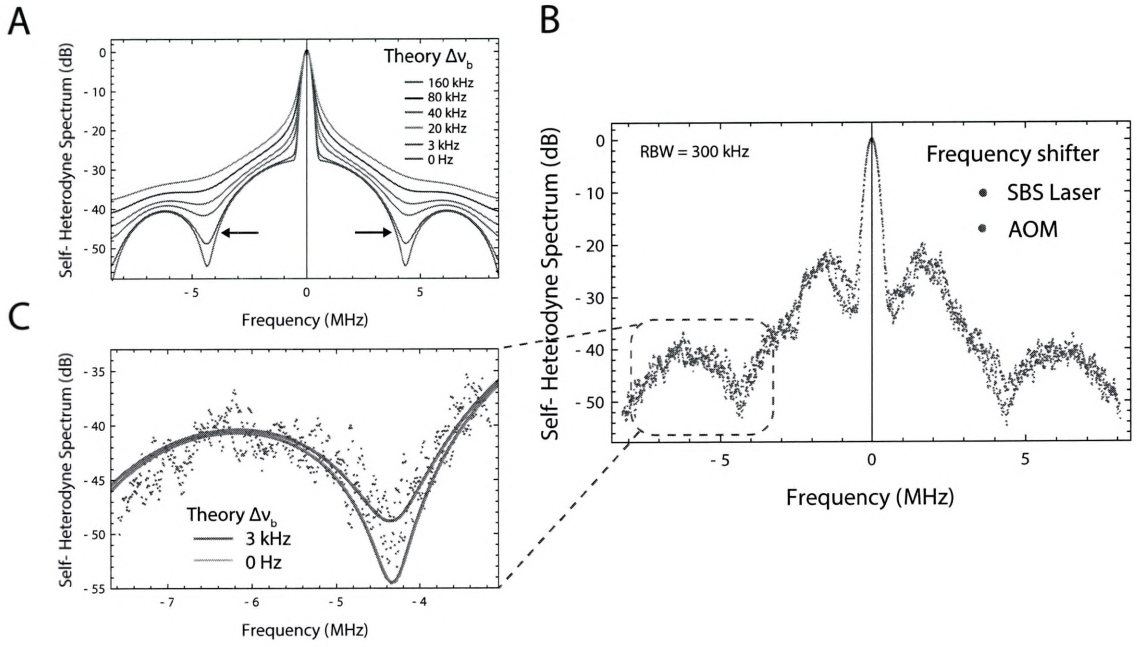

Figure 3.9: (A) Series of theoretical spectra demonstrating the effect of phonon phase noise on the self-heterodyne measurement. As the phonon linewidth increases, the fringes lose contrast. (B) Comparison of the self-heterodyne spectrum using the Brillouin laser as the frequency-shifter (Fig. 3.7) with the traditional spectrum using an AOM as the frequency-shifter (Fig.3.8A). Identical delay lengths are used in each experiment. (C) Theory-experiment comparison in the most sensitive portion of the spectrum to the phonon linewidth. Note that there is some residual phase noise that reduces the contrast of the fringes from the 0 Hz theoretical trend (evident from the spectra using the AOM as the frequency shifter). We attribute this noise to small variations in the delay arm of our fiber interferometer. From Ref. [96]. Reprinted with permission from AAAS.

wave whose phase is now uncorrelated with that of the pump. Thus, in the conventional limit, Eq. 3.70 becomes

$$\mathfrak{S}[\omega] = \frac{1}{2\pi}\int_{-\infty}^{\infty} d\tau e^{i\omega\tau}\langle\tilde{a}_{\mathrm{p}}(\tau+\tau_{\mathrm{d}})\tilde{a}_{\mathrm{p}}^{\dagger}(\tau_{\mathrm{d}})\rangle\langle a_{\mathrm{s}}^{\dagger}(\tau)a_{\mathrm{s}}(0)\rangle. \tag{3.85}$$

Applying the same technique as that of the previous section, the spectral density becomes

$$\mathfrak{S}[\omega] = \frac{|\tilde{\alpha}_{\mathrm{p}}|^2|\alpha_{\mathrm{s}}|^2}{2\pi}\int_{-\infty}^{\infty} d\tau e^{i(\omega-\Omega_{\mathrm{B}}-\Delta_{\mathrm{AOM}})\tau}e^{\frac{-(\Delta\omega_{\mathrm{p}}+\Delta\omega_{\mathrm{s}})|\tau|}{2}}. \tag{3.86}$$

Here, $\Delta\omega_{\mathrm{p}}$ and $\Delta\omega_{\mathrm{s}}$ are the linewidths for the pump and Stokes waves, respectively (angular frequency units). Evaluating Eq. 3.86, we find that the spectral density in the conventional Brillouin limit is a simple Lorentzian

$$\mathfrak{S}[\omega] \propto P_{\mathrm{s}}P_{\mathrm{p}}\frac{4(\Delta\omega_{\mathrm{p}}+\Delta\omega_{\mathrm{s}})}{(\Delta\omega_{\mathrm{p}}+\Delta\omega_{\mathrm{s}})^2+4(\omega-\Omega_{\mathrm{B}}-\Delta_{\mathrm{AOM}})^2}. \tag{3.87}$$

Note that Eq. 3.87 is independent of τ_{d}, as there is no phase coherence for interference. Thus, in the conventional Brillouin limit, the self-heterodyne spectrum is devoid of the characteristic fringes, in sharp contrast to the phonon linewidth narrowing regime explored by the silicon Brillouin laser.

3.6 Summary of laser dynamics

In this section, we present a summary and conceptual understanding of the spatio-temporal dynamics of the system. In Section 3.4.1, we saw that this system exhibits spatial dynamics and optical self-oscillation that is consistent with other Brillouin lasers. However, as derived in Section 3.4.3 and experimentally demonstrated in Section 3.5, optical self-oscillation yields uncharacteristic line-narrowing behavior, producing spectral compression of the elastic degrees of freedom.

We first discuss the spatial dynamics exhibited by this silicon Brillouin laser system. In general, there are two conditions required for Brillouin self-oscillation: (1) an optical cavity to provide feedback and (2) sufficient optical gain from stimulated Brillouin scattering to overcome the round-trip loss. In many ways, the spatial dynamics of Brillouin lasers can be

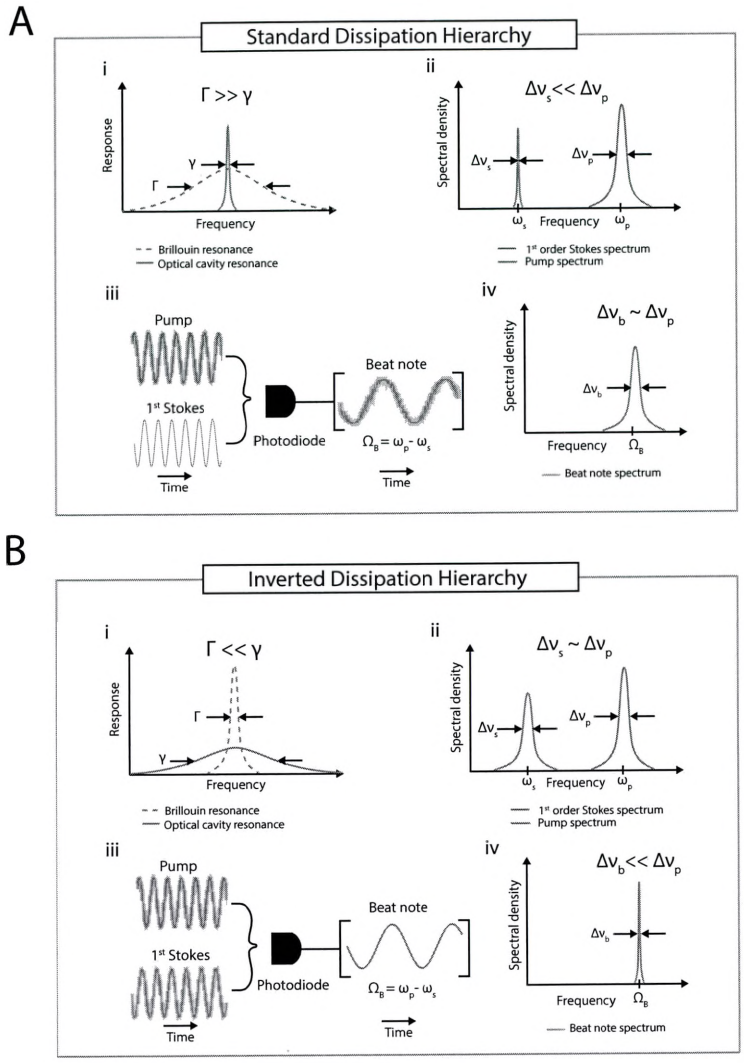

Figure 3.10: Heuristic illustration of the noise characteristics of the silicon Brillouin laser. (A) Diagram illustrating the noise properties of a Brillouin laser operating above threshold in the standard dissipation hierarchy where (i) the Brillouin gain bandwidth (or phononic decay rate, Γ) is much larger than the cavity linewidth (γ) of the optical resonator. In this limit, Brillouin lasing produces optical linewidth narrowing of the Stokes wave, resulting in the optical spectrum plotted in (ii), where the Stokes wave linewidth is narrow compared to that of the pump wave. (iii) diagrams a heterodyne measurement of the optical beat frequency between these two waves, which inherits the noise of the pump laser. This results in a noisy beat note with a linewidth approximately equal to the pump wave linewidth (iv). (B) Diagram showing the noise properties of this silicon Brillouin laser operating above threshold. (i) In this regime the dissipation hierarchy is inverted ($\Gamma << \gamma$). As a result, Brillouin lasing produces phonon linewidth narrowing, and the Stokes becomes a frequency-shifted copy of the pump, giving the optical spectrum plotted in (ii). As a result, heterodyne detection produces a clean beat note (iii) that directly reflects the phonon power spectrum (iv). From Ref. [96]. Reprinted with permission from AAAS.

related to the well-known physics of singly resonant optical parametric oscillators (OPOs). Analogous to the role of the signal wave within a singly-resonant OPO, feedback and optical gain for the Stokes wave are required for Brillouin laser oscillation. By contrast, the phonon field is spatially heavily damped and experiences no cavity feedback (see Section 3.4.1), performing the function of the ballistic idler wave in the context of singly-resonant OPO physics. Thus, while the strength of the phonon field increases dramatically above threshold, its emission can be understood as a byproduct of laser oscillation, in direct analogy with the idler wave in a self-oscillating singly resonant OPO.

With regard to the temporal dynamics, Brillouin lasers conventionally operate in a regime in which the optical fields not only live longer in space, but also in time. Specifically, the pump and Stokes dissipation rates γ_p and γ_s, respectively, are much smaller than the acoustic dissipation rate Γ. This regime of operation, which we refer to as the standard dissipation hierarchy, produces optical linewidth narrowing. As a result, the emitted Stokes wave can be viewed as a purified, frequency-shifted version of the incident pump field, as shown in Fig. 3.10A.

Our silicon Brillouin laser exhibits an intriguing combination of spatial and temporal dynamics. These properties are illustrated conceptually in Fig. 3.11A-B. In space (see Fig. 3.11A), we find that the optical fields are able to propagate freely around the cm-scale racetrack cavity, while by comparison, the phonon field decays very rapidly (~ 60 μm). In this way, the spatial dynamics are consistent with other Brillouin lasers, and consequently the dynamics exhibited by singly resonant optical parametric oscillators. In time, however, we find that the decay hierarchy is actually inverted relative to the conventional limit: the phonon lives longer in time (i.e., $\gamma_p, \gamma_s \gg \Gamma$). Thus, this Brillouin laser simultaneously operates where the spatial acoustic decay length (~ 60 μm) is far smaller than the optical decay length (~0.1-1 m), while the intrinsic phonon lifetime (77 ns) exceeds that of the optical fields ($\sim 2 - 12$ ns)—a condition made possible by the disparate velocities of light and sound. We are able to reach this unconventional regime of laser dynamics thanks to the exceptionally large Brillouin coupling in this system ($> 1000\times$ that of silica fiber).

As shown in Fig. 3.10, the unique spatio-temporal dynamics of this system produce distinct linewidth narrowing behavior. As laser oscillation ensures, both the Stokes and

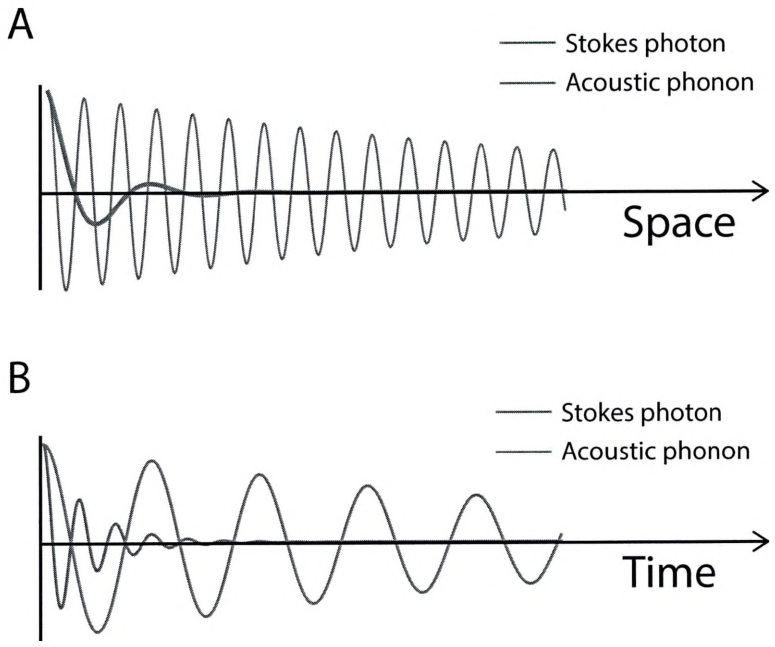

Figure 3.11: Pictorial representation of the distinct spatial and temporal dynamics exhibited by this Brillouin laser.(A) Spatial dynamics. We find that while the optical fields are able to freely propagate around a cm-scale cavity, the phonon field dies rapidly ($\sim$ 60 μm) in space. Since this system has optical feedback and no phonon feedback, it produces optical self-oscillation. (B) Temporal dynamics. In time, this decay hierarchy is reversed. The phonon lives much longer in time, leading to phonon linewidth narrowing.

phonon field experience significant linewidth narrowing relative to the spontaneous Brillouin linewidth. However, well above threshold, only the phonon field experience Schawlow-Townes narrowing. As a result, the emitted Stokes light becomes a frequency shifted, carbon copy of the pump, with residual phase noise given by the phonon power spectrum. Thus, the degree of relative coherence between the pump and Stokes waves is quantified by the phonon Schawlow-Townes linewidth, which is given by

$$\Delta\nu_{\mathrm{b}} = \frac{\Gamma}{4\pi\beta^2}(n_{\mathrm{B}}^{\mathrm{th}} + n_{\mathrm{s}}^{\mathrm{th}} + 1), \tag{3.88}$$

where $n_{\mathrm{B}}^{\mathrm{th}}$ and $n_{\mathrm{s}}^{\mathrm{th}}$ are the thermal occupations of the phonon and Stokes fields and Γ is the temporal phonon dissipation rate. Thus, the fundamental phonon linewidth is given by the quantum and optomechanical fluctuations of the oscillating Stokes and phonon fields. We see that Schawlow-Townes narrowing reduces the phonon linewidth as the coherent phonon number β^2 is increased.

This form of phonon linewidth narrowing is similar to that produced by 'phonon lasing' as demonstrated in cavity-optomechanical systems [120, 123]. However, in contrast to such phonon laser systems, this Brillouin laser does not possess a phonon cavity or any form of phonon feedback necessary to achieve phonon self-oscillation. As such, our results extend these linewidth-narrowing concepts to macroscopic Brillouin lasers systems, in which the acoustic field is heavily damped in space and does not experience cavity feedback. Here we show that, despite the high degree of spatial damping and lack of phonon feedback, optical self-oscillation can actually produce phonon linewidth narrowing, as long as the phonon lifetime exceeds that of the optical fields. This physics, which we explore for the first time, can be viewed as an extreme limit of optical parametric oscillator dynamics with a slow, ballistic, long-lived idler wave.

3.7 Conclusion and outlook

In this chapter, we have demonstrated Brillouin lasing in silicon for the first time, representing a significant milestone for Brillouin photonics and silicon-based lasers. By engineering multimode optomechanical structures that support large Brillouin couplings between distinct optical spatial modes, we have been able to tailor the Brillouin amplification dynamics to suit powerful new Brillouin laser technologies. We have designed and fabricated high-Q multimode racetrack resonator structures that take advantage of these properties to achieve robust laser oscillation. We also developed new spectroscopy methods and theoretical tools to understand the underlying dynamics, and show that the large Brillouin gains and unique elasto-optic properties of our system allows us to explore an intriguing limit of 3-wave laser physics.

With regard to the overarching theme of this dissertation, this new inter-modal laser concept yields unprecedented flexibility in design and allows us to engineer and manipulate Brillouin laser dynamics in a myriad of ways. In particular, the addition of modal degrees of freedom allow us to limit or control energy transfer dynamics produced by cascaded Brillouin lasing. The multimode nature of the interaction also allows us to individually address and independently control pump and Stokes modes. In comparison with prior Brillouin laser systems based on backward stimulated Brillouin scattering, the laser cavity circumference is not constrained and, as such, is not inhibited by tight tolerances that would otherwise present challenges for scalable integration. Furthermore, because the Brillouin gain, acoustic dissipation, and Brillouin frequency can be tailored by the geometry, the Brillouin coupling mechanism may be engineered according to the desired application and regime of dynamics.

Finally, in addition to the control achieved through phase-matching, we have seen that the introduction of an optical cavity can be used to enable and shape laser dynamics. Building on this work, we will explore how these passive optical properties, in conjunction with the nonlinear Brillouin couplings, allow us to create a new class of high-performance amplifier and non-reciprocal technologies. We will explore these concepts in Chapters 4 and 6.

Chapter 4

Resonantly enhanced non-reciprocal Brillouin amplifier

4.1 Introduction

By developing and manipulating the optomechanical properties of silicon, we have been able to (1) transform Brillouin interactions into the strongest silicon-based non-linearity, (2) shape Brillouin amplification dynamics by controlling the phase-matching condition, (3) and use these engineered couplings to achieve Brillouin lasing. Up to this point, however, it is important to note that the available Brillouin amplification made possible by these processes has been limited to 2-5 dB. By contrast, many Brillouin photonics applications—such as Brillouin-amplification based non-reciprocal devices [31], distributed Brillouin sensing [124, 125], tunable time delay [126], and RF-photonic filtering [88,89,127,128]—require 10 dB or more. Large levels of gain (50 dB) necessary for these applications have been possible in silica-based fiber-optic or chalcogenide waveguide systems [129], but so far have been out of reach in silicon. Moreover, lack of silicon-based amplifier technologies provides additional impetus to create high-performance Brillouin amplifiers within CMOS-compatible silicon-photonic circuits.

Challenges of scaling Brillouin amplification in linear waveguides

Within a given linear waveguide system, there are two ways to enhance the degree of Brillouin amplification: (1) increase the pump power and (2) extend the length of the Brillouin active devices. However, there are fundamental challenges associated with each strategy. (1) In silicon, nonlinear losses from two-photon absorption and TPA-induced free-carrier absorption quickly overtake gains from stimulated Brillouin scattering, limiting the available pump powers to the $\sim$ 100 mW level [29,130]. (2) In principle, Brillouin-active silicon waveguides can be much longer ($>$ 10 cm) than the 2-cm lengths presented in Chapter 2. However, the most immediate problem we encounter with this strategy are the effects of inhomogeneous broadening; i.e., dimensional variations along the device length lead to a smeared-out spectrum where the peak gain is significantly reduced [131]. This is because small variations in the waveguide dimensions dramatically affect the Brillouin frequency. For instance, a 1-nm change in the phonon membrane width leads to a 1 MHz change in the phonon frequency, representing a 10% change relative to the intrinsic gain bandwidth [29]. With practical fabrication considerations, these effects prevent high-performance devices with lengths beyond several centimeters. Moreover, even if these variations could be mitigated, linear and nonlinear losses prevent optimal pump levels over larger length scales without new strategies for periodic re-injection, adding significant device complexity.

Resonantly enhanced approach

In this chapter, we use a resonant geometry to profoundly enhance the available Brillouin amplification. We do this by harnessing stimulated inter-modal Brillouin gain within multi-spatial-mode racetrack resonator system that is interfaced with mode-specific couplers to allow signal light to be amplified as it is transmitted through the system. This approach allows us to transform the otherwise modest levels of Brillouin gain (3.5 dB) and amplification ($\sim$ 2 dB) possible in a cm-scale linear waveguide system into more than 30 dB of gain and 20 dB of net amplification, significantly advancing state-of-the-art performance. Moreover, we realize this physics in a compact geometry (1.5 cm) that circumvents deleterious nonlinear losses by operating at low pump powers ($<$ 40 mW) below the laser threshold. Leveraging

the unidirectional amplification produced by this phase-matched process, we also use this system to demonstrate more than 28 dB of non-reciprocal contrast between forward- and backward-propagating waves, representing the first demonstration of lossless isolation in an all silicon device at room temperature.

4.2 Resonantly enhanced device concept

In this section, we introduce the resonantly enhanced device physics through a simplified conceptual picture. A corresponding diagram is found in Fig. 4.1. We consider a ring-resonator system that is interfaced with an input (coupler A) and output coupler (coupler B), each with an associated loss rate γ_A and γ_B, respectively. Together with the internal loss rate of the resonator, γ_i, these effects yields a total loss rate $\gamma_{tot} = \gamma_A + \gamma_B + \gamma_i$.

We now consider the consequence of adding some form of gain to the system, with a temporal rate given by γ_G. Through temporal coupled mode theory [132] we find that the relevant equations of motion are given by

$$\begin{aligned} \dot{a}(t) &= -i\omega_0 a(t) - \left(\frac{\gamma_A}{2} + \frac{\gamma_B}{2} + \frac{\gamma_i}{2} - \frac{\gamma_G}{2}\right)a(t) + \sqrt{\gamma_A}S^{in}(t) \\ S^{out}(t) &= \sqrt{\gamma_B}a(t), \end{aligned} \tag{4.1}$$

where $a(t)$ is a unitless mode amplitude (normalized such that $\langle a^\dagger(t)a(t)\rangle$ = photon number), ω_0 is the resonant frequency of the cavity, and $S^{in}(t)$ and $S^{out}(t)$ are the input and output signals, respectively.[1] Solving for the output field in the Fourier domain, we find the total transmission through the system to be

$$\frac{|S^{out}[\omega_s, \gamma_G]|^2}{|S^{in}[\omega_s]|^2} = \left|\frac{2\sqrt{\gamma_A\gamma_B}}{-2i(\omega_s - \omega_0) + \gamma_A + \gamma_B + \gamma_i - \gamma_G}\right|^2. \tag{4.2}$$

As an intuitive starting point, we consider the response of the system on resonance ($\omega_s = \omega_0$) and examine the case of identical couplers such that $\gamma_A = \gamma_B = \gamma_c$. Under these conditions the transmission becomes

1. $S^{in}(t)$ and $S^{out}(t)$ are normalized such that $S^\dagger S$ = photon flux.

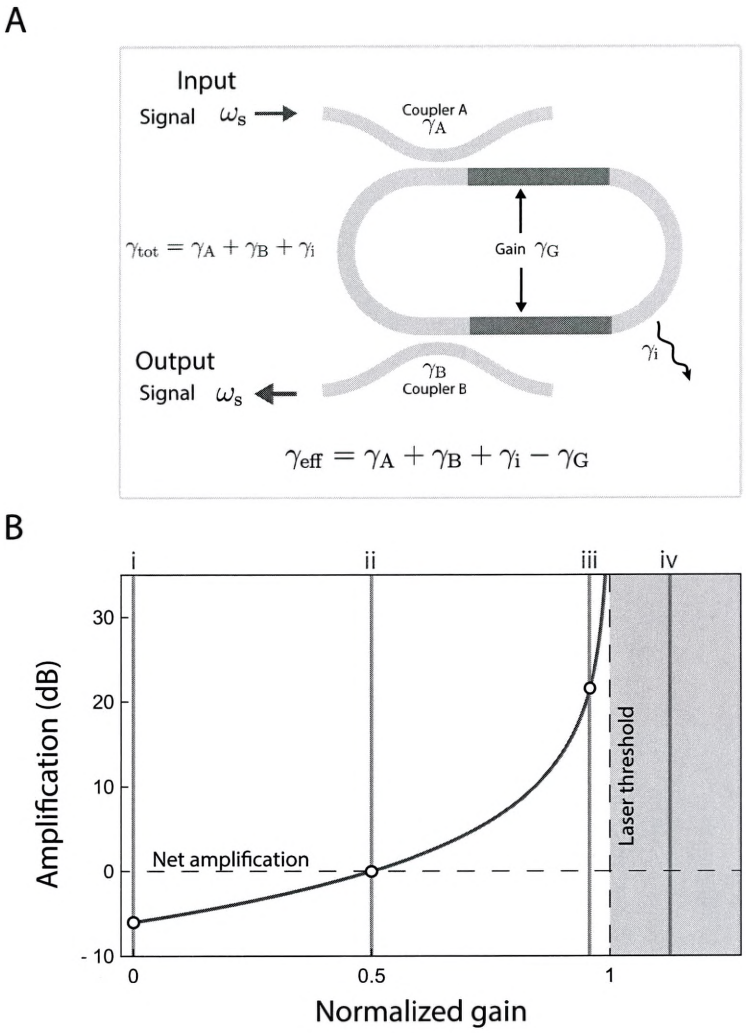

Figure 4.1: (A) Simplified resonantly enhanced device concept with amplification dynamics given by Eq. 4.2. (B) Total amplification (see Eq. 4.3) as a function of normalized gain (γ_G/γ_{tot}). For simplicity, here we take the case when $\gamma_i = \gamma_A + \gamma_B$. (i)-(iv) give 4 distinct cases as the gain is increased. (i) In the absence of gain, the resonator yields net loss given by the linear transmission through the system. (ii) When the gain is able to compensate for the internal losses of the resonator (i.e., $\gamma_G = \gamma_i$), the system yields unity transmission; this is the point of net amplification. (iii) As the gain is increased, we are able to achieve large degrees of amplification below the laser threshold. (iv) Beyond the laser threshold, the system begins to self-oscillate.

$$\frac{|S^{\text{out}}[\omega_s = \omega_0, \gamma_G]|^2}{|S^{\text{in}}[\omega_s = \omega_0]|^2} = \left| \frac{2\gamma_c}{2\gamma_c + \gamma_i - \gamma_G} \right|^2. \tag{4.3}$$

We now consider the total transmission through the system on a case by case basis, as plotted in Fig. 4.1B. (i) In the absence of gain, the total transmission becomes $|2\gamma_c/(2\gamma_c + \gamma_i)|^2$, which is simply the linear transmission through the system. (ii) When the gain is able to compensate for the internal losses of the resonator (i.e., $\gamma_G = \gamma_i$), resonant transmission through the system becomes lossless (i.e., approaches unity); in this case, the system is said to have zero net amplification. (iii) In the case when the gain exceeds the internal losses of the resonator ($\gamma_G > \gamma_i$), but does not exceed the total loss (i.e., $\gamma_G < \gamma_i + 2\gamma_c$), the system yields greater-than-unity transmission without producing self-oscillation (i.e., below the laser threshold (case iv)). In the limit when the gain approaches the total loss of the system, the degree of amplification can become arbitrarily large—in principle, limited only by pump depletion.[2] In what follows we build on the inter-modal Brillouin laser system (Chapter 3) to demonstrate this physics for the first time using stimulated Brillouin scattering.

4.3 Resonantly enhanced Brillouin amplification

We use a resonant optical configuration to manipulate and radically enhance optical amplification based on stimulated inter-modal Brillouin scattering. Our resonantly enhanced Brillouin amplifier consists of a 15 mm-circumference racetrack cavity that possesses two Brillouin-active regions (Fig. 4.2A; for experimental parameters see Appendix C). The device is fabricated from a single-crystal SOI wafer using a standard silicon-on-insulator (SOI) process. Building on the results presented in Chapter 3, the racetrack cavity is formed from a multimode silicon ridge waveguide that supports low-loss guidance of transverse electric (TE)-like symmetric and antisymmetric optical spatial modes. In the Brillouin-active regions, this multimode optical waveguide is suspended to provide acoustic guidance for

2. In the case of a resonant Brillouin amplifier, γ_G is dependent on the intracavity pump power, which can be depleted in the case of large intracavity signal powers.

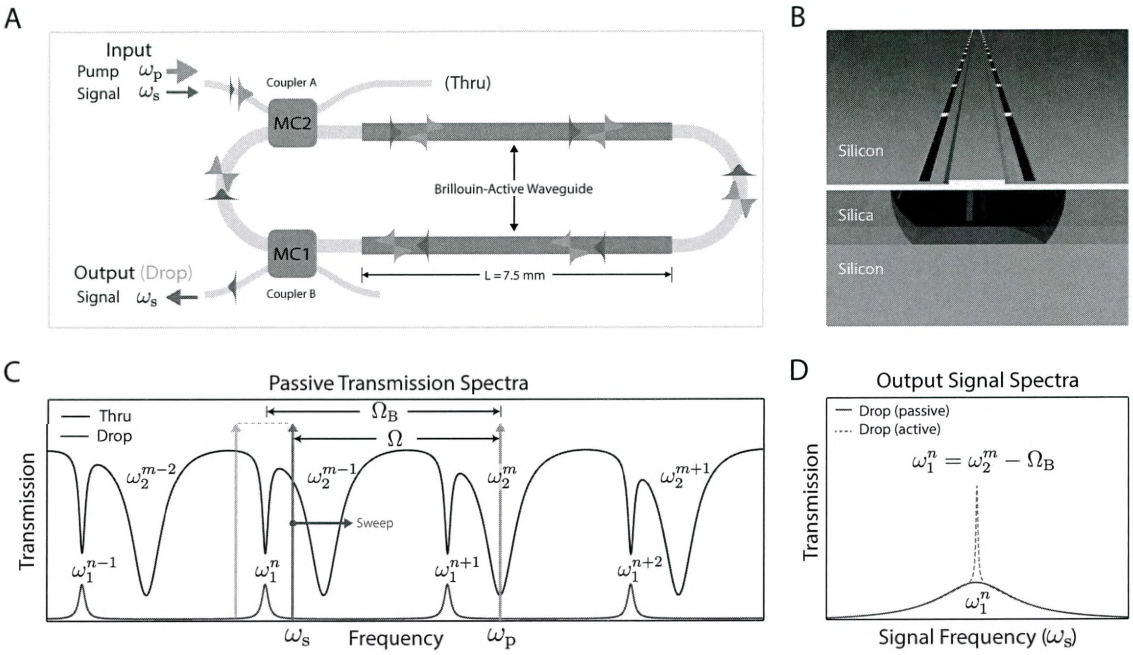

Figure 4.2: (A) Device concept for resonantly enhanced inter-modal Brillouin amplification. Leveraging the frequency selectivity of the racetrack cavity, pump (ω_p) and and signal waves (ω_s) are coupled into the antisymmetric and symmetric cavity modes, respectively, via a coupler A (mode-specific coupler MC2). As the pump and signal waves traverse the Brillouin-active segments, the pump wave resonantly amplifies the signal wave through stimulated inter-modal Brillouin scattering. The signal wave exits the system through a mode-selective coupler (MC1) (coupler B;drop port), which is designed to couple strongly to the symmetric mode and weakly to the antisymmetric mode (see Fig. 4.3). (B) Schematic illustrating the cross-sectional geometry of the Brillouin-active regions, as developed in Chapter 2. (C) Idealized optical transmission spectra of the multimode racetrack cavity at the thru and drop ports. Coupling into the racetrack resonator via a multimode coupler yields a characteristic multimode transmission spectrum at the thru port, with broad (centered at ω_2^m) and narrow (centered at ω_1^n) resonances corresponding to the antisymmetric and symmetric optical spatial modes, respectively. Resonantly-enhanced Brillouin amplification measurements are performed by coupling the pump wave (ω_p) to an antisymmetric cavity mode (ω_2^m) and sweeping the signal wave (ω_s) through a symmetric cavity mode (ω_1^n) that is red-shifted from by the Brillouin frequency (Ω_B). (D) Zoomed-in transmission spectrum for the signal wave exiting the drop port when $\omega_s \approx \omega_1^n$ with (active) and without (passive) the Brillouin gain supplied by the pump wave. Adapted from Ref. [97]. Copyright (2019) by OSA.

the 6-GHz traveling elastic wave that mediates strong inter-modal Brillouin coupling (see Fig. 4.2B; for waveguide dimensions, see Chapter 2). Within the resonator, the symmetric and antisymmetric optical spatial modes form two distinct sets of resonances, which as in Chapter 3, we denote by $\{\omega_1^n\}$ and $\{\omega_2^m\}$, respectively.

4.3.1 Passive optical properties

Robust Brillouin amplification in this inter-modal geometry is contingent upon the ability to selectively address cavity modes produced by the symmetric and antisymmetric waveguide modes. This functionality is relatively straightforward to achieve in the case of the input coupler (coupler A), labelled MC2 in Fig. 4.2A and 4.3A. Building on the mode multiplexer structure developed in Chapter 2, we design MC2 such that it preferentially couples to the antisymmetric waveguide mode, while also permitting non-zero coupling to the symmetric waveguide mode.[3] As such, the properties of coupler A, in conjunction with the frequency selectivity of the cavity, allow us to inject pump and signal waves into pairs of antisymmetric and symmetric cavity modes that satisfy the Brillouin condition, respectively.

Creating a mode-specific coupler that preferentially couples to the symmetric waveguide mode, as needed for the output coupler (coupler B), however, is in practice more difficult to attain. In principle, it is possible to achieve the desired degree of coupling using a symmetric multimode coupler, where two multimode waveguides of identical dimensions are brought together to permit evanescent coupling. The unintended consequence of this design, however, is that it actually produces more coupling to the antisymmetric waveguide mode, which would prevent any appreciable build-up of the pump wave circulating in an antisymmetric cavity mode. This occurs because the antisymmetric waveguide mode is more weakly guided and evanescent in character, and as such, it is difficult to develop coupler designs that preferentially address the more well-confined symmetric waveguide mode. We develop a new mode-selective coupler for the symmetric waveguide mode (labelled MC1) by exploiting an asymmetry in the dependence of effective mode indices on waveguide

3. The coupler consists of a 625-nm bus waveguide whose fundamental (symmetric) mode is primarily phase-matched with the antisymmetric spatial mode of the 1.5-μm racetrack waveguide, such that it couples strongly to the antisymmetric spatial mode and weakly to the symmetric spatial mode (see Table C.1).

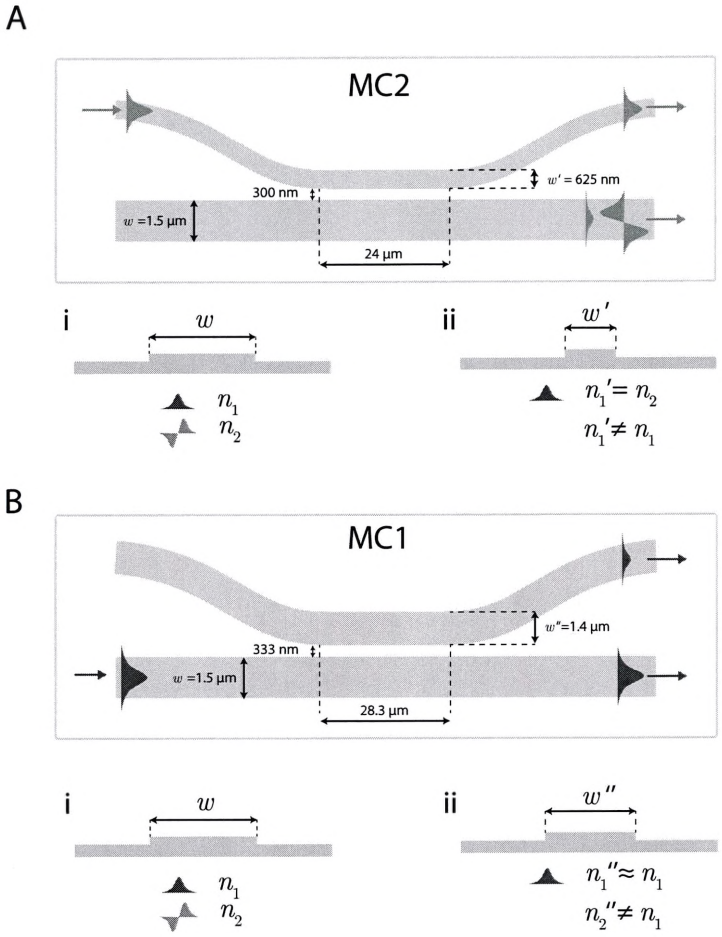

Figure 4.3: (A)-(B) Mode-specific coupler designs. (A) Mode-specific coupler 2 (MC2) is a multimode coupler that is designed to couple strongly to the antisymmetric waveguide mode and weakly to the symmetric. To do this, we use a bus waveguide (of width w') whose effective index (n_1') matches that of the antisymmetric waveguide mode (of width w). (B) Mode-specific coupler 1 (labelled MC1) is designed to couple preferentially to the symmetric waveguide mode. It consists of a bus waveguide (of width w'') whose antisymmetric spatial mode experiences a non-zero phase delay relative to that of the antisymmetric mode of the racetrack waveguide. By contrast, this perturbation leaves the symmetric modes nearly degenerate in effective mode index, permitting mode-specific coupling. Adapted from Ref. [97]. Copyright (2019) by OSA.

dimensions. Because the higher order modes are more sensitive to waveguide dimension, a slight change in waveguide width pushes the antisymmetric mode away from phase-matched coupling much more quickly than it does for the symmetric mode, as illustrated in Fig. 4.3Bi-ii. Using this concept, the bus and racetrack waveguides are designed with a slight asymmetry in width (1.4 μm and 1.5 μm, respectively) such that the fundamental modes remain phase-matched (the fundamental mode indices remain very close), while the higher order modes are not phase-matched (the mode indices become quite distinct), yielding a coupler that selectively couples out the symmetric mode (with crosstalk of ~ -10 dB). With improved fabrication, as we demonstrate in Chapter 5-6, these crosstalk levels can be driven down below -40 dB.

We measure the linear transmission response of the cavity using a swept 1.55 μm laser (Agilent 81600B; sweep rate set to 5 nm/s.[4] at low powers ($\sim$ 120 μW on-chip)). Fig. 4.4A-B plots the measured transmission (thru) spectra centered around two distinct mode pairs that satisfy the Brillouin condition ($\omega_1^n = \omega_2^m - \Omega_B$), while Fig. 4.4C shows the transmission spectra measured at the thru and drop ports over a larger wavelength range. These measurements reveal a set of high-Q symmetric cavity modes ($Q_1 \approx 10^6$) and antisymmetric cavity modes ($Q_2 = 2 \times 10^5$). Fitting these transmission spectra to a multimode resonator model (see Supplementary Materials of Ref. [95]) allows us to obtain important parameters of the system, including the multimode coupling coefficients, group velocities, and linear propagation losses (see Appendix C). This information is then used to model the amplifier dynamics derived in Section 4.3.3.

4.3.2 Operation scheme

Signal light injected into the symmetric cavity mode (ω_1^n) can be amplified through the resonant Brillouin system provided that (1) the pump wave is resonant with an antisymmetric cavity mode ($\omega_p = \omega_2^m$) and (2) the symmetric cavity mode satisfies the Brillouin condition ($\omega_1^n = \omega_2^m - \Omega_B$). We experimentally characterize this system by coupling the pump and signal waves into the antisymmetric and symmetric cavity modes of the racetrack

4. Using a triggered oscilloscope, we can convert swept transmission measurements in time to wavelength

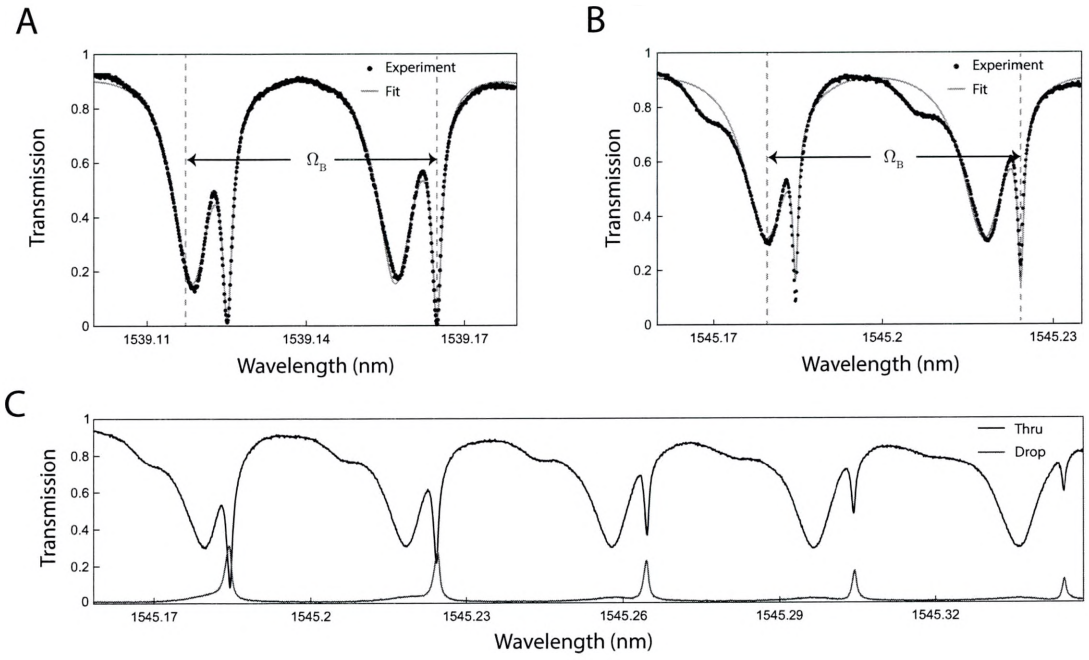

Figure 4.4: (A)-(B) Linear (thru) transmission spectra centered around two distinct mode pairs that satisfy the Brillouin condition ($\omega_1^n = \omega_2^m - \Omega_B$). Narrow (broad) resonances correspond to the symmetric (antisymmetric) spatial modes of the multimode waveguide. Fits are obtained using the multimode ring resonator theory presented in the Supplementary Materials of Ref. [95]. (C) Transmission spectra measured at the thru and drop ports over a larger wavelength range. Reproduced from Ref. [97]. Copyright (2019) by OSA.

resonator via coupler A. As described in Section 4.3.1,the co-propagating pump and signal waves nonlinearly couple as they traverse the Brillouin-active regions of the racetrack, producing Brillouin energy transfer and single-sideband gain through stimulated inter-modal Brillouin scattering [29]. As the pump power approaches the threshold for lasing, the degree of amplification is significantly enhanced (see Fig. 4.2D).

4.3.3 Theoretical analysis

We now consider the predicted theoretical response of this resonant Brillouin amplifier system. To this end, we extend the heuristic temporal-coupled mode framework discussed in Section 4.2 (see also Ref. [132]) to the case of gain supplied by inter-modal Brillouin amplification. Building on the strategy of Section 3.4.2, we begin from the mean-field equations of motion, given by

$$\begin{aligned}
\dot{a}_{\mathrm{s}}(t) &= -i\omega_1^n a_{\mathrm{s}}(t) - \frac{\gamma_{\mathrm{tot},1}}{2} a_{\mathrm{s}}(t) - ig^* a_{\mathrm{p}}(t) b^\dagger(t) + \sqrt{\gamma_{\mathrm{A},1}} S^{\mathrm{in}}(t) \\
\dot{b}(t) &= -i\Omega_{\mathrm{B}} b(t) - \frac{\Gamma}{2} b(t) - ig^* a_{\mathrm{p}}(t) a_{\mathrm{s}}^\dagger(t) \\
\dot{a}_{\mathrm{p}}(t) &= -i\omega_2^m a_{\mathrm{p}}(t) - \frac{\gamma_{\mathrm{tot},2}}{2} a_{\mathrm{p}}(t) - iga_{\mathrm{s}}(t) b(t) + \sqrt{\gamma_{\mathrm{A},2}} S_{\mathrm{p}}^{\mathrm{in}}(t).
\end{aligned} \tag{4.4}$$

As introduced in Chapter 3, $a_{\mathrm{s}}(t)$, $b(t)$, and $a_{\mathrm{p}}(t)$ are the coupled-mode amplitudes for the signal, phonon, and pump fields, respectively; $\{\omega_1^n\}$ and $\{\omega_2^m\}$ are the resonance frequencies of the cavity modes produced by the symmetric and antisymmetric waveguide modes, respectively; g is the elasto-optic coupling; $\gamma_{\mathrm{tot},(1,2)}$ is the total loss rate for the symmetric and antisymmetric spatial modes (defined by $\gamma_{\mathrm{tot},(1,2)} \equiv \gamma_{\mathrm{A},(1,2)} + \gamma_{\mathrm{B},(1,2)} + \alpha_{(1,2)} v_{\mathrm{g},(1,2)}$); $\gamma_{(\mathrm{A,B}),(1,2)}$ are the dissipation rates for the symmetric and antisymmetric spatial modes due to couplers A and B ($\gamma_{(A,B),(1,2)} \equiv -(2v_{\mathrm{g},(1,2)}/L)\ln(1-\mu^2_{(\mathrm{A,B}),(1,2)})^{1/2}$) while $\gamma_{\mathrm{R},1}$ represents the internal losses of the racetrack resonator for the symmetric mode ($\gamma_{\mathrm{R},1} = \alpha_1 v_{\mathrm{g},1}$); $v_{\mathrm{g},(1,2)}$ is the group velocity of the symmetric and antisymmetric optical spatial modes; L is the length of the racetrack resonator; $\alpha_{(1,2)}$ is the linear propagation loss of the symmetric and antisymmetric spatial mode; Γ is the dissipation rate for the acoustic field. To provide a clear connection to temporal coupled mode theory, here we represent the signal and pump

fields with $S^{\text{in}}(t)$ and $S_{\text{p}}^{\text{in}}(t)$ (with units $[\sqrt{\text{number} \times \text{Hz}}]$).[5] We note here that, for the moment, we have neglected quantum and thermal noise. We will explore the impact of vacuum and thermal fluctuations in great detail in Chapter 7, which derives the quantum-limited noise figure for these devices.

Next, we make the substitutions $a_{\text{s}}(t) = \bar{a}_{\text{s}}(t)\exp(-i\omega_{\text{s}}t)$, $a_{\text{p}}(t) = \bar{a}_{\text{p}}(t)\exp(-i\omega_{\text{p}}t)$, and $b(t) = \bar{b}(t)\exp(-i\Omega t)$ to produce the envelope equations

$$\begin{aligned}
\dot{\bar{a}}_{\text{s}}(t) &= i(\omega_{\text{s}} - \omega_1^n)\bar{a}_{\text{s}}(t) - \frac{\gamma_{\text{tot},1}}{2}\bar{a}_{\text{s}}(t) - ig^*\bar{a}_{\text{p}}(t)\bar{b}^\dagger(t) + \sqrt{\gamma_{\text{A},1}}\bar{S}^{\text{in}}(t) \\
\dot{\bar{b}}(t) &= i(\Omega - \Omega_{\text{B}})\bar{b}(t) - \frac{\Gamma}{2}\bar{b}(t) - ig^*\bar{a}_{\text{p}}(t)\bar{a}_{\text{s}}^\dagger(t) + \bar{\eta}(t) \\
\dot{\bar{a}}_{\text{p}}(t) &= i(\omega_{\text{p}} - \omega_2^m)\bar{a}_{\text{p}}(t) - \frac{\gamma_{\text{tot},2}}{2}\bar{a}_{\text{p}}(t) - ig\bar{a}_{\text{s}}(t)\bar{b}(t) + \sqrt{\gamma_{\text{A},2}}\bar{S}_{\text{p}}^{\text{in}}(t),
\end{aligned} \tag{4.5}$$

In the rotating frame, we have also transformed $S^{\text{in}}(t) = \bar{S}^{\text{in}}(t)\exp(-i\omega_{\text{s}}t)$ and $S_{\text{p}}^{\text{in}}(t) = \bar{S}_{\text{p}}^{\text{in}}(t)\exp(-i\omega_{\text{p}}t)$. We note that the above requires $\omega_{\text{p}} = \omega_{\text{s}} + \Omega$, consistent with our experimental scheme.

For simplicity, we treat the pump wave as undepleted (i.e., $\dot{\bar{a}}_{\text{p}} = 0$ and $\bar{a}_{\text{p}}(t) = \bar{a}_{\text{p}}$) and ignore the vacuum fluctuations associated with the pump. We next take a Fourier transform of Eq. 4.5, yielding

$$\begin{aligned}
-i\omega\bar{a}_{\text{s}}[\omega] &= i(\omega_{\text{s}} - \omega_1^n)\bar{a}_{\text{s}}[\omega] - \frac{\gamma_{\text{tot},1}}{2}\bar{a}_{\text{s}}[\omega] - ig^*\bar{a}_{\text{p}}\bar{b}^\dagger[\omega] + \sqrt{\gamma_{\text{A},1}}\bar{S}^{\text{in}}[\omega] \\
-i\omega\bar{b}[\omega] &= i(\Omega - \Omega_{\text{B}})\bar{b}[\omega] - \frac{\Gamma}{2}\bar{b}[\omega] - ig^*\bar{a}_{\text{p}}\bar{a}_{\text{s}}^\dagger[\omega]
\end{aligned} \tag{4.6}$$

Next, we solve these two coupled equations, yielding

$$\bar{a}_{\text{s}}[\omega] = \frac{1}{-i(\omega + \omega_{\text{s}} - \omega_1^n) + \frac{\gamma_{\text{tot},1}}{2} - \frac{|g|^2|\bar{a}_{\text{p}}|^2}{i(\omega+\Omega-\Omega_{\text{B}})+\frac{\Gamma}{2}}}\left[\sqrt{\gamma_{\text{A},1}}\bar{S}^{\text{in}}[\omega]\right]. \tag{4.7}$$

We proceed by shifting out of the rotating frame calculating the output signal spectrum by noting that $S^{\text{out}}[\omega_{\text{s}},\omega] = \sqrt{\gamma_{\text{B},1}}a_{\text{s}}[\omega_{\text{s}},\omega]$. This allows us to calculate the signal-wave amplification ($|S^{\text{out}}[\omega_{\text{s}},0]|^2/|S^{\text{in}}[\omega_{\text{s}},0]|^2$) by analyzing the spectrum at the center frequency of the input signal (i.e., $\omega = 0$), yielding

5. $S^\dagger S$ has units of photon flux.

$$\frac{|S^{\text{out}}[\omega_{\text{s}},0]|^2}{|S^{\text{in}}[\omega_{\text{s}},0]|^2} = \left| \frac{\sqrt{\gamma_{\text{A},1}}\sqrt{\gamma_{\text{B},1}}}{-i(\omega_{\text{s}}-\omega_1^n)+\frac{\gamma_{\text{tot},1}}{2}-\frac{G_{\text{B}}Pv_{\text{g},1}\Gamma/4}{i(\omega_{\text{p}}-\omega_{\text{s}}-\Omega_{\text{B}})+\Gamma/2}} \right|^2 . \tag{4.8}$$

Here, we have neglected the noise terms and used the definition $G_{\text{B}} = 4|g|^2L/(\hbar\omega_{\text{p}}\Gamma v_{\text{g},1}v_{\text{g},2})$ [75].[6] Equation 4.8 can also be obtained in the time domain by considering the steady-state response of the system.

Equation 4.8 can be used to self-consistently predict the amplification and gain bandwidth of the system and is the basis for the theoretical trends plotted in Fig. 4.6A-B. We note that Eq. 4.8 diverges at the laser threshold condition, which is an artifact of the stiff pump approximation in this analysis. While the equations are consistent with those describing parametric amplification in cavity-optomechanical systems [133], we note that this analysis requires a mean-field treatment of a distributed, heavily spatially damped phonon field, which is valid only in the presence of the pump and Stokes field (for further discussion, see Section 3.4.2).

4.3.4 Experimental results

As diagrammed in Fig. 4.5A, we use nonlinear laser spectroscopy to characterize resonantly enhanced inter-modal Brillouin amplification. All measurements are performed at room temperature and atmospheric pressure using 1.5 μm wavelengths. In this experimental scheme, light from a tunable laser is split along two paths; the upper path is used to synthesize the pump and signal waves, while the lower arm is used to create an optical local oscillator (LO) for heterodyne analysis of the emitted signal wave. The optical LO (lower arm) is generated by an acousto-optic modulator, which blue-shifts the light by $\Delta = 2\pi \times 44$ MHz. The upper path uses an intensity modulator (IM), erbium-doped fiber amplifier (EDFA), and variable optical attenuator (VOA) to synthesize pump and signal waves of a desired power and variable frequency detuning. Pump and signal waves are then coupled on-chip through a grating coupler; the light is subsequently routed to the racetrack resonator through a single-mode waveguide. Signal light exiting the device is combined

6. The Brillouin gain coefficient can alternatively be expressed as $G_{\text{B}} = 4|g|^2|a_{\text{p}}|^2/(P\Gamma v_{\text{g},1})$, which is particularly useful when relating to experimental parameters.

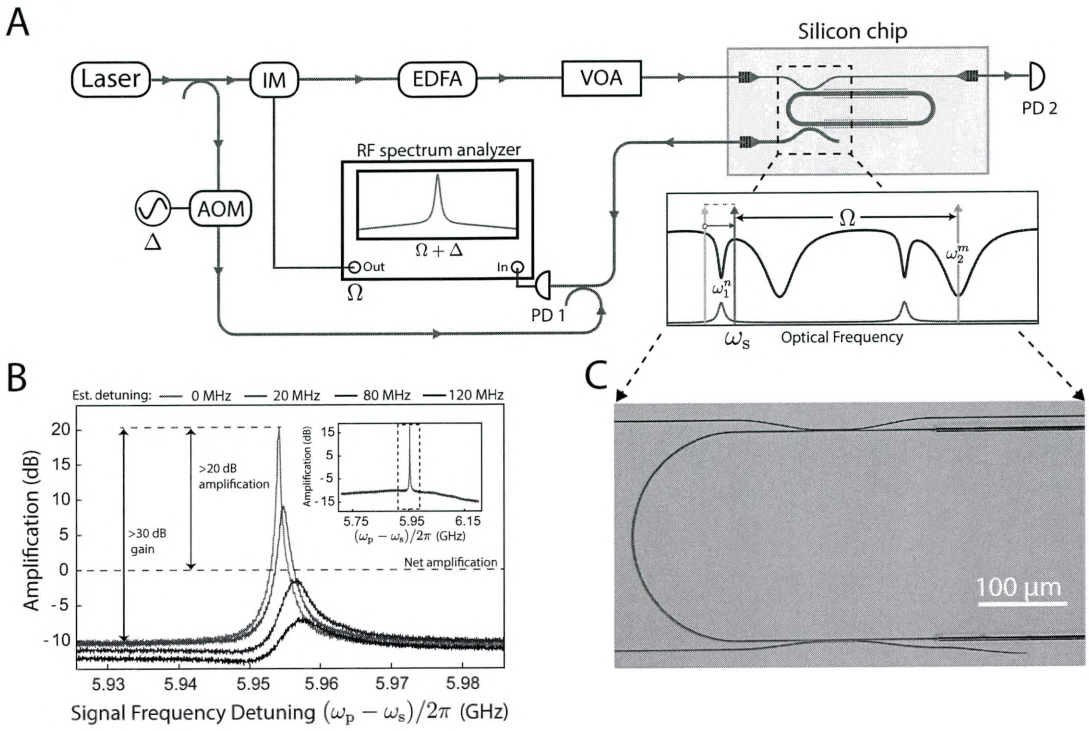

Figure 4.5: (A) Brillouin-heterodyne spectroscopy setup used to characterize resonant Brillouin amplifier. Tunable telecom-band laser light is split along two paths. One path is used to synthesize an optical local oscillator (LO) using an acousto-optic modulator (AOM), which blue-shifts the light by $\Delta = 2\pi \times 44$ MHz. The other arm synthesizes pump and signal waves with the desired frequency detuning ($\Omega = \omega_p - \omega_s$) and powers using an intensity modulator (IM), erbium-doped-fiber amplifier (EDFA), and variable optical attenuator (VOA); the light is subsequently coupled on-chip for nonlinear amplification measurements. After passing through the device, the signal wave is coupled through the drop port and off-chip, where it is combined with the blue-shifted LO and measured on a high-speed photodetector (PD 1). The RF spectrum analyzer, in conjunction with the RF signal generator, sweeps the detuning (Ω) and measures the microwave power at ($\Omega + \Delta$), permitting single-sideband measurements of $\omega_s = \omega_p - \Omega$ (without crosstalk from light at $\omega_p + \Omega$). (B) Gain spectra as a function of signal-wave detuning around the Brillouin resonance, showing more than 30 dB of gain and 20 dB of net amplification. Each trace represents a different estimated detuning of the optical cavity mode relative to the Brillouin frequency (see zoomed-out inset). Large optical cavity detunings relative to the Brillouin resonance diminish the degree of amplification and result in characteristic asymmetric line-shapes. (C) Optical micrograph (in gray scale) showing a top-down view of part of the device. Adapted from Ref. [97]. Copyright (2019) by OSA.

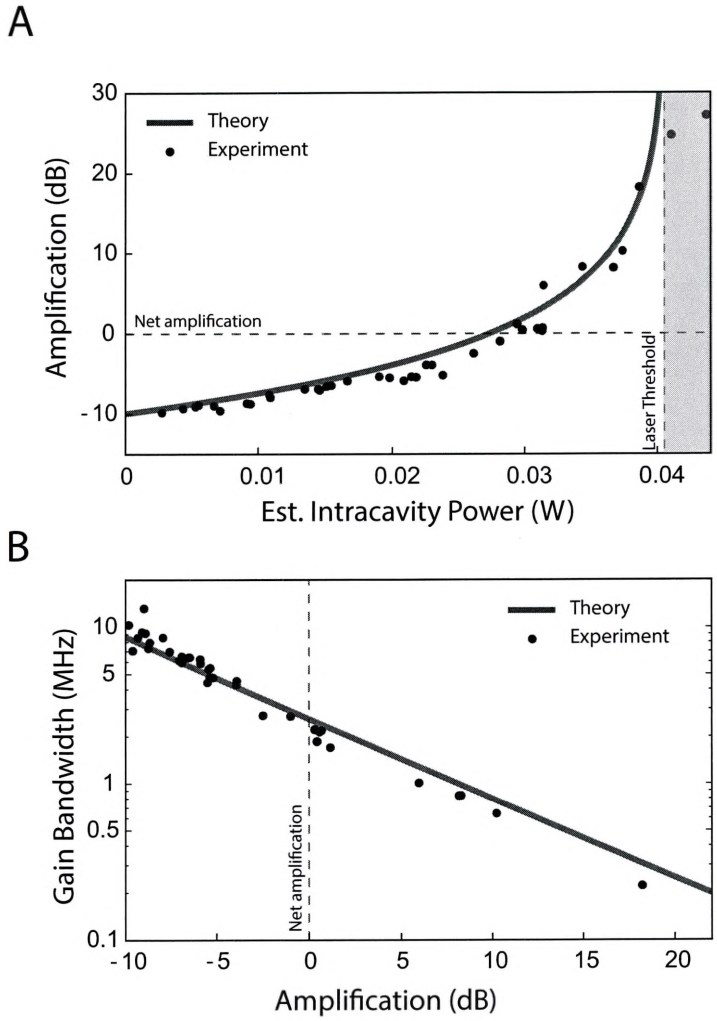

Figure 4.6: (A) Resonantly enhanced Brillouin amplification produced over a range of intracavity powers. As the pump power approaches the laser threshold power, the resonantly enhanced Brillouin amplification increases dramatically. Data is compiled from a series of power, microwave-frequency detuning, and wavelength sweeps. Theory trend is obtained from Eq. 4.8. (B) Linewidth narrowing of the gain bandwidth as a function of signal wave amplification. Theory is also obtained from Eq. 4.8. Adapted from Ref. [97]. Copyright (2019) by OSA.

with the optical LO and measured using a high-speed photo-receiver for heterodyne spectral analysis. Using a microwave oscillator of tunable frequency Ω and an intensity modulator, we synthesize a signal wave at $\omega_s = \omega_p - \Omega$ and measure the output signal synchronously at $\Omega + \Delta$ through heterodyne spectroscopy with the optical LO. By tracking at this offset frequency (Δ), we are able to selectively measure the redshifted signal wave ($\omega_p - \Omega$) without crosstalk from the blue-shifted tone ($\omega_p + \Omega$).

Using this experimental scheme, we vary the laser wavelength, pump power, and signal-wave detuning over a range of parameter to fully and systematically characterize the dynamics. In the limit of low pump power, no Brillouin gain is produced, and we recover the linear resonant response produced by the symmetric mode of the racetrack cavity. When the pump power is increased, we observe a narrow gain peak at the Brillouin frequency atop the linear resonator response (see Fig. 4.2D). As the pump power approaches the laser threshold power, we observe a dramatic increase in the degree of resonantly enhanced amplification, consistent with our theoretical predictions (see Fig. 4.6A-B). Just below threshold, this resonantly enhanced interaction is sufficient to yield in excess of 30 dB of gain, representing more than 20 dB of net amplification after accounting for losses produced by linear transmission through the resonator (see Fig. 4.5B). The degree of amplification depends strongly on the mode-pair detuning (i.e., the frequency separation $\omega_2^m - \omega_1^n$) relative to the Brillouin frequency, as shown in Fig. 4.5B. In addition, we observe that the gain bandwidth scales inversely with the amplification as a result of gain narrowing, in agreement with the predicted behavior given by Eq. 4.8 (see Fig. 4.5B).

4.3.5 Non-reciprocal amplification

As a traveling-wave nonlinear process, optical amplification from inter-modal Brillouin scattering occurs only when phase matching is satisfied. This property gives rise to an intriguing non-reciprocal response. This form of non-reciprocal gain is produced because the phonon required for the resonantly enhanced Brillouin process mediates gain between co-propagating pump and signal waves, but does not produce Brillouin coupling between counter-propagating waves [33,134]. This property arises from the time modulation induced and sustained by the coherent phonon field [135]. Alternatively, this phenomena can also be

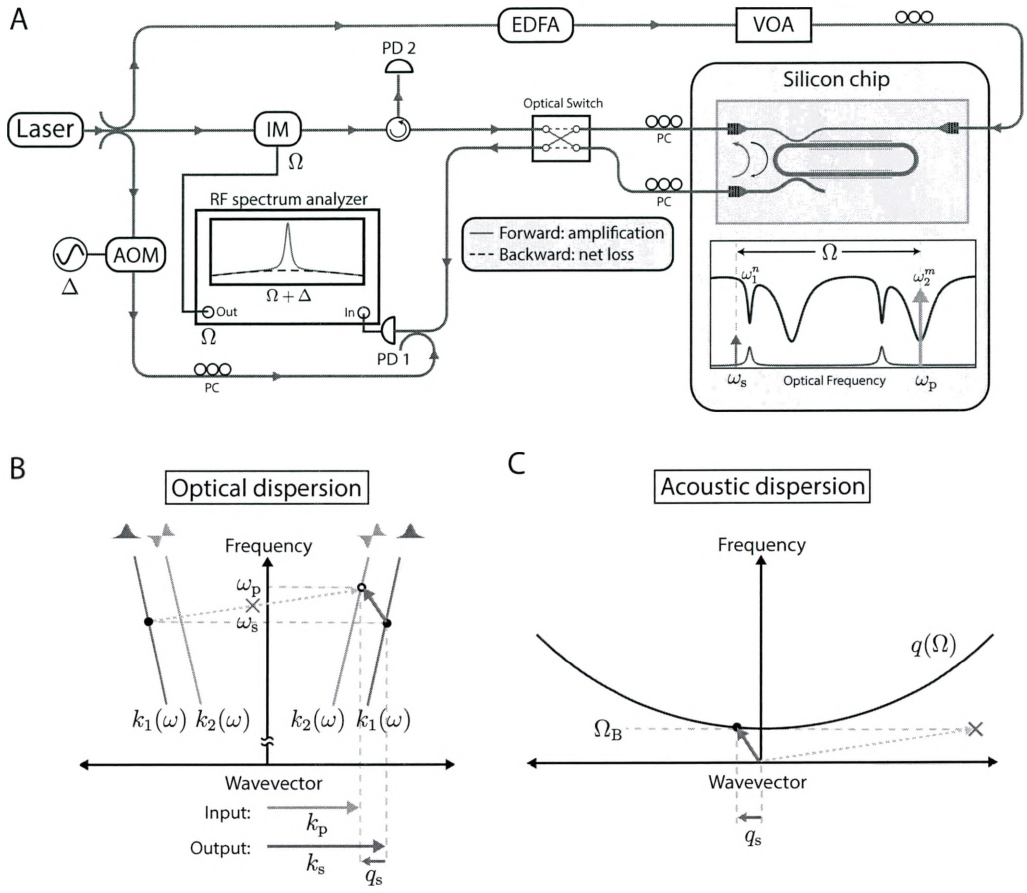

Figure 4.7: Non-reciprocal optical amplification measurements. (A) Diagram of the experimental apparatus used to characterize the non-reciprocal nature of the resonantly enhanced Brillouin amplifier. Laser light is split along three paths. The first (top) is used to generate a pump wave of a desired optical power, which is subsequently coupled on-chip. The second arm synthesizes the signal wave with the desired frequency detuning ($\Omega = \omega_\mathrm{p} - \omega_\mathrm{s}$) using an intensity modulator (IM). Finally, the third creates an optical local oscillator (LO) using an acousto-optic modulator (AOM), which blue-shifts the light by $\Delta = 44$ MHz. An optical switch directs the signal wave light on-chip such that it either co- or counter-propagates with the pump wave within the resonator. After passing through the device, the signal wave is coupled through the drop port and off-chip, where it is combined with the blue-shifted LO and measured on a high-speed photodetector (PD 1). EDFA: erbium doped fiber amplifier; VOA: variable optical attenuator; PC polarization controller. (B)-(C) illustrate energy and phase-matching conditions imposed by the optical and acoustic dispersion relations. In this diagram, the dark green arrow represents the frequency and wavevector of the phonon that mediates stimulated inter-modal Brillouin scattering, while the dotted light-green arrow shows the phonon that would be required to mediate amplification in the backward direction, which is not supported by the acoustic dispersion relation. Thus, the elastic wave that mediates forward stimulated inter-modal Brillouin scattering does not mediate a backward scattering process. Reproduced from Ref. [97]. Copyright (2019) by OSA.

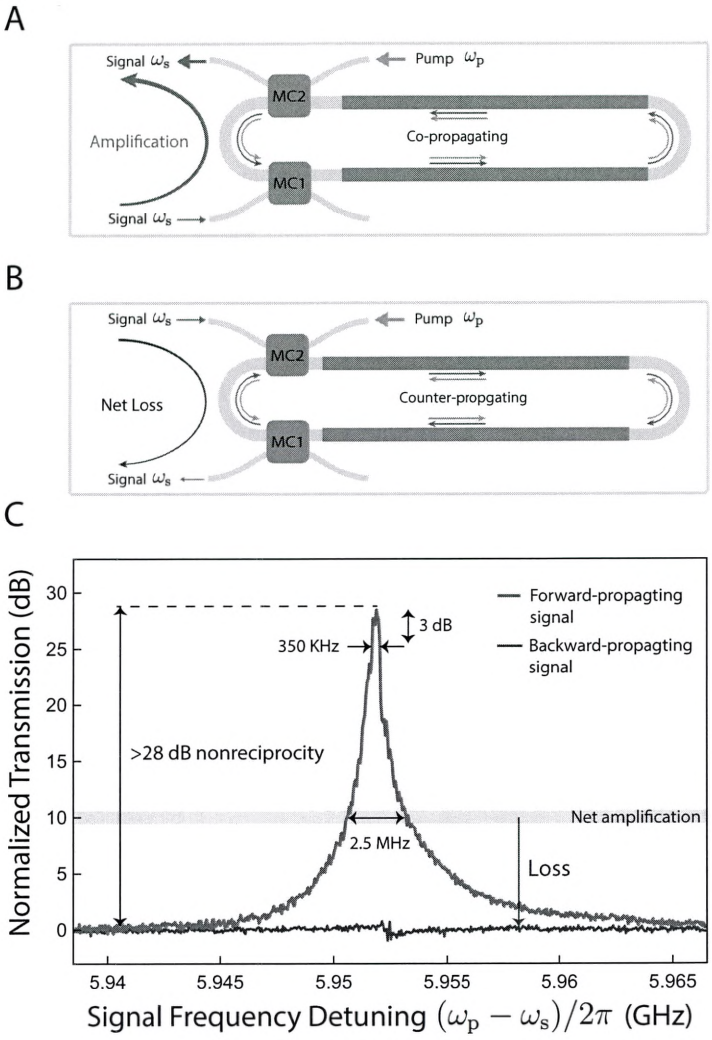

Figure 4.8: Non-reciprocal Brillouin amplification. (A) Experimental arrangement for directional amplification. Pump and signal waves are injected through respective multimode (top) and mode-specific (bottom) couplers such that they co-propagate (forward direction) within the resonator. This configuration allows pump and signal waves to nonlinearly couple through a stimulated forward inter-modal Brillouin process, yielding net amplification of the signal wave. (B) By contrast, a signal wave propagating in the opposite (backward) direction, does not experience Brillouin gain as a result of phase matching; the elastic wave that mediates forward inter-modal scattering is not phase-matched to the backward-scattering process. Thus, in this backward configuration, the signal wave experiences net loss resulting from linear transmission through the resonator. (C) Experimental demonstration of unidirectional amplification. Signal transmission through the system in the forward (red; co-propagating with the pump) and backward (gray; counter-propagating with the pump) directions as a function of signal frequency detuning $\Omega/2\pi$. This system yields a maximum 28 dB of non-reciprocity (with a FWHM of 350 KHz) and provides $>$ 10 dB of isolation over a 2.5 MHz bandwidth. Adapted from Ref. [97]. Copyright (2019) by OSA.

understood through the energy and phase-matching conditions required by this traveling-wave process (see Fig. 4.7B-C). The phonon field that mediates the Brillouin amplification cannot mediate coupling in the backward direction as a result of phase-matching. Moreover, the phonon frequency and wavevector that would be required for a backward process (between counter-propagating waves) is not supported by the acoustic dispersion relation. These phase-matching and energy-conservation considerations are diagrammatically summarized in Fig. 4.7B-C.

We explore the non-reciprocity produced by this system by coupling the pump wave into the anti-symmetric resonator mode with a counter-clockwise orientation satisfying the Brillouin condition with a symmetric cavity mode ($\omega_\mathrm{p} = \omega_2^m$, $\omega_2^m - \omega_1^n = \Omega_\mathrm{B}$); we then examine the reciprocity of the system by injecting the signal wave in the forward (Fig. 4.8A) and subsequently backward (Fig. 4.8B) directions such that the signal wave co- and counter-propagates with the pump wave within the resonator, respectively. When energy conservation is satisfied ($\omega_\mathrm{p} = \omega_\mathrm{s} + \Omega_\mathrm{B}$), the forward configuration yields net amplification (red) of the signal wave, while the backward configuration yields net loss (gray) as a result of passive transmission through the cavity. Using a fiber-coupled switch (as shown in Fig. 4.7), we alternate between the forward and backward configurations while measuring the transmission as a function of signal-wave detuning. As shown in Fig. 4.8C, these measurements reveal a peak optical non-reciprocity of 28 dB and a bandwidth of 2.5 MHz over which the system provides > 10 dB of optical isolation with no insertion loss.

4.4 Conclusion and outlook

In this chapter, we have explored a new resonantly enhanced geometry that allows us to transform a modest amount of amplification (~ 2 dB) into a much larger value (20 dB)—limited only by pump depletion within the resonator. Leveraging a highly engineerable inter-modal device concept, this new strategy allows us to sidestep the deleterious effects of both nonlinear loss [29, 130] and inhomogeneous broadening [131], by (1) enabling large levels of amplification below the modest laser threshold (~ 15 mW incident and ~ 40 mW intracavity) and (2) permitting a compact geometry over which the device can be sufficiently

uniform. With these advances, we are able to achieve record-high Brillouin gain ($\sim$ 30 dB) in silicon, representing a 500$\times$ improvement relative to a linear device of the same design (see Chapter 2).

Looking forward, this resonantly enhanced Brillouin amplifier physics lays the groundwork for a range of powerful silicon photonic device technologies. As a consequence of the phase-matching conditions imposed by inter-modal Brillouin scattering, we have shown that the resonantly enhanced Brillouin amplification is inherently uni-directional, yielding high degrees ($\sim$ 30 dB) of non-reciprocity in an all-silicon system. To our knowledge, this is the first demonstration of loss-less non-reciprocity in silicon at room temperature, and as such, represents an important step towards the development of practical isolators and circulator technology in silicon photonics. In addition, the characteristic narrowing of the gain bandwidth is a unique feature of this system (see Eq. 4.8). At the smallest linewidths ($\sim$ 200 kHz), these narrowband features correspond to an effective optical Q-factor of approximately 10^9, representing a 1000$\times$ improvement relative to state-of-the-art silicon photonics resonators. This level of performance opens the door to new narrowband signal processing applications in silicon photonics, including narrow-band optical and microwave-photonic filters [88,127], carrier recovery for microwave photonic signal processing [136], and tunable time delay [126,133,137,138].

Chapter 5

Brillouin device integration with CMOS-foundry silicon photonics

5.1 Introduction

The transformative potential of silicon photonics is deeply rooted in the concept of integration [1, 2, 139]. Alone, each photonic component offers limited utility. However, combined with the full tool set of silicon photonics, each device plays an important role to enable photonic applications that are not otherwise feasible. As such, a systems-level perspective is essential to have substantive technological impact. Moreover, the ability to develop inexpensive and scalable systems with high yield is greatly enhanced through use of complementary-metal-oxide-semiconductor (CMOS) foundry techniques that have been refined through decades of significant industry and government investment [2].

In Chapters 3-4, we have shown that it is possible to harness stimulated Brillouin scattering to create new laser, amplifier, and non-reciprocal devices in silicon, addressing important challenges in silicon photonics. Up to this point, however, we have demonstrated this device physics with prototype-scale electron-beam lithography—quite different from the high-throughput photolithography-processes currently used to fabricate commercial silicon photonics chips. Moreover, given the additional complexity from MEMS-like[1] process

1. Micro-electromechanical system (MEMS) fabrication techniques often involve the use of a hydrofluoric acid wet etch to remove the oxide undercladding. This is typically considered a non-standard process step.

steps required to create suspended optomechanical structures, it is not clear if or how these devices could interface with active silicon photonic circuits.

In this chapter, we explore new strategies to fabricate and integrate a wide range of silicon-based Brillouin devices within high-performance silicon photonic circuits. In collaboration with Sandia National Laboratories, we set out with two principal objectives: (1) fabricate functional Brillouin devices with a standard CMOS foundry process, and then (2) integrate these Brillouin systems with active photonic components for new degrees of control and added functionality. Our results demonstrate for the first time that Brillouin-photonic devices are indeed compatible with CMOS foundry silicon-photonic processes. Moreover, we show that the fidelity and high degree of uniformity offered by this new photolithography-based process enables marked improvement in the yield and performance relative to our prior electron-beam approach. Building on these results, we design and fabricate Brillouin devices that leverage and interface with fully active silicon photonic circuits for the first time. This work opens the door to powerful new ways to manipulate and harness Brillouin dynamics for fully integrated, scalable photonic technologies.

5.2 CMOS-foundry-fabricated Brillouin devices

We fabricate Brillouin-based amplifiers, filters, and lasers using a mature CMOS silicon photonic process developed at Sandia National Laboratories. Devices are fabricated on a silicon-on-insulator wafer with a 230-nm single crystal silicon layer with 3 μm of buried oxide. The layer structure of this silicon photonic platform accommodates the all-silicon optomechanical waveguide geometry described in Chapters 2-4, with an 80-nm silicon ridge atop a 150-nm phonon membrane. In this first round of fabrication, the devices are patterned in a passive SOI tape-out (i.e., no dopants, metals, Germanium, etc) within a 4 mm $\times$ 4 mm square.

Following photolithography and accompanying etch steps, we suspended the desired portions of the devices by removing the buried oxide through an HF wet etch. We then inspect the devices using an optical microscope. Micrographs for each device are shown in Figs. 5.1A-5.4A.

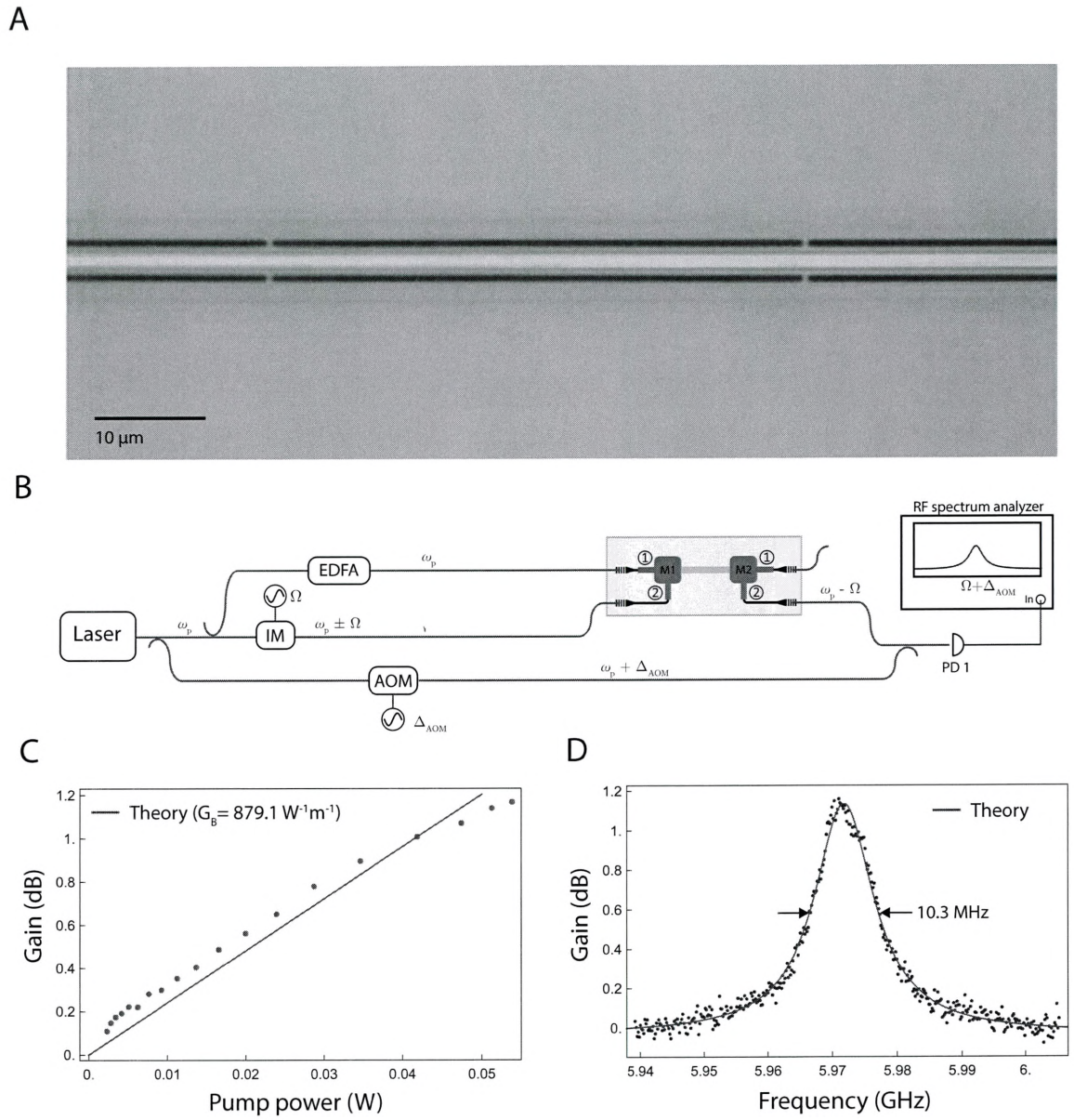

Figure 5.1: (A) Optical micrograph of inter-modal silicon waveguide fabricated with Sandia's MESA CMOS foundry process. (B) Nonlinear laser spectroscopy setup used to measure inter-modal Brillouin gain. A telecom-band laser (ω_p) is used to create an amplified pump (upper path), frequency-shifted signal (middle path), and optical local oscillator (LO) (lower path). Amplified signal wave is combined with the LO and detected with a high-speed photo-receiver. IM: intensity modulator; EDFA: erbium-doped fiber amplifier; AOM: acousto-optic modulator; PD: photo-detector. (C) Peak gain produced by stimulated inter-modal Brillouin scattering as a function of pump power. Here, the length of the Brillouin-active waveguide is 6.1 mm. These results correspond to a fitted SIMS Brillouin gain coefficient of $G_B = 879.1$ W^{-1}m^{-1}. (D) SIMS gain spectrum at a pump power of 54 mW. Theory trend is a Lorentzian fit to the data.

5.2.1 Inter-modal Brillouin waveguides

We first characterize the waveguides that are designed to produce stimulated inter-modal Brillouin scattering (SIMS). These devices consist of a serpentine pattern with 3 suspended Brillouin-active regions, each of about 2 mm in length (the total Brillouin-active length is 6.1 mm). As described in Chapter 2, we interface the multimode waveguide with integrated mode multiplexers such that we can selectively inject light into the symmetric and antiysymmetric spatial modes.

Using an erbium-doped fiber amplifier, intensity modulator, and variable optical attenuator, we synthesize a pump (ω_p) and signal wave ($\omega_s = \omega_p - \Omega$) from a tunable telecom-band external cavity diode laser (Agilent 81600B). The experimental setup is diagrammed in Fig. 5.1B. We separately inject the pump and signal waves into the symmetric and antisymmetric optical spatial modes of the Brillouin-active waveguide, respectively. As in Chapters 2-4, we also create an optical local oscillator (LO) using an acousto-optic modulator to produce a blue-shifted ($\omega_p + \Delta_{AOM}$) reference tone for heterodyne detection of the selected signal sideband $\omega_s = \omega_p - \Omega$.

We characterize the salient properties of the system by measuring the Brillouin gain spectra over a range of pump powers. Figure 5.1C plots the measured peak signal gain as a function of pump power. The theoretical trend corresponds to a Brillouin gain coefficient of $G_B = 879.1\ W^{-1}m^{-1}$. An example Brillouin spectra at a pump power of 54 mW is plotted in 5.1D, revealing a resonance full width at half maximum (FWHM) of 10.3 MHz. These results represent a significant improvement in Brillouin coupling (1.87× increase) and acoustic Q-factor (1.27× increase) relative to our prior work (see Chapter 2). These data suggest that the improved uniformity of this photo-lithographic approach significantly reduces the level of inhomogeneous broadening–a limitation in our prior electron-beam approach (see discussion in Section 4.1).

5.2.2 Forward intra-modal Brillouin waveguides

We also fabricate devices that are optimized to produce coupling through forward intra-modal Brillouin scattering. As described in Chapter 1, forward intra-modal couplings occur

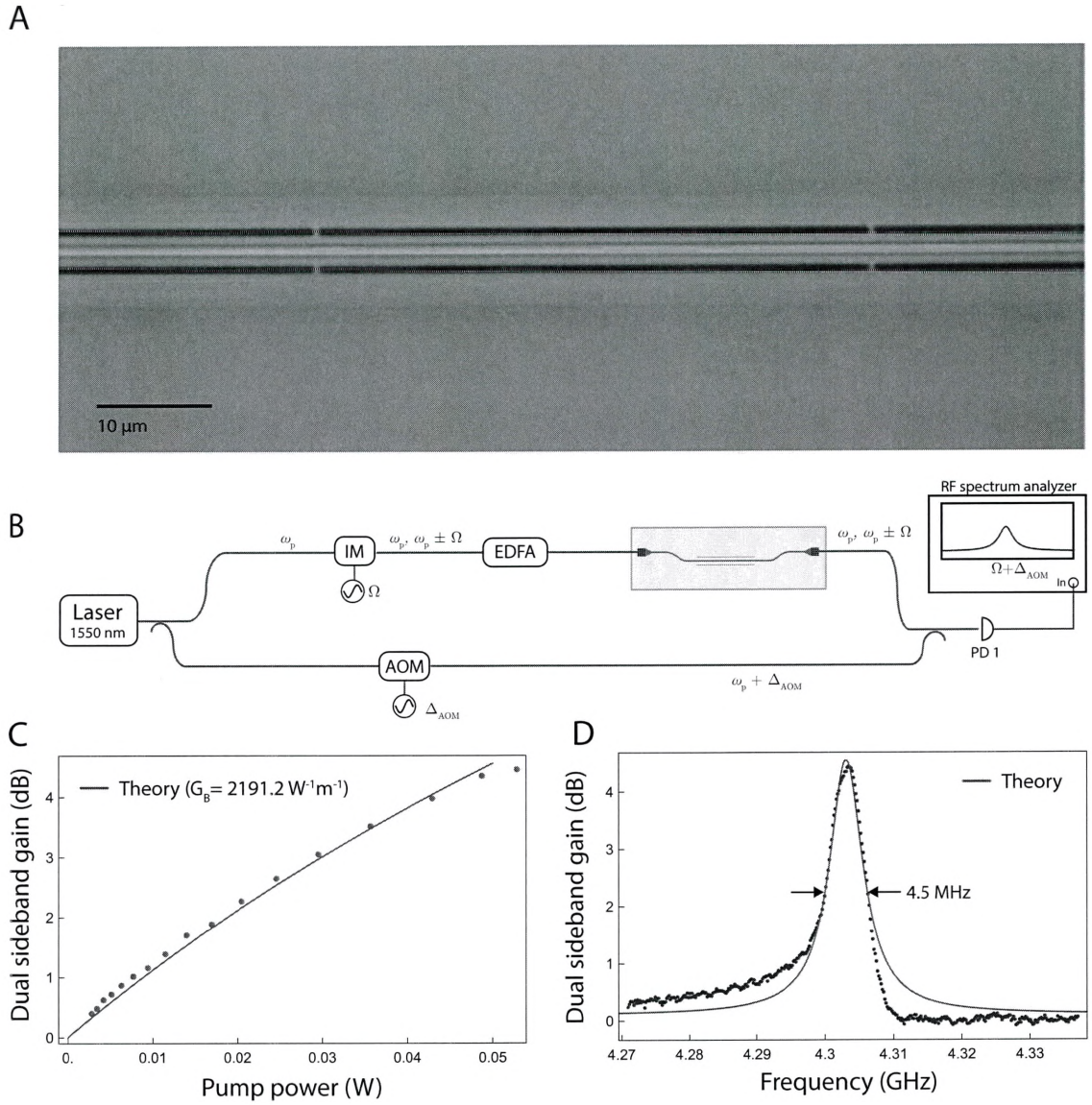

Figure 5.2: (A) Optical micrograph of forward intra-modal silicon waveguide fabricated with Sandia's MESA CMOS foundry process. (B) Nonlinear laser spectroscopy setup used to measure dual-sideband intra-modal Brillouin gain. A telecom-band laser (ω_{p}) is used to create an amplified pump and signal as well as an optical local oscillator (LO) using an acousto-optic modulator (AOM). The amplified signal wave is combined with the LO and detected with a high-speed photo-receiver. IM: intensity modulator; EDFA: erbium-doped fiber amplifier; AOM: acousto-optic modulator; PD: photo-detector. (C) Power sweep measuring the peak dual-sideband gain produced by forward intra-modal stimulated Brillouin scattering. The theory trend corresponds to a Brillouin gain coefficient of $G_{\mathrm{B}} = 2191.2\ \mathrm{W}^{-1}\mathrm{m}^{-1}$. (D) Brillouin gain spectrum demonstrating more than 4 dB of dual-sideband gain (2 dB of actual Brillouin gain), along with a Lorentzian fit.

between light fields that co-propagate in the same optical spatial mode. In contrast to inter-modal Brillouin scattering, which yields single-sideband gain, the underlying dynamics of forward intra-modal Brillouin scattering produce dual-sideband gain.

To promote large forward Brillouin couplings, we use an optical waveguide width and phonon membrane width of 1 μm and 3 μm, respectively, adapting the design of Ref. [23]. As in the case of the inter-modal Brillouin waveguide (Section 5.2.1), we increase the Brillouin-interaction lengths using a serpentine pattern, yielding a total Brillouin-active region of 6.1 mm.

To experimentally characterize the device performance, we slightly modify the experimental scheme described in Section 5.2.1. The apparatus is illustrated in Fig. 5.2B. Here, we synthesize a signal wave by directly modulating the pump wave at a frequency Ω such that the signal wave at $\omega_p - \Omega$ is co-located in the same optical path. In this way, it is straightforward to couple both waves into the same (symmetric) optical spatial mode, as is required for forward intra-modal Brillouin scattering. However, in the case of forward intra-modal Brillouin scattering, we must also consider the effect of the blue-shifted sideband ($\omega_p - \Omega$) that is also generated through intensity modulation. Since the Stokes and anti-Stokes processes phase-match to the same phonon, the presence of both sideband yields an effective scattering rate that is twice as large as that of the case of a single sideband.

We measure the dual-sideband Brillouin gain spectrum over a range of pump powers, as plotted in Fig. 5.2C. The fitted theory trend yields a Brillouin gain coefficient of $G_B = 2191.2\ \mathrm{W^{-1}m^{-1}}$. Figure 5.2D shows the Brillouin gain spectrum at a pump power of 53 mW, with a FWHM of 4.5 MHz. This represents a 1.96× improvement in the Brillouin gain coefficient and a 1.36× improvement in the acoustic quality factor relative to prior forward Brillouin active waveguides fabricated with electron-beam-based techniques (of length $L = 2.9$ cm) [23].

5.2.3 Photonic-phononic emit-receive (PPER) filters

To further analyze the impact of this CMOS-foundry fabrication on the acoustic properties of our Brillouin systems, we also fabricate Brillouin-based photonic-phononic emit-receive filters. These devices consist of an optomechanical structure with two spatially distinct

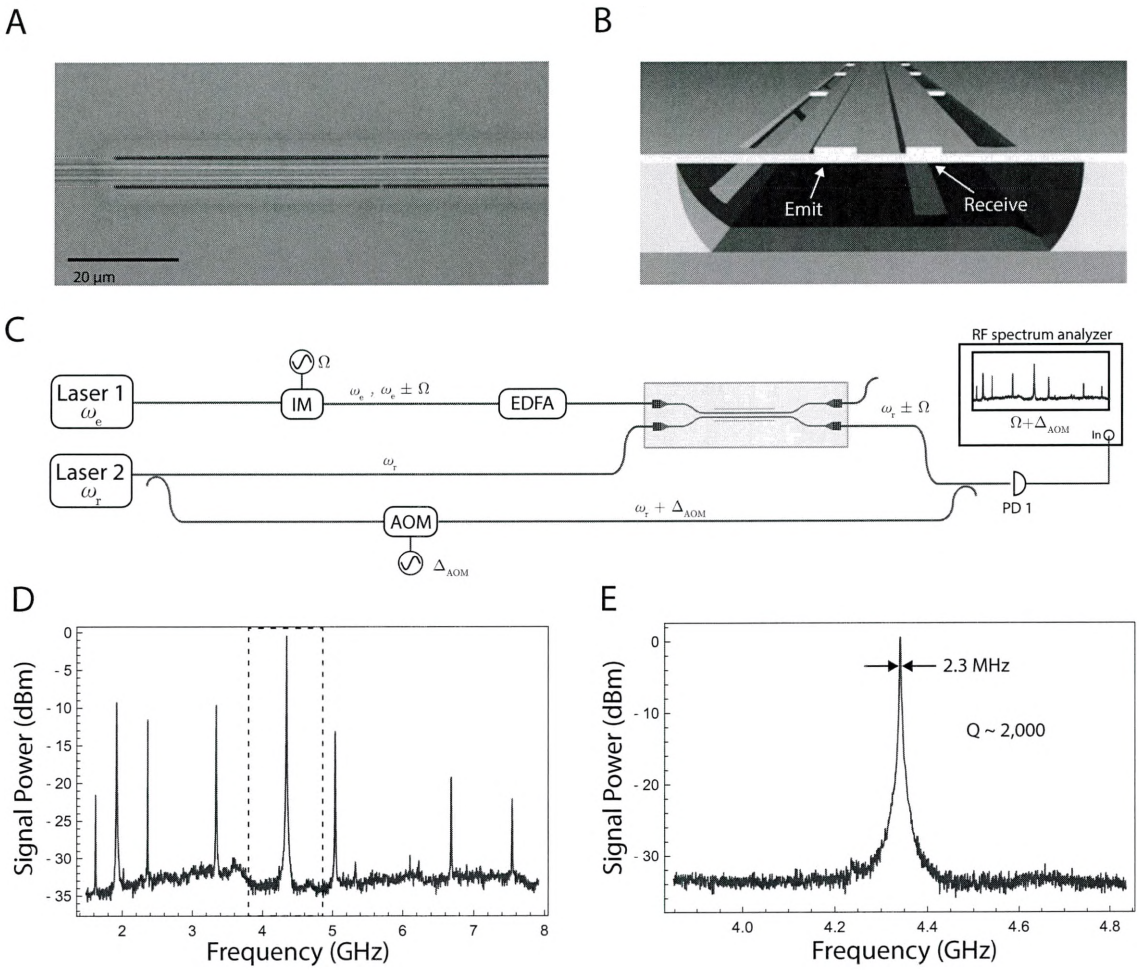

Figure 5.3: (A) Optical micrograph of photonic-phononic emit receive (PPER) device fabricated with Sandia's MESA CMOS process. (B) Schematic illustrating the transverse geometry of the PPER structure. 'Emit' and 'receive' waveguides are labelled, but in principle, both optical waveguides can function as either the 'emit' or 'receive'. (C) Experimental setup used to characterize PPER response. Intensity modulated light from laser 1 (ω_e) is coupled into the 'emit' waveguide, while light from laser 2 (oscillating at ω_r) is coupled into the receive waveguide. A portion of the light from laser 2 is directed to an acousto-optic modulator to resolve red- and blue-shifted sideband produced by Brillouin-induced phase modulation. IM: intensity modulator; EDFA: erbium-doped fiber amplifier; AOM: acousto-optic modulator; PD: photo-detector. (D) PPER response over a range of more than 6 GHz. (E) Zoomed-in resonance at 4.35 GHz. Panel B reproduced from Ref. [25].

optical waveguides, labelled 'emit' and 'receive' as shown in Fig. 5.3A-B. Through a basic PPER operation, intensity modulated light propagating in the emit waveguide drives an elastic wave that extends through receive waveguide. Through linear forward Brillouin scattering, this elastic waveguide imparts phase modulation on light propagating in the receive waveguide. This is the basis for a class of narrowband, high-rejection Brillouin filters, whose intrinsic filter bandwidths are determined by the acoustic properties of the system. In this way, PPER devices provide clear insight into the relevant acoustic properties of the system.

We characterize the performance of such PPER filters using the apparatus diagrammed in Fig. 5.3C. Telecom light from laser 1 (ω_e) is intensity modulated at Ω, amplified through an erbium-doped fiber amplifier, and directed on-chip into the emit waveguide. Light from laser 2 (ω_r) is split into two paths. The upper path couples light on-chip into the receive waveguide while the lower path is used to synthesize an optical local oscillator. At the output grating coupler, phase-modulated receive light is combined with the optical LO for heterodyne detection. To analyze the Brillouin-active PPER spectrum, we sweep the intensity modulator frequency (Ω) and synchronously detect at ($\Omega + \Delta_{AOM}$)

Fig. 5.3D plots the observed PPER spectrum, which reveals a series of resonant features with large signal-to-noise (SNR). A zoomed-in spectrum of the resonance at 4.35 GHz is plotted in Fig. 5.3E. These data demonstrate acoustic Q-factors of nearly 2,000, representing a 2-fold improvement relative to device fabricated with our electron-beam lithography process [140].

5.2.4 Inter-modal Brillouin laser resonators

We also study the performance of inter-modal Brillouin laser resonators fabricated with this new process (see Fig. 5.4A for an image). These systems are similar to those described in Chapters 3-4. The resonators consist of 5.1 mm-long multimode racetrack with two 2-mm, suspended Brillouin-active regions. The waveguide along these segments is identical to that of the linear inter-modal waveguide (see Section 5.2.1). Note that this inter-modal Brillouin resonator geometry occupies a $\sim 10\times$-smaller footprint than the laser and is $3\times$ smaller than the resonantly enhanced amplifier described in Chapters 3 and 4, respectively.

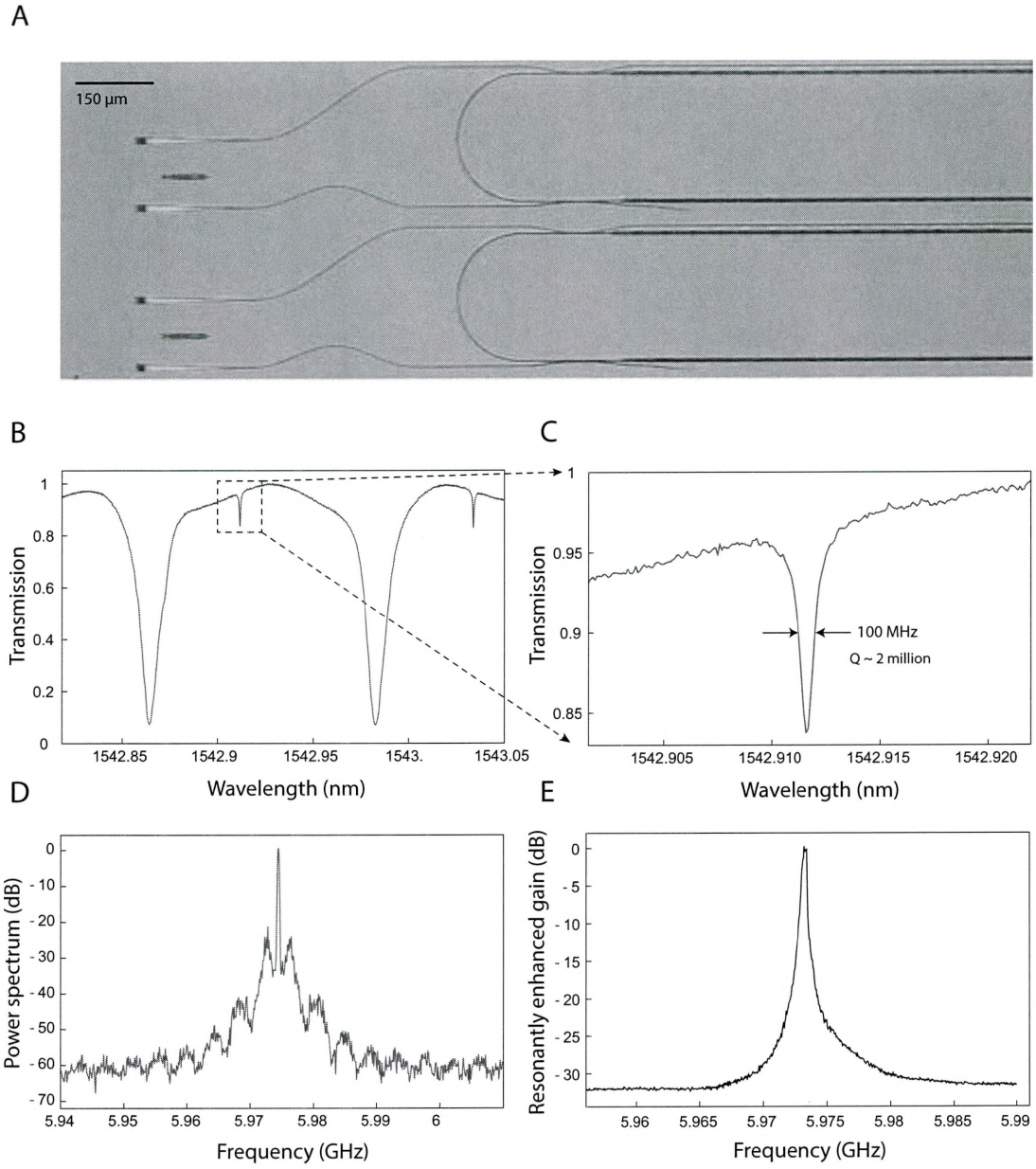

Figure 5.4: (A) Optical micrograph of two multimode Brillouin resonators fabricated with with Sandia's MESA CMOS foundry process. The overall circumference of these devices (5.1 mm) is nearly an order of magnitude smaller than that of the devices described in Chapter 3. Moreover, these new devices are interfaced with 2 additional mode-specific couplers, bring the total to 3. (B)-(C) Optical cavity spectra, revealing a characteristic multimode features. The broad (narrow) cavity resonances correspond to the antisymmetric (symmetric) waveguide mode. (C) Zoomed-in spectra of a symmetric mode cavity resonance. These devices demonstrate superb loss properties, maintaining symmetric mode Q-factors of around 2 million despite the significant reduction in footprint and addition of new couplers. We also demonstrate robust (B) Brillouin lasing and (E) resonantly enhanced amplification in these CMOS-fabricated systems.

In addition, here we interface the devices with up to 3 mode-specific couplers, opening the door to new control and functionality.

We first characterize the multimode optical spectra of the resonator, as shown in Fig. 5.4B-C. These data are obtained by measuring the transmission at the through port of an antisymmetric mode-selective coupler. The observed spectra reveal well-defined sets of broad and narrow resonances that are produced by the antisymmetric and symmetric spatial modes of the waveguide, respectively. The cavity resonances arising from the symmetric waveguide mode exhibit a Q-factor of nearly 2 million. This represents a near two-fold improvement relative to our resonantly enhanced amplifier resonators (which are also interfaced with multiple couplers), despite the significant reduction in footprint. Fitting these optical spectra to our theoretical model (see Supplementary Materials of Ref. [95]), we find that linear propagation loss around the racetrack is 0.17 dB/cm, representing state-of-the-art performance for this waveguide geometry.

We also test the devices for both lasing and resonantly enhanced amplification. We find that all four inter-modal laser resonators easily achieve Brillouin lasing (as shown in Fig. 5.4D) and can be used to achieve high degrees ($>$ 30 dB) of resonantly enhanced amplification. The high degree of repeatability bodes well for future implementation in active silicon photonic circuits.

5.2.5 Summary

We have demonstrated high-performance Brillouin amplifiers, filters, and lasers using a CMOS foundry process. These results show that suspended Brillouin devices are compatible with CMOS-based techniques and that the improved uniformity made possible through photolithography translates into enhanced device performance, yielding lower optical and mechanical loss and larger Brillouin coupling strengths.

5.3 Integration with active silicon photonic circuits

The ability to fabricate high-performance Brillouin-photonic devices with CMOS fabrication techniques opens the door to new opportunities to harness, control, and utilize Brillouin-

based device physics within active silicon photonic circuits. To this end, we seek new co-integration strategies that allow us to selectively release suspended Brillouin-active segments while protecting sensitive oxides, metals, and other layers that are susceptible to hydrofluoric acid (HF).

5.3.1 Co-integration strategy

A promising approach involves creating lithographic masks for the final HF wet-etch. Fortunately, HF is a non-oxidizing acid, and as such, leaves many common resist films intact. Thus, through lithographic control we can selectively open portions of the resist films and selectively expose them to the HF wet etch. Following the standard CMOS foundry process, our strategy consists of 3 simple steps, as outlined below.

1. Pattern an HF wet etch mask on top of an oxide-clad active silicon photonic circuit, with openings above the selected suspended portions.

2. Perform the HF wet etch. The HF will easily penetrate through the exposed oxide and through the defined slots to suspend the Brillouin-active regions of the device.

3. Remove the residual resist through a solvent clean.

Co-integration of suspended structures and active silicon photonics circuits allows us to envision a host of new device concepts. Figure 5.5 shows several such designs. Our strategy allows us to interface Brillouin amplifiers, including linear and resonant varieties as shown in Fig. 5.5, with a range of silicon-photonic modulators. This is a particularly synergistic combination in the case of single-sideband (SSB) modulators [141], whose modest output powers could benefit from high-gain Brillouin amplification. More generally, introduction of Brillouin devices to active silicon photonics allows us to fill a pressing need for high-performance silicon-based laser oscillators, amplifiers, and non-reciprocal devices.

At the same time, co-integration with active silicon photonic circuitry gives Brillouin-based devices new degrees of control and added functionality. Specifically, through precise doping and low-ohmic metal contacts, we can create devices such as p-i-n junctions and

Figure 5.5: (A)-(D) Four possible device concepts for integration within active silicon photonic circuits. The active portions are those that retain the oxide cladding while the remainder is exposed to the HF wet etch. The ability to fabricate suspended Brillouin structures with active silicon photonics allows us to interface modulators (such as a single-sideband (SSB) modulator [141]) with (A) linear and (B) resonantly enhanced Brillouin amplifiers. (C) With these active circuits, we can add new degree of control such as integrated heaters [142] and carrier sweeping [143]. (D) Integrated heaters can allow us to tune the Brillouin resonance *in situ* through the thermal-elasticity of silicon. This new control would allow us to compensate for the effects of inhomogenous broadening for significantly enhanced performance.

integrated heaters. P-i-n junctions can be used for nonlinear loss mitigation through free-carrier removal, enabling enhanced power handling. Additionally, through the large thermo-optic coefficient of silicon [144], which permits an effective 0.8 nm change for every 10 K ΔT, integrated heaters allow us to actively optimize the operation of interferometers, resonators, and other interference-based devices.

Thermal phase shifters are especially useful in the case of a resonant Brillouin amplifier, as diagrammed in Fig. 5.5, which provides large ($\sim$ 30 dB) gains but over modest ($<$ 1 MHz) bandwidths. However, since the Brillouin condition is satisfied by a pair of symmetric and antisymmetric cavity modes that occur approximately every nm, thermal control of as little as $\sim$ 1 nm could enable tunable operation of the resonant Brillouin system across the entire c-band. Moreover, as illustrated by Fig. 5.5D, thermal control may also enable active trimming of the Brillouin resonance along the device length, allowing us to compensate for unwanted inhomogeneous broadening effects that suppress large Brillouin couplings.

Beyond the device concepts presented here, co-integration of suspended Brillouin devices and active silicon photonic components opens the doors to a new realm of state-of-the-art signal processing technologies. For instance, we will have the ability to develop fully integrated RF-photonic links with state-of-the-art Brillouin based filters [22, 24, 140], resonant systems with tunable, two-point couplers [145] for optimized amplifier and non-reciprocal properties, interferometer-based high-power Brillouin amplifiers with pump suppression and nonlinear loss mitigation, distributed Brillouin sensors on a chip [21], and elector-mechanical silicon-based devices for broadband non-reciprocity.

5.3.2 Layouts and designs

We have designed a range of active Brillouin-based photonic circuits, including single-sideband modulators [141] interfaced with resonant Brillouin amplifiers, linear Brillouin amplifiers with carrier sweeping, interferometer-based forward Brillouin amplifiers, reconfigurable resonant Brillouin amplifiers with thermal tuning and carrier sweeping, and photonic-phononic emit receive (PPER) [22, 24, 140] filters with thermal Brillouin resonance tuning. These devices have recently undergone the CMOS fabrication steps and we anticipate testing in the coming months. In what follows below, we describe the basic elements of our

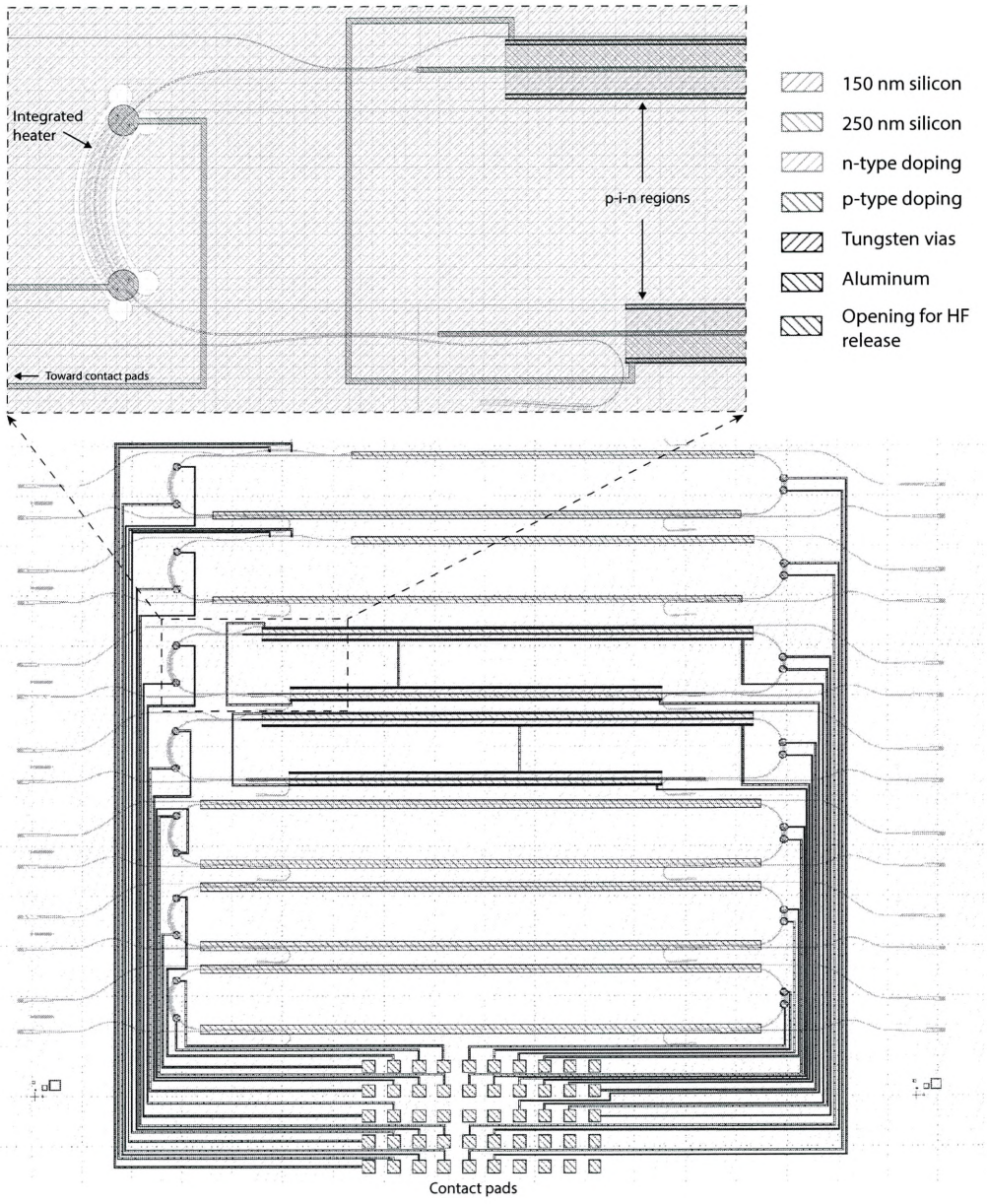

Figure 5.6: Active silicon photonic GDS layout with multimode Brillouin resonators. The layer structure is given in the top right. The devices can be controlled by the array of aluminum pads situated toward the bottom of the device. (Top) Zoomed-in GDS of laser resonator with integrated heater (left) and p-i-n carrier sweeping regions.

active Brillouin design. We highlight an active resonant Brillouin amplifier as an example.

Figure 5.6 contains a GDS layout of a set resonant Brillouin amplifiers with varying degrees of active tunability. The design is defined by a number of device layers, as detailed in the top right of Fig. 5.6. A zoomed-in section of a resonant Brillouin amplifier interfaced with an integrated heater and p-i-n junction. Apart from the slots for waveguide suspension and areas surrounding the thermal heaters, we leave a 150-nm layer of silicon throughout the chip, permitting the 250-nm silicon layer to act as a low-loss ridge waveguide. The chip will be oxide-clad except for the regions that define the HF mask. N- and p-type doped regions are used to create an extended p-i-n junction along the length of the resonator, with the intent of nonlinear loss mitigation through free-carrier removal. The n- and p-type regions have a electron and hole densities of approximately 2×10^{18} cm^{-3} and 10^{20} cm^{-3}, respectively.

N-type doping is also used as the resistive segment of the integrated heater, which has a 2-D sheet resistance of 30 $\Omega/\square$, significantly smaller than the 0.45 M$\Omega/\square$ sheet resistance of the standard silicon layer. Taking this value into consideration,[2] the integrated heater design shown in Fig. 5.6 has a calculated resistance of 480 Ω. This value should permit up to 100 K temperature shifts with < 100 mA of supplied current. Both the integrated heaters and p-i-n structures are connected to an array of contact pads (bottom of Fig. 5.6) through low-ohmic tungsten vias and planar aluminum wires. In this way, we can actively control the operation of each device through a multi-contact wedge probe.

5.4 Conclusion and outlook

In this chapter, we have shown that silicon-based Brillouin devices are compatible with standard CMOS foundry-based fabrication techniques.[3] Moreover, we have demonstrated that

2. $\Omega/\square$ may seem an odd unit choice, but can be understood in straightforward terms. We can express the resistance of a 3-D geometry in terms of the resistivity ρ, the cross-sectional area A, and the length L, such that $R_{3D} = \rho L/A$. Now, consider a 2-D geometry resulting from the collapse of a 3-D geometry of thickness t and width W. In this case, $R_{3D} = \rho L/(tW) = R_{2D}L/W$, where $R_{2D} = \rho/t$. We therefore assign R_{2D} the units of $\Omega/\square$, where the $\square$ denotes the case where $L = W$. Thus, the resistance is invariant provided that the aspect ratio of the thin film is preserved. To calculate the resistance of a rectangular geometry, we need only scale the sheet resistance R_{2D} by L/W.

3. The only additional step is a final HF-wet etch that may eventually be integrated into full process flow, as outlined in Section 5.3.1.

the improved precision and uniformity afforded by these mature processes enable significant enhancements in performance and device yield. Building on these results, we develop new strategies for co-integration to permit (1) the adaption of powerful Brillouin-based laser, amplifier, and non-reciprocal device physics to active silicon photonic circuits and (2) the addition of new functionality and control of Brillouin-based systems. To this end, we design and fabricate a range of Brillouin devices within active silicon photonic circuits. Looking forward, this work lays the groundwork for a host of rapidly reconfigurable Brillouin-based technologies—whose performance can be dynamically controlled—within active silicon photonic circuits. These capabilities add new degrees of tunability and control that can be combined with other strategies to manipulate Brillouin dynamics for high-performance integrated silicon Brillouin devices.

Chapter 6

Backscatter-immune injection-locked Brillouin laser

6.1 Introduction

In the mid-17th century, the Dutch scientist Christiaan Huygens observed that two pendulum clocks suspended on the same wooden support exhibited what he called an 'odd sympathy'; they began to oscillate synchronously and keep time at the same rate [146]. Since that time, the nonlinear dynamics associated with synchronization have been observed and utilized in a variety of mechanical, biological, and optomechanical systems [146, 147]. In particular, as nonlinear self-sustained oscillators, optical lasers can also spontaneously synchronize and assume the phase and frequency of an incoming signal [148, 149]. This property is often viewed as a drawback, as optical lasers are in general highly sensitive to unwanted feedback from back-scatter, sometimes leading to unpredictable behavior. At the same time, however, these unique nonlinear dynamics can be harnessed for a powerful and elegant stabilization technique known as injection locking [148, 149].

Through injection locking, a laser's frequency and phase can be controlled by an injected seed, provided that the signal falls within the lock range of the device [150, 151]. In contrast to other stabilization techniques, such as optical phase locked loops [152, 153] or Pound-Drever-Hall locks [154], injection locking relies only on the intrinsic nonlinear dynamics of

the laser, requiring no active feedback or complex locking electronic electronics [155]. Given its simple implementation, injection locking has found widespread use in a range of basic-science and technology applications, from signal synthesis in atomic physics demonstrations [156–158] to carrier recovery for coherent optical communications [159, 160].

Given the extensive applications and simple implementation, it is surprising that this form of injection-locked control has not been exploited in the context of low-noise Brillouin laser systems. A possible explanation for the absence of Brillouin-based injection locked technologies is that, the time dynamics conventionally exhibited by Brillouin laser systems, which require ultra high-Q optical resonators, may not be amenable to such techniques; if not derived from an ultra-narrow linewidth source itself, an injected seed may actually enhance the phase noise of the Brillouin laser. In this context, the unconventional regime of temporal dynamics exhibited by our silicon Brillouin laser, in which optical self-oscillation yields highly coherent pump and Stokes fields (see Chapter 3), unlocks new opportunities for injection-locked Brillouin laser technologies. If it is derived from the same pump laser, we will see that the injected seed actually represents the ideal low-noise input, allowing us to reduce the laser linewidth far below the Schawlow-Townes limit. Moreover, the multimode nature and enhanced flexibility of this inter-modal Brillouin design are ideally suited to injection-locked operation, allowing us to selectively control the laser gain and emission through distinct mode-selective ports.

In this chapter, we demonstrate injection-locked operation of a inter-modal silicon Brillouin laser system and explore its dynamics through a combination of analytical, numerical, and experimental analysis. We show that injection locking is a powerful tool not only for frequency stable control, but also to manipulate the intrinsic noise dynamics of the system. These dynamics permit a lock range of nearly 2 MHz ($\sim$ 20% of the Brillouin gain bandwidth) and up to 70 dB of phase noise reduction, representing a dramatic improvement beyond our previous results presented in Chapter 3. In addition, when injected with a low-power seed this process can also be viewed as a very efficient means of amplification, allowing us to use this technique to demonstrate more than 23 dB of effective net amplification. We demonstrate this physics not only with our standard electron-beam lithography process at Yale, but also with the improved CMOS foundry process described in Chapter 5,

highlighting the potential for scalable integration of injection-locked Brillouin technologies within complex silicon photonic circuits.

Moreover, this system offers a powerful new paradigm to non-reciprocal technologies. So far, the conventional strategy assumes that the laser and isolator are two distinct components: the laser source—which is highly sensitive to any feedback—is protected from unwanted back-scatter by the isolator. By contrast, here we demonstrate a laser system that is itself a non-reciprocal element. Due to the unidirectional nature of Brillouin amplification, we show that injection of a forward-propagating signal successfully controls the laser oscillation while an unwanted (backward-propagating) interferer—that would ordinarily disrupt laser performance—leaves the laser unaffected. Such behavior demonstrates not only that this Brillouin laser is back-scatter immune, in sharp contrast to conventional laser systems, but that it could also be used as either a unidirectional amplifier or a frequency-shifting optical isolator to protect sensitive chip-scale sources.

6.2 Demonstration of injection-locked operation

We consider an inter-modal laser geometry with up to 3 different mode-selective couplers, as diagrammed in Fig. 6.1A. Couplers A and B (labelled MC1) produce high-contrast input and output coupling to the symmetric cavity modes, while mode-selective coupler C (MC2) preferentially couples to the antisymmetric cavity modes. The coupler design for MC1 and MC2 is discussed in Chapter 4. Using the CMOS foundry photolithography process described in Chapter 5, MC1 and MC2 can be highly mode selective, with crosstalk levels as low as -40 and -25 dB, respectively. These mode-specific couplers enable precise control of the inter-modal nonlinear gain and laser emission as illustrated in Fig. 6.1A. As shown in Fig. 6.1D, efficient laser oscillation at ω_e occurs when the pump wave is tuned to an antisymmetric cavity resonance ω_2^m that is separated in frequency from a symmetric cavity mode ω_1^n by the Brillouin frequency Ω_B. Above threshold, we inject a seed wave into a symmetric cavity mode and tune its frequency ω_s within the vicinity of the natural laser emission frequency $\omega_e = \omega_p - \Omega_B$ to achieve injection-locked operation of the Brillouin lasing such that $\omega_e = \omega_s$.

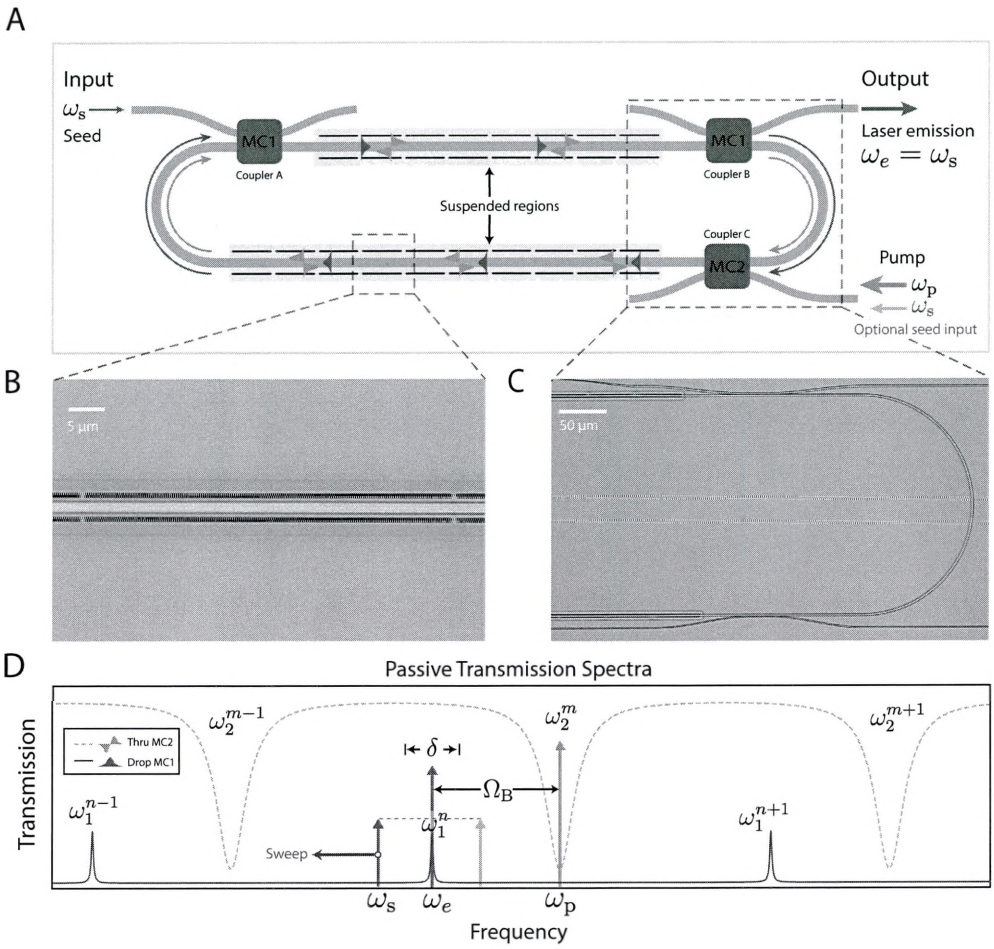

Figure 6.1: (A) Scheme for injection-locked operation of Brillouin laser. Couplers A and B (MC1) couple to the cavity modes produced by the symmetric optical spatial mode ω_1^n while coupler C (labelled MC2) is designed to couple primarily to the antisymmetric cavity modes, as described in Chapter 2. (B)-(C) Optical micrographs (gray scale) of the (A) inter-modal Brillouin waveguide and (B) resonator geometry. (C) Optical micrograph (gray scale) of the interface between the racetrack cavity and couplers B (MC1) and C (MC2). (C) Idealized transmission spectrum produced by the antisymmetric waveguide mode (dashed blue; thru port of coupler C) and symmetric waveguide mode (red; input at coupler A, output at coupler B). Efficient laser oscillation of the symmetric cavity mode ω_1^n occurs when the pump wave is tuned to an antisymmetric cavity mode that satisfies the Brillouin condition ($\omega_\mathrm{p} = \omega_2^m = \omega_1^n + \Omega_\mathrm{B}$). Laser oscillation of the symmetric mode ω_e can be phase and frequency locked by injecting a seed of sufficient power at frequency ω_s that falls within the lock range $\omega_\mathrm{e} \pm \delta/2$. We determine the lock range experimentally by sweeping the signal frequency through the natural laser emission frequency $\omega_\mathrm{p} - \Omega_\mathrm{B}$. Reproduced from Ref. [98]. Copyright (2020) by APS.

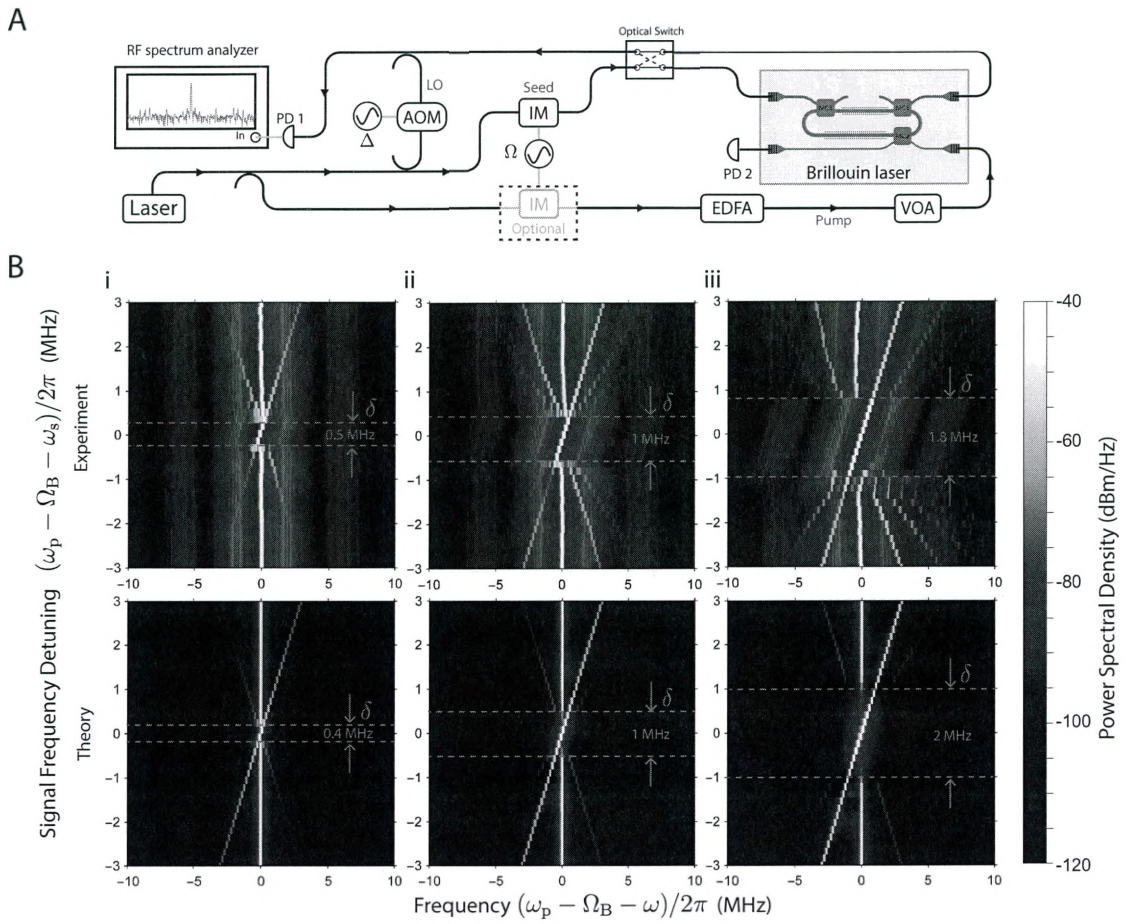

Figure 6.2: (A) Laser spectroscopy apparatus used to demonstrate and characterize injection locking. Telecom laser light from a tunable external cavity diode laser (Agilent 81600B) is split along three paths. Along the top path, an acousto-optic frequency shifter is used to generate an optical LO of frequency $\omega_p + \Delta$, where $\Delta = 44$ MHz. Light routed to the bottom path passes through an erbium-doped fiber amplifier (EDFA) and variable optical attenuator (VOA) such that pump light of a desired power can be delivered on chip, while the middle path uses an intensity modulator to synthesize a seed at $\omega_s = \omega_p - \Omega$. Optionally, the seed can be directly synthesized as a sideband of the pump wave, as in the case of the measurements presented in panels Bi-iii and in Fig. 6.4. In this case, we do not use the middle path. Fiber-optic switches and couplers route the light on and off chip through grating couplers that interface the desired ports of the system. Light exiting the chip is combined with the optical LO and detected using a high-speed photo-receiver for heterodyne spectroscopy. IM: intensity modulator; EDFA: erbium-doped fiber amplifier; AOM: acousto-optic modulator; PD: photo-detector; VOA: variable optical attenuator. (B) Measured (top) and simulated (below) injection-locking dynamics at three different seed powers ((i) 0.4 μW, (ii) 2.6 μW, (iii) 17 μW), along with corresponding coupled mode simulations (below). Note that the capture range expands with increasing seed power, and that Brillouin-mediated four-wave-mixing can occur as the seed approaches the lock range $\omega_e \pm \delta/2$. Details of the stochastic simulations are given in Section 6.3.1. Reproduced from Ref. [98]. Copyright (2020) by APS.

The injection locking dynamics of this system are characterized through heterodyne laser spectroscopy using the experimental setup diagrammed in Fig. 6.2A. The apparatus directs telecom-band laser light (λ_p) along 3 different paths to (1) supply the pump wave of a desired power using an erbium-doped fiber amplifier (EDFA) and variable optical attenuator (VOA), (2) synthesize a seed at frequency $\omega_s = \omega_p - \Omega$, and (3) create an optical local oscillator (LO) at frequency $\omega_p + \Delta$ using an acousto-optic modulator for heterodyne spectral analysis. Fiber-optic couplers and switches route the pump and seed waves onto the chip through grating couplers. Subsequently, the pump and seed waves are resonantly coupled into the antisymmetric and symmetric cavity modes using the mode-specific couplers and frequency selectivity of the resonator. Above threshold, the laser emission exits the resonator through coupler B toward the output grating coupler. Once off-chip, this laser light is combined with the AOM-shifted optical LO and detected by a high-speed photo-receiver. In conjunction with an RF-spectrum analyzer, this scheme allows us to study the heterodyne spectrum—which reveals the degree of coherence between the laser emission and the pump—with Hz-level resolution. It is important to note that such fine resolution is made possible by the stability provided through injection locking.[1]

This scheme allows us to characterize key properties of the injection locking Brillouin dynamics as a function of frequency detuning and seed power. The upper density plots in Fig. 6.2Bi-iii reveal the evolution of the power spectral density as the seed frequency ω_s is tuned through the natural laser emission frequency $\omega_p - \Omega_B$. These measurements are repeated for a set of 3 distinct signal powers (i-iii), and each plot is composed of a series of 38 spectral traces. As the seed frequency approaches the natural oscillation frequency, we observe a crescendo of four-wave-mixing-like scattering—manifest by many equally spaced tones (see Section 6.3.1 for explanation)—that abruptly transitions into injection-locked lasing over a lock range $\omega_e \pm \delta/2$. Within this range, the laser emission is captured by the seed source, assuming its frequency, phase, and coherence properties. Moreover, at the lowest seed powers, injection-locked lasing yields a dramatic power enhancement of the seed

1. This is a significant improvement relative to the case of a free-running Brillouin laser, where the resolution is limited to around 20 kHz by instabilities produced by low-frequency jitter in the pump laser frequency. See Section 3.5 for more details.

source, corresponding to an effective net amplification of more than 23 dB over a lock range of 0.5 MHz. As we increase the seed power, we observe a clear enlargement of this lock range up to a maximum $\delta = 1.8$ MHz.

6.3 Injection locking dynamics

In this section, we develop analytical and numerical tools to understand the nonlinear injection-locking dynamics and the resulting phase- and relative-intensity noise reduction properties. As introduced in Chapter 3 and Chapter 4, the mean-field equations of motion for the silicon Brillouin laser are given by [95, 97]

$$\begin{aligned}
\dot{a}_{\mathrm{s}}(t) &= -i\omega_1^n a_{\mathrm{s}}(t) - \frac{\gamma_{\mathrm{tot},1}}{2} a_{\mathrm{s}}(t) - ig^* a_{\mathrm{p}}(t) b^\dagger(t) + \sqrt{\gamma_{\mathrm{A},1}} S^{\mathrm{in}}(t) \\
\dot{b}(t) &= -i\Omega_{\mathrm{B}} b(t) - \frac{\Gamma}{2} b(t) - ig^* a_{\mathrm{p}}(t) a_{\mathrm{s}}^\dagger(t) + \eta(t) \\
\dot{a}_{\mathrm{p}}(t) &= -i\omega_2^m a_{\mathrm{p}}(t) - \frac{\gamma_{\mathrm{tot},2}}{2} a_{\mathrm{p}}(t) - iga_{\mathrm{s}}(t) b(t) + \sqrt{\gamma_{\mathrm{C},2}} S_{\mathrm{p}}^{\mathrm{in}}(t),
\end{aligned} \tag{6.1}$$

where $a_{\mathrm{s}}(t)$, $b(t)$, and $a_{\mathrm{p}}(t)$ are the coupled-mode amplitudes for the Stokes, phonon, and pump fields, respectively, with units of $[\sqrt{\text{number}}]$, $\dot{a}_{\mathrm{s}}(t)$, $\dot{b}(t)$, and $\dot{a}_{\mathrm{p}}(t)$ are the time derivatives of these same fields, $S^{\mathrm{in}}(t)$ and $S_{\mathrm{p}}^{\mathrm{in}}(t)$ represent the input seed and pump-wave fields (with units $[\sqrt{\text{number} \times \text{Hz}}]$), and $\eta(t)$ is the mechanical stochastic driving term that is consistent with the fluctuation-dissipation theorem, with a two-time correlation function of $\langle \eta(t')\eta^\dagger(t) \rangle = \Gamma(n_{\mathrm{th}} + 1)\delta(t - t')$, where n_{th} is the thermal occupation of the phonon field and Γ is the phonon dissipation rate. We denote the Hermitian conjugate with † and use * for the complex conjugate. Here, g is the Brillouin coupling rate (related to the Brillouin gain coefficient by $G_{\mathrm{B}} = 4|g|^2|a_{\mathrm{p}}|^2/P_{\mathrm{p}}\Gamma v_{\mathrm{g},1}$, where P_{p} is the pump power and $v_{\mathrm{g},1}$ is the group velocity of the first spatial mode), $\gamma_{(\mathrm{A,B,C}),(1,2)}$ are the dissipation rates produced by couplers A, B, or C for light propagating in the symmetric (1) or antisymmetric (2) spatial modes, and $\gamma_{\mathrm{tot},(1,2)}$ are the total dissipation rates associated with resonant symmetric (ω_1^n) and antisymmetric modes (ω_2^m). Since the system is dominated by the thermal noise of the phonon field, for simplicity we neglect optical vacuum fluctuations.

We next move to the rotating frame by substituting the slowly varying envelopes $\bar{a}_{\mathrm{s}}(t)$, $\bar{b}(t)$, and $\bar{a}_{\mathrm{p}}(t)$, which are defined by $a_{\mathrm{s}}(t) = \bar{a}_{\mathrm{s}}(t)\exp(-i\omega_{\mathrm{s}}t)$, $a_{\mathrm{p}}(t) = \bar{a}_{\mathrm{p}}(t)\exp(-i\omega_{\mathrm{p}}t)$,

and $b(t) = \bar{b}(t)\exp(-i\Omega t)$. The terms $\bar{\eta}(t)$, $\bar{S}^{\text{in}}(t)$, and $\bar{S}_{\text{p}}^{\text{in}}(t)$ are shifted in like manner. This transformation yields

$$\begin{aligned}
\dot{\bar{a}}_{\text{s}}(t) &= i(\omega_{\text{s}} - \omega_1^n)\bar{a}_{\text{s}}(t) - \frac{\gamma_{\text{tot},1}}{2}\bar{a}_{\text{s}}(t) - ig^*\bar{a}_{\text{p}}(t)\bar{b}^\dagger(t) + \sqrt{\gamma_{\text{A},1}}\bar{S}^{\text{in}}(t) \\
\dot{\bar{b}}(t) &= i(\Omega - \Omega_{\text{B}})\bar{b}(t) - \frac{\Gamma}{2}\bar{b}(t) - ig^*\bar{a}_{\text{p}}(t)\bar{a}_{\text{s}}^\dagger(t) + \bar{\eta}(t) \\
\dot{\bar{a}}_{\text{p}}(t) &= i(\omega_{\text{p}} - \omega_2^m)\bar{a}_{\text{p}}(t) - \frac{\gamma_{\text{tot},2}}{2}\bar{a}_{\text{p}}(t) - ig\bar{a}_{\text{s}}(t)\bar{b}(t) + \sqrt{\gamma_{\text{C},2}}\bar{S}_{\text{p}}^{\text{in}}(t),
\end{aligned} \tag{6.2}$$

where conservation of energy requires $\omega_{\text{p}} = \omega_{\text{s}} + \Omega_{\text{B}}$.

6.3.1 Stochastic simulations

Building on this analytical framework, we develop stochastic simulations to understand the nonlinear injection-locking dynamics of the system. Similar methods are used in Chapter 3 to predict Schawlow-Townes narrowing. The numerical approach described in this section is the basis for the bottom 3 plots of Fig. 6.2D.

We begin by discretizing the equations of motion in the rotating frame (Eq. 6.2), which yields

$$\begin{aligned}
a_{\text{p},j+1} &= a_{\text{p},j} - \Delta t[\frac{\gamma_{\text{tot},2}}{2}a_{\text{p},j} + iga_{\text{s},j}b_j - \sqrt{\gamma_{\text{tot},2}}\bar{S}_{\text{p},j}^{\text{in}}] \\
a_{\text{s},j+1} &= a_{\text{s},j} - \Delta t[\frac{\gamma_{\text{tot},1}}{2}a_{\text{s},j} + iga_{\text{s},j}b_j^* - \sqrt{\gamma_{\text{tot},2}}\bar{S}_j^{\text{in}}] \\
b_{j+1} &= b_j - \Delta t[\frac{\Gamma}{2}b_j + iga_{\text{p},j}a_{\text{s},j}^* - \bar{\eta}_j],
\end{aligned} \tag{6.3}$$

where Δt is the interval of the chosen time step and subscript $_j$ identifies the index of the complex mode amplitude in discrete time increments Δt (i.e., such that a_j is $a(t)$ for: $\Delta t * (j-1) < t < \Delta t * j$). We note that, for simplicity, we assume that each mode is on resonance. We also neglect optical vacuum fluctuations and assume no input noise in the optical pump and signal fields. In this analysis, source fields of Eq. 6.3 can be expressed as

$$\begin{aligned}
\bar{S}_{\text{p},j}^{\text{in}} &= \sqrt{\frac{P_{\text{p,in}}}{\hbar\omega_{\text{p}}}} \\
\bar{S}_j^{\text{in}} &= \sqrt{\frac{P_{\text{s,in}}}{\hbar\omega_{\text{s}}}}e^{-i(\omega_{\text{s}}-\omega_{\text{e}})\Delta t} \\
\bar{\eta}_j &= \sqrt{\frac{n_{\text{th}}\Gamma}{2\Delta t}}(R_1 + iR_2),
\end{aligned} \tag{6.4}$$

where $P_{\mathrm{p,in}}$ and $P_{\mathrm{s,in}}$ are the optical powers of the input pump and seed fields and R_1 and R_2 are normally distributed random Gaussian numbers with variance 1 and mean 0.

Using this framework, we carry out a series of stochastic simulations over a range of seed powers and detunings. These simulations use a discrete time domain comprised of 5×10^6 time steps, each of duration $\Delta t = 10^{-10}$. As shown in Fig. 6.2D, the lock ranges (δ) obtained from these theoretical simulations (bottom) demonstrate excellent agreement with our experimental observations. We also note that, in good qualitative agreement with our measurements, these simulations exhibit the same four-wave-mixing-like dynamics when the seed frequency is in sufficient proximity of the lock range. These spectral features are intriguing given that our simulations include only the Brillouin nonlinearity and do not include Kerr nonlinearities. This is a manifestation of the fact that, like Kerr and Raman interactions, stimulated Brillouin scattering is fundamentally a $\chi^{(3)}$ nonlinearity, although in contrast to electronic Kerr nonlinearities, this wave mixing is mediated by phonons. Thus, within the Brillouin gain bandwidth ($\sim$ 9 MHz) and less stringent phase-matching bandwidth ($\sim$ 90 GHz; see Section 8.6), phonon-mediated four-wave-mixing can occur, as evidenced by our measurements and simulations.

6.3.2 Relative intensity noise (RIN) and phase noise reduction

Building on the analysis in Section 6.3, we explore the time dynamics of injection locking and the resulting noise properties. As discussed in Chapter 3, there is a well-defined dissipation hierarchy between the pump, Stokes, and phonon fields (given by $\gamma_{\mathrm{tot},2} \gg \gamma_{\mathrm{tot},1} \gg \Gamma$, respectively) in our silicon Brillouin system, which allows us to adiabatically eliminate the pump and Stokes fields as

$$\begin{aligned} \bar{a}_{\mathrm{p}} &= \frac{2}{\gamma_{\mathrm{tot},2}}(-ig\bar{a}_{\mathrm{s}}\bar{b} + \sqrt{\gamma_{\mathrm{C},2}}\bar{S}_{\mathrm{p}}^{\mathrm{in}}) \\ \bar{a}_{\mathrm{s}} &= \frac{\chi_{\mathrm{s}}\left[\sqrt{\gamma_{\mathrm{A},1}}\bar{S}^{\mathrm{in}} - 2ig^*\sqrt{\gamma_{\mathrm{C},2}}\bar{S}_{\mathrm{p}}^{\mathrm{in}}/\gamma_{\mathrm{tot},2}\bar{b}^\dagger\right]}{1 + 2|g|^2|\bar{b}|^2\chi_{\mathrm{s}}/\gamma_{\mathrm{tot},2}}, \end{aligned} \tag{6.5}$$

where the Stokes susceptibility χ_{s} is given by $\chi_{\mathrm{s}} = (-i(\omega_{\mathrm{s}} - \omega_1^n) + \gamma_{\mathrm{tot},1}/2)^{-1}$ and we have taken the pump to be on resonance (i.e., $\omega_{\mathrm{p}} = \omega_2^m$). Inserting these expressions into Eq. 6.2 yields the following nonlinear equation of motion for the phonon degrees of freedom:

$$\dot{\bar{b}}(t) = Q(t)\bar{b}(t)^2 + M(t)\bar{b}(t) + W(t) + \bar{\eta}(t), \tag{6.6}$$

where $Q(t)$, $M(t)$, $W(t)$, and $\sigma(t)$ are defined by

$$\begin{aligned}
Q(t) &= -\sigma(t)\left[\frac{2ig|g|^2|\chi_s|^2\sqrt{\gamma_{A,1}\gamma_{C,2}}\bar{S}_p^{in*}\bar{S}^{in}}{\gamma_{tot,2}}\right] \\
M(t) &= i(\Omega - \Omega_B) - \frac{\Gamma}{2} - \sigma(t)\left[|\chi_s|^2|g|^2\gamma_{A,1}|S^{in}|^2 - \frac{2|g|^2\gamma_{C,2}|S_p^{in}|^2\chi_s^*}{\gamma_{tot,2}}\right] \\
W(t) &= \sigma(t)\big[-ig^*\chi_s^*\sqrt{\gamma_{A,1}\gamma_{C,2}}\bar{S}^{in*}S_p^{in}\big] \\
\sigma(t) &= \frac{2}{\gamma_{tot,2}|1 + 2|g|^2|\bar{b}(t)|^2\chi_s/\gamma_{tot,2}|^2}.
\end{aligned} \tag{6.7}$$

Following the same approach developed in Section 3.4.4, we separately analyze the phase noise and relative intensity noise using the substitution

$$\bar{b}(t) = (\beta + \delta\beta(t))e^{i\phi(t)}, \tag{6.8}$$

where real-valued $\delta\beta(t)$ and $\phi(t)$ represent the intrinsic zero-mean amplitude and phase fluctuations of the laser system, respectively. Inserting this expression into Eq. 6.6, we find

$$\begin{aligned}
\delta\dot{\beta}(t)e^{i\phi(t)} + i\dot{\phi}(t)(\beta + \delta\beta(t))e^{i\phi(t)} = Q(t)(\beta + \delta\beta(t))^2e^{2i\phi(t)} + M(t)(\beta + \delta\beta(t))e^{i\phi(t)} \\
+ W(t) + \bar{\eta}(t).
\end{aligned} \tag{6.9}$$

Assuming resonant conditions (i.e., $\omega_s = \omega_1^n$) and considering the relative phases between $W(t)$ and $Q(t)$, we can rewrite these expressions as

$$\begin{aligned}
W(t) &= |W(t)|e^{i\phi_0} \\
Q(t) &= -|Q(t)|e^{-i\phi_0}
\end{aligned} \tag{6.10}$$

where the time-independent phase ϕ_0 is defined as $\phi_0 = \arg[-ig^*S^{in*}S_p^{in}]$. As such, Eq. 6.9 can be re-expressed as

$$\delta\dot{\beta}(t) + i\dot{\phi}(t)(\beta + \delta\beta(t)) = -|Q(t)|(\beta + \delta\beta(t))^2 e^{i(\phi(t)-\phi_0)} + M(t)(\beta + \delta\beta(t)) + |W(t)|e^{-i(\phi(t)-\phi_0)} + \bar{\eta}(t). \tag{6.11}$$

Here, we have used the fact that the Langevin term $\bar{\eta}(t)$ is uncorrelated with $e^{-i\phi(t)}$.[2] Assuming small phase fluctuations when injection-locked, we expand $e^{i(\phi(t)-\phi_0)}$ to first order as $e^{i(\phi(t)-\phi_0)} \approx 1 + i(\phi(t) - \phi_0)$, yielding

$$\delta\dot{\beta}(t) + i\dot{\phi}(t)(\beta + \delta\beta(t)) = -|Q(t)|(\beta + \delta\beta(t))^2(1 + i(\phi(t) - \phi_0)) + M(t)(\beta + \delta\beta(t)) + |W(t)|(1 - i(\phi(t) - \phi_0)) + \bar{\eta}(t). \tag{6.12}$$

Separating Eq. 6.12 into its real and imaginary parts yields two independent equations of motion for the amplitude and phase fluctuations, allowing us to calculate the expected relative intensity noise and phase noise reduction due to injection locking, respectively.

Relative intensity noise (RIN) reduction

From the time dynamics contained in Eq. 6.12, we first calculate the two-sided spectrum of the relative intensity noise (RIN), which is defined by [161]

$$\text{RIN} \equiv \frac{1}{P^2}\int_{-\infty}^{\infty} d\tau \langle \delta P(t+\tau)\delta P(t)\rangle e^{i2\pi f\tau}, \tag{6.13}$$

where P is the power and $\delta P(t)$ are the zero-mean power fluctuations.

To capture the salient nonlinear effects produced by pump depletion, we Taylor expand $\sigma(t)$ to first order—using $\delta\beta(t) \ll \beta$—to isolate time-independent and time-dependent parts such that

$$\sigma(t) \approx \sigma - \sigma_{\text{RIN}}\delta\beta(t), \tag{6.14}$$

2. As we will see later, $\bar{\eta}(t)$ is the driving term in the phase evolution (see Eq. 6.22). We recall that $\bar{\eta}(t)$ is delta-correlated in time. This implies that, since the phase responds after some non-zero time interval, the phase is instantaneously uncorrelated with the Langevin source.

where σ and σ_{RIN} are defined as

$$\begin{aligned}\sigma &= \frac{2}{\gamma_{\mathrm{tot},2}|1+4|g|^2\beta^2/(\gamma_{\mathrm{tot},2}\gamma_{\mathrm{tot},1})|^2} \\ \sigma_{\mathrm{RIN}} &= \frac{4\gamma_{\mathrm{tot},1}^2|g|^2\beta}{\gamma_{\mathrm{tot},2}^2\big(\gamma_1/2+2|g|^2\beta^2/\gamma_{\mathrm{tot},2}\big)^3}.\end{aligned} \tag{6.15}$$

Under this approximation, $Q(t)$, $W(t)$, and $M(t)$ (defined by Eq. 6.7) can be expressed as

$$\begin{aligned}Q(t) &= Q\left(1-\frac{\sigma_{\mathrm{RIN}}\delta\beta(t)}{\sigma}\right) \\ W(t) &= W\left(1-\frac{\sigma_{\mathrm{RIN}}\delta\beta(t)}{\sigma}\right) \\ M(t) &= M-\frac{\sigma_{\mathrm{RIN}}(M-i\big(\Omega-\Omega_{\mathrm{B}}\big)+\frac{\Gamma}{2}\big)}{\sigma}\delta\beta(t),\end{aligned} \tag{6.16}$$

where we have used Eqs. 6.14, Eqs. 6.15, and 6.7. Here Q, W, and M are the time independent contributions of $Q(t)$, $W(t)$, and $M(t)$ (i.e., take definitions with $\sigma(t)\to\sigma$ in Eq. 6.7).

To analyze the RIN reduction permitted by injection locking, we apply these expressions and isolate the real part of Eq. 6.12, which yields

$$\delta\dot{\beta}(t) = \beta+|Q|\beta^2+|W|-\frac{\Gamma_{\mathrm{RIN}}}{2}\delta\beta(t)+\frac{\bar{\eta}(t)+\bar{\eta}^\dagger(t)}{2}, \tag{6.17}$$

where $(\bar{\eta}(t)+\bar{\eta}^\dagger(t))/2$ is the real part of the Langevin term $\eta(t)$ and the amplitude fluctuation decay rate Γ_{RIN} is given by

$$\Gamma_{\mathrm{RIN}} = \frac{\sigma_{\mathrm{RIN}}}{\sigma}\left(\beta\Gamma-2|Q|\beta^2+2|W|+\frac{4\beta|Q|\sigma}{\sigma_{\mathrm{RIN}}}\right). \tag{6.18}$$

We have also used the fact that the real part of M ($\Re[M]$) vanishes above threshold; in other words, the Brillouin gain balances the total loss to an excellent approximation [162].

Now, solving Eq. 6.17 we find

$$\delta\beta(t) = \int_{-\infty}^{t}dt'\left[-|Q|\beta^2+|W|+\frac{\bar{\eta}(t')+\bar{\eta}^\dagger(t')}{2}\right]e^{-\frac{\Gamma_{\mathrm{RIN}}}{2}(t-t')}, \tag{6.19}$$

where we are integrating over the dummy variable t'.

Taking the expectation value of Eq. 6.19, and using the fact that $\delta\beta(t)$ is a stochastic

variable with zero mean (i.e., $\langle \delta\beta(t) \rangle = 0$), we find that $-|Q|\beta^2 + |W| = 0$. Using this relationship, the expression for Γ_{RIN} (Eq. 6.18) can be simplified as $\Gamma_{\mathrm{RIN}} = \sigma_{\mathrm{RIN}}\beta\Gamma/\sigma + 4|W|/\beta$. To find the relative intensity noise, we must evaluate $\langle \delta\beta(t+\tau)\delta\beta(t) \rangle$, which yields

$$\begin{aligned} \langle \delta\beta(t+\tau)\delta\beta(t) \rangle &= \frac{1}{4}\int_{-\infty}^{t} dt'(2n_{\mathrm{th}}+1)\Gamma e^{-\frac{\Gamma_{\mathrm{RIN}}}{2}(2t'-2t-\tau)} \\ &= \frac{\Gamma(2n_{\mathrm{th}}+1)}{4\Gamma_{\mathrm{RIN}}}\left[e^{-\frac{\Gamma_{\mathrm{RIN}}}{2}|\tau|}\right]. \end{aligned} \tag{6.20}$$

here we have assumed that the Brillouin-active phonons are at thermal equilibrium such that $\langle \eta(t')\eta^{\dagger}(t) \rangle = \Gamma(n_{\mathrm{th}}+1)\delta(t-t')$, where n_{th} is the thermal occupation of the phonon field.

Since the power $P \propto (\beta + \delta\beta(t))^2$, the power fluctuations δP are proportional to $2\beta\delta\beta$, again assuming small amplitude fluctuations (i.e., $\delta\beta(t) \ll \beta$). As such, the RIN becomes

$$\begin{aligned} \mathrm{RIN} &\equiv \frac{1}{P^2}\int_{-\infty}^{\infty} d\tau \langle \delta P(t+\tau)\delta P(t) \rangle e^{i2\pi f\tau} \\ &= \frac{4}{\beta^2}\int_{-\infty}^{\infty} d\tau \langle \delta\beta(t+\tau)\delta\beta(t) \rangle e^{i2\pi f\tau} \\ &= \frac{\Gamma(2n_{\mathrm{th}}+1)}{\beta^2\Gamma_{\mathrm{RIN}}}\frac{1}{(\Gamma_{\mathrm{RIN}}/2)^2 + (2\pi f)^2}, \end{aligned} \tag{6.21}$$

which is the central result of this section.

As evident from Eq. 6.21, the RIN spectrum is defined by a characteristic Lorentzian shape with a FWHM given by $\Gamma_{\mathrm{RIN}} = \sigma_{\mathrm{RIN}}\beta\Gamma/\sigma + 4|W|/\beta$. In this expression, $\sigma_{\mathrm{RIN}}\beta\Gamma/\sigma$ represents the intrinsic decay rate for amplitude fluctuations in the absence of an injection seed, and, as it should be, is consistent with our RIN analysis of the Brillouin laser dynamics in Chapter 3. The $4|W|/\beta$ term represents the additional damping of the amplitude fluctuations due to the injected seed ($|W|$ is proportional to the seed input; see Eq. 6.7). In this way, injection locking yields significant reduction of the RIN at low frequencies.

Phase noise reduction

We now consider the phase noise properties of the system and characterize the extent to which the laser emission replicates the injected seed. The relevant differential equation is obtained by taking the imaginary part of Eq. 6.12, yielding

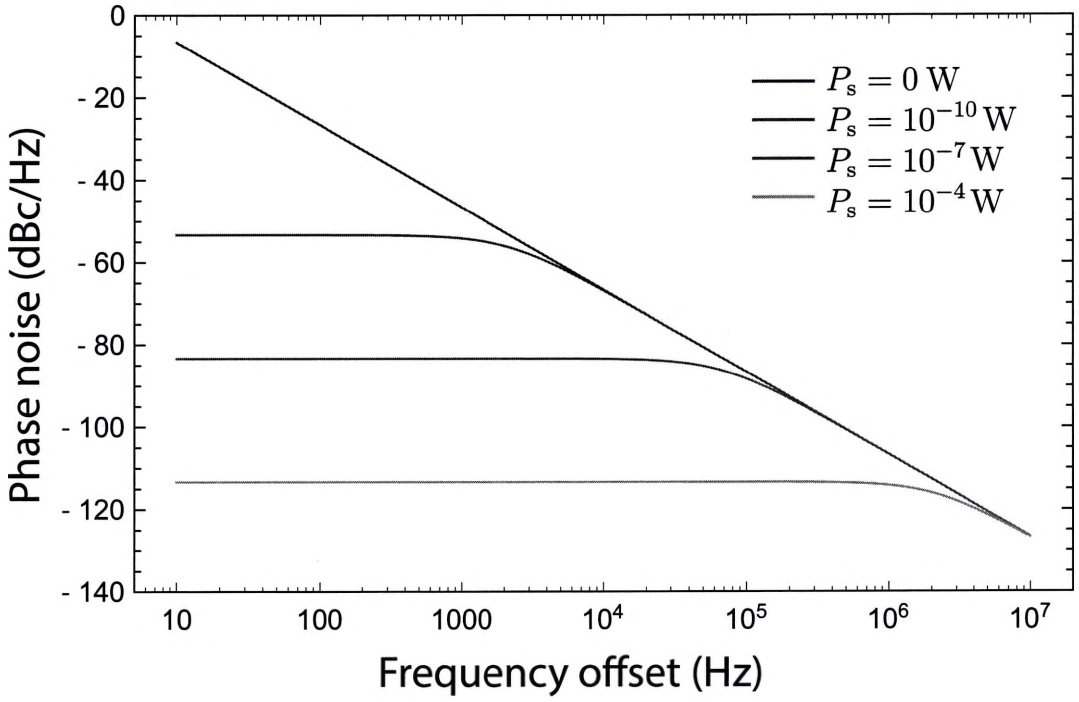

Figure 6.3: Phase noise (given by Eq. 6.25) as a function of offset frequency with typical operating parameters. Note that injection locking produces phase noise reduction over the entire lock range. This phase noise is reduced as the seed power is increased. Reproduced from Ref. [98]. Copyright (2020) by APS.

$$\dot{\phi}(t) = \Big[|Q|\beta + \frac{|W|}{\beta}\Big](\phi_0 - \phi(t)) + \frac{\bar{\eta}(t) - \bar{\eta}^\dagger(t)}{2i\beta}, \tag{6.22}$$

which yields a formal solution given by

$$\phi(t) = \phi_0 + \int_{-\infty}^{t} dt' \Big[\frac{\bar{\eta}(t') - \bar{\eta}^\dagger(t')}{2i\beta}\Big] e^{-\left[|Q|\beta + \frac{|W|}{\beta}\right](t-t')}. \tag{6.23}$$

With the solution to the phase fluctuations $\phi(t)$, we find the auto-correlation function

$$\langle \phi(t+\tau)\phi(t)\rangle = \frac{\Gamma(2n_{\text{th}}+1)}{8\beta^2\big[|Q|\beta + \frac{|W|}{\beta}\big]} e^{-\left[|Q|\beta + \frac{|W|}{\beta}\right]|\tau|}, \tag{6.24}$$

where we have again used the auto-correlation function $\langle \eta(t')\eta^\dagger(t)\rangle = \Gamma(n_{\text{th}}+1)\delta(t-t')$ for the Langevin driving term. This yields the phase noise

$$\begin{aligned} \mathscr{L}(f) &\equiv \int_{-\infty}^{\infty} d\tau \langle \phi(t+\tau)\phi(t)\rangle e^{i2\pi f\tau} \\ &= \frac{\Gamma(2n_{\text{th}}+1)}{4\beta^2} \frac{1}{(2|W|/\beta)^2 + (2\pi f)^2}. \end{aligned} \tag{6.25}$$

We note that, as before, we have used the relationship $-|Q|\beta^2 + |W| = 0$. From Eq. 6.25, we infer the lock range to be the FWHM of the phase noise spectrum such that $\delta = 2|W|/(\pi\beta)$ [163].[3] Thus, taking the limit as $f \to 0$, the phase noise relative to the injected seed is given by

$$\begin{aligned} \mathscr{L}(0) &= \frac{\Gamma(2n_{\text{th}}+1)}{16|W|^2} \\ &= \frac{2n_{\text{th}}+1}{16G_{\text{B}}P_{\text{p}}v_{\text{g}}\big(\frac{\gamma_{\text{A},1}P_{\text{s}}}{\hbar\omega_{\text{s}}\gamma_{\text{tot},1}^2}\big)}, \end{aligned} \tag{6.26}$$

where G_{B} is the Brillouin gain coefficient, P_{p} is the intracavity pump power, v_{g} is the optical group velocity, and P_{s} is the input seed power.

As evident from Eq. 6.26, we observe that the phase noise reduction is determined by the ratio of the thermal phonon number (n_{th}) to the coherent seed input (P_{s}). Fig. 6.3

3. The phase noise of the freely oscillating Brillouin laser can be recovered from Eq. 6.25 by taking the case of $|W|^2 \to 0$.

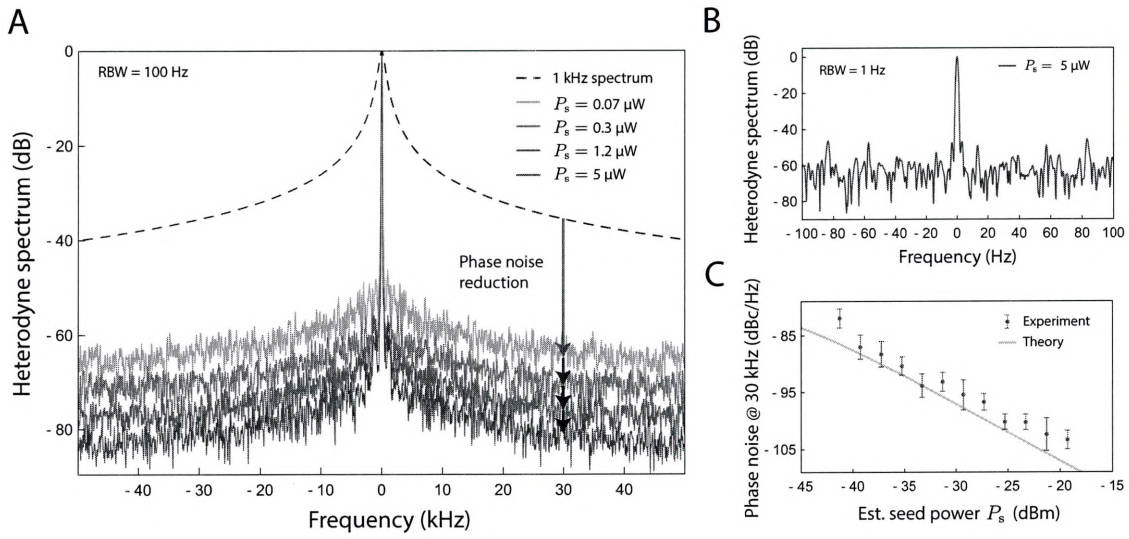

Figure 6.4: (A) Optical heterodyne spectra (RBW=100 Hz) of the injection locked Brillouin laser emission at various seed powers (detected at PD1; the local oscillator is the transmitted pump). The phase noise over a broad spectrum is monotonically reduced as the signal power is increased. Relative to phase noise produced by a typical 1 kHz spectrum (dotted dark red) of a free-running Brillouin laser [95], we achieve > 50 dB of phase noise suppression from 10 Hz to 50 kHz (in dBc/Hz). (B) Zoomed-in heterodyne spectrum (RBW=1 Hz) of the injection-locked laser. Phase noise reduction is most dramatic at low offset frequencies. (C) Phase noise at 30 kHz as a function of seed power, demonstrating good agreement with the theoretical trend (Eq. 6.25) derived in Section 6.3.2. See Appendix A.2 of Ref. [98] for more details. Reproduced from Ref. [98]. Copyright (2020) by APS.

plots the estimated phase noise (Eq. 6.25) spectrum for 4 different seed powers. Increasing the seed power both enhances the overall phase noise reduction and its bandwidth (given by the lock range), which is consistent with the behavior of injection-locked microwave oscillators [163].

Experimental phase noise measurements

We characterize these phase noise reduction properties using the experimental scheme described in Fig. 6.2A. For the measurements, we use the optional intensity modulator to directly synthesize the seed from the pump. The resulting injection-locked Brillouin laser emission is detected by the high-speed photo-receiver labelled PD 2. Fig. 6.4A-B displays high resolution (RBW = 100 Hz, RBW = 1 Hz) spectra of the laser emission beat note, revealing a highly monochromatic resolution-bandwidth-limited signal.

Since the spectrum is phase-noise dominated (i.e., because $\beta^2 \gg \delta\beta(t)^2$), the phase noise can be determined by analyzing the noise relative to the carrier. Relative to the free-running silicon Brillouin laser (with a Stokes-pump beat-note linewidth of 1 kHz) [95], this measurement demonstrates a phase noise reduction of more than 50 dB at both 30 kHz and 10 Hz offsets. We also measure the phase noise as a function of seed power, as shown in Fig. 6.4C, revealing good agreement with the theoretical trend predicted by Eq. 6.25.[4] At the largest seed powers, the measured phase noise relative to the pump laser is nearly -105 dBc/Hz, corresponding to approximately 70 dB of phase noise reduction.[5]

6.4 Unique inter-modal Brillouin properties

6.4.1 Single-sideband emission

Because the laser gain mechanism is based on a phase-matched inter-modal Brillouin interaction, it is inherently a single-sideband process. This property, in conjunction with

4. The theoretical trend presented in Fig. 6.4C is obtained from Eq. 6.25 using system parameters that are corroborated by independent measurements (including a passive characterization of the device and laser threshold conditions) and falls within the measurement uncertainty of the input seed power (which is obtained by analyzing the heterodyne spectrum when the seed frequency is well outside the lock range).

5. Relative to a free-running Brillouin laser with a 1 kHz phonon linewidth.

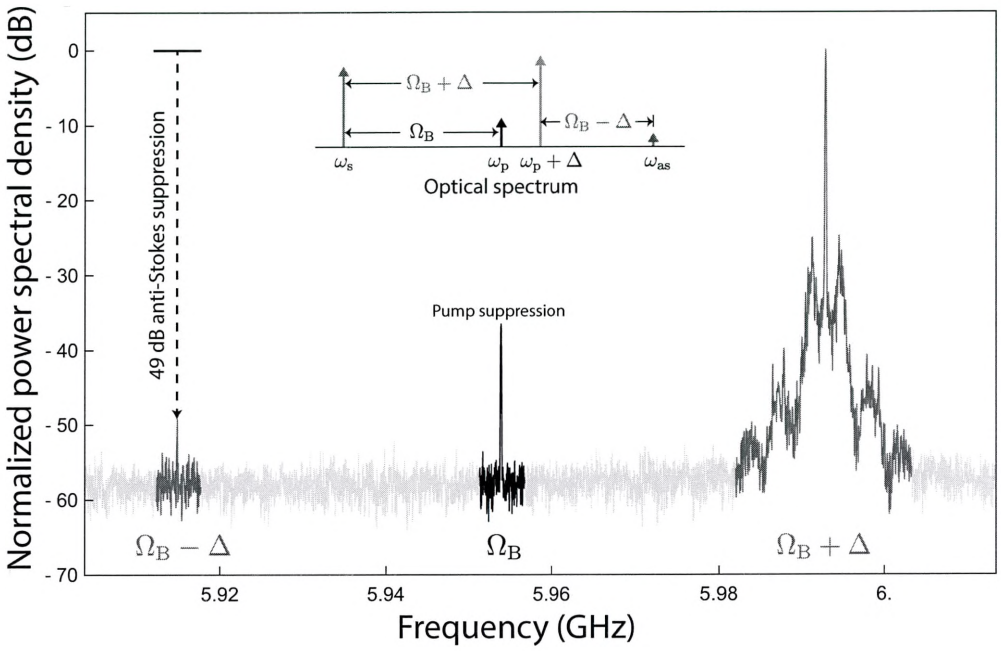

Figure 6.5: Heterodyne power spectrum revealing single-sideband emission with large anti-Stokes and pump suppression. We note that the Brillouin laser is not injection locked for these measurements. The inset diagrams the optical tones that produce three distinct microwave signals at $\Omega_B + \Delta$, Ω_B, and $\Omega_B - \Delta$, where Δ is the offset frequency of the optical local oscillator (LO). In this heterodyne configuration, emitted Stokes radiation interferes with the frequency-shifted LO to produce a beat note at $\Omega_B + \Delta$ (red). Note the characteristic fringes of the sub-coherence spectrum that arise from a small delay between the signal and LO, as we saw in Section 3.5 (see also Refs. [95, 164]). The Stokes and anti-Stokes light can also interfere with residual pump light to produce a beat note at Ω_B (black), while the anti-Stokes light beating with the optical LO yields a tone at $\Omega_B - \Delta$ (blue). From this spectrum, we observe record-large 49 dB of anti-Stokes suppression. Taking into consideration the strength of the optical LO, this spectrum also demonstrates nearly 50 dB of pump suppression relative to the intracavity pump power, thanks to the performance of the mode-specific couplers. Reproduced from Ref. [98]. Copyright (2020) by APS.

performance of mode-specific couplers, enables Stokes laser emission with significant pump and anti-Stokes suppression, in contrast to conventional cavity-optomechanics [78] and forward Brillouin scattering [165].[6] Figure 6.5 plots the laser output power spectrum obtained through heterodyne detection using the apparatus diagrammed in Figure 6.2A. In this experimental scheme, the frequency-shifted optical (Δ) local oscillator (LO) allows us to measure the relative strengths of the emitted Stokes and unwanted anti-Stokes light, as well as any residual pump light; in this case, optical beat notes of the frequency-shifted LO with the Stokes, pump, and anti-Stokes field results in unique microwave tones that can be analyzed simultaneously, as conceptually illustrated with the inset of Fig. 6.5.

Here, the measured heterodyne spectrum in Fig. 6.5 demonstrates nearly 50 dB of anti-Stokes suppression. This contrast is made possible by (1) the phase-matching-induced symmetry breaking between the Stokes and the anti-Stokes phonon wavevectors (i.e. $q_{\mathrm{as}} \neq q_{\mathrm{s}}$) and (2) the frequency selectivity of the cavity (i.e., $\omega_{\mathrm{as}} \neq \omega_2^m$). In addition, the mode-specific couplers also prevent unwanted pump light from exiting the laser resonator with the emitted Stokes light. Here, only 1 part in 10^5 of the intracavity pump light exits the mode specific coupler, reducing the transmitted pump powers significantly below the emitted Stokes powers.

6.4.2 Non-reciprocal control and back-scatter immunity

As we demonstrated in Chapter 4, an unusual property of this traveling-wave laser is that the gain is intrinsically non-reciprocal. This feature has intriguing consequences on the reciprocity of laser itself. We are able to explore these dynamics for the first time through injection locking. Through these experiments, we use a fiber-optic switch to rapidly alternate between forward and backward injection configurations (see Fig. 6.2 and Fig. 6.6A-B), allowing us to analyze the resulting laser dynamics. As shown in Fig. 6.6A, when the seed is coupled into the resonator such that it co-propagates with the self-oscillating Stokes wave, we achieve a stable injection lock. By contrast, when the seed enters in the counter-propagating direction, the laser emission is unaffected by its presence (see Fig. 6.6Bii). This

6. This is made possible by the modal degrees of freedom and stringent phase-matching conditions of stimulated inter-modal Brillouin scattering.

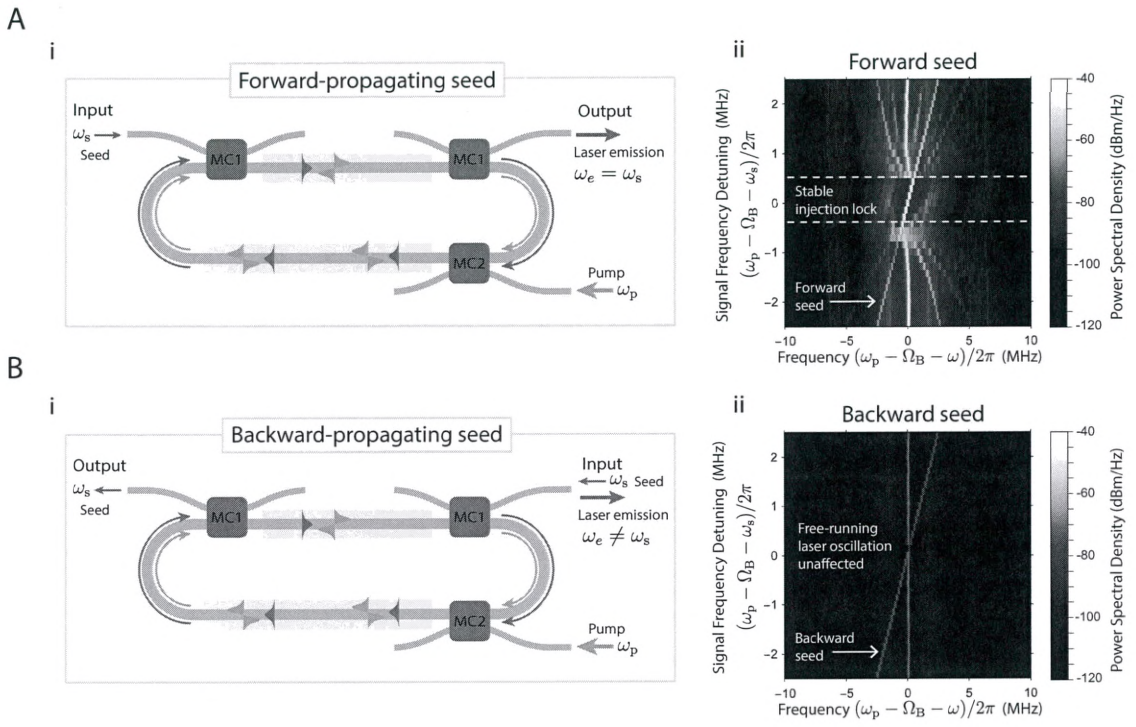

Figure 6.6: Experimental demonstration of non-reciprocal laser dynamics through injection locking. (Ai) Operation scheme for injection locking in the forward direction. The seed is coupled into the resonator such that it co-propagates with the pump and self-oscillating Stokes mode. (Aii) Experimental density plot demonstrating injection-locking in the forward direction. (Bi) Seed light is injected in the backward direction such that it counter-propagates with the light in the cavity. (Bii) Experimental density plot demonstrating back-scatter immunity. In this case, the laser emission is unaffected by the presence of the seed. Reproduced from Ref. [98]. Copyright (2020) by APS.

robustness to unwanted external feedback is in stark contrast to conventional lasers, whose behavior would be substantially impacted by such a backward-propagating signal [166,167].

6.5 Conclusion and outlook

In this chapter, we have demonstrated injection locking in a silicon Brillouin laser and explored its unique dynamics through combination of experimental, numerical, and analytical analysis. Devices are fabricated with standard electron-beam lithography and with high-fidelity CMOS foundry processes (described in Chapter 5), allowing us to fully take advantage of modal degrees of freedom to precisely control the laser gain and emission. We have shown that this system is capable of injection-locked operation over a lock range of nearly 2 MHz, representing a significant fraction of the Brillouin gain bandwidth. Importantly, our results highlight new strategies for dramatic phase-noise reduction, high-gain amplification, and back-scatter immunity in an all-silicon system.

Injection locking presents new opportunities to control and manipulate the Brillouin laser dynamics. First, using a seed synthesized from a stable microwave oscillator, injection locking gives us the ability to control the frequency of the laser emission with Hz-level precision. Second, thanks to the unique spatio-temporal dynamics of this silicon Brillouin laser system, we can leverage injection locking to dramatically reduce the phase noise of the laser emission relative to the pump. Given the inverted dissipation hierarchy of this system (see Chapter 3 for more details), the free-running laser emission can be viewed as a frequency shifted version input pump laser, with modest levels of residual phase noise (1 kHz linewidth) due to the presence of thermal phonons. The most straightforward approach to reduce the residual phase noise is through the standard form of Schawlow-Townes linewidth narrowing, which scales as $1/P_{\mathrm{p}}$ (see Section 3.4.4 for more details). By contrast, here we use injection locking to reduce the phase noise by $\sim$ 70 dB relative to that of the free-running laser oscillator (see Fig. 6.4A,C and Section 6.3.2 for more details). For context, this same degree of phase noise reduction through Schawlow-Townes linewidth narrowing would require $10^7\times$ the pump power.

These injection locking dynamics may lend themselves to a range of powerful silicon

photonics device physics. First, this system permits large degrees (> 20 dB) of low-noise amplification in an all-silicon system. The amplification can be further scaled by leveraging the phase coherence between the input seed and output lasers to coherently combine a parallel array of injection-locked Brillouin lasers. Second, the intrinsic single sideband nature of this process may open the door to new single-sideband (SSB) modulation schemes. SSB modulators are crucial components for applications ranging from communications to spectroscopy, but existing technologies require a complex array of photonic modulators that must maintain phase stable operation [141]. We have shown that, through the well-resolved phase matching conditions and the design of our mode-specific couplers, we can achieve single-sideband emission with nearly 50 dB of anti-Stokes and carrier suppression. In this way, this injection locked system may be combined with existing intensity modulators to achieve high-performance single sideband modulation. Finally, the unique properties of this Brillouin system offer a powerful new approach to chip-scale optical non-reciprocity in silicon photonics. The phase-matched nature of the gain process allows us to control the laser emission only when injecting a seed in the forward direction. As such, an unwanted back-ward propagating interferer leaves the laser unaffected. This form of back-scatter immunity represents a dramatic departure from conventional laser systems and could be a key resource in the development of robust integrated photonics systems.

Chapter 7

Noise dynamics in Brillouin amplifier systems

7.1 Introduction

In dissipative open systems, noise is what maintains the detailed balance necessary for thermodynamic equilibrium. This relationship between dissipation and noise—known as the fluctuation-dissipation theorem—gives rise to a host of interesting dynamics in the context of Brillouin physics. As we have already discussed in Chapter 3 and Chapter 6, thermal and zero-point optomechanical noise sources place a fundamental limitation on the linewidth of Brillouin laser systems. In this Chapter, we (1) study the effect of these optomechanical fluctuations on the performance of Brillouin amplifier physics, (2) develop concrete performance metrics, (3) and discuss strategies to manage noise.

In what follows, we present a general and didactic treatment of the noise figure for both linear and resonant Brillouin amplifiers systems (described in Chapters 2 and 4, respectively). We adopt an unambiguous formulation for the optical noise figure in which the excess noise is compared to the zero-point optical background [168]. We base our calculations on the equations derived from the traveling-wave Hamiltonian framework discussed in Chapter 1 (see also Ref. [75]). Building on this formalism, we introduce Langevin terms to represent the of thermal and zero-point fluctuations of the acoustic and optical fields,

with correlation properties that are consistent with the fluctuation dissipation theorem. This analysis reveals that the thermal occupation of the phonons is the key parameter in determining the noise figure, and we discuss strategies to manipulate this important parameter. We also extend this analysis to calculate a range of other properties including the out-of-band noise figure and the noise figure of a Brillouin-amplification-based filter within an RF-photonic link. These formulations establish concrete guidelines for noise-conscious design of future Brillouin-based photonic systems.

7.2 Noise figure definitions

From a systems perspective, one of the most important metrics is the noise factor, which quantifies how the signal-to-noise ratio changes as a result of amplification. In general, the noise factor (F) can be defined by the ratio of the input and output signal-to-noise ratios (SNR), such that

$$\mathrm{F} = \frac{\mathrm{SNR}_1}{\mathrm{SNR}_2}, \tag{7.1}$$

where SNR_1 and SNR_2 are the input and output signal to noise ratios. We note that it is often common to refer to the noise figure, which is simply the noise factor on a dB scale (i.e., $\mathrm{NF} \equiv 10\log_{10}\mathrm{F}$). Throughout this chapter, we speak of the noise factor and noise figure interchangeably.

We can also recast the noise factor in terms of the gain and additive noise of the amplifier, which can be expressed as

$$\begin{aligned} \mathrm{F} = \frac{\mathrm{SNR}_1}{\mathrm{SNR}_2} &= \frac{\left(\frac{\text{Signal in}}{\text{Noise in}}\right)}{\left(\frac{\text{Gain}\times\text{Signal in}}{\text{Gain}\times\text{Noise in}+\text{Additive noise}}\right)} \\ &= 1 + \left(\frac{\text{Additive noise}}{\text{Gain} \times \text{Noise in}}\right). \end{aligned} \tag{7.2}$$

Equation 7.2 reveals that the noise factor is inherently a measure of how the additive noise of the amplifier compares with the amplified input noise. We also note that the noise

factor is generally considered an intrinsic property of a system, and as such, should be independent of the signal. This condition holds when the gain, input noise, and additive noise are each independent of the signal.

In many instances it is important to consider the noise factor of system comprised of multiple subsystems. When the noise factor is signal independent, we can easily calculate the noise factor of the composite system from the noise factors of each individual system. This leads to the well-known Friis formula for cascading amplifiers

$$F_{\text{total}} = F_1 + \frac{F_2 - 1}{G_1} + \frac{F_3 - 1}{G_1 G_2} .... \tag{7.3}$$

Here, $F_{(1,2,3)}$ and $G_{(1,2,3)}$ represent the noise factors and gains for subsystems 1,2,3, respectively. Friis' formula underscores the intuition that the lowest noise figures are possible by placing the component with the lowest noise figure first.

7.2.1 Noise figure of RF or microwave systems

To properly define the noise figure of optical amplifiers, we gain important insights by first considering the noise figure of an RF amplifier. In this case, the dominant input noise is thermal in nature and is often referred to as Johnson noise. Thus, the noise over some bandwidth B is proportional to the thermal energy of the system $K_{\text{B}}T$, such that the noise factor becomes

$$\begin{aligned} \text{F} = \frac{\text{SNR}_1}{\text{SNR}_2} &= \frac{\left(\frac{\text{Signal in}}{K_{\text{B}}TB}\right)}{\left(\frac{\text{Gain}\times\text{Signal in}}{\text{Gain}\times K_{\text{B}}TB + \text{Additive noise}}\right)} \\ &= 1 + \left(\frac{\text{Additive noise}}{\text{Gain} \times K_{\text{B}}TB}\right). \end{aligned} \tag{7.4}$$

We note that, since the noise factor is signal independent,[1] the cascading formula applies.

1. Given that the gain and additive noise are also signal independent.

7.2.2 Noise figure of optical amplifiers

We next seek an unambiguous formulation of the noise figure for optical amplifiers. Here, we must be careful to properly account for the noise sources associated with optical fields. In particular, it may be tempting to consider shot noise, which grows in strength as the number of photons (i.e., $\langle \delta n^2 \rangle = \bar{n}$), as the relevant noise source in optical amplifiers. If we are to choose this definition, the noise factor can be expressed as

$$\begin{aligned} \mathrm{F} = \frac{\mathrm{SNR}_1}{\mathrm{SNR}_2} &= \frac{\left(\frac{\bar{n}^2}{\bar{n}}\right)}{\left(\frac{\mathrm{Gain}\times\bar{n}^2}{\mathrm{Gain}\times\bar{n}+\mathrm{Additive\ noise}}\right)} \\ &= 1 + \left(\frac{\mathrm{Additive\ noise}}{\mathrm{Gain}\times\bar{n}}\right). \end{aligned} \tag{7.5}$$

However, as discussed in Ref. [168], this definition becomes impractical for the analysis of more complex systems. Namely, since the noise figure now depends upon the signal strength, Friis' cascading formula no longer applies. Moreover, since shot noise requires some form of detection, this choice would be ill-defined when considering the power spectrum in the optical domain.

We recall that for an RF amplifier (where $k_\mathrm{b}T \gg \hbar\omega$), the relevant input noise arises from fundamental thermal fluctuations. Given the high frequencies of the optical domain, this noise source is negligible (i.e., $k_\mathrm{b}T \ll \hbar\omega$), meaning that vacuum fluctuations are the dominant source of noise. Thus, we can consider the fundamental optical noise produced by vacuum fluctuations as the relevant background noise, which yields

$$\mathrm{F} = \frac{\mathrm{SNR}_1}{\mathrm{SNR}_2} = 1 + \frac{\mathrm{Additive\ noise}}{\mathrm{Gain}\times\hbar\omega B}. \tag{7.6}$$

The definition expressed by Eq. 7.6 shows that (1) the relevant background is determined by the optical energy and (2) that the noise figure is signal independent, as it should be [168]. Building on this more practical formulation, we proceed to calculate the noise figure of both linear and resonant Brillouin amplifier systems.

7.3 Noise figure of Brillouin amplifier systems

In what follows, we seek to characterize the noise figure of both linear and resonant Brillouin amplifiers. In Section 7.3.1, we derive the noise figure for a linear (non-resonant) Brillouin amplifier. We begin by calculating the noise produced by the zero-point optical background within a passive waveguide. We then derive the noise figure of a Brillouin-active waveguide and explore the limit of large and small Brillouin gain. In Section 7.3.2, we proceed to analyze the noise figure of a resonantly enhanced Brillouin amplifier, starting first with the noise dynamics of a simple optical mode in the presence of gain and loss, and then calculating the noise figure for an optical mode that is supplied with Brillouin gain. Section 7.3.3 defines and derives the out-of-band noise figures for both linear and resonantly enhanced Brillouin amplifiers, highlighting the low out-of-band noise performance of Brillouin-based devices useful in channelization applications [169, 170]. Finally, Section 7.3.4 uses this framework to predict the performance of a resonant Brillouin amplifier within an RF-photonic link.

7.3.1 Linear waveguide Brillouin amplifier

Passive waveguide

In this section, we use the definition given by Eq. 7.6 to calculate the noise figure that results from Brillouin amplification in a linear (non-resonant) system, such as the type described in Chapter 2. We begin by analyzing the quantum-optical noise within a waveguide in the presence of non-zero propagation loss. In the absence of Brillouin gain, the equation of motion for the Stokes field can be written as [75, 77]

$$\dot{\bar{A}}_{\mathrm{s}}(z,t) + i(\omega_0 - \omega_{\mathrm{s}})\bar{A}_{\mathrm{s}}(z,t) + \frac{\alpha v_{\mathrm{g}}}{2}\bar{A}_{\mathrm{s}}(z,t) + v_{\mathrm{g}}\frac{\partial \bar{A}_{\mathrm{s}}(z,t)}{\partial z} = N_{\mathrm{i}}(z,t). \tag{7.7}$$

Here, $\bar{A}(z,t)$ is the Stokes envelope under the rotating wave approximation ($|\bar{A}(z,t)|^2$ has units of [Number][m]$^{-1}$),[2] α is the optical propagation loss (with units [m]$^{-1}$), v_{g} is the group velocity, and $N_{\mathrm{i}}(z,t)$ is the Langevin term representing the quantum fluctuations within the

2. As discussed in Chapter 1, these envelopes are normalized such that $\int dz' \bar{A}^{\dagger}(z',t)\bar{A}(z',t) =$ photon number.

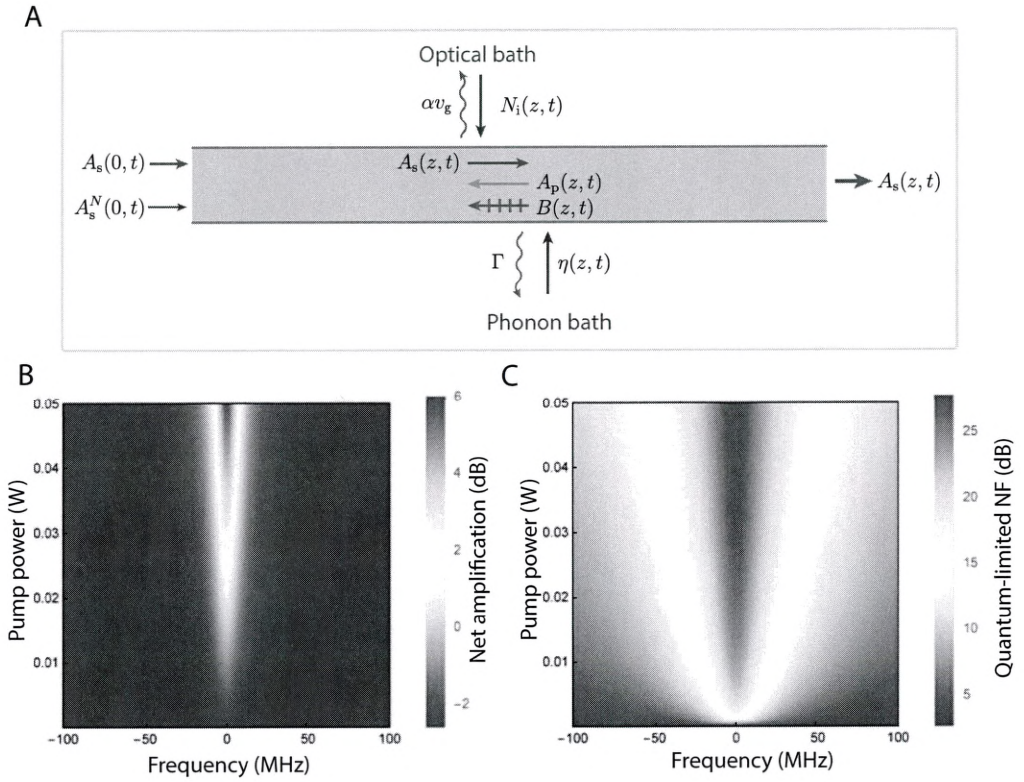

Figure 7.1: Linear (non-resonant) Brillouin amplifier. Panel (A) diagrams the Brillouin amplification and noise processes. (B) Net amplification as a function of pump power and detuning from the Brillouin resonance (with $G_B = 400\ \mathrm{W^{-1}m^{-1}}$, $z = 0.1$ m, $\alpha = 6\ \mathrm{m^{-1}}$, $v_g = 7 \times 10^7\ \mathrm{ms^{-1}}$, $\Omega = 2\pi \times 10$ GHz, and $\Gamma = 2\pi \times 15$ MHz). (C) optical noise figure (relative to the zero-point optical background), given by Eq. 7.22 with the same parameters used in panel (B)).

waveguide, with a two-time correlation of the form $\langle N_{\mathrm{i}}(z',t')N_{\mathrm{i}}^{\dagger}(z,t)\rangle = \alpha v_{\mathrm{g}}\delta(z'-z)\delta(t'-t)$. We proceed by taking a Fourier transform in time, yielding

$$i(\omega_0-\omega_{\mathrm{s}}-\omega)\bar{A}_{\mathrm{s}}[z,\omega]+\frac{\alpha v_{\mathrm{g}}}{2}\bar{A}_{\mathrm{s}}[z,\omega]+v_{\mathrm{g}}\frac{\partial\bar{A}_{\mathrm{s}}[z,\omega]}{\partial z}=N_{\mathrm{i}}[z,\omega]. \tag{7.8}$$

The integral solution to this differential equation is given by

$$\bar{A}_{\mathrm{s}}[z,\omega]=\int_{-\infty}^{z}dz'\frac{N_{\mathrm{i}}[z',\omega]}{v_{\mathrm{g}}}e^{-\frac{1}{v_{\mathrm{g}}\chi}(z-z')}, \tag{7.9}$$

where the susceptibility χ is defined by

$$\chi=\frac{1}{i(\omega_0-\omega_{\mathrm{s}}-\omega)+\frac{\alpha v_{\mathrm{g}}}{2}}. \tag{7.10}$$

From Eq. 7.9, we compute the number spectral density per unit length of the vacuum fluctuations within the waveguide ($\mathscr{A}_{\mathrm{s}}[z,\omega]=\lim_{T\to\infty}(1/T)|\bar{A}_{\mathrm{s}}[z,\omega]|^2$ [171]), yielding

$$\begin{aligned}\mathscr{A}_{\mathrm{s}}[z,\omega]&=\lim_{T\to\infty}\frac{1}{T}\int_{-\infty}^{z}dz_1\int_{-\infty}^{z}dz_2\frac{\langle N_{\mathrm{i}}[z_1,\omega]N_{\mathrm{i}}^{\dagger}[z_2,\omega]\rangle}{v_{\mathrm{g}}^2}e^{\frac{1}{v_{\mathrm{g}}}(-\frac{1}{\chi^*}(z-z_1)-\frac{1}{\chi}(z-z_2))}\\&=\int_{-\infty}^{z}dz_1\int_{-\infty}^{z}dz_2\frac{\delta(z_1-z_2)}{v_{\mathrm{g}}}e^{\frac{1}{v_{\mathrm{g}}}(-\frac{1}{\chi^*}(z-z_1)-\frac{1}{\chi}(z-z_2))}\\&=\frac{1}{v_{\mathrm{g}}}.\end{aligned} \tag{7.11}$$

Thus, in the absence of gain, the spectral density of the optical vacuum fluctuations is white, with a value given by $\mathscr{A}_{\mathrm{s}}[z,\omega]=1/v_{\mathrm{g}}$. Converting this value into an equivalent power spectral density yields $\mathfrak{S}(\omega)=\hbar\omega_{\mathrm{s}}v_{\mathrm{g}}\mathscr{A}_{\mathrm{s}}[z,\omega]=\hbar\omega_{\mathrm{s}}Hz^{-1}$, a natural consequence of the anti-normal ordering chosen in our definition [168].

Brillouin-active waveguide

We next analyze the system in the presence of Brillouin gain. Here, we specifically consider the case of backward Brillouin scattering, as illustrated in Fig. 7.1A; however, we note that the results derived in this section apply quite generally a number of Brillouin processes, such as forward inter-modal and inter-polarization scattering—in short, any Brillouin process in

which the Stokes and anti-Stokes processes are sufficiently decoupled [29, 75]. In the case of backward SBS, the equations of motion can be written as [75, 77]

$$\begin{aligned}\dot{A}_{\rm s}(z,t)+i\omega_0 A_{\rm s}(z,t)+v_{\rm g}\frac{\partial A_{\rm s}(z,t)}{\partial z}+\frac{\alpha v_{\rm g}}{2}A_{\rm s}(z,t)&=-ig^*_{\rm s,p}A_{\rm p}(z,t)B^\dagger(z,t)+N_{\rm i}(z,t)\\ \dot{B}(z,t)+i\Omega_{\rm B}B(z,t)+\frac{\Gamma}{2}B(z,t)-v_{\rm B}\frac{\partial B(z,t)}{\partial z}&=-ig^*_{\rm s,p}A_{\rm p}(z,t)A^\dagger_{\rm s}(z,t)+\eta(z,t),\end{aligned} \tag{7.12}$$

where $A_{\rm s}(z,t)$, $B(z,t)$, and $A_{\rm p}(z,t)$ represent the mode amplitudes for the Stokes wave, Brillouin-active elastic wave, and pump wave, respectively; $\Omega_{\rm B}$ is the Brillouin frequency, $v_{\rm B}$ is the phonon group velocity, Γ is the phonon dissipation rate, $g_{\rm s,p}$ is the acousto-optic coupling rate, and $\eta(z,t)$ is the Langevin term responsible for keeping the phonon field in thermal equilibrium (with a spatio-temporal correlation function given by $\langle\eta(z',t')\eta^\dagger(z,t)\rangle = (n_{\rm th}+1)\Gamma\delta(z'-z)\delta(t'-t)$ [75]). Here, $n_{\rm th}$ is the thermal occupation of the Brillouin-active phonon field, given by the Bose distribution ($n_{\rm th}=[\exp(\hbar\Omega_{\rm b}/(k_{\rm b}T))-1]^{-1}$). For simplicity, we assume that the Stokes wave is small enough to neglect pump depletion. See Fig. 7.1A for a visual representation of these definitions.

Next, we transform to the rotating frame such that $A_{\rm s}(z,t) = \bar{A}_{\rm s}(z,t)\exp[-i\omega_{\rm s}t]$, $A_{\rm p}(z,t) = \bar{A}_{\rm p}\exp[-i\omega_{\rm p}t]$, and $B(z,t) = \bar{B}(z,t)\exp[-i\Omega t]$, with frequencies defined as $\omega_{\rm p}\equiv\omega_{\rm s}+\Omega$. Under this transformation, the equations of motion become

$$\begin{aligned}\dot{\bar{A}}_{\rm s}(z,t)+i(\omega_0-\omega_{\rm s})\bar{A}_{\rm s}(z,t)+v_{\rm g}\frac{\partial\bar{A}_{\rm s}(z,t)}{\partial z}+\frac{\alpha v_{\rm g}}{2}\bar{A}_{\rm s}(z,t)&=-ig^*_{\rm s,p}\bar{A}_{\rm p}\bar{B}^\dagger(z,t)+N_{\rm i}(z,t)\\ \dot{\bar{B}}(z,t)+i(\Omega_{\rm B}-\Omega)\bar{B}(z,t)+\frac{\Gamma}{2}\bar{B}(z,t)-v_{\rm B}\frac{\partial\bar{B}(z,t)}{\partial z}&=-ig^*_{\rm s,p}\bar{A}_{\rm p}\bar{A}^\dagger_{\rm s}(z,t)+\eta(z,t).\end{aligned} \tag{7.13}$$

Note that the Langevin terms have also been rotated without explicit change of notation. Next, we take a Fourier transform in time, yielding

$$\begin{aligned}i(\omega_0-\omega_{\rm s}-\omega)\bar{A}_{\rm s}[z,\omega]+\frac{\alpha v_{\rm g}}{2}\bar{A}_{\rm s}[z,\omega]+v_{\rm g}\frac{\partial\bar{A}_{\rm s}[z,\omega]}{\partial z}&=-ig^*_{\rm s,p}\bar{A}_{\rm p}\bar{B}^\dagger[z,\omega]+N_{\rm i}[z,\omega]\\ i(\Omega_{\rm B}-\Omega-\omega)\bar{B}[z,\omega]+\frac{\Gamma}{2}\bar{B}[z,\omega]-v_{\rm B}\frac{\partial\bar{B}[z,\omega]}{\partial z}&=-ig^*_{\rm s,p}\bar{A}_{\rm p}\bar{A}^\dagger_{\rm s}[z,\omega]+\eta[z,\omega]\end{aligned} \tag{7.14}$$

We will see that this representation is particularly convenient when analyzing the spectral character of the noise.

In practically all Brillouin systems, the phonon field is spatially heavily damped relative to the optical fields, i.e., the spatial dynamics of the phonon field adiabatically follow the optical fields. Thus, to a good approximation, the elastic wave is sourced by the local forcing function produced by the interference between pump and Stokes waves [12,95] (i.e., $\partial\bar{B}[z,\omega]/\partial z \approx 0$),[3] as well as the Langevin term representing the thermal bath. This approximation yields

$$\begin{aligned} i(\omega_0-\omega_s-\omega)\bar{A}_s[z,\omega]+\frac{\alpha v_g}{2}\bar{A}_s[z,\omega]+v_g\frac{\partial\bar{A}_s[z,\omega]}{\partial z} &= -ig^*_{s,p}\bar{A}_p\bar{B}^\dagger[z,\omega]+N_i[z,\omega] \\ i(\Omega_B-\Omega-\omega)\bar{B}[z,\omega]+\frac{\Gamma}{2}\bar{B}[z,\omega] &= -ig^*_{s,p}\bar{A}_p\bar{A}_s^\dagger[z,\omega]+\eta[z,\omega]. \end{aligned} \tag{7.15}$$

Now, solving for the Stokes field we find

$$\begin{aligned} \frac{\partial\bar{A}_s[z,\omega]}{\partial z} = \frac{1}{v_g}\Bigg[&-i(\omega_0-\omega_s-\omega)-\frac{v_g\alpha}{2}+\frac{v_g G_B P\Gamma\chi_B^*}{4}\Bigg]\bar{A}_s[z,\omega] \\ &-\frac{ig^*_{s,p}\bar{A}_p\chi_B^*\eta^\dagger[z,\omega]}{v_g}+\frac{N_i[z,\omega]}{v_g}, \end{aligned} \tag{7.16}$$

where $G_B = 4|g_{s,p}|^2/(\hbar\omega_p\Gamma v_g^2) = 4|g_{s,p}|^2|\bar{A}_p|^2/(P\Gamma v_g)$,[4] and P is the power of the pump wave, and $\chi_B \equiv (i(\Omega_B-\Omega-\omega)+\Gamma/2)^{-1}$.

We solve Eq. 7.16 with the integrating factor method, yielding

$$\begin{aligned} \bar{A}_s[z,\omega] = \int_0^z dz'\Bigg[&-\frac{ig^*\bar{A}_p\chi_B^*\eta^\dagger[z',\omega]}{v_g}+\frac{N_i[z',\omega]}{v_g}\Bigg]e^{-M(z-z')} \\ &+\left(\bar{A}_s[0,\omega]+\bar{A}_s^N[0,\omega]\right)e^{-Mz}, \end{aligned} \tag{7.17}$$

where $A_s^N[0,\omega]$ represents the input noise field associated with optical vacuum fluctuations (not to be confused with the distributed noise from vacuum fluctuations $N_i[z,\omega]$ associated with loss along the length of the waveguide), and we have defined

3. As noted in Chapter 1, setting $\partial\bar{B}[z,\omega]/\partial z = 0$ is equivalent to the formal adiabatic elimination in space.

4. We can reparameterize the Brillouin gain by noting that $P = \hbar\omega_p v_g|\bar{A}_p|^2$.

$$M \equiv \frac{1}{v_g}\left[i(\omega_0 - \omega_s - \omega) + \frac{v_g\alpha}{2} - \frac{v_g G_B P\Gamma\chi_B^*}{4}\right]. \tag{7.18}$$

Thus, the number spectral density per unit length ($\mathscr{A}_s[z,\omega] = \lim_{T\to\infty}(1/T)|\bar{A}_s[z,\omega]|^2$ [171]) of the Stokes wave at position z is given by

$$\begin{aligned}
\mathscr{A}_s[z,\omega] &= \underbrace{\mathscr{A}_s[0,\omega]e^{-2\Re[M]z}}_{\text{Amplified input signal}} \\
&\quad + \underbrace{\mathscr{A}_s^N[0,\omega]e^{-2\Re[M]z} + \lim_{T\to\infty}\frac{1}{T}\int_0^z dz_1\int_0^z dz_2 \frac{\langle N_i^\dagger[z_1,\omega]N_i[z_2,\omega]\rangle}{v_g^2}e^{-M^*(z-z_1)-M(z-z_2)}}_{\text{Optical vacuum fluctuations}} \\
&\quad + \underbrace{\lim_{T\to\infty}\frac{1}{T}\int_0^z dz_1\int_0^z dz_2 \frac{G_B P\Gamma|\chi_B|^2}{4v_g^2}\langle\eta^\dagger[z_1,\omega]\eta[z_2,\omega]\rangle e^{-M^*(z-z_1)-M(z-z_2)}}_{\text{Thermal mechanical noise}} \\
&= \underbrace{\mathscr{A}_s[0,\omega]e^{-2\Re[M]z}}_{\text{Amplified input signal}} + \underbrace{\frac{\alpha}{2v_g\Re[M]}\left[1-e^{-2\Re[M]z}\right] + \frac{1}{v_g}e^{-2\Re[M]z}}_{\text{Optical vacuum fluctuations}} \\
&\quad + \underbrace{\frac{|\chi_B|^2 G_B P\Gamma^2(n_{th}+1)}{8v_g\Re[M]}\left[1-e^{-2\Re[M]z}\right]}_{\text{Thermal mechanical noise}}
\end{aligned} \tag{7.19}$$

where $\Re[M]$ represents the real part of M. Above we have labeled the terms according to their physical significance. These include the amplified input signal, the optical vacuum fluctuations, and the thermal-mechanical noise.

From Eq. 7.19, we can calculate the amplification and effective optical noise figure of the device. The net amplification is given by the first term in Eq. 7.19 (i.e., $|A_s[z,\omega]|^2/|A_s[0,\omega]|^2 = e^{-2\Re[M]z}$, where $-2\Re[M]$ is the spatial rate of amplification), while the noise factor (F) is defined as F = $\mathrm{SNR}_1/\mathrm{SNR}_2$, where SNR_1 and SNR_2 are the input and output signal to noise ratios, respectively.

For simplicity, we consider an input signal spectrum of the form $\mathscr{A}_s[0,\omega] = |A_s^{in}|^2\delta(\omega)$. Thus, the input signal to noise is

$$\begin{aligned} \mathrm{SNR}_1 &= \frac{\int_{-\Delta\omega}^{\Delta\omega} d\omega' |A_\mathrm{s}^\mathrm{in}|^2 \delta(\omega)}{\int_{-\Delta\omega}^{\Delta\omega} d\omega' \frac{1}{v_\mathrm{g}}} \\ &= \frac{|A_\mathrm{s}^\mathrm{in}|^2 v_\mathrm{g}}{2\Delta\omega}, \end{aligned} \tag{7.20}$$

while the output signal-to-noise ratio (SNR_2) is

$$\mathrm{SNR}_2 = \frac{|A_\mathrm{s}^\mathrm{in}|^2 e^{-2\Re[M]z}}{2\Delta\omega \left[\frac{\alpha}{2v_\mathrm{g}\Re[M]} \left[1 - e^{-2\Re[M]z}\right] + \frac{1}{v_\mathrm{g}} e^{-2\Re[M]z} + \frac{|\chi_\mathrm{B}|^2 G_\mathrm{B} P \Gamma^2 (n_\mathrm{th}+1)}{8 v_\mathrm{g} \Re[M]} \left[1 - e^{-2\Re[M]z}\right] \right]} \tag{7.21}$$

Here, n_th is the occupation of the Brillouin-active phonon mode and $\Delta\omega$ is related to the bandwidth B by $\Delta\omega = \pi B$. We note that here we are assuming that $\Delta\omega$ is small relative to the Brillouin gain bandwidth. Thus, the optical noise factor of a non-resonant Brillouin amplifier relative to the zero-point background is

$$\mathrm{F} \equiv \frac{\mathrm{SNR}_1}{\mathrm{SNR}_2} = 1 + \frac{\left(|\chi_\mathrm{B}|^2 G_\mathrm{B} P \Gamma^2 (n_\mathrm{th}+1) + 4\alpha\right)\left[1 - e^{-2\Re[M]z}\right]}{8\Re[M] e^{-2\Re[M]z}}. \tag{7.22}$$

Equation 7.22 is the central result of this section and is used to generate Fig. 7.1C. We note that the noise figure is independent of the bandwidth as long as $\Delta\omega \ll \Gamma$. In the limit of large Brillouin amplification, the noise factor becomes

$$\mathrm{F} \approx n_\mathrm{th} + 2, \tag{7.23}$$

which agrees qualitatively with prior calculations [56,172]. Thus, relative to the zero-point background, the upper limit of the noise figure of an optical Brillouin amplifier depends only on the thermal occupation of the phonon field.

By contrast, in the limit when the Brillouin gain G_B or pump power is negligible, the noise factor converges to a value that is consistent with the linear loss of the system, yielding

$$\mathrm{F} = e^{\alpha z}. \tag{7.24}$$

Since the background noise associated with optical vacuum fluctuations must remain un-

changed, we see that a reduction in the signal power due to loss must yield a corresponding increase in the noise factor.

7.3.2 Noise figure of a resonant Brillouin amplifier

In this section, we analyze the noise figure of a resonantly enhanced Brillouin amplifier system, which, as we saw in Chapter 4, can be used to significantly enhance the available Brillouin gain in a compact geometry.

Optical vacuum fluctuations

We first consider the noise properties of a passive resonant system that is interfaced with an input (coupler 1) and output coupler (coupler 2). In the rotating frame, the equation of motion for the optical mode of interest and the output field are given by

$$\begin{aligned} \dot{\bar{a}}(t) &= i(\omega-\omega_n)\bar{a}(t) - \frac{\gamma_{\text{tot}}}{2}\bar{a}(t) + \sqrt{\gamma_1}S_1^{\text{N}}(t) + \sqrt{\gamma_2}S_2^{\text{N}}(t) + \sqrt{\gamma_{\text{i}}}S_{\text{i}}^{\text{N}}(t) \\ S_2^{\text{N,out}}(t) &= \sqrt{\gamma_2}\bar{a}(t) - S_2^{\text{N}}(t) \end{aligned} \tag{7.25}$$

where ω_n is the frequency nth overtone of the resonator, the total optical loss rate γ_{tot} is given by $\gamma_{\text{tot}} = \gamma_1 + \gamma_2 + \gamma_{\text{i}}$; γ_1, γ_2, and γ_{i} are the loss rates resulting from the couplers and internal losses of the ring, respectively, while $S_1^{\text{N}}(t), S_2^{\text{N}}(t)$, and $S_{\text{i}}^{\text{N}}(t)$ are the accompanying noise sources that are consistent with the fluctuation-dissipation theorem. See Fig. 7.2 for a visual representation of this model. As in Chapters 3, 4 and 6, $\bar{a}(t)$ has units of $[\sqrt{\text{number}}]$. We assume that the noise sources are uncorrelated with each other and delta correlated in time, such that

$$\begin{aligned} \langle S_1^{\text{N}}(t')S_1^{\text{N}\dagger}(t)\rangle &= Q_1\delta(t-t') \\ \langle S_2^{\text{N}}(t')S_2^{\text{N}\dagger}(t)\rangle &= Q_2\delta(t-t') \\ \langle S_{\text{i}}^{\text{N}}(t')S_{\text{i}}^{\text{N}\dagger}(t)\rangle &= Q_{\text{i}}\delta(t-t') \\ \langle S_{\text{i}}^{\text{N}}(t')S_1^{\text{N}\dagger}(t)\rangle = \langle S_{\text{i}}^{\text{N}}(t')S_2^{\text{N}\dagger}(t)\rangle &= \langle S_1^{\text{N}}(t')S_2^{\text{N}\dagger}(t)\rangle = 0. \end{aligned} \tag{7.26}$$

where the Q parameters will be derived below. Using the integrating factor method, we solve for the optical mode $\bar{a}(t)$, yielding

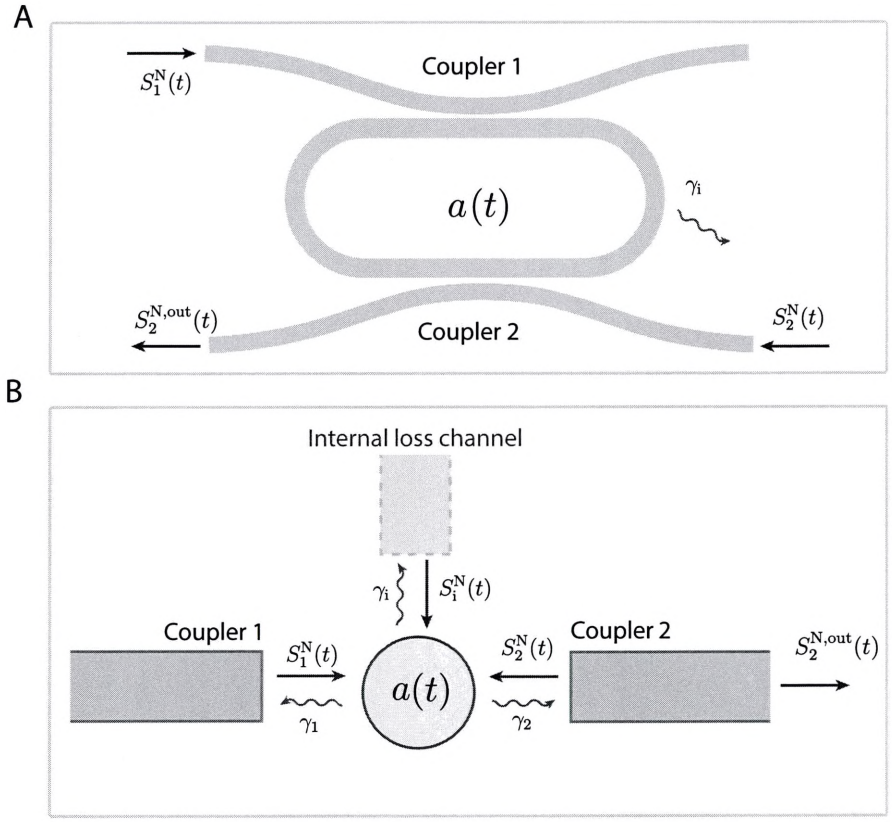

Figure 7.2: (A) Detailed balance within an optical resonator. (B) Coupler 1, coupler 2, and the internal losses of the resonator each contribute vacuum noise in a way that is consistent with the fluctuation-dissipation theorem.

$$\bar{a}(t) = \int_{-\infty}^{t} dt' \left[\sqrt{\gamma_1} S_1^{\mathrm{N}}(t') + \sqrt{\gamma_2} S_2^{\mathrm{N}}(t') + \sqrt{\gamma_{\mathrm{i}}} S_{\mathrm{i}}^{\mathrm{N}}(t')\right] e^{-(t-t')/\chi} \tag{7.27}$$

where we have define the susceptibility χ as $\chi \equiv (-i(\omega - \omega_n) + \frac{\gamma_{\mathrm{tot}}}{2})^{-1}$

With this framework, we can now establish the properties of the noise sources such that they represent the optical vacuum fluctuations. We know that for an oscillator in the ground state, $\langle \bar{a}(t)\bar{a}^{\dagger}(t)\rangle = 1$. Thus,

$$\begin{aligned}
1 = \langle \bar{a}(t)\bar{a}^{\dagger}(t)\rangle &= \langle \int_{-\infty}^{t} dt_1 \left[\sqrt{\gamma_1} S_1^{\mathrm{N}}(t_1) + \sqrt{\gamma_2} S_2^{\mathrm{N}}(t_1) + \sqrt{\gamma_{\mathrm{i}}} S_{\mathrm{i}}^{\mathrm{N}}(t_1)\right] e^{-(t-t_1)/\chi} \\
&\times \int_{-\infty}^{t} dt_2 \left[\sqrt{\gamma_1} S_1^{\mathrm{N}\dagger}(t_2) + \sqrt{\gamma_2} S_2^{\mathrm{N}\dagger}(t_2) + \sqrt{\gamma_{\mathrm{i}}} S_{\mathrm{i}}^{\mathrm{N}\dagger}(t_2)\right] e^{-(t-t_2)/\chi^*} \rangle \\
&= \int_{-\infty}^{t} dt_1 \int_{-\infty}^{t} dt_2 \left[\gamma_1 Q_1 \delta(t_1 - t_2) + \gamma_2 Q_2 \delta(t_1 - t_2) + \gamma_{\mathrm{i}} Q_{\mathrm{i}} \delta(t_1 - t_2)\right] \\
&\times e^{-2t\Re(1/\chi) + (1/\chi^*)t_1 + (1/\chi)t_2} \\
&= \frac{1}{2\Re(1/\chi)} \left[\gamma_1 Q_1 + \gamma_2 Q_2 + \gamma_{\mathrm{i}} Q_{\mathrm{i}}\right]
\end{aligned} \tag{7.28}$$

From Eq. 7.28, we find $Q_1 = Q_2 = Q_{\mathrm{i}} = 1$.[5] With recourse to the Wiener-Khinchin theorem, we can calculate the power spectral density of the vacuum fluctuations in a waveguide, which yields

$$\begin{aligned}
\mathfrak{S}_1^{\mathrm{N}}[\omega] = \lim_{T\to\infty} \frac{1}{T} |S_1^{\mathrm{N}}[\omega]|^2 &= \int_{-\infty}^{\infty} d\tau \langle S_1^{\mathrm{N}}(t+\tau) S_1^{\mathrm{N}\dagger}(t)\rangle e^{i\omega\tau} \\
&= \int_{-\infty}^{\infty} d\tau \delta(\tau) e^{i\omega\tau} \\
&= 1,
\end{aligned} \tag{7.29}$$

where the same calculation holds for $|S_2^{\mathrm{N}}[\omega]|^2$ and $|S_{\mathrm{i}}^{\mathrm{N}}[\omega]|^2$. We note that we have used anti-normal ordering to be consistent with the definition for the optical noise figure in Eq. 7.6. Equipped with this knowledge, we can now solve for the output noise exiting coupler 2 ($S_2^{\mathrm{N,out}}(t)$), defined by $S_2^{\mathrm{N,out}}(t) = \sqrt{\gamma_2}\bar{a}(t) - S_2^{\mathrm{N}}(t)$ [132].

5. One can show that this is true since coupler 1, coupler 2, and the internal losses are independent degrees of freedom. For example, we could take $\gamma_2 = \gamma_{\mathrm{i}} = 0$, revealing that $Q_1 = 1$. This same logic applies to coupler 2 and the internal losses as well.

For this, we transform Eq. 7.25 to the frequency domain, yielding

$$-i\omega a[\omega] = -i\omega_n a[\omega] - \frac{\gamma_{\text{tot}}}{2}a[\omega] + \sqrt{\gamma_1}S_1^{\text{N}}[\omega] + \sqrt{\gamma_2}S_2^{\text{N}}[\omega] + \sqrt{\gamma_i}S_i^{\text{N}}[\omega]. \tag{7.30}$$

Since $S_2^{\text{N,out}}[\omega] = \sqrt{\gamma_2}a[\omega] - S_2^{\text{N}}[\omega]$, the power spectral density of the noise exiting port 2 is given by

$$\begin{aligned}\mathfrak{S}_2^{\text{N,out}}[\omega] = \lim_{T\to\infty}\frac{1}{T}|S_2^{\text{N,out}}[\omega]|^2 &= \lim_{T\to\infty}\frac{1}{T}\Big[\gamma_2|a^\dagger[\omega]|^2 - \sqrt{\gamma_2}a^\dagger[\omega]S_2^{\text{N}}[\omega] \\ &\quad - \sqrt{\gamma_2}S_2^{\text{N}\dagger}[\omega]a[\omega] + |S_2^{\text{N}}[\omega]|^2\Big] \\ &= |\chi[\omega]|^2\gamma_2\gamma_{\text{tot}} - 2\gamma_2\Re(\chi[\omega]) + 1 \\ &= 1,\end{aligned} \tag{7.31}$$

where we have again defined $\chi[\omega] \equiv (-i(\omega - \omega_n) + \gamma_{\text{tot}}/2)^{-1}$. Thus, the power spectral density of the noise exiting the output port (port 2) is equal to that entering the input port (port 1).

The moment we add gain to the system, however, this equality no longer holds. For instance, for a gain mechanism adding no additional noise to the system (i.e., $\chi_{\text{G}}[\omega] = (i(\omega_n - \omega) + \gamma_{\text{tot}}/2 - G/2)^{-1}$), the output power spectral density becomes

$$\begin{aligned}\mathfrak{S}_2^{\text{N,out}}[\omega] = \lim_{T\to\infty}\frac{1}{T}|S_2^{\text{N,out}}[\omega]|^2 &= \lim_{T\to\infty}\frac{1}{T}\Big[\gamma_2|a^\dagger[\omega]|^2 - \sqrt{\gamma_2}a^\dagger[\omega]S_2^{\text{N}}[\omega] \\ &\quad - \sqrt{\gamma_2}S_2^{\text{N}\dagger}[\omega]a[\omega] + |S_2^{\text{N}}[\omega]|^2\Big] \\ &= |\chi_{\text{G}}[\omega]|^2\gamma_2\gamma_{\text{tot}} - 2\gamma_2\Re(\chi_{\text{G}}[\omega]) + 1 \\ &= \frac{\gamma_2 G}{(\omega_n - \omega)^2 + (G/2 - \gamma_{\text{tot}}/2)^2} + 1.\end{aligned} \tag{7.32}$$

Thus, the noise spectrum is no longer white, but frequency-dependent. This result would be consistent with a perfect amplifier (e.g., a gain medium with perfect population inversion that contributes no additional loss or noise to the system). However, we will see that our

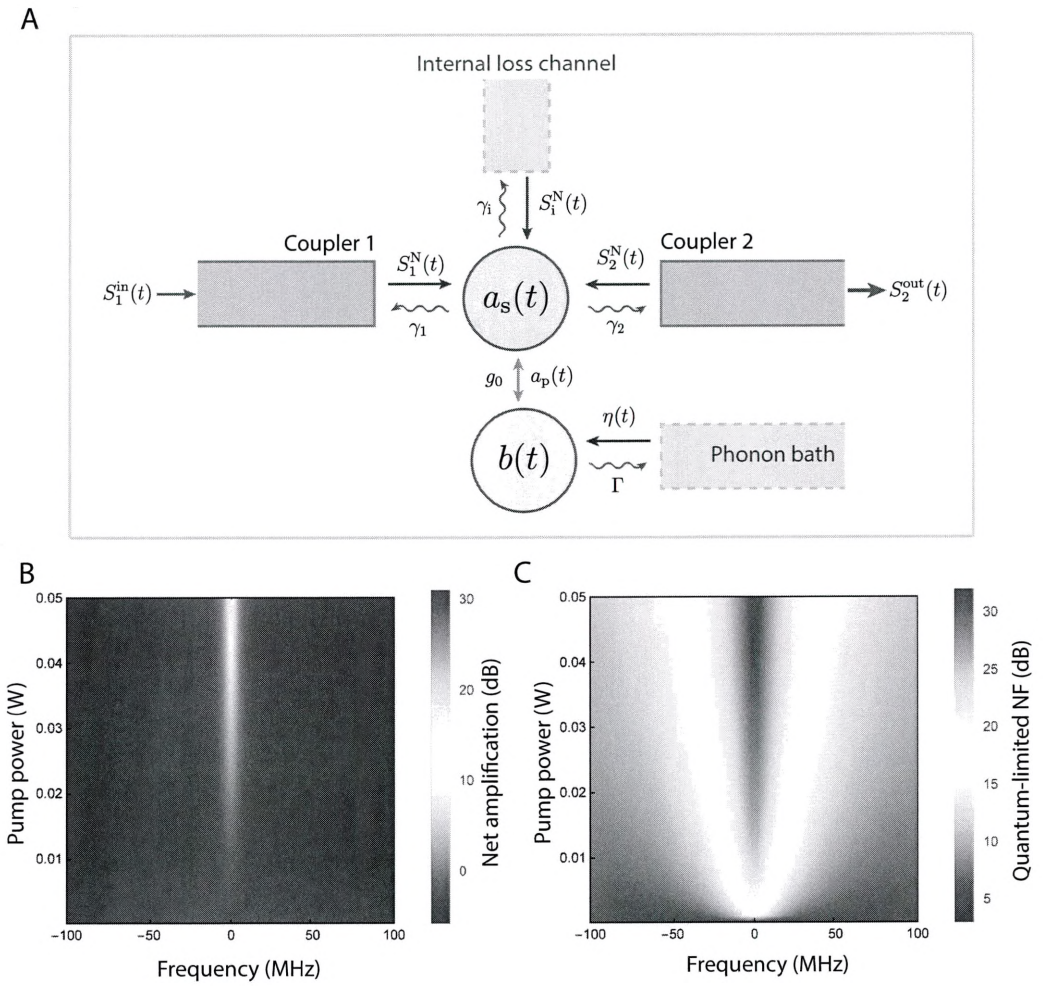

Figure 7.3: Resonant Brillouin amplifier. Panel (A) diagrams the Brillouin amplification and noise processes. (B) Net amplification as a function of pump power and detuning from the Brillouin resonance (with $G_B = 400$ W^{-1}m^{-1}, $L = 0.015$ m, $\gamma_1 = \gamma_2 = 2\pi \times 90$ MHz, $\alpha = 6$ m^{-1}, $v_g = 7 \times 10^7$ ms^{-1}, $\Omega = 2\pi \times 10$ GHz, and $\Gamma = 2\pi \times 15$ MHz). (C) optical noise figure (relative to the zero-point optical background), given by Eq. 7.43 with the same parameters used in panel (B)).

Brillouin amplifier system introduces additional noise terms that arise from interaction with thermally populated phonon fields.

Resonant Brillouin amplification

Building on the treatment of a single-mode optical resonator, we now analyze the noise figure of a resonantly enhanced Brillouin amplifier by introducing Brillouin gain to the system. A complementary derivation is contained within the supplemental information of Ref. [97]. Under the stiff pump approximation, the mean-field equations of motion for the Stokes ($a_{\mathrm{s}}(t)$), phonon ($b(t)$) fields can be written as [97]

$$\begin{aligned}\dot{a}_{\mathrm{s}}(t) &= -i\omega_n a_{\mathrm{s}}(t) - \frac{\gamma_{\mathrm{tot}}}{2}a_{\mathrm{s}}(t) - ig^* a_{\mathrm{p}}(t)b^\dagger(t) + \sqrt{\gamma_1}S_1^{\mathrm{in}}(t) \\ &\quad + \sqrt{\gamma_1}S_1^{\mathrm{N}}(t) + \sqrt{\gamma_2}S_2^{\mathrm{N}}(t) + \sqrt{\gamma_{\mathrm{i}}}S_{\mathrm{i}}^{\mathrm{N}}(t) \\ \dot{b}(t) &= -i\Omega_{\mathrm{B}}b(t) - \frac{\Gamma}{2}b(t) - ig^* a_{\mathrm{p}}(t)a_{\mathrm{s}}^\dagger(t) + \eta(t).\end{aligned} \tag{7.33}$$

Here, $S_1^{\mathrm{in}}(t)$ is the input signal, $\eta(t)$ is the Langevin term representing the thermal and quantum fluctuations for the phonon field (with a two-time correlation function given by $\langle\eta(t')\eta^\dagger(t)\rangle = \Gamma(n_{\mathrm{th}}+1)\delta(t-t')$), and g is the mean-field elasto-optic coupling. See Fig. 7.3A for a visual representation of these definitions. We next move these equations of motion to the rotating frame, yielding

$$\begin{aligned}\dot{\bar{a}}_{\mathrm{s}}(t) &= i(\omega_{\mathrm{s}} - \omega_n)\bar{a}_{\mathrm{s}}(t) - \frac{\gamma_{\mathrm{tot}}}{2}\bar{a}_{\mathrm{s}}(t) - ig^*\bar{a}_{\mathrm{p}}\bar{b}^\dagger(t) + \sqrt{\gamma_1}S_1^{\mathrm{in}}(t) \\ &\quad + \sqrt{\gamma_1}S_1^{\mathrm{N}}(t) + \sqrt{\gamma_2}S_2^{\mathrm{N}}(t) + \sqrt{\gamma_{\mathrm{i}}}S_{\mathrm{i}}^{\mathrm{N}}(t) \\ \dot{\bar{b}}(t) &= i(\Omega - \Omega_{\mathrm{B}})\bar{b}(t) - \frac{\Gamma}{2}\bar{b}(t) - ig^*\bar{a}_{\mathrm{p}}\bar{a}_{\mathrm{s}}^\dagger(t) + \eta(t).\end{aligned} \tag{7.34}$$

Here, we have rotated the fields such that $a_{\mathrm{s}}(t) = \bar{a}_{\mathrm{s}}(t)e^{-i\omega_{\mathrm{s}}t}$, $b(t) = \bar{b}(t)e^{-i\Omega t}$, $a_{\mathrm{p}}(t) = \bar{a}_{\mathrm{p}}e^{-i\omega_{\mathrm{p}}t}$, and $\omega_{\mathrm{p}} = \omega_{\mathrm{s}} + \Omega$. We have also rotated the signal and noise fields without an explicit change of notation.

To proceed, we transform these equations into the frequency domain via a Fourier transform in time, yielding

$$
\begin{aligned}
-i(\omega_{\mathrm{s}}-\omega_n+\omega)\bar{a}_{\mathrm{s}}[\omega] &= -\frac{\gamma_{\mathrm{tot}}}{2}\bar{a}_{\mathrm{s}}[\omega]-ig^{*}\bar{a}_{\mathrm{p}}\bar{b}^{\dagger}[\omega]+\sqrt{\gamma_1}S_1^{\mathrm{in}}[\omega] \\
&\quad +\sqrt{\gamma_1}S_1^{\mathrm{N}}[\omega]+\sqrt{\gamma_2}S_2^{\mathrm{N}}[\omega]+\sqrt{\gamma_{\mathrm{i}}}S_{\mathrm{i}}^{\mathrm{N}}[\omega] \\
-i(\Omega-\Omega_{\mathrm{B}}+\omega)\bar{b}[\omega] &= -\frac{\Gamma}{2}\bar{b}[\omega]-ig^{*}\bar{a}_{\mathrm{p}}\bar{a}_{\mathrm{s}}^{\dagger}[\omega]+\eta[\omega].
\end{aligned}
\tag{7.35}
$$

Solving for the Stokes field, we find

$$
\begin{aligned}
\bar{a}_{\mathrm{s}}[\omega] = \frac{1}{-i(\omega_{\mathrm{s}}+\omega-\omega_n)+\frac{\gamma_{\mathrm{tot}}}{2}-\frac{|g|^2|\bar{a}_{\mathrm{p}}|^2}{i(\Omega+\omega-\Omega_{\mathrm{B}})+\frac{\Gamma}{2}}}\Bigg[&\frac{-ig^{*}\bar{a}_{\mathrm{p}}\eta^{\dagger}[\omega]}{i(\Omega+\omega-\Omega_{\mathrm{B}})+\frac{\Gamma}{2}} \\
&+\sqrt{\gamma_1}S_1^{\mathrm{in}}[\omega]+\sqrt{\gamma_1}S_1^{\mathrm{N}}[\omega]+\sqrt{\gamma_2}S_2^{\mathrm{N}}[\omega]+\sqrt{\gamma_{\mathrm{i}}}S_{\mathrm{i}}^{\mathrm{N}}[\omega]\Bigg].
\end{aligned}
\tag{7.36}
$$

Using the constitutive identity $S_2^{\mathrm{out}}(t) = -S_2^{\mathrm{in}}(t)+\sqrt{\gamma_2}a_{\mathrm{s}}(t)$, the output signal at port 2 becomes

$$
\begin{aligned}
S_2^{\mathrm{out}}[\omega] = T[\omega]\Bigg[&\frac{-ig^{*}\bar{a}_{\mathrm{p}}\eta^{\dagger}[\omega]}{i(\Omega+\omega-\Omega_{\mathrm{B}})+\frac{\Gamma}{2}} \\
&+\sqrt{\gamma_1}S_1^{\mathrm{in}}[\omega]+\sqrt{\gamma_1}S_1^{\mathrm{N}}[\omega]+\sqrt{\gamma_2}S_2^{\mathrm{N}}[\omega]+\sqrt{\gamma_{\mathrm{i}}}S_{\mathrm{i}}^{\mathrm{N}}[\omega]\Bigg]-S_2^{\mathrm{N}}[\omega],
\end{aligned}
\tag{7.37}
$$

where the transfer function $T[\omega]$ is defined as

$$
T[\omega] \equiv \frac{\sqrt{\gamma_2}}{-i(\omega_{\mathrm{s}}+\omega-\omega_n)+\frac{\gamma_{\mathrm{tot}}}{2}-\frac{|g|^2|\bar{a}_{\mathrm{p}}|^2}{i(\Omega+\omega-\Omega_{\mathrm{B}})+\frac{\Gamma}{2}}}.
\tag{7.38}
$$

The output power spectral density ($\mathfrak{S}^{\mathrm{out}}[\omega] = \lim_{T\to\infty}(1/T)|S^{\mathrm{out}}[\omega]|^2$ [171]) becomes

$$
\begin{aligned}
\mathfrak{S}_2^{\mathrm{out}}[\omega] = |T[\omega]|^2\Bigg[&\underbrace{\gamma_1\mathfrak{S}_1^{\mathrm{in}}[\omega]}_{\text{Input Signal}}+\underbrace{\frac{G_{\mathrm{B}}Pv_{\mathrm{g}}\Gamma^2(n_{\mathrm{th}}+1)}{4((\omega+\omega_{\mathrm{p}}-\omega_{\mathrm{s}}-\Omega_{\mathrm{B}})^2+(\frac{\Gamma}{2})^2)}}_{\text{Thermal-mechanical Noise}} \\
&\underbrace{+\gamma_1\mathfrak{S}_1^{\mathrm{N}}[\omega]+\left|\sqrt{\gamma_2}-\frac{1}{T[\omega]}\right|^2\mathfrak{S}_2^{\mathrm{N}}[\omega]+\gamma_{\mathrm{i}}\mathfrak{S}_{\mathrm{i}}^{\mathrm{N}}[\omega]}_{\text{Optical Vacuum Fluctuations}}\Bigg].
\end{aligned}
\tag{7.39}
$$

where above we have labeled the terms according to their physical significance. These include the spectral density of the input signal, the thermal-mechanical noise, and the Brillouin-gain-modified optical vacuum fluctuations. Here, G_{B} is the Brillouin gain coeffi-

cient given by $G_{\mathrm{B}} = 4|g|^2|\bar{a}_{\mathrm{p}}|^2/(P\Gamma v_{\mathrm{g}})$.[6] From Eq. 7.39, we can calculate the amplification and noise figure of the resonantly enhanced Brillouin amplifier system. The net amplification is given by the first term ($|S_2^{\mathrm{out}}[\omega]|^2/|S_1^{\mathrm{in}}[\omega]|^2 = \gamma_1|T[\omega]|^2$), while the noise figure can be determined by examining the input and output noise sources.

The input signal-to-noise ratio (SNR_1) is given by the input signal strength relative to the zero-point background. For simplicity, we assume an input signal spectrum of the form $\mathfrak{S}_1^{\mathrm{in}}[\omega] = |S^{\mathrm{in}}|^2\delta(\omega)$. Thus, the input signal-to-noise ratio is

$$\begin{aligned}\mathrm{SNR}_1 &= \frac{\int_{-\Delta\omega}^{\Delta\omega} d\omega |S^{\mathrm{in}}|^2\delta(\omega)}{\int_{-\Delta\omega}^{\Delta\omega} d\omega \mathfrak{S}_1^{\mathrm{N}}[\omega]} \\ &\simeq \frac{|S^{\mathrm{in}}|^2}{2\Delta\omega}.\end{aligned} \tag{7.40}$$

The output signal to noise ratio is

$$\begin{aligned}\mathrm{SNR}_2 &= \frac{\int_{-\Delta\omega}^{\Delta\omega} d\omega \gamma_1 |S^{\mathrm{in}}|^2\delta(\omega)}{\int_{-\Delta\omega}^{\Delta\omega} d\omega N_{\mathrm{b}}[\omega] + \gamma_1\mathfrak{S}_1^{\mathrm{N}}[\omega] + |\sqrt{\gamma_2} - \frac{1}{T[\omega]}|^2\mathfrak{S}_2^{\mathrm{N}}[\omega] + \gamma_{\mathrm{i}}\mathfrak{S}_{\mathrm{i}}^{\mathrm{N}}[\omega]} \\ &\simeq \frac{\gamma_1|S^{\mathrm{in}}|^2}{2\Delta\omega\Big[N_{\mathrm{b}}[\omega] + \Big(\gamma_1 + |\sqrt{\gamma_2} - \frac{1}{T[\omega]}|^2 + \gamma_{\mathrm{i}}\Big)\Big]},\end{aligned} \tag{7.41}$$

where we have assume that $\Delta\omega$ is much smaller than the gain bandwidth and defined the spontaneous Brillouin scattering rate ($N_{\mathrm{b}}[\omega]$) as

$$N_{\mathrm{b}}[\omega] \equiv \frac{G_{\mathrm{B}}Pv_{\mathrm{g}}\Gamma^2(n_{\mathrm{th}}+1)}{4((\omega+\omega_{\mathrm{p}}-\omega_{\mathrm{s}}-\Omega_{\mathrm{B}})^2 + (\frac{\Gamma}{2})^2)}. \tag{7.42}$$

Thus, the noise factor for the resonantly enhanced Brillouin amplifier is

$$\mathrm{F} = \frac{\Big[N_{\mathrm{b}}[\omega] + \Big(\gamma_1 + \big|\sqrt{\gamma_2} - \frac{1}{T[\omega]}\big|^2 + \gamma_{\mathrm{i}}\Big)\Big]}{\gamma_1}. \tag{7.43}$$

This is the main result of this section. Comparing Fig. 7.1 with Fig. 7.3, we see that, for typical experimental parameters, the noise figure of the resonant Brillouin amplifier is consistent with that of a non-resonant Brillouin amplifier. This is notable given that the available amplification of the resonant Brillouin amplifier may exceed that of its non-

6. The Brillouin gain coefficient can also be expressed as $G_{\mathrm{B}} = 4|g|^2L/(\hbar\omega_{\mathrm{p}}\Gamma v_{\mathrm{g}}^2)$ since $P = \hbar\omega_{\mathrm{p}}|\bar{a}_{\mathrm{p}}|^2/L$.

resonant counterpart (see Fig. 7.1B and Fig. 7.3B).

In the limit of large pump powers and assuming a resonant configuration (i.e., $\omega_p - \omega_s = \Omega_B$ and evaluating at $\omega = 0$), the noise factor becomes dominated by spontaneous Brillouin scattering and simplifies to become

$$F \approx \frac{N_b[0]}{\gamma_1} + \frac{\gamma_{tot}}{\gamma_1} = \frac{G_B P v_g (n_{th} + 1)}{\gamma_1} + \frac{\gamma_{tot}}{\gamma_1}. \tag{7.44}$$

Thus, the noise figure is the ratio between the spontaneous Brillouin scattering rate (numerator) and the dissipation rate associated with the input coupler. In the special case of no internal losses and identical couplers (i.e., $\gamma_i = 0$ and $\gamma_1 = \gamma_2$), the noise factor becomes $F \approx n_{th} + 3$ as the system approaches the laser threshold (the optimal condition for large amplification). Under these conditions, the noise figure closely resembles that of a linear (non-resonant) Brillouin amplifier (see Eq. 7.23).

By contrast, in the limit of low pump powers and again assuming the resonant condition, the noise factor becomes

$$F \approx \frac{\left[\left(\gamma_1 + |\sqrt{\gamma_2} - \frac{1}{T[0]}|^2 + \gamma_i\right)\right]}{\gamma_1} = \frac{(\gamma_1 + \gamma_2 + \gamma_i)^2}{4\gamma_1\gamma_2}, \tag{7.45}$$

which is simply the loss produced by linear transmission through the resonant system.

7.3.3 Out-of-band noise figure

A unique property of Brillouin amplifiers is that they produce exceptionally low out-of-band noise. This is because the thermal-mechanical noise, which is the dominant noise source, is narrowly centered around the Brillouin resonance and drops off dramatically at large frequency detunings. As such, the Brillouin gain can be used to selectively amplify signals within desired narrow bandwidth while effectively suppressing out-of-band noise—which may prove advantageous in applications such as carrier recovery or channelization [136, 169, 170]. To characterize this property, we define an out-of-band noise factor as

$$F[\delta] \equiv \frac{SNR_1[\delta]}{SNR_2[\delta]} \equiv \frac{\frac{\text{Input Signal}}{\text{Input Noise at } \delta}}{\frac{\text{Output Signal}}{\text{Output Noise at } \delta}}, \tag{7.46}$$

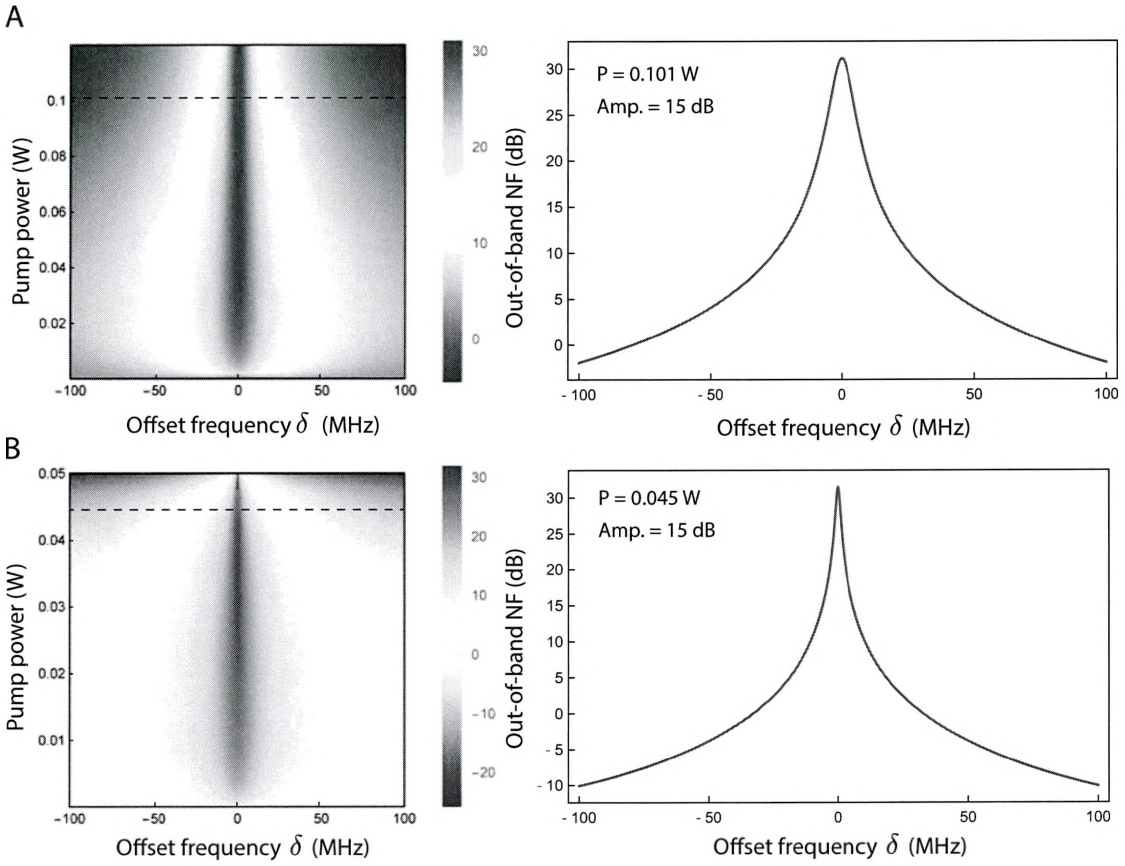

Figure 7.4: Out-of-band noise figures for (A) linear and (B) resonant Brillouin amplifiers. Dashed lines correspond to data that is shown in 1-D plots on right. Note that the out-of-band noise figure can be less than unity, indicating that the out-of-band signal-to-noise ratio can improve through the amplification process. Plots are generated from Eq. 7.47 and 7.48 with parameters given in captions of Fig. 7.1 and 7.3.

where δ is the detuning from the resonance condition (i.e., $\omega_p = \omega_s + \Omega_B$ and $\delta = \omega$, which is centered around ω_s). More specifically, the out-of-band noise factor is determined by considering a resonant signal wave relative to the noise separated in frequency by δ.

From Eq. 7.20 and Eq. 7.21, we calculate the out-of-band noise factor for a linear (non-resonant) Brillouin amplifier, yielding

$$\mathrm{F}_{\mathrm{Linear}}[\delta] = e^{-\left(G_B P - \frac{G_B P \Gamma^2 |\chi_B[\delta]|^2}{4}\right) z} + \frac{\left(|\chi_B[\delta]|^2 G_B P \Gamma^2 (n_{th}+1) + 4\alpha\right)\left[1 - e^{-\left(\alpha - \frac{G_B P \Gamma^2 |\chi_B[\delta]|^2}{4}\right) z}\right]}{\left(4\alpha - G_B P \Gamma^2 |\chi_B[\delta]|^2\right) e^{-(\alpha - G_B P) z}}, \tag{7.47}$$

where $\chi_B[\delta] \equiv (-i\delta + \Gamma/2)^{-1}$. Starting from Eq. 7.40 and 7.41, we use the same approach to calculate the out-of-band noise factor for a resonant amplifier, which yields

$$\mathrm{F}_{\mathrm{Resonant}}[\delta] = \frac{|T[\delta]|^2}{|T[0]|^2} \frac{\left[N_b[\omega] + \left(\gamma_1 + |\sqrt{\gamma_2} - \frac{1}{T[\delta]}|^2 + \gamma_i\right)\right]}{\gamma_1}. \tag{7.48}$$

where $T[\delta] = \sqrt{\gamma_2}/(-i\delta + \gamma_{tot}/2 - G_B P v_g \Gamma/(4(i(\delta - \Omega_B) + \Gamma/2)))$.

To illustrate the low out-of-band noise characteristics of both linear and resonant Brillouin amplifiers, we consider experimental parameters used in Figs. 7.1 and 7.3 and calculate the out-of-band noise figure (NF[δ]), as plotted in Fig. 7.4. For instance, with a frequency separation given by $\delta = 3\Gamma = 2\pi \times 45$ MHz and a pump power of $P = 0.101$ W, the linear Brillouin amplifier has an out-of-band noise figure of 5 dB while yielding more than 15 dB of net amplification. For this same level of amplification, the resonant Brillouin amplifier yields even better performance, with an out-of-band noise figure of -3 dB. This is possible because the signal and out-of-band noise do not experience the same gain. As such, the out-of-band signal-to-noise ratio can actually improve as the signal wave is amplified, which could be a useful functionality for carrier recovery [136], channelization [169, 170], or to suppress unwanted out-of-band spurs.

7.3.4 Performance as a narrow-band amplifier in RF-photonic link

The narrow gain bandwidths made possible through Brillouin amplification may lend themselves to filtering and amplification schemes within RF-photonic systems. An RF-photonic

link is a system that encodes RF or microwave signals on an optical carrier. The signals can then be processed in the optical domain and demodulated back to the RF domain. In what follows, we theoretically investigate the performance of the resonantly enhanced Brillouin amplifier within an RF-photonic link.

Simple RF photonic link

We first consider a simple RF photonic link that is comprised of a phase modulator, an optical local oscillator, and a high-speed photo-detector [173, 174]. This system, which could be useful to transmit RF-signals over long distances, will be used as a reference to understand the impact of the Brillouin amplifier on the noise performance of the link. As diagrammed in Fig. 7.5A, an input RF-field of power $P_{\mathrm{RF}}^{\mathrm{in}}$ and frequency Ω is used to synthesize an optical signal wave ($S_{\mathrm{M}}^{\mathrm{in}}(t)$) through phase modulation.

Following the phase modulator, the optical signal wave (first optical sideband) can be expressed as

$$S_{\mathrm{M}}^{\mathrm{in}}(t) = \sqrt{\frac{P_{\mathrm{c}}}{\hbar\omega_{\mathrm{c}}}} J_{-1}\left(\pi\sqrt{2R_{\mathrm{M}}P_{\mathrm{RF}}^{\mathrm{in}}}/V_{\pi}\right) e^{-i(\omega_{\mathrm{c}}-\Omega)t}, \tag{7.49}$$

where P_{c} are ω_{c} are the respective carrier-wave power and center frequency, R_{M} is the impedance of the phase modulator, and V_{π} is the half-wave voltage of the phase modulator. Here, $J_{-1}(x)$ is a Bessel function of the first kind of order -1 and argument x.

In the limit of small input RF powers, Eq. 7.49 can be written as

$$S_{\mathrm{M}}^{\mathrm{in}}(t) = \sqrt{\frac{P_{\mathrm{c}}}{\hbar\omega_{\mathrm{c}}}} \left[\pi\sqrt{2R_{\mathrm{M}}P_{\mathrm{RF}}^{\mathrm{in}}}/2V_{\pi}\right] e^{-i(\omega_{\mathrm{c}}-\Omega)t}. \tag{7.50}$$

Following synthesis, the signal ($S_{\mathrm{M}}^{\mathrm{in}}(t)$) and local oscillator ($S_{\mathrm{LO}}(t) = \sqrt{P_{\mathrm{LO}}/\hbar\omega_{\mathrm{c}}}e^{-i(\omega_{\mathrm{c}}+\Delta)t}$) waves are combined through a coupler of coupling μ^2 and measured using a photo-detector of impedance R_{D}. Upon detection, the RF output power spectral density $P_{\mathrm{RF}}^{\mathrm{out}}[\omega]$ can be calculated from the photo-current correlation function the using the Wiener-Khinchin theorem:

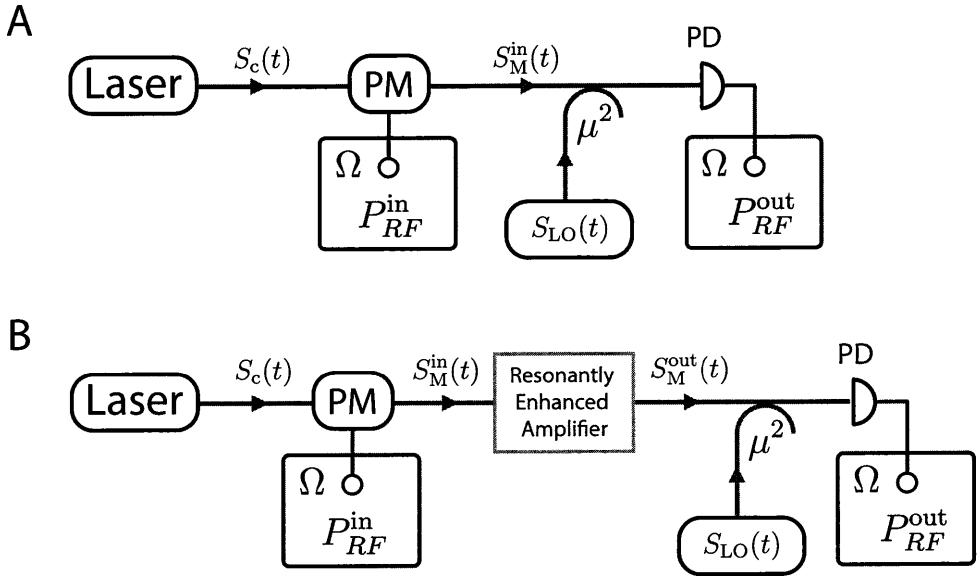

Figure 7.5: (A) Simple RF-photonic link composed of a phase-modulator (PM), optical local oscillator, and high-speed receiver (PD). (B) Modified RF-photonic link with resonantly enhanced Brillouin amplifier.

$$P_{\mathrm{RF}}^{\mathrm{out}}[\omega] = R_{\mathrm{D}} \int_{-\infty}^{\infty} d\tau \langle I(t+\tau) I(t) \rangle e^{i\omega\tau}. \tag{7.51}$$

In this simple RF-photonic link, the photo-current can be expressed as

$$I(t) = \left| \mu S^{\mathrm{in}}(t) + i\sqrt{1-\mu^2} S_{\mathrm{LO}}(t) \right|^2 (e\eta). \tag{7.52}$$

where e is the electron charge and η is the quantum efficiency of the photo-detector.

With this photo-current, the (single-sided) output RF power spectral density is given by

$$P_{\mathrm{RF}}^{\mathrm{out}}[\omega] = 8\pi P_{\mathrm{RF}}^{\mathrm{in}} R_{\mathrm{D}} R_{\mathrm{M}} \mu^2 (1-\mu^2) \frac{P_{\mathrm{LO}}}{\hbar\omega_{\mathrm{LO}}} \frac{P_{\mathrm{c}}}{\hbar\omega_{\mathrm{c}}} \left(\frac{\pi}{2V_\pi} \right)^2 (e\eta)^2 \delta(\omega - (\Omega + \Delta)). \tag{7.53}$$

Integrating over the signal of interest, the RF link gain (output RF signal relative to the input RF signal) is

$$G = 4 P_{\mathrm{RF}}^{\mathrm{in}} R_{\mathrm{D}} R_{\mathrm{M}} \mu^2 (1-\mu^2) \frac{P_{\mathrm{LO}}}{\hbar\omega_{\mathrm{LO}}} \frac{P_{\mathrm{c}}}{\hbar\omega_{\mathrm{c}}} \left(\frac{\pi}{2V_\pi} \right)^2 (e\eta)^2. \tag{7.54}$$

We next calculate the noise figure of this simple RF-photonic link, which is fundamentally limited by Johnson and shot noise. In this photonic link, the input noise over a bandwidth (B) is given by

$$N_{\mathrm{in}} = B[K_{\mathrm{B}}T], \tag{7.55}$$

while the output RF noise can be expressed as

$$N_{\mathrm{out}} = B[\underbrace{K_{\mathrm{B}}T + GK_{\mathrm{B}}T}_{\substack{\text{Thermal resistor} \\ \text{noise}}} + \underbrace{2\mu^2 \eta e^2 (P_{\mathrm{LO}}/\hbar\omega_{\mathrm{LO}}) R_{\mathrm{D}}}_{\text{Shot noise}}]. \tag{7.56}$$

Here we have assumed a small optical signal wave such that the shot noise is dominated by the optical local oscillator. With the input and output noise, the noise factor of the RF-photonic link becomes

$$\mathrm{F} = \frac{\mathrm{SNR}_1}{\mathrm{SNR}_2} = \frac{(G+1)K_{\mathrm{B}}T + 2\eta e^2 (P_{\mathrm{LO}}/\hbar\omega_{\mathrm{LO}}) R_{\mathrm{D}}}{GK_{\mathrm{B}}T}. \tag{7.57}$$

Resonant Brillouin amplifier within RF-photonic link

We now add the resonantly enhanced Brillouin amplifier to the RF-photonic link (see Fig. 7.5B) and calculate the new link gain and noise figure. In this case, the RF output power spectral density can be expressed as

$$\begin{aligned} P_{\mathrm{RF}}^{\mathrm{out}}[\omega] &= R_{\mathrm{D}} \int_{-\infty}^{\infty} d\tau \langle I(t+\tau) I(t) \rangle e^{i\omega\tau} \\ &= 2R_{\mathrm{D}}(e\eta)^2 \mu^2 (1-\mu^2) |S^{\mathrm{LO}}|^2 \mathrm{Re}\left[\int_{-\infty}^{\infty} d\tau \langle S_{\mathrm{M}}^{\mathrm{out}\dagger}(t+\tau) S_{\mathrm{M}}^{\mathrm{out}}(t) \rangle e^{i\omega\tau} \right] \\ &= 2R_{\mathrm{D}}(e\eta)^2 \mu^2 (1-\mu^2) \left(\frac{P_{\mathrm{LO}}}{\hbar\omega_{\mathrm{LO}}} \right) \mathrm{Re}\left[|S_{\mathrm{M}}^{\mathrm{out}}[\omega - \omega_{\mathrm{LO}}]|^2 \right]. \end{aligned} \tag{7.58}$$

Here, $S_{\mathrm{M}}^{\mathrm{out}}(t)$ is the modulated signal wave following the resonantly enhanced Brillouin amplifier. We note that $|S_{\mathrm{M}}^{\mathrm{out}}[\omega - \omega_{\mathrm{LO}}]|^2$ can be obtained from Eq. 7.38, such that the modified link gain ($\bar{G}$) becomes

$$\bar{G} = 4P_{\mathrm{RF}}^{\mathrm{in}} R_{\mathrm{D}} R_{\mathrm{M}} \mu^2 (1-\mu^2) \frac{P_{\mathrm{LO}}}{\hbar\omega_{\mathrm{LO}}} \frac{P_{\mathrm{c}}}{\hbar\omega_{\mathrm{c}}} \left(\frac{\pi}{2V_\pi} \right)^2 (e\eta)^2 \gamma_1 |T[0]|^2, \tag{7.59}$$

where $T[\omega]$ is given by Eq. 7.38 with the substitution $\omega_{\mathrm{s}} \rightarrow \omega_{\mathrm{c}} - \Omega$.

We now consider the relevant sources of noise within the system. In addition to the Johnson and shot noise already present in the RF-photonic link, the resonantly enhanced Brillouin amplifier produces additional noise through spontaneous Brillouin scattering. Over a small bandwidth B ($B \ll \Gamma/2\pi$), this produces a noise power

$$\begin{aligned} N_{\mathrm{RF}}^{\mathrm{th}} &= (1/\pi) \int_{-B/2}^{B/2} d\omega R_{\mathrm{D}} (e\eta)^2 (P_{\mathrm{LO}}/\hbar\omega_{\mathrm{LO}}) (\mu^2(1-\mu^2)) |T[\omega]|^2 N_{\mathrm{b}}[\omega] \\ &\simeq \frac{B}{\pi} R_{\mathrm{D}} (e\eta)^2 (P_{\mathrm{LO}}/\hbar\omega_{\mathrm{LO}}) (\mu^2(1-\mu^2)) |T[0]|^2 N_{\mathrm{b}}[0], \end{aligned} \tag{7.60}$$

where $N_{\mathrm{b}}[\omega]$ is given by Eq. 7.42 with the substitution $\omega_{\mathrm{s}} \rightarrow \omega_{\mathrm{c}} - \Omega$.

Here we have ignored optical vacuum fluctuations, which is a good approximation given the parameters of our system (i.e., $n_{\mathrm{th}} \gg 1$). From Eq. 7.60, we can calculate the effective noise factor for the RF-photonic link, which yields

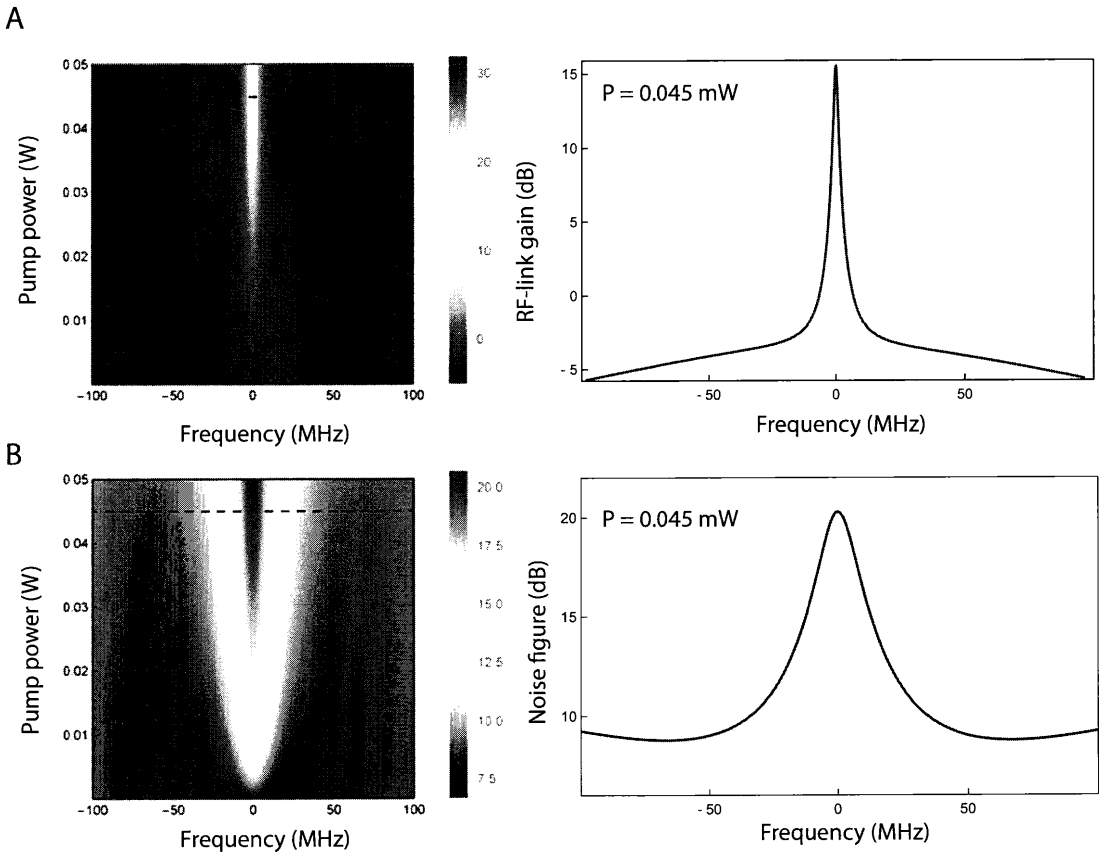

Figure 7.6: Calculated (A) RF link gain (Eq. 7.59) and (B) noise figure (Eq. 7.61) of an RF photonic link with a resonant Brillouin amplifier (depicted in Fig. 7.5B) with $R_{\mathrm{D}} = R_{\mathrm{M}} = 50$ Ω, $\mu^2 = 0.5$, $P_{\mathrm{c}} = 20$ mW, $V_{\pi} = 0.3$ V, and $P_{\mathrm{LO}} = 0.5$ mW, and $\eta = 0.95$. Dashed lines correspond to data that is shown in 1-D plots on right.

$$\mathrm{F} = \frac{\mathrm{SNR}_1}{\mathrm{SNR}_2} = \frac{(\bar{G}+1)K_\mathrm{B}T + 2\eta\mu^2 e^2 (P_\mathrm{LO}/\hbar\omega_\mathrm{LO})R_\mathrm{D}}{\bar{G}K_\mathrm{B}T} + \frac{\frac{1}{\pi}R_\mathrm{D}(e\eta)^2(P_\mathrm{LO}/\hbar\omega_\mathrm{LO})(\mu^2(1-\mu^2))|T[0]|^2 N_\mathrm{b}[0]}{\bar{G}K_\mathrm{B}T}. \tag{7.61}$$

The first term in Eq. 7.61 reveals the contribution of the RF-link to the noise factor while the second term results from the Brillouin noise.

RF-photonic link comparison

We plot the link gain (Eq. 7.59) and noise figure (Eq. 7.61) of the Brillouin RF-photonic link in Fig. 7.6. For these calculations, we assume $R_\mathrm{D} = R_\mathrm{M} = 50\ \Omega$, $\mu^2 = 0.5$, $P_\mathrm{c} = 25$ mW, $V_\pi = 0.3$ V, and $P_\mathrm{LO} = 0.5$ mW. With the addition of the Brillouin amplifier, the link gain is enhanced to 20 dB while the NF becomes 24.7 dB at a pump power that approaches the laser threshold. By comparison, the RF-link without the Brillouin amplifier with these same chosen parameters yields a link gain of 0 dB and a NF of 5 dB. We note that this level of performance requires a low V_π modulation scheme.

7.4 Conclusion and outlook

In this chapter, we have theoretically characterized the in- and out-of-band optical noise figure of linear and resonant Brillouin amplifiers. This analysis is based on a well-defined formulation of the optical noise figure, in which the additive sources of optomechanical noise are compared relative to the zero-point optical background. As such, it is important to note that our calculations represent the worst-case (i.e., upper bound) of the noise figure. Most practical input signals will be limited by other sources of noise, such as relative intensity noise (RIN), amplified spontaneous emission (ASE) noise, or relaxation oscillations. In particular, in the case of the RF-photonic link, we saw that the relevant background noise is resistor or Johnson noise, which, as in the case of the optomechanical Brillouin noise, is thermal in nature. Thus, as we observed in Section 7.3.4, the noise figure supported by Brillouin amplifiers within RF-photonic systems can be better than those in all-optical systems.

A compelling feature of Brillouin amplifiers is that they produce exceptionally low out-of-band noise. This useful property is captured by our definition of the out-of-band noise figure, which compares the input and output signal to noise ratios. Our analysis reveals that, in the limit of large Brillouin gains, the out-of-band noise can actually be negative. This means that the out-of-band SNR actually improves as the signal wave is amplified. This unique feature could be a useful resource for applications in carrier recovery, channelization, or to suppress unwanted out-of-band spurs.

Throughout this analysis, we find that the optical noise figure depends critically on the thermal occupation of the Brillouin-active phonon modes. In fact, in the limit of high Brillouin gains, the in-band optical noise figure is virtually independent of all other parameters (see Eqs. 7.23 and 7.44). As the thermal occupation of the phonons is given by the Bose distribution, improved noise figures are possible by either increasing the Brillouin frequency or lowering the operating temperature. Higher frequencies than those studied here, are possible, for instance in bulk silicon or diamond systems, which support Brillouin frequencies in the range of 30-60 GHz. Alternatively, there may exist other strategies to radically increase the Brillouin frequencies supported by our optomechanical silicon waveguides. For instance, by engineering the polarization of the relevant optical fields, we can in principle couple to a distinct set of Lamb-like elastic modes whose mechanical motion is confined in the vertical ($\sim$ 0.2 μm) rather than the horizontal ($\sim$ 3 μm) dimensions of the waveguide geometry. This approach could yield a more than a 10-fold increase in the Brillouin frequency, translating directly into a $> 10\times$ improvement in the noise figure.

Reducing the operating temperature also directly improves the noise figure of these devices. For many applications, however, ambient operating conditions are necessary. In this context, there is a pressing need to develop other strategies to manipulate noise in these Brillouin systems. As we demonstrate for the first time in Chapter 8, we can use laser light to optomechanically cool the relevant group of phonons that participate in these Brillouin interactions. This form of Brillouin-based optomechanical cooling enables *in situ* and dynamical control of noise and dissipation, opening the door to new strategies for improved performance in a range of Brillouin-photonic systems.

Chapter 8

Optomechanical cooling in continuous systems through spontaneous inter-modal Brillouin scattering

8.1 Introduction

Thermal-mechanical noise, as discussed in Chapters 3 and 7, fundamentally limits the performance of practically all Brillouin-based technologies, from lasers and amplifiers to filters and non-reciprocal devices. Due to the fluctuation-dissipation theorem, this noise source cannot be suppressed by simply adding more damping; in fact, dissipation is the link between an open system and the thermal bath—the more damping, the more noise power is required to maintain thermal equilibrium. Thus, in order to reduce the thermal phonon occupation in mechanical system, we must expose it to a thermal bath of a lower effective temperature.

In the case of a simple, discrete mechanical mode, this form of cooling can actually be achieved coupling the vibrational degree of freedom to an optical cavity [78]. Given frequency scales that are orders of magnitude larger that those of mechanical systems,

optical photons exhibit essentially no thermal fluctuations at room temperature (i.e., $n_{\mathrm{th}} \lessapprox 10^{-10}$). In this way, optomechanical coupling can be engineered to expose the phonon mode to a cold optical bath—supplying optomechanical damping while imparting in return virtually no thermal fluctuations.

In cavity-optomechanical systems, the ability to control the thermal fluctuations of a mechanical resonator has been used to great effect, opening the door to precision metrology [175], quantum state generation [176–178], and fundamental tests of quantum decoherence [179]. This form of cooling ordinarily requires an optical cavity to the break the symmetry between the Stokes (heating) and the anti-Stokes (cooling) processes; with the proper detuning, the cavity resonance changes the density of states such that the anti-Stokes (cooling) process is favored over the Stokes (heating) process [78]. In this way, if the optical lifetime is shorter than that of the phonon, thermal energy will extracted from the mechanical system, reducing its overall occupation.

In connection to optomechanical cooling, intriguing questions arise in the case of Brillouin systems, sometimes referred to as continuum optomechanical systems [180], which in general possess no optical cavity or discrete phonon modes [12]. In contrast to lumped-element cavity-optomechanical devices, translational invariance in these Brillouin systems give rise to a continuum of available optical and acoustic states [181]. As of a few years ago, however, it was not been clear how or if optomechanical cooling concepts could be implemented in such continuous systems and what would determine their dynamics. In fact, prior studies suggested that, considering the experimental parameters of our system, such continuum optomechanical cooling would be almost negligible ($\Delta T/T \sim 10^{-4}$) [182].

In this chapter, we demonstrate laser cooling of a continuous optomechanical system. In this translationally invariant system, we are able use the distinct phase-matching conditions of spontaneous inter-modal Brillouin scattering to break the symmetry between the Stokes (heating) and anti-Stokes (cooling) processes; this strategy allows us to selectively cool phonons within a continuous band of accessible states—without the need for an optical or acoustic resonator. Through theoretical analysis, in conjunction with a new form of wavevector-selective phonon spectroscopy, we show that optical phase matching concentrates the optomechanical cooling over a select band of acoustic wavevectors. As a result,

this form of cooling is more than 1000× stronger than previously predicted, allowing us to reduce the temperature of a band of thermal phonons by more than 30 K from room temperature ($\Delta T/T \sim 10^{-1}$). This demonstration opens the door to new strategies to manipulate and control noise and dissipation in a range of powerful Brillouin-photonic technologies.

8.2 Continuum optomechanical cooling concepts

We demonstrate optomechanical cooling in a continuous system using phase-matched inter-modal Brillouin scattering within a 2.3 cm-long multimode photonic-photonic waveguide. As described in Appendix A, this optomechanical silicon waveguide is fabricated from a single-crystal silicon-on-insulator (SOI) wafer and is designed to support low-loss optical guidance within symmetric and antisymmetric TE-like optical spatial modes (for more details, see Chapter 2). These symmetric and antisymmetric spatial modes have propagation constants given by $k_1(\omega)$ and $k_2(\omega)$, respectively. When suspended, this all-silicon structures also supports a number of Brillouin-active elastic modes; in particular, a 6-GHz antisymmetric lamb-like wave mediates the largest Brillouin coupling, with a Brillouin gain coefficient of $G_B \cong 470$ $W^{-1}m^{-1}$. The spectral width obtained from stimulated and spontaneous measurements indicate that elastic energy in this traveling-wave system dissipates at a rate $\Gamma/(2\pi) \cong 14$ MHz), corresponding to a decay length $l_c \cong 60$ μm. As a result, the intrinsic spatial length scale of the phonons is nearly 400× shorter than the continuously suspended optomechanical silicon waveguide—a clear indication that this device operates in the continuum optomechanical limit.[1] Thus, since the phonon field is not confined in the direction of propagation, this system allows us to probe and control a continuum of available acoustic states in ways that are not possible with conventional cavity-optomechanical systems.

In this continuous system, we use phase-matched spontaneous inter-modal Brillouin scattering to selectively cool a small set of traveling-wave phonons. To do this, we couple probe light of frequency ω_p (green in Fig. 8.1A) in the symmetric optical spatial mode

1. Since the device length is equivalent to many spatial decay lengths, the phonon field does not form standing modes (i.e., there is no confinement in the direction of propagation).

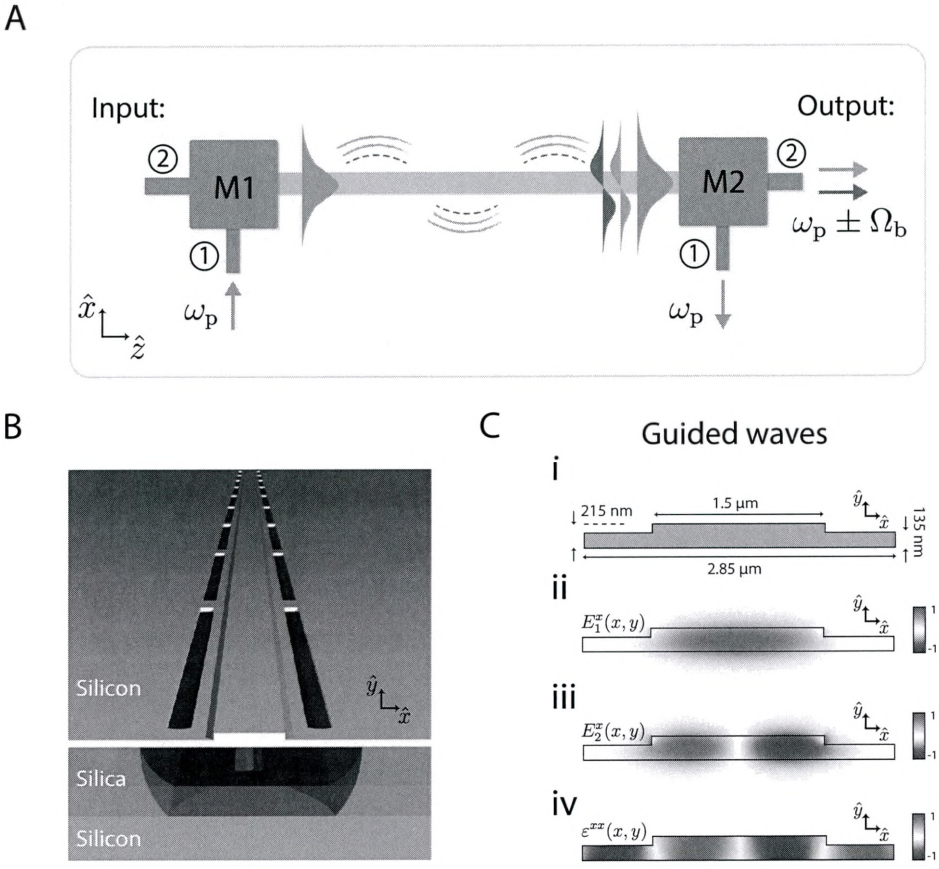

Figure 8.1: (A) Inter-modal Brillouin system used to demonstrate continuum optomechanical cooling. Probe light (green) of frequency ω_p is coupled into the symmetric spatial mode of a Brillouin-active silicon waveguide through an integrated mode multiplexer (M1). This light interacts with forward- and backward-propagating thermal phonon fields, which produce spontaneous Stokes (red) and anti-Stokes (blue) light in the antisymmetric waveguide mode, respectively. An integrated mode multiplexer (M2) then demultiplexes the scattered light for spectral analysis. (B) depiction of the multimode optomechanical waveguide structure. Panels (Cii) and (Ciii) plot the x-polarized component of the TE-like symmetric ($E_1^x(x,y)$) and antisymmetric ($E_2^x(x,y)$) simulated mode profiles, respectively. (Civ) shows the simulated strain profile (ε^{xx}) of the 6-GHz elastic mode that mediates spontaneous inter-modal scattering. This is same antisymmetric Lamb-like elastic wave that mediates amplification and lasing in Chapters 2-6. Adapted from Ref. [99]. Copyright (2018) by APS.

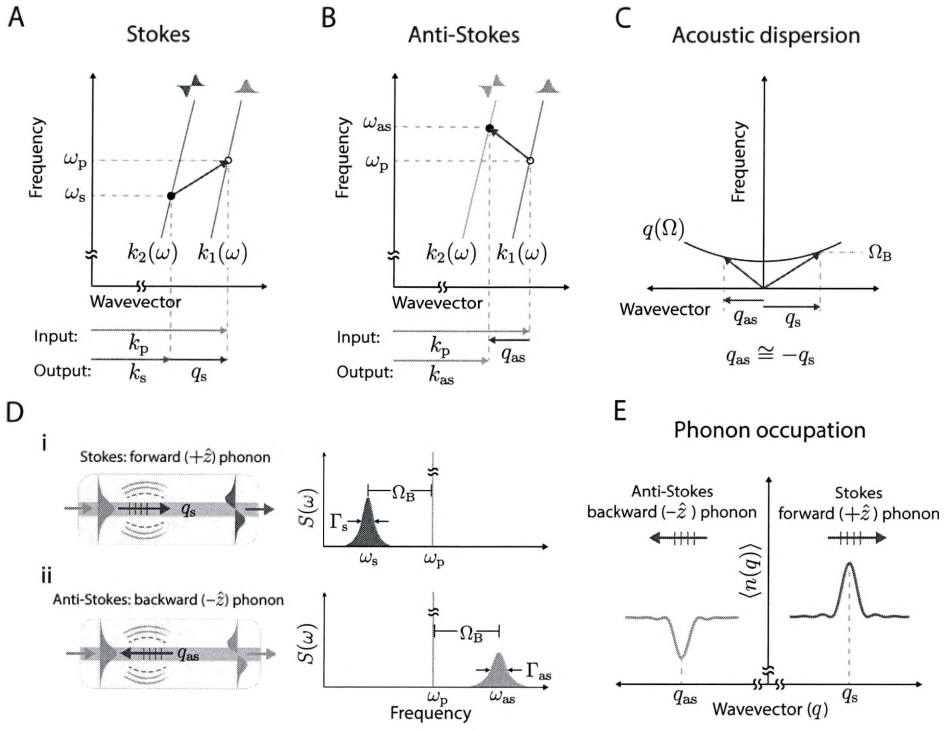

Figure 8.2: (A)-(B) 2-dimensional representation of the energy conservation and phase-matching conditions for the (A) Stokes and (B) anti-Stokes process. (C) Acoustic dispersion relation and wavevectors of the distinct forward- and backward- propagating phonons that participate in the spontaneous Stokes and anti-Stokes process, respectively. (D) diagrams illustrating the basic interaction and spectrum produced by the (i) Stokes and (ii) anti-Stokes process. The spectral width of each sideband reveals the lifetimes of the phonons that phase-match to each process. (E) Spontaneous inter-modal Brillouin scattering reduces the thermal occupation $\langle n(q) \rangle$ of phase-matched backward-propagating phonons while increasing that of the phase-matched forward propagating phonons. This process pushes the average momentum of the thermal bath of phonons out of equilibrium, yielding net phonon flux in the forward direction. Adapted from Ref. [99]. Copyright (2018) by APS.

of the multimode optomechanical waveguide. As this light traverses the Brillouin-active waveguide, it interacts with thermally driven phonons through spontaneous inter-modal Brillouin scattering. In this process, forward- and backward-propagating phonons produce Stokes and anti-Stokes sidebands, respectively, that propagate in the antisymmetric spatial mode of the Brillouin-active waveguide (Fig. 8.2Di-ii). Following the interaction region, an integrated mode-multiplexer (M2) separates light propagating in the symmetric optical spatial mode from the light traveling in the anti-symmetric spatial mode (see Fig. 8.1A), allowing for sensitive spectral analysis of the Stokes and anti-Stokes waves.

As we discussed in Chapters 2-3, inter-modal Brillouin scattering produces a form of dispersive symmetry breaking that fundamentally decouples the Stokes and anti-Stokes processes. In the context of continuum optomechanics, we note that, from the perspective of the phonons, the Stokes and anti-Stokes processes can be viewed as heating and cooling processes, respectively. We also point out that this form of symmetry breaking is quite distinct from that of sideband cooling in cavity-optomechanical systems, where the optical cavity feedback is often necessary to favor the anti-Stokes process over the Stokes. In this continuous system, by contrast, the direction of propagation of the traveling-wave phonons offers new degrees of control. Here, symmetry breaking arises because the Stokes and anti-Stokes processes are mediated by distinct groups of phonons; specifically, phase-matching requires that $q_{\mathrm{s}}(\Omega_{\mathrm{B}}) = k_1(\omega_{\mathrm{p}}) - k_2(\omega_{\mathrm{s}})$ and $q_{\mathrm{as}}(\Omega_{\mathrm{B}}) = k_2(\omega_{\mathrm{as}}) - k_1(\omega_{\mathrm{p}})$, where ω_{s} and ω_{as} are the respective Stokes and anti-Stokes frequencies, and $q_{\mathrm{s}}(\Omega_{\mathrm{B}})$ and $q_{\mathrm{as}}(\Omega_{\mathrm{B}})$ are the respective propagation constants of the Stokes and anti-Stokes phonons at the Brillouin frequency Ω_{B}. As a result, the Stokes process is mediated by a forward-propagating acoustic field while the anti-Stokes process is mediated by a backward-propagating acoustic field, as illustrated in Fig. 8.2A-C. In this configuration, phase-matched forward-traveling phonons experience heating while phase-matched backward-traveling phonons experience cooling (see Fig. 8.2E). We note that these intriguing optomechanical dynamics are not readily available with forward intra-modal processes in which Stokes and anti-Stokes processes couple to the same group of phonons with nearly identical rates [182, 183], thus highlighting the unique properties of inter-modal scattering processes. As such, it is interesting to note that backward Brillouin processes may also be used for continuum optomechanical cooling. As

shown in Fig. 8.2D, the spectral width of each sideband (Γ_s, Γ_{as}) gives a direct measure of the associated dissipation rates and lifetimes of the phonons that mediate the Stokes and anti-Stokes processes, respectively [75].

Due to the phase-matching-induced symmetry breaking, spontaneous inter-modal Brillouin scattering allows us to probe and precisely control the thermodynamic state of the phonons. For the phase-matched backward-propagating (anti-Stokes) phonons, the presence of a strong probe field adds a form of optomechanical damping; phonons annihilated by this scattering process are converted to anti-Stokes photons, which escape the system at a rate much greater than the intrinsic dissipation rate of the phonon field. As a result, the anti-Stokes process reduces the average lifetime and consequently the occupation of the phonon field (see Eq. 8.16). In other words, cooling of the anti-Stokes phonons is manifest as both a reduction in the phonon lifetime—or broadening of the spontaneous linewidth (Γ_{as})—and a decrease of the anti-Stokes scattering efficiency (e_{as}).[2] By contrast, the presence of a strong probe field yields linewidth narrowing of the Stokes sideband and increases the Stokes scattering efficiency (e_s).

These two, intrinsically-decoupled processes occur simultaneously, heating forward-propagating phonons and cooling backward-propagating phonons in this continuous waveguide system (see Fig. 8.2E). Detailed balance normally leads one to expect that the forward- (Φ_f) and backward-propagating (Φ_b) phonon fluxes are equal (i.e., $\Phi_f = \Phi_b$). Under these conditions, however, the forward- and backward- propagating phonon fluxes are no longer balanced (i.e., $\Phi_f > \Phi_b$), yielding an unusual form of non-reciprocal bath engineering.

8.3 Theoretical cooling dynamics

We begin by developing a succinct spatio-temporal model to understand the salient dynamics produced by optomechanical cooling in a continuous system. In this section, we outline a derivation for the effect of spontaneous inter-modal Brillouin scattering on the anti-Stokes phonon lifetime and population. As discussed in Chapter 1, the intrinsic decoupling between Stokes and anti-Stokes processes allow us to examine the dynamics of each separately.

2. The scattering efficiency is defined by the total spontaneous scattered power relative to the probe power.

Starting from the formalism developed in Ref. [75], the Hamiltonian for the spontaneous Brillouin interaction can be expressed as

$$\begin{aligned} H &= \hbar \int_{-\infty}^{\infty} dz' A_{\mathrm{p}}^{\dagger}(z',t)\omega_1(\hat{k}_{z'})A_{\mathrm{p}}(z',t) \\ &+ \hbar \int_{-\infty}^{\infty} dz' A_{\mathrm{as}}^{\dagger}(z',t)\omega_2(\hat{k}_{z'})A_{\mathrm{as}}(z',t) \\ &+ \hbar \int_{-\infty}^{\infty} dq' \Omega_{q'} b_{q'}^{\dagger} b_{q'} \\ &+ \frac{\hbar}{\sqrt{2\pi}} \int_{-\infty}^{\infty} dq' \int_0^L dz' g_{\mathrm{p,as}} A_{\mathrm{as}}^{\dagger}(z',t) A_{\mathrm{p}}(z',t) b_{q'} e^{i(q'-\Delta k_{\mathrm{as}})z'} \\ &+ \frac{\hbar}{\sqrt{2\pi}} \int_{-\infty}^{\infty} dq' \int_0^L dz' g_{\mathrm{p,as}}^{*} A_{\mathrm{as}}(z',t) A_p^{\dagger}(z',t) b_{q'}^{\dagger} e^{-i(q'-\Delta k_{as})z'}. \end{aligned} \tag{8.1}$$

Here, the wavevector difference between pump and anti-Stokes fields is defined by $\Delta k_{\mathrm{as}} \equiv k_2(\omega_{\mathrm{as}}) - k_1(\omega_{\mathrm{p}})$, $g_{\mathrm{p,as}}$ is the Brillouin coupling rate[3] and the Taylor expansion of the symmetric and antisymmetric optical mode dispersion relations in the z basis are given by $\omega_{\mathrm{i}}(\hat{k}_z) \equiv \sum_{n=0}^{\infty} \frac{1}{n!} \frac{\partial^n \omega_{\mathrm{i}}}{\partial k^n} (-i\frac{\partial}{\partial z})^n$. Notice that we have chosen to represent the optical fields as spatial envelopes and the phonon field as a continuous sum over wavevector mode amplitudes. This choice is particularly convenient because the phonon density of states is constant in wavevector space, and the mode occupation is well-defined for each phonon wavevector.

From the Heisenberg equations of motion, we calculate the spatio-temporal dynamics of the continuous phonon and anti-Stokes fields. Using the fact that $[A_{\mathrm{as}}(z',t), A_{\mathrm{as}}^{\dagger}(z,t)] = \delta(z-z')$ and $[b_{q'}(t), b_q^{\dagger}(t)] = \delta(q-q')$ [75], the equations of motion are given by

$$\begin{aligned} \dot{b}_q(t) &= -i\Omega_q b_q(t) - \frac{\Gamma}{2} b_q(t) + \eta_q(t) \\ &\quad - \frac{i g_{\mathrm{p,as}}^{*} A_{\mathrm{p}}^{\dagger}(t)}{\sqrt{2\pi}} \int_0^L dz' A_{\mathrm{as}}(z',t) e^{-i(q-\Delta k_{\mathrm{as}})z'} \\ \dot{A}_{\mathrm{as}}(z,t) &= -v_{\mathrm{g}} \frac{\partial}{\partial z} A_{\mathrm{as}}(z,t) - i\omega_{\mathrm{as}} A_{\mathrm{as}}(z,t) \\ &\quad - \frac{\gamma}{2} A_{\mathrm{as}}(z,t) - \frac{i g_{\mathrm{p,as}} A_{\mathrm{p}}(t)}{\sqrt{2\pi}} \int_{-\infty}^{\infty} dq' b_{q'}(t) e^{i(q'-\Delta k_{\mathrm{as}})z}. \end{aligned} \tag{8.2}$$

3. Given by the acoustic-optic overlap and photo-elastic tensor. See Chapter 1. We note that $g_{\mathrm{p,as}}$ represents the distributed optomechanical coupling (with units of [Hz]$\sqrt{[\mathrm{m}]}$), which is distinct from the lumped-element optomechanical coupling used in Chapters 3, 4, and 6.

We take a moment to summarize the steps and assumptions required to derive the coupled phonon and anti-Stokes equations above. To begin, we assume the that the probe wave (A_{p}) experiences negligible linear loss and remains undepleted through the spontaneous process (i.e., $A_{\mathrm{p}}(z,t) = A_{\mathrm{p}}(t)$)—an excellent approximation for the present system. To include the effects of dissipation, we introduce the phonon decay rate, Γ, and an associated Langevin stochastic driving term $\eta_q(t)$, which maintains the system in thermal equilibrium in the absence of optical forcing; $\eta_q(t)$ has a two-time correlation function given by $\langle \eta^{\dagger}_{q'}(t')\eta_q(t)\rangle = n_{\mathrm{th}}\Gamma\delta(t-t')\delta(q-q')$, where, as before, n_{th} is given by the Bose distribution ($n_{\mathrm{th}} = [\exp(\hbar\Omega_{\mathrm{B}}/(k_{\mathrm{b}}T)) - 1]^{-1}$). Here we treat the optical fields classically and ignore the Langevin driving force associated with the optical anti-Stokes dissipation rate (γ), since the thermal occupation of the anti-Stokes field is, for our purposes, negligible (i.e., $n_{\mathrm{as}} \cong 10^{-14}$). Finally we note that, because this is a relatively narrowband process, we ignore higher order dispersion for the optical fields (i.e., limit the Taylor expansion of $\omega_{\mathrm{i}}(\hat{k}_z)$ to first order).

We now make our routine transformation to the rotating frame, which simplifies the equations of motion and allows us to formally solve the dynamics of the anti-Stokes field. We do this by introducing $A_{\mathrm{as}}(z,t) = \bar{A}_{\mathrm{as}}(z,t)e^{-i\omega t}$, $A_{\mathrm{p}}(z,t) = \bar{A}_{\mathrm{p}}(z,t)e^{-i\omega_{\mathrm{p}}t}$, and $b_q(t) = \bar{b}_q(t)e^{-i\Omega t}$ (where $\Omega = \omega - \omega_{\mathrm{p}}$). The resulting equations of motion are given by

$$\begin{aligned}\dot{\bar{A}}_{\mathrm{as}}(z,t) = &-v_{\mathrm{g}}\frac{\partial}{\partial z}\bar{A}_{\mathrm{as}}(z,t) + [-i(\omega_{\mathrm{as}}-\omega) - \frac{\gamma}{2}]\bar{A}_{\mathrm{as}}(z,t) \\ &- \frac{ig_{\mathrm{p,as}}\bar{A}_{\mathrm{p}}(t)}{\sqrt{2\pi}}\int_{-\infty}^{\infty} dq'\bar{b}_{q'}(t)e^{i(q'-\Delta k_{\mathrm{as}})z}.\end{aligned} \tag{8.3}$$

Leveraging the same strategy used in Chapter 3, we greatly simplify the equations of motion by noting that the optical anti-Stokes field decays much more rapidly in time than that of the Brillouin-active phonon (i.e., $\gamma \gg \Gamma$). This decay hierarchy is valid considering the linear propagation loss of the optical fields and the transit time across the device. In this case, the temporal dynamics of the anti-Stokes field adiabatically follow those of the phonon field, allowing us to eliminate the temporal dynamics of the anti-Stokes field. In this limit, the anti-Stokes mode envelope amplitude is given by

$$\bar{A}_{\mathrm{as}}(z,t) = \frac{-ig_{\mathrm{p,as}}\bar{A}_{\mathrm{p}}(t)}{v_{\mathrm{g}}\sqrt{2\pi}} \int_0^z dz' \int_{-\infty}^{\infty} dq' \bar{b}_{q'} e^{i(q'-\Delta k_{\mathrm{as}})z' - \frac{\gamma}{2v_{\mathrm{g},2}}(z-z')}. \tag{8.4}$$

Given that $2v_{\mathrm{g}} \gg \gamma L$, the factor $\exp\{-\frac{\gamma}{2v_{\mathrm{g},2}}(z-z')\}$ within the integrand is, to a good approximation, unity. Consequently, since the optical propagation loss over the length of the waveguide is small, the anti-Stokes field at position z can be understood as a spatially filtered continuous sum of phonon mode amplitudes in the wavevector basis. With this simplification (i.e., plugging Eq. 8.4 into Eq. 8.2), we have

$$\begin{aligned}\dot{\bar{b}}_q &= -i(\Omega_q - \Omega)\bar{b}_q - \frac{\Gamma}{2}\bar{b}_q + \eta_q(t) \\ &\quad - \frac{|g_{\mathrm{p,as}}|^2|\bar{A}_p|^2}{v_{\mathrm{g},2}(2\pi)} \int_0^L dz' \int_0^{z'} dz'' \int_{-\infty}^{\infty} dq' \bar{b}_{q'} e^{i(q'-\Delta k_{\mathrm{as}})z'' - i(q-\Delta k_{\mathrm{as}})z'}.\end{aligned} \tag{8.5}$$

We first evaluate the spatial integrals resulting from the optomechanical coupling term. The resulting integrand can then be separated into real and imaginary parts. We are interested in the case where $q = \Delta k_{\mathrm{as}}$ and $\Omega = \Omega_{\Delta k_{\mathrm{as}}}$, or when the phonon wavevector is defined by optimal phase-matching with the optical fields. These conditions yield

$$\begin{aligned}\dot{\bar{b}}_{\Delta k_{\mathrm{as}}} &= -\frac{\Gamma}{2}\bar{b}_{\Delta k_{\mathrm{as}}} + \eta_{\Delta k_{\mathrm{as}}}(t) \\ &\quad - \frac{|g_{\mathrm{p,as}}|^2|A_p|^2}{v_{\mathrm{g},2}(2\pi)} \int_{-\infty}^{\infty} dq' \bar{b}_{q'} \left[\frac{1-\cos\left[L(\Delta k_{\mathrm{as}} - q')\right]}{(\Delta k_{\mathrm{as}} - q')^2} + i\frac{L(q'-\Delta k_{\mathrm{as}}) + \sin\left[L(\Delta k_{\mathrm{as}} - q')\right]}{(\Delta k_{\mathrm{as}} - q')^2}\right].\end{aligned} \tag{8.6}$$

The real and imaginary coefficients multiplying $\bar{b}_{q'}$ in the integrand are sharply peaked even and odd functions (about $q' = \Delta k_{\mathrm{as}}$), respectively. We also note that $\bar{b}_{q'}$ is nearly symmetrically distributed about $q' = \Delta k_{\mathrm{as}}$ due to the thermal distribution. These conditions yield an approximate equation of motion for the phonon field, given by

$$\dot{b}_{\Delta k_{\mathrm{as}}} = -i\Omega_{\Delta k_{\mathrm{as}}} b_{\Delta k_{\mathrm{as}}} - \frac{\Gamma_{\mathrm{as,eff}}}{2} b_{\Delta k_{\mathrm{as}}} + \eta_{\Delta k_{\mathrm{as}}}(t), \tag{8.7}$$

where $\Gamma_{\mathrm{as,eff}} = \Gamma\left(1 + G_{\mathrm{B}}P_{\mathrm{p}}L/4\right)$. Here, P_{p} is the probe power and G_{B} is the Brillouin gain coefficient (with units $\mathrm{W}^{-1}\mathrm{m}^{-1}$) defined by $G_{\mathrm{B}} = 4|g_{\mathrm{s,p}}|^2/(\hbar\omega_{\mathrm{p}}\Gamma v_{\mathrm{g}} v_{\mathrm{g,p}}) = 4|g_{\mathrm{s,p}}|^2|\bar{A}_{\mathrm{p}}|^2/(P\Gamma v_{\mathrm{g}})$.[4]

4. We can reparameterize the Brillouin gain by noting that $P = \hbar\omega_{\mathrm{p}} v_{\mathrm{g,p}}|\bar{A}_{\mathrm{p}}|^2$.

Equation 8.7 reveals that the presence of the strong pump modifies the equation of motion for the phonon through an additional damping term. The anti-Stokes process annihilates a phonon and a pump photon to generate an anti-Stokes (or blue-shifted) photon. Hence, the anti-Stokes process reduces the average lifetime of the phonon, evident as a correction to the damping rate.

We now return to Eq. 8.5, in order to make a transformation that simplifies our analysis and provides a direct connection to our measurements. We begin by defining

$$\begin{aligned}\beta(z,t) &\equiv \int_0^z dz' \int_{-\infty}^{\infty} dq' \bar{b}_{q'}(t) e^{i(q'-\Delta k_{\mathrm{as}})z'} \\ \xi(z,t) &\equiv \int_0^z dz' \int_{-\infty}^{\infty} dq' \eta_{q'}(t) e^{i(q'-\Delta k_{\mathrm{as}})z'}.\end{aligned} \tag{8.8}$$

Here, $\beta(z,t)$ represents the amplitude of the band of phase-matched phonons that interact with the probe wave (see Eq. 8.4), and $\xi(z,t)$ is the Langevin force under this same transformation. We note that $\beta(z,t)$ can be viewed as a continuous sum of the envelope operator $B(z,t)$ in Chapter 1 centered around Δk_{as}. Re-expressing Eq. 8.5 in terms of $\beta(z,t)$ and $\xi(z,t)$ yields

$$\dot{\beta}(z,t) = -\frac{\Gamma}{2}\beta(z,t) + \xi(z,t) - \frac{|g_{\mathrm{p,as}}|^2 |A_{\mathrm{p}}|^2}{v_{\mathrm{g}}} \int_0^z dz' \beta(z',t). \tag{8.9}$$

Equation 8.9 can then be used to derive the thermal phonon reduction in the high and moderate Brillouin coupling limits, as outlined below.

8.3.1 Limit of large Brillouin couplings

We first derive the most general solution for amplitude of the band of phase-matched phonons, which is particularly useful in the case of large Brillouin couplings (i.e., $G_{\mathrm{B}} P_{\mathrm{p}} L \gg 1$). To do this, we solve Eq. 8.9 through a Laplace transform in z. This yields the following solution for $\beta(z,t)$, given by

$$\beta(z,t) = \int_{-\infty}^{t} dt' e^{-\frac{\Gamma}{2}(t-t')}\xi(z,t') - \int_{-\infty}^{t} dt' \int_{0}^{z} dz' e^{-\frac{\Gamma}{2}(t-t')}\sqrt{\frac{\bar{G}(t-t')}{z-z'}} J_1\left[\sqrt{4\bar{G}(t-t')(z-z')}\right]\xi(z',t'), \tag{8.10}$$

where $\bar{G} \equiv |g_{\mathrm{p,as}}|^2 |A_{\mathrm{P}}|^2 / v_{\mathrm{g}}$. Next, we calculate the effective phonon occupation by taking $\langle \beta^{\dagger}(L,t)\beta(L,t)\rangle$ relative to the thermal value ($\langle \beta_{\mathrm{th}}^{\dagger}(L,t)\beta_{\mathrm{th}}(L,t)\rangle$), yielding

$$\frac{\langle \beta^{\dagger}\beta\rangle}{\langle \beta_{\mathrm{th}}^{\dagger}\beta_{\mathrm{th}}\rangle} = 1 + \frac{\Gamma}{L}\Bigg\{ - \int_{-\infty}^{t} dt' \int_{0}^{L} dz' z' e^{-\Gamma(t-t')}\sqrt{\frac{\bar{G}(t-t')}{(L-z')}} J_1\left[\sqrt{4\bar{G}(t-t')(L-z')}\right] + \int_{-\infty}^{t} dt' \int_{0}^{L} dz' \int_{0}^{L} dz'' e^{-\Gamma(t-t')} \mathrm{Min}(z',z'') \frac{\bar{G}(t-t')}{\sqrt{(L-z')(L-z'')}} \times J_1\left[\sqrt{4\bar{G}(t-t')(L-z')}\right] J_1\left[\sqrt{4\bar{G}(t-t')(L-z'')}\right]\Bigg\} \tag{8.11}$$

where $\mathrm{Min}(z',z'') \equiv (z'+z'')/2 - |z'-z''|/2$. While analytical integration of Eq. 8.11 becomes intractable, this expression can be used to numerically calculate the degree of optomechanical cooling over a full range of device lengths, Brillouin gain coefficients, and pump powers.

8.3.2 Limit of moderate Brillouin couplings

Alternatively, we can instead take a more conceptual approach and employ certain approximations that are suited to our present Brillouin system. In particular, to draw out the important dynamics for our inter-modal Brillouin system, we consider the case of moderate Brillouin couplings, such that $G_{\mathrm{B}}P_{\mathrm{p}}L \sim 1$ and $(G_{\mathrm{B}}P_{\mathrm{p}}L/4)^2 \ll 1$, which is a good approximation considering the experimental parameters of our system. To do this, we instead perform a temporal Fourier transform on Eq. 8.9 and take a spatial derivative, which yields

$$\frac{dB[z,\omega]}{dz} = -\frac{\chi G_{\mathrm{B}}P_{\mathrm{p}}\Gamma}{4} B[z,\omega] + \chi \int_{-\infty}^{\infty} dq' \tilde{\eta}_{q'} e^{i(q'-\Delta k_{\mathrm{as}}^{(1)})z}. \tag{8.12}$$

Here, we have defined $\chi \equiv 1/(-i\omega + \Gamma/2)$, $B[z,\omega]$ is the Fourier transform of $\beta(z,t)$, and $\tilde{\eta}_{q'}$

is the Fourier transformed Langevin force (i.e., $\tilde{\eta}_{q'}[\omega] = \mathscr{F}[\eta_{q'}] \equiv 1/(2\pi)\int_{-\infty}^{\infty}\eta_{q'}(t)e^{-i\omega t}$). We have also used the fact that $|g_{\mathrm{p,as}}|^2|A_{\mathrm{p}}|^2/v_{\mathrm{g}} = G_{\mathrm{B}}P_{\mathrm{p}}\Gamma/4$ [75].

Solving Eq. 8.12 yields

$$B[z,\omega] = \int_0^z dz' \int_{-\infty}^{\infty} dq' \chi\tilde{\eta}_{q'} e^{-\frac{\chi G_{\mathrm{B}}\Gamma P_{\mathrm{p}}(z-z')}{4}} e^{i(q'-\Delta k_{\mathrm{as}})z'}. \tag{8.13}$$

To simplify the inverse Fourier transform, we Taylor expand $e^{-\frac{\chi G_{\mathrm{B}}\Gamma P_{\mathrm{p}}(z-z')}{4}}$ to first order, which, as mentioned earlier is a good approximation in view of the probe power, Brillouin gain coefficient, and length of this system. We then perform an inverse Fourier transform via the convolution theorem, yielding the solution for $\beta(z,t)$, which is given by

$$\beta(z,t) = \int_0^z dz' \int_{-\infty}^{\infty} dq' \int_0^{\infty} dt' \left[1 - \frac{\Gamma G_{\mathrm{B}} P_{\mathrm{p}}(z-z')}{4} t'\right] \eta_{q'}(t-t') e^{-\frac{\Gamma}{2}t'} e^{i(q'-\Delta k_{\mathrm{as}})z'}. \tag{8.14}$$

For comparison, we also calculate the phonon field ($\beta_{\mathrm{th}}(z,t)$) in the absence of optomechanical cooling (i.e., $P_{\mathrm{p}} = 0$)

$$\beta_{\mathrm{th}}(z,t) = \int_0^z dz' \int_{-\infty}^{\infty} dq' \int_0^{\infty} dt' \eta_{q'}(t-t') e^{-\frac{\Gamma}{2}t'} e^{i(q'-\Delta k_{\mathrm{as}})z'}. \tag{8.15}$$

As a result, the modified occupation of the band of phonons interacting with the probe wave ($\langle n(\Delta k_{\mathrm{as}})\rangle$) relative the thermal occupation ($\langle n_{\mathrm{th}}(\Delta k_{\mathrm{as}})\rangle$) is given by

$$\begin{aligned}
\frac{\langle n(\Delta k_{\mathrm{as}})\rangle}{\langle n_{\mathrm{th}}(\Delta k_{\mathrm{as}})\rangle} &= \frac{\langle \beta^{\dagger}(L,t)\beta(L,t)\rangle}{\langle \beta_{\mathrm{th}}^{\dagger}(L,t)\beta_{\mathrm{th}}(L,t)\rangle} \\
&= 1 - \frac{G_{\mathrm{B}}P_{\mathrm{p}}L}{4} + \frac{G_{\mathrm{B}}^2 P_{\mathrm{p}}^2 L^2}{24} \\
&\approx 1 - \frac{G_{\mathrm{B}}P_{\mathrm{p}}L}{4} \\
&\approx \frac{\Gamma}{\Gamma_{\mathrm{as,eff}}},
\end{aligned} \tag{8.16}$$

where the approximations assume that $(G_{\mathrm{B}}P_{\mathrm{p}}L/4)^2 \ll 1$. From Eq. 8.16, we observe that the additional damping produced by spontaneous anti-Stokes yields an overall reduction in the thermal occupation.

As a point of comparison, we can rewrite $G_{\mathrm{B}}P_{\mathrm{p}}L$ in terms of an effective optical decay rate (γ_{eff}) given by the transit time, such that

$$G_{\mathrm{B}}P_{\mathrm{p}}L = \frac{4|g_{\mathrm{p,as}}|^2|A_{\mathrm{p}}|^2L}{\Gamma v_{\mathrm{g}}} = \frac{4|g_{\mathrm{p,as}}|^2|A_{\mathrm{p}}|^2}{\Gamma\gamma_{\mathrm{eff}}}, \tag{8.17}$$

where $\gamma_{\mathrm{eff}} = v_{\mathrm{g}}/L$. $|A_{\mathrm{p}}|^2$ represents the number of probe photons per unit length and $g_{\mathrm{p,as}}$ is the distributed optomechanical coupling. Recast in this form, $G_{\mathrm{B}}P_{\mathrm{p}}L$ more closely resembles the expression for cooling in cavity-optomechanical systems [78]—although additional distinctions emerge in the high $G_{\mathrm{B}}P_{\mathrm{p}}L$ limit (see Eq. 8.11).

Following a similar derivation one can show that the effective dissipation rate for Stokes phonons is $\Gamma_{\mathrm{s,eff}} = \Gamma\Big(1 - G_{\mathrm{B}}P_{\mathrm{p}}L/4\Big)$, and the phonon occupation is

$$\begin{aligned}\frac{\langle n(\Delta k_{\mathrm{s}})\rangle}{\langle n_{\mathrm{th}}(\Delta k_{\mathrm{s}})\rangle} &= 1 + \frac{G_{\mathrm{B}}P_{\mathrm{p}}L}{4} + \frac{G_{\mathrm{B}}^2P_{\mathrm{p}}^2L^2}{24} \\ &\approx 1 + \frac{G_{\mathrm{B}}P_{\mathrm{p}}L}{4} \\ &\approx \frac{\Gamma}{\Gamma_{\mathrm{s,eff}}}\end{aligned} \tag{8.18}$$

Thus, the spontaneous Stokes process reduces the damping and increases the thermal occupation of the phonon field. With our theoretical predictions in hand, we proceed to characterize these dynamics experimentally.

8.4 Observation of continuum optomechanical cooling

We use spontaneous inter-modal Brillouin scattering within our multimode optomechanical silicon waveguide to produce and observe continuum optomechanical cooling. Measurements at room temperature and atmospheric pressure are carried out using the experimental scheme diagrammed in Fig. 8.3A. Probe light of wavelength 1535.5 nm is generated by a continuous wave (CW) tunable external cavity laser and split along two paths. The lower path is used to synthesize a blue-shifted local oscillator by passing the light through an acousto-optic frequency shifter oscillating at frequency $\Delta = 2\pi \times 44$ MHz. In the upper path, the probe wave intensity is controlled using an erbium-doped fiber amplifier

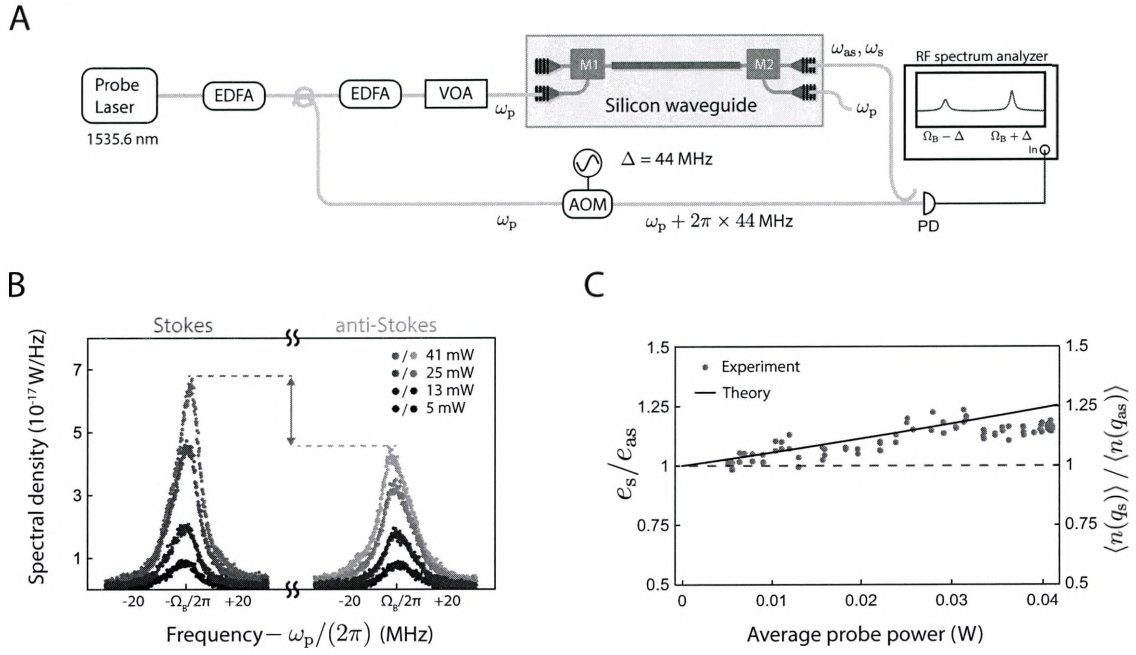

Figure 8.3: Spontaneous inter-modal Brillouin measurements. (A) Experimental scheme used to probe and modify the phonon dynamics. A CW telecom laser (vacuum wavelength of 1535.5 nm) is used to synthesize a strong probe wave (upper arm) and a 44-MHz blue-shifted optical local oscillator (using an acousto-optic modulator (AOM)) for heterodyne detection (lower arm). The probe wave intensity is controlled using an erbium-doped fiber amplifier (EDFA) and a variable optical attenuator (VOA) before being coupled on-chip. Scattered Stokes and anti-Stokes light is coupled off chip and combined with the blue-shifted optical local oscillator (LO), which allows us to discriminate between the Stokes and anti-Stokes sidebands. (B) a series of Stokes and anti-Stokes heterodyne spectra at four distinct probe powers. Note the power-dependent asymmetry between the Stokes and anti-Stokes spectra in both the peak spectral density and spectral width. (C) shows the relative scattering efficiencies of the Stokes and anti-Stokes processes (and respective phonon occupations) as the probe power is increased. Adapted from Ref. [99]. Copyright (2018) by APS.

(EDFA) and a variable optical attenuator (VOA) before being coupled on chip. Following the Brillouin-active waveguide, the spontaneously scattered light is separated from the probe wave using an integrated mode multiplexer and routed off-chip, where it is combined with the optical local oscillator for spectral analysis. Heterodyne detection with a frequency-shifted LO converts the spontaneous optical spectra into to distinct microwave signals (of center frequency $\Omega_B + \Delta$ and $\Omega_B - \Delta$, corresponding to Stokes and anti-Stokes optical frequencies of $\omega_p - \Omega_B$ and $\omega_p + \Omega_B$, respectively), whose spectra are subsequently recorded on a radio-frequency spectrum analyzer. In this way, heterodyne spectroscopy permits sensitive, frequency-resolved, high-resolution spectral measurements of Stokes and anti-Stokes sidebands. Since the scattered Stokes and anti-Stokes waves can be expressed as a linear product between the probe and phonon fields (see Section 8.3), this heterodyne measurement provides a window into the internal phonon dynamics, just as in the case of our silicon Brillouin laser (see Chapter 3).

As we increase the probe power, we observe a power-dependent asymmetry in both scattering efficiency and linewidth of the spontaneously-generated Stokes and anti-Stokes sidebands, in agreement with our theoretical predictions presented in Section 8.3. Figure 8.3B plots a series of heterodyne Stokes and anti-Stokes spectra at various probe powers. At low powers (i.e., when $G_B P_p L \ll 1$), the Stokes and anti-Stokes spectra exhibit nearly identical scattering efficiencies and linewidths. However, as the probe power increases ($G_B P_p L \to 1$), the anti-Stokes scattering efficiency decreases relative to that of the Stokes. (Fig. 8.4B). In addition, as shown in Fig. 8.4A the anti-Stokes (Stokes) spectrum exhibits appreciable spectral broadening (narrowing), revealing a Brillouin-induced reduction (increase) in phonon lifetime. This linewidth broadening corresponds to a reduction in anti-Stokes phonon population by approximately 11%, or 32 K of effective cooling (see Eq. 8.16).

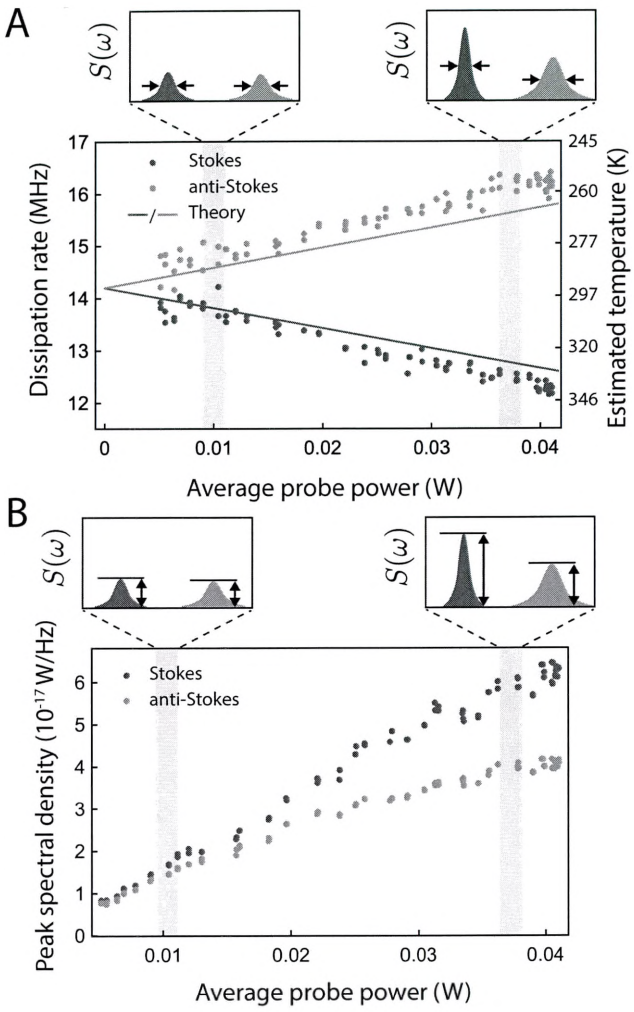

Figure 8.4: (A) fitted linewidths of the Stokes and anti-Stokes spectra as a function of probe power, together with the theoretical trends obtained from Section 8.3. The temperature is also estimated using the model derived in Section 8.3. These measurements reveal that the collective lifetime of the anti-Stokes phonons is reduced while that of the Stokes phonons is enhanced. At a maximum probe power of 42 mW, this asymmetry in spectral width corresponds to more than 30 K of cooling/heating from room temperature. (B) plots the peak spectral density of these spectra as a function of probe power. As a first order benchmark, the observed scattering efficiencies for the Stokes and anti-Stokes process are approximately 3.3×10^{-8}, in agreement with the predicted value (3.15×10^{-8}) for spontaneous forward Brillouin scattering [75]. Adapted from Ref. [99]. Copyright (2018) by APS.

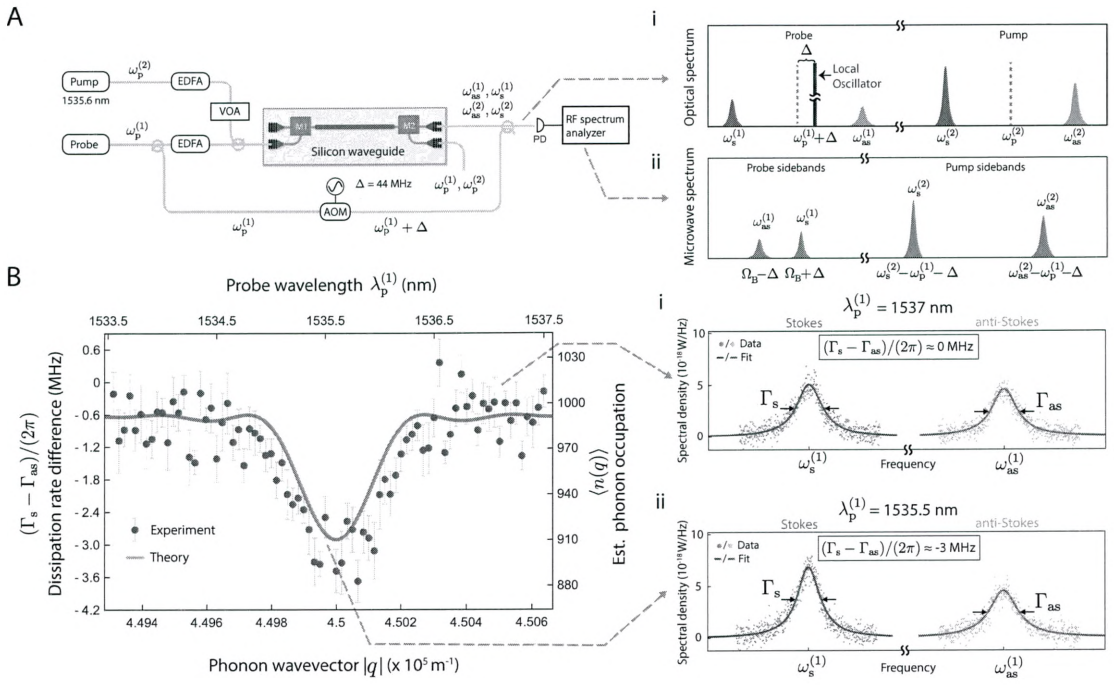

Figure 8.5: (A) Experimental setup for wavevector-resolved phonon spectroscopy involving two, tunable CW lasers–labeled the probe laser (indexed by superscript $^{(1)}$) and the pump laser (indexed by superscript $^{(2)}$). The probe laser is used to measure the dynamics of the acoustic states that satisfy the phase-matching condition given by the probe wavelength, while the pump laser is used to modify the phonon dynamics. Here, we again use an optical local oscillator discriminate between the spontaneous sidebands of the probe and the pump, as shown in Panels (Ai-ii). Since the optical LO (blue-shifted 44 MHz by the AOM) is synthesized from the probe source, the heterodyne Stokes and anti-Stokes signals centered at ($\Omega_B + \Delta$ MHz and $\Omega_B - \Delta$ MHz, respectively) originate entirely from the spontaneously scattered probe light. EDFA: erbium-doped fiber amplifier; AOM: acousto-optic modulator; PD: photo-detector. (B) Difference in Stokes and anti-Stokes phonon dissipation rates (spectral widths of the Stokes and anti-Stokes sidebands produced by the probe laser) as a function of probe wavelength while the pump wavelength remains fixed at $\lambda_p^{(2)} = 1535.6$ nm. Each data point represents the difference between Stokes and anti-Stokes dissipation rates at a pump power ($P_p^{(2)}$) of 30 mW, obtained by fitting the measured spectral widths over a series of 10 different pump powers. The theoretical trend obtained from Eq. 8.28 is superimposed. The phonon wavevector is calculated from the effective phase and group indices of the two optical spatial modes supported by the silicon waveguide, and the anti-Stokes phonon occupation is estimated by a comparison with the spatio-temporal theory. (Bi) Example spectra (of the probe sidebands) when the probe wave is not phase-matched to the same acoustic states as the pump wave. In this case, the dissipation rates for the Stokes and anti-Stokes phonons remain constant as the pump power increases. (Bii) Example spectra (of the probe sidebands) when the probe wave is phase-matched to the same group of phonons as the pump wave. Here, increasing the pump power enhances the dissipation rate asymmetry (see also Appendix D). These data reveal that the pump wave reduces the phonon occupation over a narrow band of phonon wavevectors, with a bandwidth given by $\Delta q = 2.78/L$. Adapted from Ref. [99]. Copyright (2018) by APS.

8.5 Pump-probe experiments and wavevector-selective phonon spectroscopy

From these measurements, we observe that the Stokes and anti-Stokes spectra evolve in a power-dependent fashion that is consistent with the predicted dynamics of continuum optomechanical cooling, as derived in Section 8.3. To ensure that these effects are not due to optical-only gain filtering (i.e., spectral narrowing or broadening associated with optical nonlinear gain or loss,[5] respectively), we use distinct continuous-wave cooling (pump) and probing fields to modify and observe the cooling dynamics. In this way, we isolate the underlying phonon dynamics and unambiguously observe the effect of spontaneous Brillouin scattering on the phonon temperature. Due to the phase-matching conditions, these pump-probe measurements can be viewed as a form of wavevector-resolved phonon spectroscopy, revealing a powerful new form of optomechanical control not possible in conventional cavity-optomechanical systems. We first describe our measurements and then derive corresponding theoretical pump-probe dynamics for wavevector-resolved phonon spectroscopy.

As illustrated in Fig. 8.2A, these experiments involve synthesizing an additional continuous wave pump source of frequency $\omega_{\mathrm{p}}^{(2)}$ (distinct from the probe frequency $\omega_{\mathrm{p}}^{(1)}$), which is used to cool the phonon field through spontaneous Brillouin scattering. Using weak probe field of frequency $\omega_{\mathrm{p}}^{(1)}$, we simultaneously measure the scattered probe sidebands over a range of wavelengths to characterize the modification of the phonon dynamics induced by the strong pump wave. Due to the optical phase-matching conditions, the center frequencies of the pump and the probe waves determine the set of phonon wavevectors with which each field interacts (for more details, see Section 8.6). In this way, phase-matching permits us to probe the phonon dynamics as a function of acoustic wavevector—simply by tuning the wavelength of the probe field. This form of wavevector-resolved phonon spectroscopy is performed by coupling both the pump and probe waves into the symmetric mode of the Brillouin-active waveguide, as shown in Fig. 8.5A. Through spontaneous inter-modal Brillouin scattering, these waves produce two distinct sets of Stokes and anti-Stokes sidebands,

5. For example, a Lorentzian optical spectrum undergoing loss (gain) with a Lorentzian spectral profile would would undergo spectral broadening (narrowing).

which are subsequently demultiplexed from the pump and probe waves and routed off-chip for spectral analysis.

To analyze the phonon dynamics, we isolate the spontaneously generated probe sidebands from the fields generated by the pump wave using the frequency selectivity provided by heterodyne detection. By synthesizing a local oscillator (LO) from the probe wave and combining the scattered fields with the LO on a high-speed photo-receiver (Fig. 28.5A), the Stokes and anti-Stokes light generated by the probe wave produce signals at respective microwave frequencies $\Omega_b + \Delta$ and $\Omega_b - \Delta$ while the scattered light associated with the pump produce microwave signals at vastly different frequencies (i.e., $|(\omega_p^{(2)} - \Omega_b) - (\omega_p^{(1)} + \Delta)|$ and $|(\omega_p^{(2)} + \Omega_b) - (\omega_p^{(1)} + \Delta)|$, respectively)—permitting crosstalk-free measurements of the probe scattered sidebands provided that $|\omega_p^{(2)} - \omega_p^{(1)}|/(2\pi) > 100$ MHz and $|\omega_p^{(2)} - (\omega_p^{(1)} \pm \Omega_B)|/(2\pi) > 100$ MHz. Thus, since the optical local oscillator is synthesized from the probe wave (and the pump and probe are of different frequencies), the resulting microwave signals at $\Omega_b + \Delta$ and $\Omega_b - \Delta$ originate entirely from the optical Stokes and anti-Stokes sidebands of the weak probe wave, respectively.

Using this experimental scheme, we perform thermal phonon spectroscopy and observe the cooling effects produced by the pump wave as a function of phonon wavevector. To do this, we keep the pump wavelength fixed while performing heterodyne spectral analysis of the scattered probe sidebands over a range of probe wavelengths and pump powers. The results plotted in Fig. 8.5B show the dissipation rate difference between Stokes and anti-Stokes spectra and the estimated anti-Stokes phonon occupation as a function of phonon wavevector. Each data point represents the average change in dissipation rate (and phonon number) that is obtained from a series of spectral measurements as the pump power is increased. Example spectra of the scattered probe sidebands when the probe wave is (is not) phase-matched to the same group of phonons as the pump wave are plotted in Fig. 8.5Bii (Fig. 8.5Bi). High resolution cooling data is presented in Fig. 8.6, revealing that the dissipation rate asymmetry can be used to faithfully predict the change in phonon occupation. Importantly, these pump-probe experiments show that spontaneous Brillouin scattering produces cooling over a narrow band of phonon wavevectors, with a wavevector bandwidth inversely proportional to the length of the device. Thus, this form of optomechanical cool-

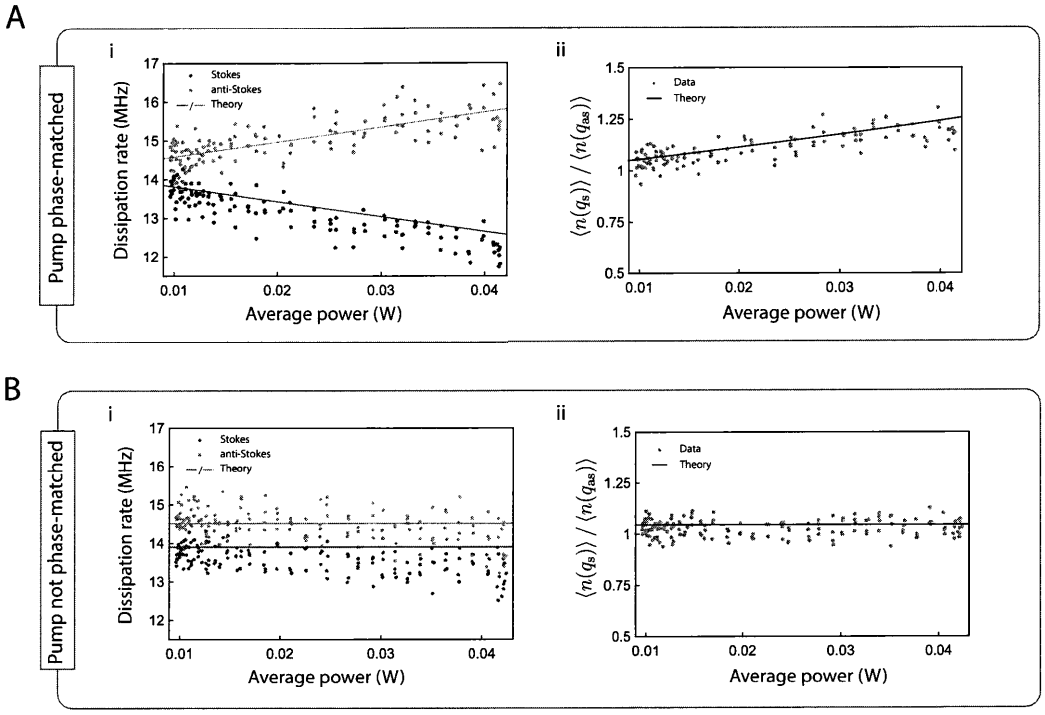

Figure 8.6: Additional pump-probe measurements. (Ai)-(Aii) plot the dissipation rates and relative phonon occupations salient effects of a strong pump wave on the probe spectra when the pump is within the phase matching bandwidth ($\lambda_p^{(2)} = 1535.6$ nm, $\lambda_p^{(1)} = 1535.53$ nm). When this phase-matching condition is satisfied (i.e., the pump wave is interacting with the same band of phonon wavevectors), we observe that the anti-Stokes (Stokes) probe spectra experiences linewidth broadening (narrowing) as the pump power is increased (see panel (Ai)), revealing that the pump wave coherently modifies the lifetimes of the Stokes and anti-Stokes phonons. Panel (Aii) plots the ratio of Stokes to anti-Stokes power (proportional to the ratio of phonon occupations) as a function of total on-chip power and the theoretical trend from the expected change in Stokes and anti-Stokes phonon occupations. Panel (Bi)-(Bii) plots the spectral widths and relative powers of the Stokes and anti-Stokes light (along with associated theoretical trends) when the pump wave is not phase-matched to the phonons interacting with the probe wave ($\lambda_p^{(2)} = 1537.3$ nm, $\lambda_p^{(1)} = 1535.53$ nm). We observe that the spectral widths and ratio of Stokes to anti-Stokes powers remains constant as a function of pump power, which is consistent with the theoretical trend (black). Note that the constant dissipation rate asymmetry is due to the presence of the probe wave. Adapted from Ref. [99]. Copyright (2018) by APS.

ing produces a cold window in wavevector space, distinct from the cold frequency windows typically produced by optomechanical resonators [184,185]. As such, this waveguide system gives access to a continuum of phonon modes that can be optomechanically controlled in a wavevector-selective fashion.

8.6 Pump-probe cooling dynamics

In this section, we derive the dynamics of our pump-probe experiments and show how phase-matching allows us to perform wavevector-resolved measurements of the phonon occupation. These measurements involve the use of a strong pump wave (of amplitude $A_{\mathrm{p}}^{(2)}$) to modify the phonon dynamics and a weak probe wave (of amplitude $A_{\mathrm{p}}^{(1)}$) to measure the phonon occupation. In this case, the interaction Hamiltonian of the system is given by

$$\begin{aligned} H_{\mathrm{int}} = &\frac{\hbar}{\sqrt{2\pi}}\times \\ &\Bigg[\int_{-\infty}^{\infty} dq' \int_0^L dz' g_{\mathrm{p,as}} A_{\mathrm{as}}^{(1)\dagger}(z',t) A_{\mathrm{p}}^{(1)}(z',t) b_{q'} e^{i(q'-\Delta k_{\mathrm{as}}^{(1)})z'} \\ &+ \int_{-\infty}^{\infty} dq' \int_0^L dz' g_{\mathrm{p,as}}^{*} A_{\mathrm{as}}^{(1)}(z',t) A_{p}^{(1)\dagger}(z',t) b_{q'}^{\dagger} e^{-i(q'-\Delta k_{\mathrm{as}}^{(1)})z'} \\ &+ \int_{-\infty}^{\infty} dq' \int_0^L dz' g_{\mathrm{p,as}} A_{\mathrm{as}}^{(2)\dagger}(z',t) A_{\mathrm{p}}^{(2)}(z',t) b_{q'} e^{i(q'-\Delta k_{\mathrm{as}}^{(2)})z'} \\ &+ \int_{-\infty}^{\infty} dq' \int_0^L dz' g_{\mathrm{p,as}}^{*} A_{\mathrm{as}}^{(2)}(z',t) A_{p}^{(2)\dagger}(z',t) b_{q'}^{\dagger} e^{-i(q'-\Delta k_{\mathrm{as}}^{(2)})z'}\Bigg], \end{aligned} \tag{8.19}$$

where the superscripts $^{(1)}$ and $^{(2)}$ index the optical probe and pump fields, respectively. Here, we note that the phase-matching conditions $\Delta k_{\mathrm{as}}^{(1)}$ and $\Delta k_{\mathrm{as}}^{(2)}$ are given simply by the group velocities of the two spatial modes and the wavelengths of the probe and pump waves, respectively, which in general are distinct (for further details see Eq. 8.31). Following the same approach used to derive Eqs. 8.1-8.5, we compute the equation for the phonon field of wavevector q, given by

$$\begin{aligned}\dot{\bar{b}}_q &= -i(\Omega_q - \Omega)\bar{b}_q - \frac{\Gamma}{2}\bar{b}_q - \eta_q(t) \\ &- \frac{|g_{\mathrm{p,as}}|^2|\bar{A}_p^{(1)}|^2}{v_{\mathrm{g}}(2\pi)}\int_0^L dz'\int_0^{z'} dz''\int_{-\infty}^{\infty} dq'\bar{b}_{q'}e^{i(q'-\Delta k_{\mathrm{as}}^{(1)})z''-i(q-\Delta k_{\mathrm{as}}^{(1)})z'} \\ &- \frac{|g_{\mathrm{p,as}}|^2|\bar{A}_p^{(2)}|^2}{v_{\mathrm{g}}(2\pi)}\int_0^L dz'\int_0^{z'} dz''\int_{-\infty}^{\infty} dq'\bar{b}_{q'}e^{i(q'-\Delta k_{\mathrm{as}}^{(2)})z''-i(q-\Delta k_{\mathrm{as}}^{(2)})z'}.\end{aligned} \tag{8.20}$$

From Eq. 8.20, it is evident that both the probe and the pump waves can contribute to Brillouin cooling as long as they satisfy phase matching. This produces a system of equations describing the coupled dynamics of the phonon bands interacting with the probe and pump waves (i.e., setting $q = \Delta k_{\mathrm{as}}^{(1)}$ and $q = \Delta k_{\mathrm{as}}^{(2)}$, respectively).

We now transform Eq. 8.20 using the same procedure used to obtain Eq. 8.9. We begin by defining

$$\beta^{(m)}(z,t) \equiv \int_0^z dz'\int_{-\infty}^{\infty} dq'\bar{b}_{q'}(t)e^{i(q'-\Delta k_{\mathrm{as}}^{(m)})z'}, \tag{8.21}$$

where $m = (1,2)$. From Eq. 8.21, it can be seen that $\beta^{(1)}(z,t)$ and $\beta^{(2)}(z,t)$ represent the narrow bands of phonons that phase-match with the probe and pump waves, respectively. Rewriting Eq. 8.20 in terms of these new spatially dependent functions yields the following coupled integral equations given by

$$\begin{aligned}\dot{\beta}^{(1)}(z,t) &= -\frac{\Gamma}{2}\beta^{(1)}(z,t) + \xi^{(1)}(z,t) \\ &- \frac{|g_{\mathrm{p,as}}|^2|A_{\mathrm{p}}^{(1)}|^2}{v_{\mathrm{g}}}\int_0^z dz'\beta^{(1)}(z',t) \\ &- \frac{|g_{\mathrm{p,as}}|^2|A_{\mathrm{p}}^{(2)}|^2}{v_{\mathrm{g},2}}\int_0^z dz'\beta^{(2)}(z',t)e^{i(\Delta k_{\mathrm{as}}^{(2)}-\Delta k_{\mathrm{as}}^{(1)})z'} \\ \dot{\beta}^{(2)}(z,t) &= -\frac{\Gamma}{2}\beta^{(2)}(z,t) + \xi^{(2)}(z,t) \\ &- \frac{|g_{\mathrm{p,as}}|^2|A_{\mathrm{p}}^{(1)}|^2}{v_{\mathrm{g}}}\int_0^z dz'\beta^{(2)}(z',t) \\ &- \frac{|g_{\mathrm{p,as}}|^2|A_{\mathrm{p}}^{(1)}|^2}{v_{\mathrm{g},2}}\int_0^z dz'\beta^{(1)}(z',t)e^{i(\Delta k_{\mathrm{as}}^{(1)}-\Delta k_{\mathrm{as}}^{(2)})z'}.\end{aligned} \tag{8.22}$$

Here, $\xi^{(1,2)}(z,t)$ is the Langevin force describing the thermal fluctuations of these phonon

bands, defined by $\xi^{(1,2)}(z,t) \equiv \int_0^z dz' \int_{-\infty}^{\infty} dq' \eta_{q'}(t) e^{i(q'-\Delta k_{\rm as}^{(1,2)})z'}$. We next note that $|g_{\rm p,as}|^2 |A_{\rm p}^{(1,2)}|^2 / v_{\rm g}$ can be rewritten as $G_{\rm B} P_{\rm p}^{(1,2)} \Gamma/4$, where $P_{\rm p}^{(1,2)}$ is the power of the probe and pump waves, respectively. Rewriting Eq. 8.22 in terms of these constants and taking the Fourier transform in time yields

$$\begin{aligned} -i\omega B^{(1)}[z,\omega] = &-\frac{\Gamma}{2} B^{(1)}[z,\omega] + \tilde{\xi}^{(1)}[z,\omega] \\ &- \frac{G_{\rm B} P_{\rm p}^{(1)} \Gamma}{4} \int_0^z dz' B^{(1)}[z',\omega] \\ &- \frac{G_{\rm B} P_{\rm p}^{(2)} \Gamma}{4} \int_0^z dz' B^{(2)}[z',\omega] e^{i(\Delta k_{\rm as}^{(2)} - \Delta k_{\rm as}^{(1)})z'} \end{aligned} \tag{8.23}$$

$$\begin{aligned} -i\omega B^{(2)}[z,\omega] = &-\frac{\Gamma}{2} B^{(2)}[z,\omega] + \tilde{\xi}^{(2)}[z,\omega] \\ &- \frac{G_{\rm B} P_{\rm p}^{(2)} \Gamma}{4} \int_0^z dz' B^{(2)}[z',\omega] \\ &- \frac{G_{\rm B} P_{\rm p}^{(1)} \Gamma}{4} \int_0^z dz' B^{(1)}[z',\omega] e^{i(\Delta k_{\rm as}^{(1)} - \Delta k_{\rm as}^{(2)})z'}. \end{aligned} \tag{8.24}$$

Here, $B^{(1,2)}[z,\omega]$ and $\tilde{\xi}^{(1,2)}[z,\omega]$ are the Fourier-transformed phonon fields and Langevin force, respectively. Taking the spatial derivative of these equations yields

$$\begin{aligned} \frac{dB^{(1)}[z,\omega]}{dz} = &-\frac{\chi G_{\rm B} P_{\rm p}^{(1)} \Gamma}{4} B^{(1)}[z,\omega] \\ &- \frac{\chi G_{\rm B} P_{\rm p}^{(2)} \Gamma}{4} B^{(2)}[z,\omega] e^{i(\Delta k_{\rm as}^{(2)} - \Delta k_{\rm as}^{(1)})z} \\ &+ \chi \int_{-\infty}^{\infty} dq' \tilde{\eta}_{q'} e^{i(q' - \Delta k_{\rm as}^{(1)})z} \\ \frac{dB^{(2)}[z,\omega]}{dz} = &-\frac{\chi G_{\rm B} P_{\rm p}^{(2)} \Gamma}{4} B^{(2)}[z,\omega] \\ &- \frac{\chi G_{\rm B} P_{\rm p}^{(1)} \Gamma}{4} B^{(1)}[z,\omega] e^{i(\Delta k_{\rm as}^{(2)} - \Delta k_{\rm as}^{(1)})z} \\ &+ \chi \int_{-\infty}^{\infty} dq' \tilde{\eta}_{q'} e^{i(q' - \Delta k_{\rm as}^{(2)})z}. \end{aligned} \tag{8.25}$$

Here, $\chi \equiv 1/(-i\omega + \Gamma/2)$ and $\tilde{\eta}_{q'}$ is the Fourier-transformed Langevin force (i.e., $\tilde{\eta}_{q'}[\omega] = \mathscr{F}[\eta_{q'}] \equiv 1/(2\pi) \int_{-\infty}^{\infty} \eta_{q'}(t) e^{-i\omega t}$). We solve Eq. 8.25 perturbatively in a manner that is consistent with our experimental parameters. Here we assume that the probe wave is weak and that the strong pump wave modifies the phonon dynamics to first order. This analysis requires that $G_{\rm B} P_{\rm p}^{(1)} L/4 \ll 1$ and $(G_{\rm B} P_{\rm p}^{(2)} L/4)^2 \ll 1$, which is well-satisfied in our pump-

probe experiments. Under this approximation, Eq. 8.25 simplifies to

$$\begin{aligned} B^{(1)}[z,\omega] &= \int_{-\infty}^{\infty} dq' \int_0^z dz' \chi \tilde{\eta}_{q'} e^{i(q'-\Delta k_{\text{as}}^{(1)})z'} \\ &\quad - \frac{G_{\text{B}} P_{\text{p}}^{(2)} \Gamma}{4} \int_0^L dz' B^{(2)}[z',\omega] e^{i(\Delta k_{\text{as}}^{(2)} - \Delta k_{\text{as}}^{(1)})z'} \\ B^{(2)}[z,\omega] &= \int_{-\infty}^{\infty} dq' \int_0^z dz' \chi \tilde{\eta}_{q'} e^{i(q'-\Delta k_{\text{as}}^{(2)})z'} \end{aligned} \tag{8.26}$$

Substituting $B^{(2)}[z,\omega]$ into the equation for $B^{(1)}[z,\omega]$ and performing the inverse Fourier transform yields

$$\begin{aligned} \beta^{(1)}(z,t) &= \int_{-\infty}^{\infty} dq' \int_0^z dz' \int_0^{\infty} dt' \eta_{q'}(t-t') e^{-\frac{\Gamma}{2}t'} e^{i(q'-\Delta k_{\text{as}}^{(1)})z'} \\ &\quad - \frac{G_{\text{B}} P_{\text{p}}^{(2)} \Gamma}{4} \int_{-\infty}^{\infty} dq' \int_0^z dz' \int_0^{z'} dz'' \\ &\quad \times \int_0^{\infty} dt' \eta_{q'}(t-t') t' e^{-\frac{\Gamma}{2}t'} e^{i(q'-\Delta k_{\text{as}}^{(2)})z''} e^{i(\Delta k_{\text{as}}^{(2)} - \Delta k_{\text{as}}^{(1)})z'}. \end{aligned} \tag{8.27}$$

From Eq. 8.27, we compute the occupation of the group of phonons interacting with the probe wave relative to the equilibrium value. This computation yields

$$\begin{aligned} \frac{\langle n^{(1)}(\Delta k_{\text{as}})\rangle}{\langle n_{\text{th}}^{(1)}(\Delta k_{\text{as}})\rangle} &= \frac{\langle \beta^{(1)\dagger}(L,t)\beta^{(1)}(L,t)\rangle}{\langle \beta_{\text{th}}^{(1)\dagger}(L,t)\beta_{\text{th}}^{(1)}(L,t)\rangle} \\ &= 1 - \frac{G_{\text{B}} P_{\text{p}}^{(2)} L}{4} \operatorname{sinc}^2\left[\frac{(\Delta k_{\text{as}}^{(2)} - \Delta k_{\text{as}}^{(1)})L}{2}\right] \\ &\quad + O\Big(\Big[\frac{G_{\text{B}} P_{\text{p}}^{(2)} L}{4}\Big]^2\Big) \\ &\approx 1 - \frac{G_{\text{B}} P_{\text{p}}^{(2)} L}{4} \operatorname{sinc}^2\left[\frac{(\Delta k_{\text{as}}^{(2)} - \Delta k_{\text{as}}^{(1)})L}{2}\right]. \end{aligned} \tag{8.28}$$

This is the central result of this section. Thus, if the necessary conditions are satisfied (i.e., $G_{\text{B}} P_{\text{p}}^{(1)} L/4 \ll 1$ and $(G_{\text{B}} P_{\text{p}}^{(2)} L/4)^2 \ll 1$), we can, to an excellent approximation, use the anti-Stokes light generated from the probe wave to measure the phonon occupation and effective temperature of the band of phonons that are phase-matched to the probe wave. We note that the theoretical trend in Fig. 8.5B was obtained directly from Eq. 8.28, which agrees well with our experimental data. It is evident that Eq. 8.28 reaches a minimum when the pump wave is optimally phase-matched to the probe wave (i.e., $\Delta k_{\text{as}}^{(2)} = \Delta k_{\text{as}}^{(1)}$), which occurs when the probe and pump wavelengths are equal $\lambda_{\text{p}}^{(1)} = \lambda_{\text{p}}^{(2)}$ (see Section 8.6).

In this case, the phonon occupation is

$$\frac{\langle n^{(1)}(\Delta k_{\mathrm{as}})\rangle}{\langle n_{\mathrm{th}}^{(1)}(\Delta k_{\mathrm{as}})\rangle} \approx 1 - \frac{G_{\mathrm{B}} P_{\mathrm{p}}^{(2)} L}{4}, \tag{8.29}$$

which, as a cross-check, agrees with the single-probe theory (see Eq. 8.16).

Incorporating the known parameters of our system, we next calculate the phase-matching bandwidth of phonon wavevectors that are appreciably cooled through spontaneous intermodal Brillouin scattering. We begin by stating the phase-matching condition required by the anti-Stokes scattering process of the probe wave, namely that $q_{\mathrm{as}}^{(1)}(\Omega_{\mathrm{B}}) = \Delta k_{\mathrm{as}}^{(1)} \equiv k_2(\omega_{\mathrm{p}}^{(1)} + \Omega_{\mathrm{B}}) - k_1(\omega_{\mathrm{p}}^{(1)})$, where $q_{\mathrm{as}}^{(1)}(\Omega_{\mathrm{B}})$ is the wavevector of the phonon field interacting with the probe wave. Thus, the wavevector of the phonon field is dictated by the frequencies and propagation constants of the two optical fields. Now, if we consider the phonon wavevector that interacts with the pump frequency ($q_{\mathrm{as}}^{(2)}(\Omega_{\mathrm{B}})$), such that $\omega_{\mathrm{p}}^{(2)} = \omega_{\mathrm{p}}^{(1)} + \Delta\omega$, we find that the difference between the two phonon wavevectors is given by

$$\begin{aligned} q_{\mathrm{as}}^{(2)}(\Omega_{\mathrm{B}}) - q_{\mathrm{as}}^{(1)}(\Omega_{\mathrm{B}}) &= \Delta k_{\mathrm{as}}^{(2)} - \Delta k_{\mathrm{as}}^{(1)} \\ &= k_2(\omega_{\mathrm{p}}^{(2)} + \Omega_{\mathrm{B}}) - k_1(\omega_{\mathrm{p}}^{(2)}) \\ &\quad - [k_2(\omega_{\mathrm{p}}^{(1)} + \Omega_{\mathrm{B}}) - k_1(\omega_{\mathrm{p}}^{(1)})]. \end{aligned} \tag{8.30}$$

Ignoring higher order dispersion (which is a good approximation in the waveguides under study), we can simplify this expression in terms of the group velocities of the two interacting optical spatial modes ($v_{g,1}$ and $v_{g,2}$ for the symmetric and antisymmetric spatial mode, respectively). This simplification yields an expression given by

$$\Delta k_{\mathrm{as}}^{(2)} - \Delta k_{\mathrm{as}}^{(1)} = \left[\frac{1}{v_{g,2}} - \frac{1}{v_{g,1}}\right]\Delta\omega. \tag{8.31}$$

Here, $\Delta\omega = \omega_{\mathrm{p}}^{(2)} - \omega_{\mathrm{p}}^{(1)}$. Equation 8.28 reveals that the full width at half maximum (FWHM) in k-space is $(\Delta k_{\mathrm{as}}^{(2)} - \Delta k_{\mathrm{as}}^{(1)})/2 = 2.78/L$. As a result, the FWHM of the phase-matching bandwidth (in $\Delta f = \Delta\omega/2\pi$) becomes

$$\mathrm{FWHM} = \frac{2.78}{\pi L}\left[\frac{1}{|\frac{1}{v_{g,1}} - \frac{1}{v_{g,2}}|}\right]. \tag{8.32}$$

Inserting the parameters of this silicon system, we find that the phase-matching bandwidth is 91.4 GHz (0.72 nm). This calculation finds good qualitative agreement with the phase-matching bandwidth exhibited by the pump probe experiments (see Fig. 8.5B). Thus, by shifting the pump wavelength by several nm, we can cool an entirely different group of phonons. In this way, the conditions set by phase-matching permit cooling of continuously accessible groups of phonons in a wavevector-selective fashion.

8.7 Conclusion and outlook

8.7.1 Physical insights into the dynamics of continuous optomechanical systems

These studies help us to understand some of the unusual dynamics exhibited by continuous optomechanical systems. As derived in Eqs. 8.16 and 8.29 and evident in our experiments, we observe that significant cooling can be achieved when $G_{\mathrm{B}}P_{\mathrm{p}}L \gtrapprox 1$. It is interesting to note that the degree of cooling does not depend on the group velocity of the phonons and consequently acoustic density of states in frequency, in sharp contrast to previous analysis [182]. Instead, we see that the degree of cooling depends critically on the device length. This is particularly striking given that the coherence length ($l_{\mathrm{c}} = v_{\mathrm{b}}/\Gamma$) is approximately 60 μm—in contrast to the 2.3-cm length of the waveguide; these parameters correspond to a total acoustic propagation loss of approximately 10,000 dB over the device length. As such, it is clear that in the absence of light, the thermal phonon field is spatially uncorrelated along the device length.

In spite of these extreme spatial dynamics, we observe that the phonon field behaves essentially as a single entity in the presence of spontaneous Brillouin scattering. This is because the acoustic states that participate in the spontaneous Brillouin process are determined not by the frequency bandwidth of the Brillouin resonance (phonon dissipation rate) and acoustic density of states (phonon group velocity) but rather by the optical phase-matching condition; in a continuous system that is much larger than the intrinsic acoustic decay length, this is by far the more stringent criterion. In other words, due to the disparate velocities of light and sound, optical phase-matching plays the dominant role in selecting

the acoustic states that participate in the cooling process. In this way, phase-matching concentrates the optomechanical cooling process over a narrow band of acoustic wave vectors, allowing us to significantly alter the phonon occupation in a wavevector-selective fashion.

Our results reveal that the optical fields phase-match to an exceptionally narrow band of phonon wavevectors, with a phase-matching bandwidth (full width at half maximum) determined by the length of the system (i.e., $\Delta q = \Delta k_{\mathrm{as}}^{(2)} - \Delta k_{\mathrm{as}}^{(1)} = 2.78/L$). Hence, although the effect of cooling becomes more pronounced as the length increases, Brillouin cooling occurs over a narrower bandwidth of phonon wavevectors. It is important to note that our analysis is only valid for the case when the optical dissipation rate is greater than that of the acoustic. If this temporal dissipation hierarchy is not satisfied, energy transferred from the acoustic field to the optical fields may return the acoustic field, instead of escaping the system. Thus, longer systems may face a fundamental challenge to achieve Brillouin cooling; the upper limit of optical dissipation rate, which is set by the transit time, cannot be smaller than the acoustic dissipation rate. This sets a practical limitation to the length over which cooling can occur, namely that $L \ll \frac{v_{\mathrm{g}}}{\Gamma}$. In the case of this silicon optomechanical waveguide, this constraint corresponds to a length of about 1 m.

In summary, we find that substantial continuum optomechanical cooling is predicated upon three essential conditions. First, there needs to be dispersive symmetry breaking between the Stokes and the anti-Stokes process. Second, the optical dissipation rate — either due to propagation losses or the finite length of the system —must be much greater than the acoustic dissipation rate ($\gamma \gg \Gamma$). Finally, for large Brillouin cooling, the product of Brillouin gain, probe power, and length needs to be at least of order 1 (i.e., $G_{\mathrm{b}} P L \gtrapprox O(1)$).

8.7.2 Manipulating noise and dissipation in Brillouin technologies

As we seek new ways to utilize and shape Brillouin dynamics, this form of optomechanical cooling presents compelling opportunities to manipulate and enhance the performance of a range of Brillouin-photonic technologies. In particular, continuum optomechanical cooling unlocks strategies for reservoir and dissipation engineering [186] over unprecedented optical and acoustic bandwidths [78]—a new tool to mitigate noise and manipulate dissipation in continuous optomechanical systems. For instance, as we observed in Chapter 7, the optical

noise figure of Brillouin amplifier systems is fundamentally determined by the thermal occupation of the Brillouin-active phonon field. Given this critical dependence, the ability to mitigate thermal noise in these systems would directly translate into an improvement in the optical noise figure. Reservoir-engineered Brillouin amplifiers of this kind would allow us to reach state-of-the-art noise performance while providing record-high Brillouin gain.

Furthermore, as we demonstrated in Chapter 3 and 6, the linewidths of both silicon Brillouin laser systems and conventional Brillouin lasers are fundamentally determined by the thermal occupation of the Brillouin-active phonons [81, 95]. Thus, optomechanical cooling of this form may be used as a powerful tool to improve the noise performance of Brillouin laser systems. Moreover, our results pave the way for new strategies to shape the internal Brillouin dynamics through *in situ*, dynamical control of dissipation and nonlinear susceptibility. The ability to engineer dissipation may allow continuous explorations of disparate 3-wave laser dynamics—from the acoustic linewidth narrowing [95] to optical linewidth narrowing regimes [81]. Beyond Brillouin lasers and amplifiers, the ability to control both noise and dissipation could permit new Brillouin-based filtering schemes with tunable bandwidths and enhanced noise performance [22, 140].

As we have demonstrated in this chapter, multimode dispersion and phase-matching in this continuum optomechanical system allows us to selectively address and cool phonons as a function of acoustic wavevector, simply by tuning the wavelength of the laser light. These dynamics permit a range of potential schemes in which a secondary cooling laser may be used to reduce the thermal occupation of phonons that mediate Brillouin amplification, filtering, or lasing, resulting in improved noise performance. A key requirement in such schemes is that the set of wavevectors addressed by the anti-Stokes (cooling) process must be the same as the wavevectors of the phonons mediating Brillouin amplification.

This condition can be met, for instance, by injecting slightly detuned cooling light into the opposite spatial mode of that of the pump used to achieve amplification. Dispersion engineering could dramatically enhance the ability to address the same sets of acoustic states at disparate wavelengths. Alternatively, configurations in which pump and cooling light counter-propagate within the same spatial mode can also satisfy this phase-matching condition. Furthermore, inter-modal photonic-phononic emit receive structures [187]—which

permit optomechanical coupling between optically distinct waveguides—could add new degrees of control and enhanced flexibility for future cooling schemes. Finally, these cooling dynamics may be adapted to and radically enhanced by resonant geometries (as in Chapter 4) and/or mid-infrared wavelengths, as we describe in Chapter 9, opening the door to cooling that is orders of magnitude stronger than possible with telecom-band linear waveguide systems.

Chapter 9

Mid-infrared nonlinear silicon photonics

9.1 Introduction

The ability to tune the nonlinear SBS coupling strength over a range of parameters represents a central objective as we seek new ways to control and manipulate Brillouin dynamics. To this end, numerous design strategies have been explored to enhance optomechanical coupling by confining the optical and elastic mode energies into smaller volumes [30, 69]. In silicon, however, there is a nontrivial trade-off between the enhancement of the intrinsic coupling and the resulting increase in linear and nonlinear loss. Specifically, at the telecom wavelengths where silicon photonics circuits typically operate, two-photon absorption (TPA) and TPA-induced free-carrier absorption quickly overtake the nonlinear growth supplied by Brillouin gain [188].

Two-photon absorption is a nonlinear optical process resulting from the imaginary component of the nonlinear susceptibility $\chi^{(3)}$. In semiconductor systems, the underlying physics becomes quite clear by noting that the energy of two photons must be sufficient to excite a carrier in the valence band into the conduction band, as shown in Fig. 9.1C. This photo-excited carrier can subsequently induce absorption of another photon within the conduction band through TPA-induced free-carrier absorption. In the limit of small signal powers, the

competition between Brillouin gain and nonlinear loss can be described by the following ordinary differential equation, given by [23]

$$\begin{aligned}\frac{dP_{\mathrm{p}}}{dz} &= -\alpha P_{\mathrm{p}} - \beta_{\mathrm{TPA}} P_{\mathrm{p}}^2 - \gamma_{\mathrm{FCA}} P_{\mathrm{p}}^3 - G_{\mathrm{B}} P_{\mathrm{p}} P_{\mathrm{s}} \\ \frac{dP_{\mathrm{s}}}{dz} &= -\alpha P_{\mathrm{s}} - 2\beta_{\mathrm{TPA}} P_{\mathrm{p}} P_{\mathrm{s}} - \gamma_{\mathrm{FCA}} P_{\mathrm{p}}^2 P_{\mathrm{s}} + G_{\mathrm{B}} P_{\mathrm{p}} P_{\mathrm{s}},\end{aligned} \tag{9.1}$$

where P_{s} is the Stokes power, P_{p} is the pump power, α is the linear propagation loss coefficient, β_{TPA} is the TPA coefficient, γ_{FCA} is the TPA-induced free carrier coefficient, and G_{B} is the Brillouin gain coefficient. For simplicity we have assumed a single-mode waveguide system and consider the case in which the Stokes power is significantly smaller than that of the pump (i.e., $P_{\mathrm{s}}^2/P_{\mathrm{p}}^2 \ll 1$). From Eq. 9.1, we note while the nonlinear coupling strength is enhanced linearly with increasing pump power, the TPA and TPA-induced free carrier absorption grow as P^2 and P^3, respectively.

However, these nonlinear loss dynamics fundamentally change in the case of long wavelengths, specifically beyond 2.1 μm, where the collective energy of two photons is no longer sufficient to bridge the band gap. As a result, nonlinear loss from two-photon absorption and TPA-induced free-carrier absorption vanish in this mid-infrared region. In this case, three photons are required to produce what we call three photon absorption (3PA) (see Fig. 9.1D), and the nonlinear power dynamics are now given by

$$\begin{aligned}\frac{dP_{\mathrm{p}}}{dz} &= -\alpha P_{\mathrm{p}} - \gamma_{\mathrm{3PA}} P_{\mathrm{p}}^3 - \chi_{\mathrm{FCA}} P_{\mathrm{p}}^4 - G_{\mathrm{B}} P_{\mathrm{p}} P_{\mathrm{s}} \\ \frac{dP_{\mathrm{s}}}{dz} &= -\alpha P_{\mathrm{s}} - \gamma_{\mathrm{TPA}} P_{\mathrm{p}}^2 P_{\mathrm{s}} - \chi_{\mathrm{FCA}} P_{\mathrm{p}}^3 P_{\mathrm{s}} + G_{\mathrm{B}} P_{\mathrm{p}} P_{\mathrm{s}},\end{aligned} \tag{9.2}$$

where γ_{3PA} and χ_{FCA} are the nonlinear loss terms arising from 3 photon absorption (3PA) and 3PA-induced free-carrier absorption, respectively. Fig. 9.1A plots a comparison of the estimated nonlinear losses at 1.5 μm and 2.8 μm within a 1.5- and 2.5-μm waveguide, respectively. These estimates suggest more than a 20-fold increase in power handling at longer wavelengths, which directly translates into much stronger Brillouin coupling. As an example, Fig. 9.1B plots the Brillouin amplification in the presence of linear and nonlinear loss as a function of input pump power for both telecom (blue) and mid-infrared (red) wavelengths. These predictions indicate that, due to improved power handling, mid-infrared

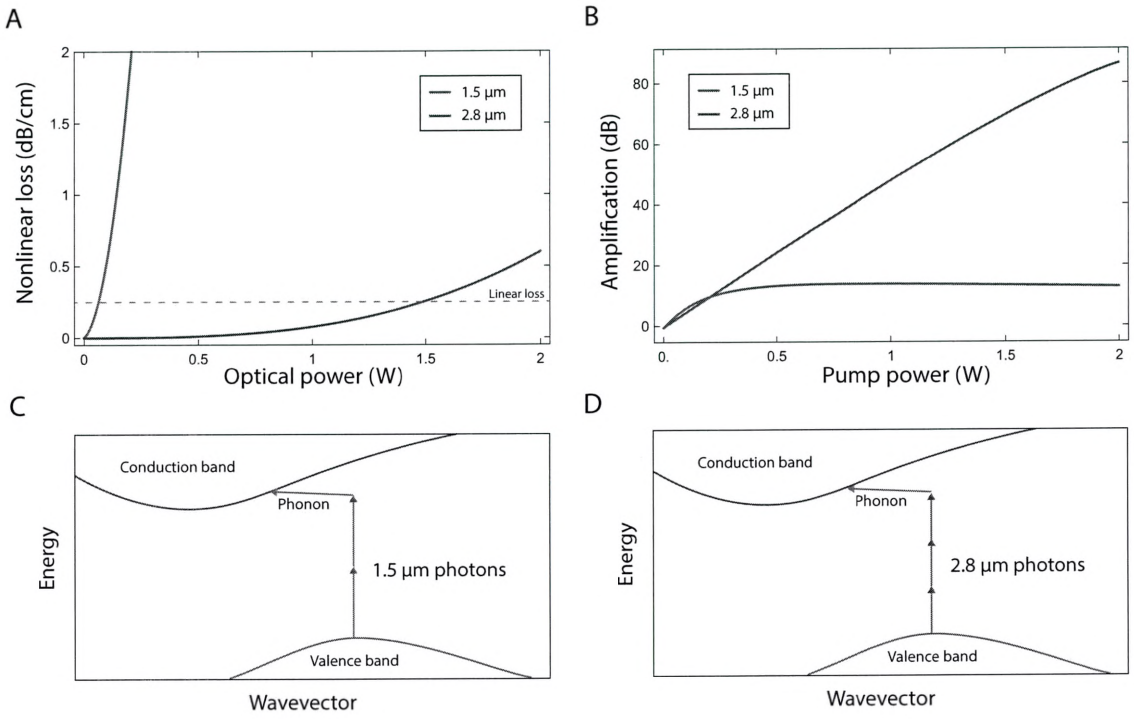

Figure 9.1: (A) estimated nonlinear propagation loss at telecom (blue) and mid-infrared (red) wavelengths. For the telecom (1.5 μm) wavelengths, two-photon-absorption (TPA) and TPA-induced free-carrier-absorption loss coefficients are taken from Ref. [29]. For mid-infrared wavelengths, three-photon-absorption (3PA) and 3PA-induced free-carrier absorption are estimated from bulk 3PA z-scan measurements [189] and free-carrier lifetimes in our silicon waveguides [29]. (B) Estimated small-signal (1 nW) Brillouin amplification in the presence of linear and nonlinear propagation loss within a 2-cm silicon Brillouin waveguide at telecom (blue) and mid-infrared (red) wavelengths. These estimates suggest that at telecom wavelengths, the available Brillouin gain plateaus to a maximum value of 15 dB—in sharp contrast to nearly unlimited Brillouin amplification possible using high-power mid-infrared light.

Brillouin amplification in silicon may be many orders of magnitude larger than what is possible at conventional telecom wavelengths, opening the door to radically enhanced nonlinear couplings for Brillouin-based laser, amplifier, and filter technologies.

Given this potential, the development of mid-infrared optomechanical waveguides and new experimental tools for mid-infrared device characterization would permit access to previously inaccessible regimes of Brillouin dynamics. In this chapter, we report our progress on the development of the mid-infrared experimental apparatus, optomechanical waveguides, and device concepts for future Brillouin-photonic technologies.

9.2 Experimental scheme

9.2.1 Mid-infrared challenges

The mid-infrared spectral region has been referred to as the new frontier of emerging photonic technologies [190]—the opportunities are as promising as they are challenging [191]. While this wavelength range has long been recognized as ideally suited for remote sensing, free-space communications and chemical detection technologies [191], mid-infrared photonic technologies have lagged behind their near-infrared and visible counter-parts. There are two principal reasons for this relative lack of maturity.

First, from 2.5 μm and beyond, propagation loss in silica-based optical fiber increases dramatically due to phonon absorption [192]. Lack of standard fiber-optic technologies in the mid-infrared not only inhibits otherwise routine routing of optical signals, but also limits the availability of standard components such as variable optical attenuators, high-speed modulators, polarization controllers, etc.—many of the essential building blocks of our nonlinear Brillouin laser spectroscopy system.

Second, the mid-infrared spectral region is hampered by a lack of high-speed, low-noise detectors. Traditionally, narrow-bandgap semiconductors have been used in the context of mid-infrared photo-detection, with energy scales that match those of mid-infrared photons. However, these systems are slow—typically limited to MHz frequencies, clearly not suitable for GHz-scale Brillouin spectroscopy. Moreover, these detectors are hindered by large levels of dark current, which grows exponentially with $K_{\mathrm{B}}T/E_{\mathrm{g}}$ [193]. As such, sensitive

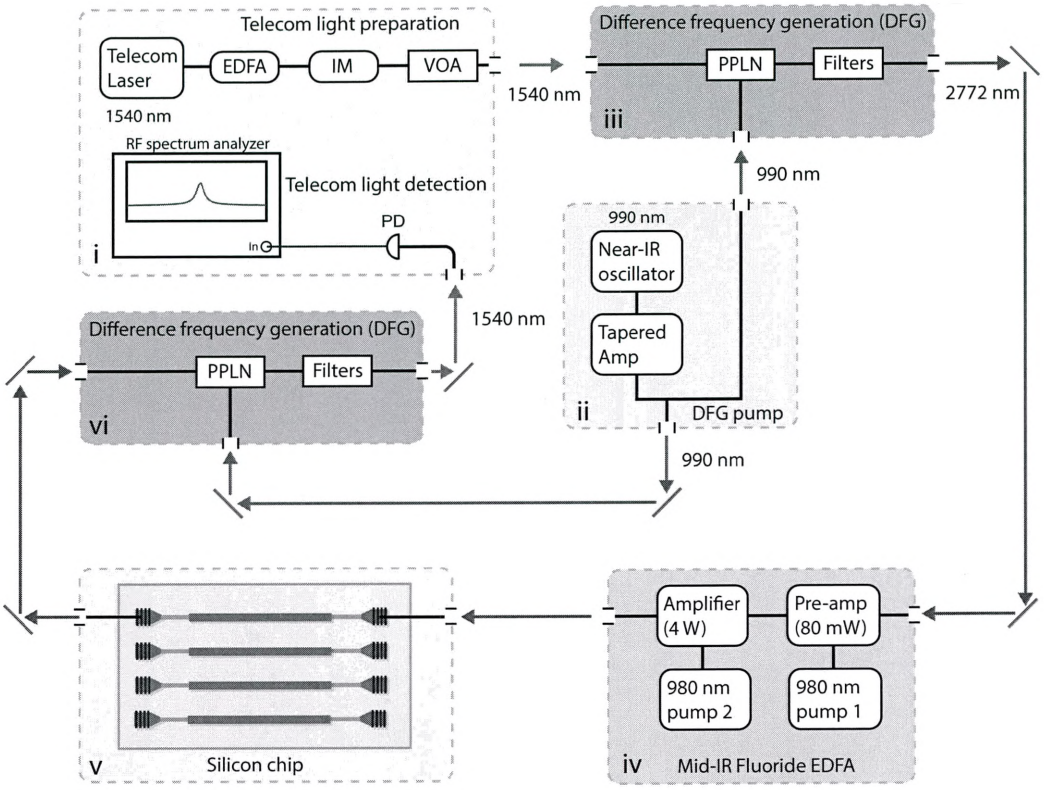

Figure 9.2: Experimental scheme for high-power nonlinear spectroscopy in the mid-infrared. We circumvent the lack of mid-infrared sources, modulators, and detectors using nonlinear wave mixing to convert between telecom and mid-infrared wavelengths. (i) Telecom light preparation and detection. We shape the spectral content of telecom light for nonlinear laser spectroscopy using a combination of amplifiers, modulators, and attenuators. Combined with 990 nm pump light (ii), the telecom-band light (1540 nm) is used to synthesize high-fidelity mid-infrared light (2772 nm) through difference frequency generation (DFG), as shown in sub-system (iii). Mid-infrared light is subsequently amplified by a two-stage, custom-made erbium-doped fluoride fiber amplifier (iv), which can boost ~ 0.1 mW mid-infrared signals to a level of more than 4 W. Amplified mid-infrared pump light is coupled, through grating couplers, onto a silicon chip, which may possess a range of Brillouin-photonic or other nonlinear optic devices. Light exiting these devices is then converted back to telecom-band frequencies through difference frequency generation (vi) for high-speed telecom-light detection (i). Our experimental strategy combines the advantages of mature telecom-band photonic devices with high-power mid-infrared optics to achieve large and highly controlled nonlinear couplings. EDFA: erbium-doped fiber amplifier; IM: intensity modulator; VOA: variable optical attenuator; PPLN: periodically poled lithium niobate; PD: photo-detector.

mid-infrared detection often requires some form of multi-stage thermo-electric or cryogenic cooling.

In light of these significant challenges, we have developed new strategies to generate, route, and detect mid-infrared light. Our approach, detailed below, allows us to explore new mid-infrared nonlinear optics in silicon with all the functionality of standard, high-performance telecom technologies.

9.2.2 General scheme

Our experimental strategy consists of 6 distinct operations and corresponding sub-systems, as diagrammed in Fig. 9.2. First, telecom light is prepared—using a combination of modulators, amplifiers, and variable optical attenuators—according to the desired experimental study. In the case of forward intra-modal Brillouin scattering experiments, for instance, a strong telecom-band carrier and weak intensity-modulated sidebands would synthesized at this stage. At the same time, a strong (up to 3 W) near-infrared (990-nm) pump laser is generated using a external-cavity diode laser and tapered amplifier (see Fig. 9.2ii). These light fields are subsequently combined within a periodically-poled lithium niobate (PPLN) sample, which, through a $\chi^{(2)}$-based difference frequency generation (DFG) process, is used to synthesize tunable mid-infrared light (see Fig 9.2iii). Provided a narrowband near-infrared pump source, nonlinear wavelength conversion of this form produces a carbon copy of the telecom-band light at a wavelength of approximately 2772 nm. In this way, we are able to generate tunable mid-infrared light whose spectral content can be shaped with standard telecom-band components.

To achieve powers necessary to demonstrate radically enhanced Brillouin couplings, mid-infrared light is amplified up to 4 W using a two-stage, erbium-doped fluoride fiber amplifier diagrammed in Fig. 9.2iv. Once at the desired power levels, the mid-infrared light is directed on-chip through grating couplers (see 9.2v), which may interface any number of amplifier, laser, or filter devices. The spectral content of light passing through any of these devices will be modified through the desired nonlinear process. Subsequently, this light can be converted back down to telecom wavelengths through the inverse difference frequency generation process (see Fig. 9.2vi), permitting high-speed photo-detection and

analysis with standard telecom-grade equipment (see Fig. 9.2i). This approach allows us to leverage inexpensive and high-performance telecom sources, modulators, and detectors for precision, high-power nonlinear spectroscopy in the mid-infrared. In what follows, we describe in greater detail the most important experimental sub-systems of our apparatus.

9.2.3 Difference frequency generation

Difference frequency generation is a three-wave nonlinear process in which two optical waves, generally referred to as the pump (ω_p) and signal (ω_s) waves, interact to produce an idler wave at their difference frequency ($\omega_\mathrm{i} = \omega_\mathrm{p} - \omega_\mathrm{s}$) [12]. As such, this process can be used as a form of classical wavelength conversion. In addition to energy conservation, efficient nonlinear conversion is governed by the phase-matching condition given by $k_\mathrm{p} = k_\mathrm{i} + k_\mathrm{s}$. This condition can be re-expressed in terms of the frequency-dependent refractive index ($n(\omega)$) as

$$n(\omega_\mathrm{p})\omega_\mathrm{p} = n(\omega_\mathrm{s})\omega_\mathrm{s} + n(\omega_\mathrm{i})\omega_\mathrm{i}. \tag{9.3}$$

From Eq. 9.3, we observe that the phase-matching condition cannot be satisfied in normally dispersive media where the index grows with frequency. To achieve robust difference frequency generation over a range of wavelengths, we use a temperature-controlled, periodically poled lithium niobate (PPLN) crystal. Here the periodic poling (or periodic inversion of the nonlinearity) creates a quasi-phase-matching condition of the form

$$k_\mathrm{p} = k_\mathrm{s} + k_\mathrm{i} + k_\mathrm{g}, \tag{9.4}$$

where k_g is the wavevector associated with the grating period λ_g (i.e., $k_\mathrm{g} = 2\pi/\lambda_\mathrm{g}$). In this way, the grating period can be chosen to permit phase-matched operation with various signal and idler frequencies. Moreover, thermal control of the periodically poled lithium niobate sample allows us to fine tune the phase-matching condition in a dynamical, *in situ* fashion.

When optimally phase-matched, difference frequency generation produces an idler wave with an efficiency (η) given by [194]

$$\eta = \frac{2\omega_{\mathrm{i}}^2 d_{\mathrm{eff}}^2 L^2 I_{\mathrm{p}}}{c^3 \epsilon_0 n(\omega_{\mathrm{s}}) n(\omega_{\mathrm{i}})}, \tag{9.5}$$

where d_{eff} is the $\chi^{(2)}$ nonlinear coefficient (with units of [pm]/[V]), L is the effective interaction length, and I_{p} is the pump intensity.

The experimental system used to produce and characterize difference frequency generation is shown in Fig. 9.3A-B. A telecom-band signal wave and a near-infrared pump wave are combined along the same optical path using a long-pass dichroic mirror. Subsequently, the light is focused using an off-axis parabolic mirror with a focal length of 10.1 cm. This reflective element places the beam waist of each wave (46 μm and 61 μm, respectively) at the mid-point of the 5-cm-long periodically poled lithium niobate crystal (micrograph shown in Fig. 9.3C). The PPLN crystal is housed within a high-temperature oven with sub-°C stability. The PPLN crystal grating is 30 μm, permitting phase-matched difference frequency generation at a nominal temperature of 140 °C. The mid-infrared idler is then isolated from the pump and signal waves using a Germanium window, after which, light is collected on a PbSe AC-coupled detector. To improve the sensitivity of our measurement, we modulate the pump-light intensity using an optical chopper, and then measure the signal through lock-in detection. Thus, by filtering out the 990 nm pump light, the detected lock-in signal originates entirely from generated mid-infrared light.

Using this experimental scheme, we use pump and signal powers of 860 mW and 290 mW to generate 0.2 mW of mid-infrared idler light. This corresponds to an efficiency of 0.07%, in rough agreement with our theoretical estimate of $\sim 0.2\%$. The variation between our measurements and predictions may be attributed to non-idealities in the pump beam profile that result in reduced spatial overlap between the pump and signal fields.

Figure 9.3D shows the normalized idler power as function of signal wavelength, revealing a characteristic phase-matching spectrum with a FHWM of about 6 nm. This same bandwidth corresponds to a mid-infrared range of approximately 20 nm. This phase-matching condition can also be varied by controlling the environmental temperature of the sample, as shown in Fig. 9.3E. The flexibility provided by both the telecom signal source as well as the PPLN temperature controller allows us to readily tune the mid-infrared idler wavelength

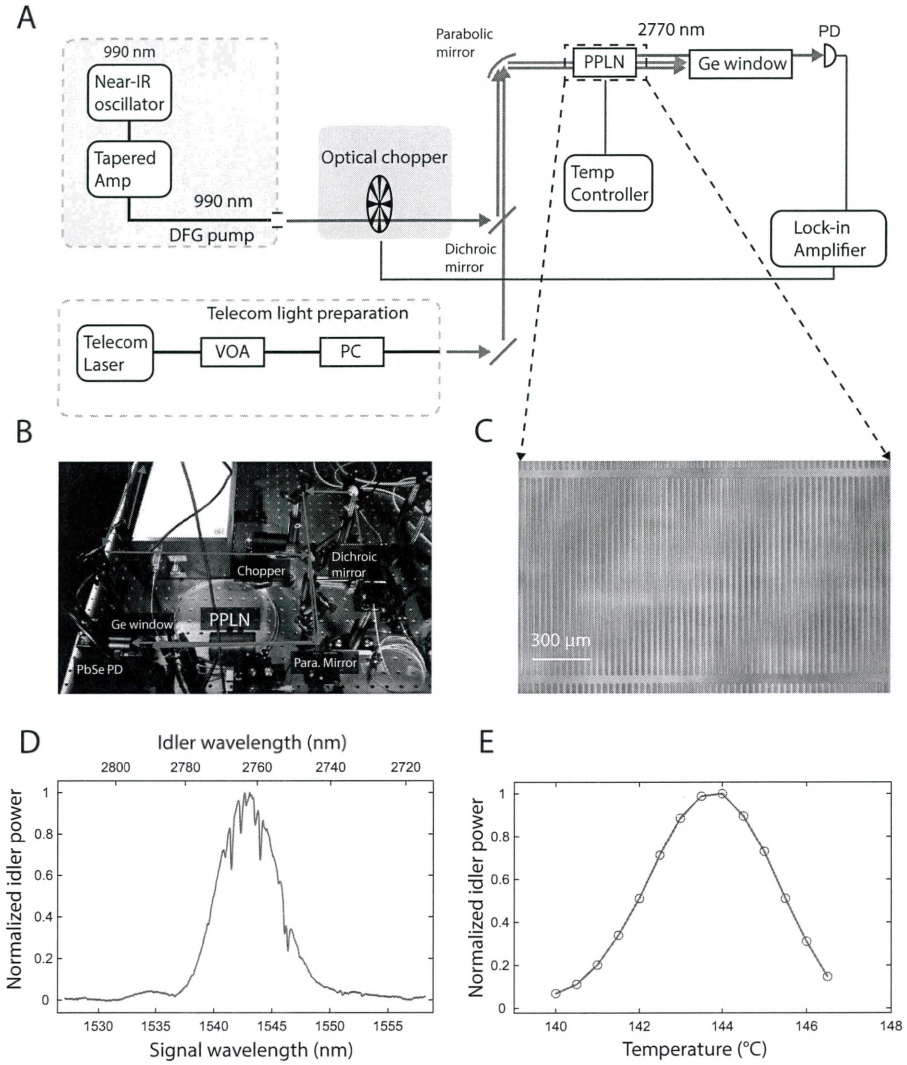

Figure 9.3: Difference frequency generation for mid-infrared nonlinear device characterization. (A) Experimental scheme used to generate and detect mid-infrared light. Telecom signal light and high power (up to $\sim$ 3 W) 990 nm pump light are combined in the same optical path using a long-pass dichroic mirror and subsequently focused into a temperature-controlled periodically poled lithium niobate (PPLN) crystal. Within this $\chi^{(2)}$ quasi phase-matched nonlinear medium, mid-infrared light is generated through difference frequency generation (DFG). Following the PPLN sample, mid-infrared light is isolated from the telecom and near-infrared light are filtered using a Germanium window. We use an optical chopper and a lock-in amplifier for high-sensitivity detection of the generated mid-infrared light. PC: polarization controller; VOA: variable optical attenuator; PPLN: periodically poled lithium niobate. (B) Photograph of the experimental apparatus. (C) Optical micrograph of the periodically poled lithium niobate sample. (D) Normalized mid-infrared idler power as a function of signal wavelength, revealing a characteristic sinc-like response with a 6-nm FWHM bandwidth. (E) Normalized idler power as a function of temperature. The thermo-optic response of the PPLN crystal permits fine tuning of the phase-matching condition.

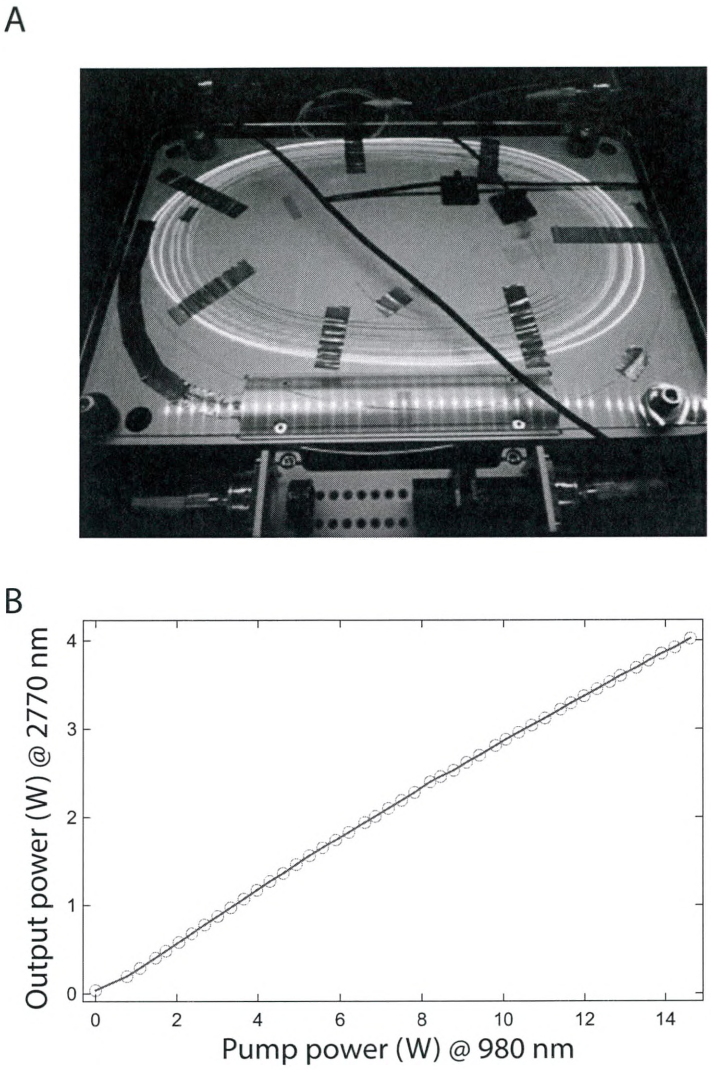

Figure 9.4: (A) Photograph of the two-stage mid-infrared fiber amplifier. The pre-amplifier is housed underneath the high-power amplifier. A mid-infrared isolator prevents parasitic lasing. (B) Output mid-infrared power as a function of 980-nm pump power. 980-nm pump powers are estimated from the supplied current and efficiency of the 980-nm pump source.

over more than 30 nm.

9.2.4 Mid-infrared amplifier

As described above, nonlinear mixing within a temperature-controlled PPLN crystal permits flexible mid-infrared light generation, with total output powers approaching the mW level. However, to take advantage of silicon's low nonlinear loss properties and achieve the desired nonlinear Brillouin couplings, this light must be amplified to the Watt level; this degree of amplification would require more than 30 dB of gain.

It is well known that the rare-earth ion Erbium can be used to produce efficient optical amplification at 1.55 μm wavelengths, providing the basis for efficient erbium-doped silica-based fiber amplifiers in the c-band [172]. Less known, however, is that erbium possesses an even stronger and broader gain spectrum at 2.8 μm. Unfortunately, this amplification window is inaccessible in traditional silica fiber, as multiphonon absorption renders the material opaque past 2.5 μm [192]. By contrast, fluoride fiber systems, in particular those based on ZBLAN glass, are excellent host material for erbium. Erbium-doped fluoride fibers have recently been leveraged for high-power amplifiers [195], lasers [196, 197], and supercontinuum generation [198]. In the context of amplifiers, the 2.8 μm transition is unique as it does not involve the ground state. As such, the doped-fiber retains its low-loss properties in the absence of optical pumping—in contrast with the 1.55 μm transition.

We use a two-stage, fluoride-based EDFA to achieve record high levels of amplification necessary to bring a $\sim$ 0.2-mW signal to the multiple-Watt level. This custom-made system (Femtum 2800), comprised of a low-noise pre-amplifier and high-power final amplifier, is displayed in Fig. 9.4A. Each amplifier is powered by a 980-nm pump diode of maximum output power 30 W and 9 W, respectively. The pre-amplifier boosts $\sim$mW mid-infrared optical signal to approximately 80 mW. The light is subsequently transmitted through a mid-infrared free-space isolator, which prevents parasitic lasing that would otherwise arise from unwanted back-scatter, and is then coupled into the high-power amplifier.

We characterize this two-stage amplifier system using as low as 0.1 mW of light mid-infrared DFB laser, whose center frequency falls within the gain bandwidth of the amplifier. Figure 9.4B plots the mid-infrared output power as a function of 980-nm pump power,

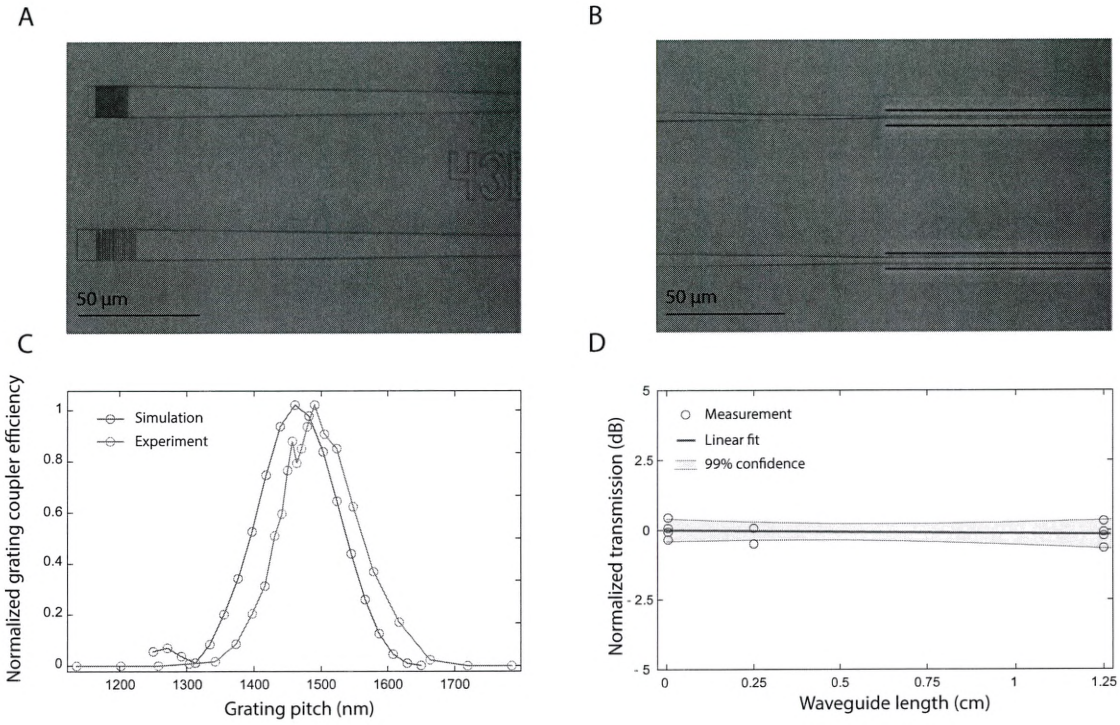

Figure 9.5: (A) Optical micrograph of telecom-band (upper) and mid-infrared (lower) grating couplers. (B) Corresponding suspended optical waveguides. (C) Simulated and measured mid-infrared grating coupler efficiencies as a function of grating pitch (nm). The experimental data is obtained by analyzing the total transmission through the waveguide system using a 2770-nm distributed feedback (DFB) laser, while the simulated data is obtained from finite-element method (COMSOL) simulations of a single grating coupler. Data are normalized to the peak values for a comparison with the simulation. (D) Preliminary cut-back measurements showing the normalized transmission as a function of waveguide length. The linear fit corresponds to a linear propagation loss of 0.12 ± 0.17 dB/cm, which suggests the potential for low propagation losses in the mid-infrared. These measurements are taken directly after the HF-wet etch process.

demonstrating a total output power of 4 W at a maximum pump power of 14 W. Thus, overall, this two-stage amplifier provides more than 40 dB of gain. This amplifier, in conjunction with our difference frequency generation system, allows us to synthesize spectrally re-configurable, high-power mid-infrared light.

9.2.5 Silicon devices

In this section, we describe the chip alignment setup and preliminary measurements of passive silicon devices. We couple mid-infrared light into our silicon waveguides through use of grating couplers of the type shown in Fig. 9.5A. Reference devices optimized for telecom wavelengths are fabricated adjacent to the those intended for mid-infrared wavelengths. The mid-infrared grating design consists of 10 equally spaced teeth, with a nominal pitch of 1500 nm. Simulated grating coupler efficiencies are presented in Fig. 9.4C.

We experimentally characterize our devices using a mid-infrared DFB laser (Nanoplus DFB-260300) in conjunction with lock-in detection to enhance sensitivity. Light emitted from the DFB laser is transmitted through a mid-infrared half waveplate for polarization control and subsequently coupled into a single-mode ZBLAN patch cord, which channels the light towards the desired grating coupler. We fabricate grating coupler designs with a range of pitch parameters; normalized transmission measurements are presented in Fig. 9.4D, showing good agreement with the simulated behavior. We also fabricate devices of various suspended waveguide lengths to characterize the linear propagation losses through cut-back measurements. Normalized transmission measurements are plotted as a function of waveguide length in Fig. 9.4D. A linear fit from these data suggests potential for low propagation loss (0.12 ± 0.17 dB/cm), though additional measurements are required for greater confidence levels. This is particularly true in the case of cut-back measurements, which require consistent fiber-to-chip separation and grating coupler performance. To eliminate these potential sources of error, future measurements could involve the characterization of silicon ring resonators to determine the intrinsic propagation losses. Finally, we note that the measurements presented in Fig. 9.4D were taken immediately following the final HF wet etch. Preliminary measurements over the course of many hours suggest that native oxide growth on the silicon waveguide surface introduces additional loss mechanisms. Fur-

ther study and innovation in our fabrication process may be therefore necessary to more permanently maintain low propagation loss.

9.3 Conclusion and outlook

In this chapter, we have demonstrated the essential capabilities necessary to (1) perform high-power mid-infrared nonlinear spectroscopy in silicon and (2) manipulate Brillouin dynamics through radically enhanced mid-infrared pump powers. We have developed and characterized a robust difference frequency generation system, allowing us to spectrally translate telecom light to the mid-infrared in a tunable and reconfigurable fashion. Using a fluoride-based erbium-doped fiber amplifier, we have also demonstrated ultra-high gain amplification of small ($\sim$ 0.2 mW) mid-infrared signals to the 4 W level. In addition, we have designed and fabricated mid-infrared silicon photonic devices with good grating coupler performance and moderate-to-low linear losses. The ability to access nonlinear couplings that are potentially orders of magnitude stronger than those possible at telecom wavelengths lays the groundwork for a powerful new set of integrated nonlinear photonic device physics. In this section, we highlight many of these opportunities now within reach.

9.3.1 High power Brillouin amplifiers and lasers

Given the lack of TPA-induced nonlinear loss mechanism, the mid-infrared spectral region opens the door to levels of Brillouin amplification not previously possible in linear silicon waveguide systems. As estimated in Fig. 9.1B, small signal amplification of more than 80 dB may be possible; this would represent a $> 10^7$-fold improvement beyond what is possible in linear waveguide systems at 1.55 μm. Such large degrees of amplification also have important consequences in the context of silicon Brillouin laser systems. Through Schawlow-Townes line narrowing, which scales inversely with the circulating Stokes power (see Eq. 9.6), the newly accessible intracavity powers in excess of 1 W may permit sub-Hz phonon linewidths. Moreover, since the accessible intracavity pump powers may be orders of magnitude higher than the pump threshold, we have the opportunity to fundamentally change the regime of linewidth narrowing dynamics. Specifically, by increasing the phonon

dissipation rate—readily achieved by tailoring the waveguide geometry—such that it significantly exceeds that of the optical fields, the silicon-based Brillouin laser will exhibit optical linewidth narrowing. In this case, the resulting optical linewidth is given by [81]

$$\Delta\nu = \frac{\gamma}{4\pi N_{\mathrm{s}}}\left(n_{\mathrm{B}}^{\mathrm{th}} + n_{\mathrm{s}}^{\mathrm{th}} + 1\right), \tag{9.6}$$

where γ is the optical dissipation rate, $n_{\mathrm{B}}^{\mathrm{th}}$ is the thermal phonon occupation, $n_{\mathrm{s}}^{\mathrm{th}}$ is the thermal Stokes occupation, and N_{s} is the coherent Stokes number. With mid-infrared pump powers, integrated silicon Brillouin lasers with Hz-level Schawlow-Townes optical linewidths may be feasible (see Fig. 9.6A), representing orders-of-magnitude improvement beyond state-of-the-art mid-infrared semi-conductor lasers [199].

9.3.2 Optomechanical cooling

The radically enhanced nonlinear coupling strengths available in the mid-infrared can also be used to access new regimes of Brillouin-based optomechanical cooling, as we demonstrate for the first time in Chapter 8. In the case of continuous (or linear-waveguide) systems, mid-infrared pump powers of 1 W could be used to reduce the occupation of phase-matched phonons by nearly a factor of 10 (see Fig. 9.6B), which would directly translate into an improvement in the optical noise figure. At the same time, combining optomechanical cooling dynamics with the resonantly enhanced structures of Chapter 4, effective cooling factors of 10-100 may be possible, allowing us to improve the optical noise figure of resonant Brillouin amplifiers by orders of magnitude.

In conjunction with mid-infrared silicon-based Brillouin lasers, the new regimes of optomechanical cooling can be used for phononic dissipation engineering [186], allowing us to tune the elastic damping to access the desired regime of temporal linewidth-narrowing dynamics. Moreover, in the case of optical linewidth narrowing, the use of optomechanical cooling reduces the fundamental optomechanical noise present in the system (see $n_{\mathrm{B}}^{\mathrm{th}}$ in Eq. 9.6), permitting further reduction of the optical linewidth beyond the conventional Schawlow-Townes limit.

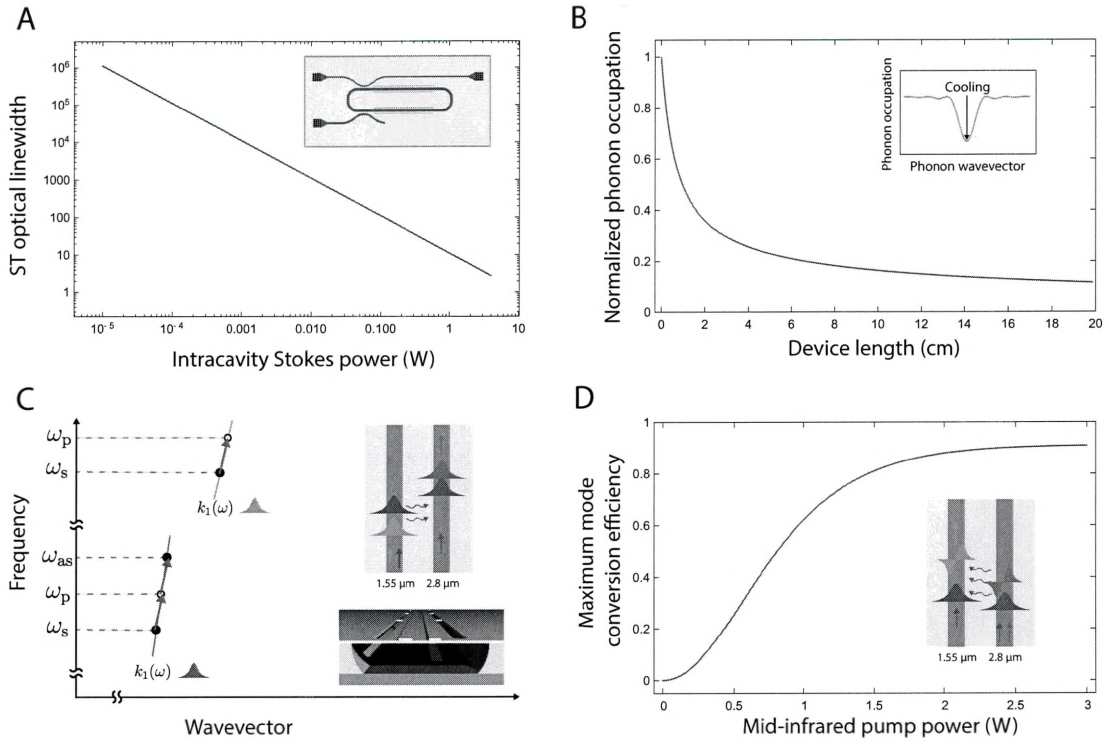

Figure 9.6: (A) Estimated optical Schawlow-Townes linewidth for a mid-infrared silicon Brillouin laser operating in the optical linewidth narrowing regime (i.e., acoustic dissipation rate (Γ) > optical dissipation rate (γ). (B) Theoretical optomechanical cooling in a continuous system as a function of device length in the case of large Brillouin coupling accessible in the mid-infrared; here $G_{\mathrm{B}} = 470\ \mathrm{W}^{-1}\mathrm{m}^{-1}$, $P_{\mathrm{p}} = 1$ W). Adapted from Ref. [99]. (C) Phase-matching considerations for an intra-modal photonic-phononic emit-receive (PPER) process in which the emit waveguide channels telecom-band light and the receive waveguide guides mid-infrared light. In this case, pump and Stokes waves at 1.55 μm drive a traveling-elastic wave, which in turn, phase modulates light at 2.8 μm. PPER illustration adapted from Ref. [140]. (D) Maximum non-reciprocal mode conversion efficiency possible through inter-modal PPER process as a function of mid-infrared pump power. Near-unity conversion efficiency should be possible, highlighting potential for broadband isolator and circulator technologies with low insertion loss.

9.3.3 Photonic-phononic emit-receive devices

Another promising opportunity for research in the mid-infrared involves the use of the photonic-phononic emit-receive (PPER) devices described in Chapter 5. At telecom wavelengths, we have used these systems to demonstrate RF-photonic filtering schemes with passbands that are nearly 100× narrower than what is possible with conventional silicon-photonic devices. Because these structures involve two separate optical waveguides that are coupled through traveling elastic waves, one can think of these systems as producing a form of wavelength conversion [140]. In particular, in the case of forward intra-modal Brillouin scattering, the phase-matching conditions are reasonably well satisfied over extremely large wavelength shifts in spite of waveguide and material dispersion, as illustrated by Fig. 9.6C. In this way, we may be able to use these PPER dynamics to achieve at least one direction of wavelength conversion. For instance, we can imagine using 1.55 μm light in the emit waveguide to transduce a traveling elastic wave, which can then phase-modulate mid-infrared light in the receive waveguide. The modulated mid-infrared light can then be frequency-converted to the telecom band and detected with a high-speed receiver. Since this particular implementation requires only a single wavelength conversion step, it is likely one of the most accessible initial demonstrations.

Furthermore, generalizing these PPER structures to optical waveguides that support multiple optical spatial modes opens the doors to new, high-performance non-reciprocal devices. Through recent experiments, we have achieved proof-of-concept demonstrations of this form of non-reciprocal modulation at 1.55 μm, which produces unidirectional mode conversion over large ($>$ 1 nm) bandwidths [187]. However, nonlinear losses at 1.55 μm limit the power handling of the device so as to limit the overall modulation efficiency to 1%; in other words, only 1% of the light in the receive waveguide is mode converted through inter-modal Brillouin scattering. To adapt this device physics to create a broadband isolator, we must increase the pump power to achieve efficiencies that approach unity. As such, the ability to access large nonlinear couplings in the mid-infrared may provide a promising avenue to achieve such efficiencies (as shown in Fig. 9.6D), opening the door to ultra-broadband, optically driven acousto-optic silicon isolators.

9.3.4 Other optical nonlinearities

Beyond Brillouin interactions, the radically enhanced optical powers supported in mid-infrared silicon waveguide systems allows us to shape the strength and character of interactions arising from other nonlinearities, such as Raman or Kerr nonlinearities [12, 200]. In the context of Raman processes, the mid-infrared spectral regions opens to door to powerful Raman-based amplifier [201] and laser technologies [202]. Relative to Brillouin interactions, Raman-based amplifiers benefit from much larger gain bandwidths, and in particular, lower thermal noise given the high frequencies ($\sim$ 15 THz) of the optical phonon that mediate such nonlinear interactions. Thus, given that the thermal occupation is much less than 1, the optical noise factor of these devices may actually approach quantum limits (as predicted in Chapter 7). With regard to new types of mid-infrared lasers, the naturally large frequency shifted associated with Raman processes could prove advantageous for shifting large optical powers over several hundred nanometers in a highly efficient manner.

Kerr-based processes, resulting from the intensity dependence of the refractive index, also show great promise for mid-infrared silicon-photonic technologies. For instance, degenerate four-wave mixing processes in the mid-infrared may enable large levels of broadband parametric amplification [203, 204]. Since these interactions are electronic in nature, the optical noise figure of such Kerr-based amplifiers is not limited by any sources of optomechanical noise. Furthermore, resonant structures, such as those we demonstrate in this dissertation (see Chapter 4 and 5), may be used to harness this form of parametric gain to create high-performance resonantly enhanced amplifiers [205], continuous wave optical parametric oscillators [206], and squeezed-light sources [207] in the mid-infrared. Four-wave mixing processes may also prove useful in the context of silicon-based wavelength conversion for an array of important classical and quantum applications [193, 208].

Chapter 10

Conclusion

10.1 Summary

In this dissertation, we have developed and explored new strategies to shape and manipulate Brillouin dynamics through modal engineering, optical feedback, active silicon photonic control, synchronization, optomechanical reservoir engineering, and high-power mid-infrared photonics. Individually and collectively, these newly developed tools lay the groundwork necessary to take full advantage of the unique properties of Brillouin interactions for the next generation of silicon-based lasers, amplifiers, filters, and non-reciprocal devices within CMOS-foundry-compatible silicon photonic circuits.

Fundamental to this dissertation research is our ability to use phase-matching to shape traveling-wave Brillouin dynamics as we so desire. Through structural control, we have created Brillouin couplings that were not previously possible in conventional silicon photonic waveguides. Moreover, we have shown that multimode waveguide engineering allows us to shape the fundamental Brillouin physics through inter-modal scattering processes. Due to the unique phase-matching conditions, such interactions produce a type of dispersive symmetry breaking that decouples the Stokes (phonon generation) from the anti-Stokes (phonon annihilation) process, yielding single-sideband gain in a forward scattering geometry. The simple amplification dynamics and modal degrees of freedom enabled through this new on-chip process provide an elegant framework for practical Brillouin-based technologies in silicon photonics.

By introducing optical feedback in the form of a high-Q multimode resonators, we have shown that we are able to radically enhance this single-sideband process, transforming the modest $\sim$ 2-dB gain possible in a linear waveguide into more than 30 dB. Due to phase-matching, this high-gain amplification is intrinsically unidirectional, yielding large non-reciprocal contrast with no insertion loss for the first time in silicon photonics. Furthermore, when the total optical gain for the Stokes wave exceeds the round-trip loss, we show that this system begins to self-oscillate, representing the first demonstration of Brillouin lasing in silicon. This inter-modal laser system we have demonstrated is a dramatic departure from conventional Brillouin laser designs, yielding unprecedented size and frequency scalability and new degrees of control through mode engineering. Moreover, due to the unique spatio-temporal dynamics of the interacting optical and elastic waves, this system allows us to explore an intriguing limit of 3-wave laser physics. We have developed new experimental and theoretical tools to characterize and understand these dynamics.

Building on this work, we have developed new strategies to control the laser emission through injection locking. By introducing a coherent seed, we have shown that we are able to control the laser emission with sub-Hz resolution. In addition, due to the unique spatio-temporal dynamics of the system, we are able to dramatically reduce the phase-noise of the laser emission, achieving approximately 7 orders of magnitude phase-noise suppression below the Schawlow-Townes limit.

Through a combination of experimental and theoretical analysis, we have shown how fundamental optomechanical fluctuations place limitations on the linewidth and effective noise figure of Brillouin lasers and amplifiers. In our quest to further mitigate noise in Brillouin-photonic systems, we have demonstrated a new type of traveling-wave optomechanical control. Harnessing the symmetry breaking produced by phase-matching in multimode systems, we have shown that spontaneous anti-Stokes Brillouin scattering can be used to selectively cool propagating phonons in a continuous system. Through a new type of wavevector-resolved phonon spectroscopy, we have shown that this process produces a cold thermal window in wavevector space which can then be leveraged to suppress noise and control dissipation for improved performance of Brillouin-based amplifiers, lasers, and filters.

Through our collaboration with Sandia National Laboratories, we have shown that this flexible Brillouin-based physics is not only possible with prototype-scale electron-beam lithography, but also accessible in CMOS-foundry compatible systems. Our results have demonstrated that, due to improved precision and uniformity, CMOS-foundry fabrication yields Brillouin amplifier, laser, and filter technologies with significantly enhanced performance in terms of Brillouin coupling, optical losses, and acoustic Q-factors. These results reveal that Brillouin devices are remarkably amenable to standard silicon photonic device fabrication, a crucial step towards co-integration within complex photonic circuits. Building on these results, we have developed a wide range of active-silicon photonic circuit designs that synergistically combine Brillouin device physics with active silicon photonic control.

10.2 Impact

In the broader context of silicon photonics, the new device physics we have introduced in this dissertation addresses long-standing challenges in terms of silicon-based lasers, amplifiers, and non-reciprocal elements. Moreover, our efforts to adapt silicon-based Brillouin devices to standard CMOS processes is a significant step towards the introduction of these technologies into production-scale photonic circuits. With the new tools presented here, we have the ability to shape Brillouin dynamics and improve performance according to the desired application.

While the strategies we have explored are individually compelling, together they are significantly more powerful. For instance, harnessing optomechanical cooling physics within Brillouin amplifiers enables both noise mitigation and dissipation engineering, allowing us to improve the noise figure and tune the gain bandwidth. Such performance can be additionally enhanced through the use of optical feedback to radically boost both the unidirectional amplification and cooling. With our new active designs, these devices will be thermally tunable, permitting reconfigurable operation across the entire c-band. Furthermore, access to strong mid-infrared nonlinear couplings may permit effective nonlinear couplings that are orders of magnitude larger than possible at telecom wavelengths, admitting new regimes of optomechanical cooling, laser dynamics, and amplification physics.

Adapting the strategies developed in this dissertation to other nonlinearities opens the door to a diverse array of advanced and complementary silicon photonic devices. We have seen, from the Brillouin amplification dynamics, that the noise figure depends critically on the thermal phonon occupation. As a result, high phonon frequencies are desirable for the best noise performance. In this respect, Raman interactions may offer important advantages in applications with low-noise tolerance since the average thermal occupation of THz-frequency phonons is nearly zero. Thus, adapting our resonantly enhanced amplifier concept to Raman interactions may be a key step toward high-gain, ultra-low noise figure amplifiers in silicon photonics. In addition, Kerr-based interactions, such as four-wave mixing, may be of great utility due to the potential to achieve quantum-limited performance. By engineering multimode Kerr couplings, we may be able to use the same resonant and non-resonant design strategies developed in this dissertation. Importantly, we can leverage phase-matching in inter-modal processes to achieve unidirectional amplification and back-scatter immune optical parametric oscillation. Furthermore, lack of thermal noise in these electronic-based nonlinearities enables important quantum applications in single-photon generation [17, 18] and quantum frequency conversion [19]. In this way, we can use a systems-level approach to identify, harness, and manipulate the unique properties of each nonlinearity to create the next generation of powerful integrated photonic circuits.

Appendix A

Standard fabrication process

Brillouin devices are fabricated from a single crystal silicon-on-insulator wafer with 215 nm of silicon atop 3 μm buried oxide. Optical waveguides are patterned with hydrogen silsesquioxane (HSQ) negative photoresist using electron-beam lithography. After development in Microposit^{TM} MF^{TM}-312, we perform a chlorine reactive ion dry etch (RIE) to remove 80 nm of silicon. Slots are patterned with either ZEP520A or CSAR positive photoresist through a second electron-beam exposure. These slots are subsequently developed with Xylenes. We then perform a second chlorine RIE etch, which removes the silicon in the slot regions down to the buried oxide. Finally, we perform a wet etch with 49% hydrofluoric acid to remove the oxide undercladding and suspend the Brillouin-active regions of the device.

Appendix B

Silicon Brillouin laser: system parameters

Optical properties	value
L	4.576 cm
FSR (symmetric)	1.614 GHz
FSR (anti-symmetric)	1.570 GHz
r_2	0.54
μ_2	0.84
r_1	0.97
μ_1	0.24
α_2	15.8 m^{-1}
α_1	6.0 m^{-1}
$v_{g,2}$	7.163 $\times 10^7$ m/s
$v_{g,1}$	7.385 $\times 10^7$ m/s
γ_2	2π 481 MHz
γ_1	2π 83 MHz
$I_{threshold}$	5.4×10^6 Wcm^{-2}
Pump linewidth	13 kHz

Table B.1: Optical parameters

B.1 Data analysis

In this section, we describe the methods used to analyze the experimental data. This section has been reproduced and adapted from the supplementary materials of Ref. [95].

Acoustic properties	value
Ω_B	2π 6.02 GHz
g	11.1 kHz
Γ_0	2π 13.1 MHz
q	4.5×10^5 m^{-1}
$v_{b,group}$	826 m/s
$v_{b,phase}$	8.4×10^4 m/s

Table B.2: Acoustic parameters

Nonlinear optical properties	value
Brillouin Gain	
G_B	400 W^{-1}m^{-1}
Kerr coefficients	
γ_k^{11}	74 ± 11 m^{-1}W^{-1}
γ_k^{22}	71 ± 11 m^{-1}W^{-1}
$\gamma_k^{12} = \gamma_k^{21}$	44 ± 7 m^{-1}W^{-1}
TPA coefficients	
β^{11}	34 ± 10 m^{-1}W^{-1}
β^{22}	30 ± 9 m^{-1}W^{-1}
$\beta^{12} = \beta^{21}$	20 ± 6 m^{-1}W^{-1}
FCA coefficients	
γ^{111}	900 ± 400 m^{-1}W^{-2}
γ^{222}	720 ± 430 m^{-1}W^{-2}
$\gamma^{211} \approx \gamma^{122}$	310 ± 200 m^{-1}W^{-2}

Table B.3: Nonlinear optical parameters

We use high-resolution heterodyne spectroscopy to characterize the power and linewidth of the emitted Stokes light. This involves synthesizing an optical local oscillator (LO), which is 44 MHz blue-detuned from the incident pump field, and combining it with the emitted Stokes light on a high-speed photo-receiver (see Fig. 3.6A).

Through careful calibration of the detector response and the optical local oscillator power, these microwave spectra provide an accurate measure of the Stokes power as well as the optical linewidth relative to that of the pump wave. By simultaneously measuring the power and the heterodyne beat note from a reference pump wave (beat note produced by the reference pump wave and the LO), we can calibrate the power spectral density of the microwave spectrum—thus allowing us to determine the emitted Stokes power. Also, because the optical LO is synthesized from the pump laser, the heterodyne beat note gives

an accurate measure of the emitted Stokes linewidth when the emitted Stokes spectrum is broader than the pump laser (below threshold). Above threshold (when the beat note linewidth is much smaller than that of the pump linewidth), we use the sub-coherence self-heterodyne technique to characterize the pump-Stokes coherence.

B.1.1 Slope efficiency

In Fig. 3.6C, we plot the Stokes power as a function of injected pump power. The output (on-chip) Stokes power is determined through a calibrated heterodyne measurement. While performing this heterodyne spectroscopy, we simultaneously measure the input and transmitted pump powers through the chip. By monitoring the input and transmitted pump powers and using the racetrack resonator properties analyzed in Section 3 (including coupling and linear loss), we infer the detuning of the pump from resonance and estimate the intra-cavity pump powers. The data presented in Fig. 3.6C represent the measured Stokes powers (left y-axis) as a function of intracavity pump power (top x-axis). For comparison, the bottom x-axis assumes a zero-detuned resonant enhancement factor (≈ 1.8), showing the effective input pump power. The right y-axis indicates the estimated intracavity Stokes power assuming the intracavity to bus waveguide power conversion factor of 0.0075.

B.1.2 Linewidth measurements

This section discusses the analysis of the data presented in Fig. 3.7C.

Heterodyne measurements

Below threshold, we use standard heterodyne spectroscopy to determine the linewidth of the phonon field. To avoid spectral distortion due to pump mode hopping, we acquire rapid spectral traces at different output Stokes powers. We then apply a moving average (with a bin size smaller than linewidth to avoid distortion) to spectrally smooth the data for consistent Lorentzian fits. The data presented in Fig. 3.7C are acquired using a resolution bandwidth of 20 kHz. Above threshold, the phonon linewidths are resolution-bandwidth limited. To simplify the representation of the data in Fig. 3.7C, we only include spectral measurements below threshold.

Sub-coherence self-heterodyne measurements

We determine the excess phase-noise linewidth of the Stokes wave relative to the pump wave (i.e., phonon linewidth) above threshold using the sub-coherence delayed self-heterodyne technique discussed in Section 3.5. To do this, we fit the theoretical spectrum (Eq. 3.83) to the measured spectra; since data for these measurements is obtained using the max hold functionality, we must be careful to analyze only the spectra that have not been distorted due to frequency jitter. We extract the phonon linewidth by fitting the power, pump linewidth, and phonon linewidth to the peak spectral density and the fringe-like portion of the spectrum (the feature highlighted in Fig. 3.9C), which is most sensitive to phonon phase noise. This method is only possible at large Stokes powers, where there is sufficient signal to noise so that the fringes do not become obscured by the noise floor.

As discussed in the Fig. 3.9 caption, instabilities in the fiber delay line of the interferometer add approximately ~ 500 Hz of phase noise to the sub-coherence self heterodyne measurements (obtained from a self-heterodyne measurement using an AOM as the frequency shifter). Therefore, to get an accurate measurement the phonon phase-noise within the silicon Brillouin laser, we normalize our sub-coherence self-heterodyne measured linewidths by subtracting the residual phase noise.

For a comparison with the spectral measurements below threshold (not resolution bandwidth limited), we convert the beat-note power into a peak spectral density (x-axis of Fig. 3.7C) by using the fact that the integral of a Lorentzian is proportional to the peak height multiplied by the width. In this way, we convert the sub-coherence spectrum into an equivalent Lorentzian that has a FWHM given by the measured linewidth and a peak height given by the peak spectral density. Thus, by dividing the Stokes power by the measured linewidth (and multiplying by $2/\pi$), we obtain the equivalent peak spectral density used for this comparison (plotted in Fig. 3.7C).

As discussed, these sub-coherence self-heterodyne measurements demonstrate the pump-Stokes coherence produced by optical self-oscillation in this system. While these data permit a measurement of the phonon linewidth and corroborate the regime of dynamics (presence of fringes and measurements of phonon linewidths below that of the pump, see Section 3.5),

the data do not yield sufficient precision to clearly determine the linewidth narrowing trend as function of total Stokes power. To attain the necessary level of precision, this type of analysis would likely require more sophisticated control of all variables that influence laser oscillation. Nevertheless, these data establish an upper bound on the phonon linewidths above threshold and clearly reveal the pump-Stokes phase coherence unique to this limit of Brillouin laser oscillation.

Appendix C

Resonantly enhanced amplifier: system parameters and data analysis

Optical properties	Description	Value
L	Circumference of the resonator	1.57 cm
W_{m}	Acoustic membrane width	2.85 μm
W_{o}	Optical waveguide width	1.5 μm
FSR_1	Free spectral range of symmetric mode	5.02 GHz
FSR_2	Free spectral range of antisymmetric mode	4.87 GHz
$\mu^2_{\mathrm{A},1}$	Coupling through coupler A into the symmetric mode	0.045-0.16
$\mu^2_{\mathrm{A},2}$	Coupling through coupler A into the antisymmetric mode	0.62-0.71
$\mu^2_{\mathrm{B},1}$	Coupling through coupler B into the symmetric mode	0.01-0.07
$\mu^2_{\mathrm{B},2}$	Coupling through coupler B into the antisymmetric mode	0.007-0.016
α_1	Symmetric spatial mode propagation loss	6.7 m^{-1}
α_2	Antisymmetric spatial mode propagation loss	20.6 m^{-1}
$v_{\mathrm{g},1}$	Symmetric spatial mode group velocity	7.91 $\times 10^7$ m/s
$v_{\mathrm{g},2}$	Antisymmetric spatial mode group velocity	7.67 $\times 10^7$ m/s
Ω_{B}	Brillouin frequency	2π 5.95 GHz
Γ	Acoustic dissipation rate	2π 9 MHz
G_{B}	Brillouin gain coefficient	380 $\mathrm{W}^{-1}\mathrm{m}^{-1}$

Table C.1: Experimental parameters of the non-reciprocal resonantly enhanced silicon Brillouin amplifier.

In this section, we detail the experimental parameters of the resonantly enhanced Brillouin system (Chapter 4) and how they are determined. All parameters in the system are corroborated by a self-consistent model of the amplifier dynamics. We enumerate these pa-

rameters in Table C.1. The passive optical properties of the resonator system are obtained by fitting the transmission spectrum to a multi-spatial-mode resonator model (for more details, see Supplementary Materials of Ref. [95]). As the couplers A and B are wavelength dependent, we indicate an approximate range for each coupling coefficient. The acoustic dissipation rate is determined by analyzing the Brillouin-gain bandwidths at low intracavity pump powers. The Brillouin-gain coefficient is extracted by fitting the mean-field model to our measurements. Altogether, these parameters are in agreement with those previously obtained in similar device geometries [95].

To determine the degree of net amplification (for Fig. 4.5-4.6), we calibrate the signal-wave transmission through the resonant system by comparing it to the signal-wave transmission through a linear device on the same chip (placed 600 μm away). Data for Fig. 4.6A-B were obtained by acquiring traces as the signal-wave detuning (Ω) is swept through the Brillouin frequency (Ω_{B})) while sweeping the pump power and varying pump wavelength around the dual-resonance condition (i.e., $\omega_{\mathrm{p}} = \omega_2^m$, $\omega_{\mathrm{p}} - \Omega_{\mathrm{B}} = \omega_1^n$). The data in Fig. 4.6A-B represent the traces obtained with near-zero detuning ($\omega_{\mathrm{p}} - \Omega_{\mathrm{B}} - \omega_1^n$). Intracavity powers are estimated using the passive ring resonator parameters and accounting for the effects of nonlinear loss (studied in detail in the supplementary information of Ref. [29]); additionally, this analysis is consistent with the power-dependent nature of the directional couplers.

Appendix D

Parameters for optomechanical cooling

In this appendix we list the relevant parameters for Chapter 8. All of the parameters in our model are corroborated by independent measurements and simulations (i.e., no fitting parameters). In this section, we list the important parameters of our system and give an account of how each is determined.

Parameters	Value
L	2.305 cm
$v_{g,1}$	7.385 $\times 10^7$ m/s
$v_{g,2}$	7.163 $\times 10^7$ m/s
Δk_{as}	-4.5×10^5 m^{-1}
γ	$2\pi\times$ 180 MHz
Γ	$2\pi\times$ 14.2 MHz
G_b	470 W^{-1}m^{-1}
Ω_B	$2\pi\times$ 6.02 GHz

L, the length of the system, is simply given by the length of the suspended region of the device. The group velocities of the symmetric and antisymmetric optical spatial modes ($v_{g,1}$ and $v_{g,2}$, respectively) are determined through racetrack ring free spectral range (FSR) measurements (see Supplementary Materials of Ref. [95]). The wavevector mismatch be-

tween the two optical spatial modes ($\Delta k_{as} = k_2(\omega_p + \Omega_B) - k_1(\omega_p)$) was found through finite element simulations. As required by phase-matching, this wavevector mismatch gives the wavevector of the phonon field (i.e., $q = \Delta k_{as}$). γ, the optical dissipation rate of the anti-symmetric optical spatial mode, is given by the linear propagation loss of the antisymmetric optical waveguide mode (i.e., $\gamma = v_g \alpha$).

The acoustic dissipation rate (Γ) is given by the spectral width of the spontaneous Stokes and anti-Stokes spectra at low pump powers. The Brillouin gain coefficient (G_B) was found from nonlinear laser spectroscopy measurements presented in Ref. [29]. These measurements were performed on a device of identical dimensions. Ω_B, the Brillouin frequency, is determined through the heterodyne spectroscopy presented in this work.

In addition to these parameters, we use the nonlinear loss coefficients given in the supplement of Ref. [29] to determine the average on-chip probe and scattered powers.

Appendix E

Bibliography

[1] G.T. Reed and A.P. Knights. *Silicon Photonics: An Introduction.* Wiley, 2004.

[2] B. Jalali and S. Fathpour. Silicon photonics. *J. Lightwave Technol.*, 24(12):4600–4615, Dec 2006.

[3] Richard Soref. The past, present, and future of silicon photonics. *J. Sel. Top. Quantum Electron.*, 12(6):1678–1687, 2006.

[4] J Leuthold, C Koos, and W Freude. Nonlinear silicon photonics. *Nat. Photonics*, 4(8):535, 2010.

[5] Lukas Chrostowski and Michael Hochberg. *Silicon photonics design: from devices to systems.* Cambridge University Press, 2015.

[6] C Doerr, Long Chen, Diedrik Vermeulen, Torben Nielsen, Saeid Azemati, Scott Stulz, Greg McBrien, X-M Xu, Benny Mikkelsen, Mehrdad Givehchi, et al. Single-chip silicon photonics 100-gb/s coherent transceiver. In *Optical Fiber Communication Conference*, pages Th5C–1. Optical Society of America, 2014.

[7] Weifeng Zhang and Jianping Yao. Silicon-based integrated microwave photonics. *IEEE Journal of Quantum Electronics*, 52(1):1–12, 2015.

[8] Lionel Tombez, EJ Zhang, JS Orcutt, Swetha Kamlapurkar, and WMJ Green. Methane absorption spectroscopy on a silicon photonic chip. *Optica*, 4(11):1322–1325, 2017.

[9] Brandon Redding, Seng Fatt Liew, Raktim Sarma, and Hui Cao. Compact spectrometer based on a disordered photonic chip. *Nat. Photonics*, 7(9):746, 2013.

[10] Tom Claes, Jordi Girones Molera, Katrien De Vos, Etienne Schacht, Roel Baets, and Peter Bienstman. Label-free biosensing with a slot-waveguide-based ring resonator in silicon on insulator. *IEEE Photonics Journal*, 1(3):197–204, 2009.

[11] Nicholas C Harris, Gregory R Steinbrecher, Mihika Prabhu, Yoav Lahini, Jacob Mower, Darius Bunandar, Changchen Chen, Franco NC Wong, Tom Baehr-Jones, Michael Hochberg, et al. Quantum transport simulations in a programmable nanophotonic processor. *Nat. Photonics*, 11(7):447, 2017.

[12] R.W. Boyd. *Nonlinear Optics.* Elsevier Science, 2003.

[13] Govind P Agrawal. *Nonlinear fiber optics.* Academic Press, 2007.

[14] Ozdal Boyraz and Bahram Jalali. Demonstration of a silicon Raman laser. *Opt. Express*, 12(21):5269–5273, 2004.

[15] Bart Kuyken, Takuro Ideguchi, Simon Holzner, Ming Yan, Theodor W Hänsch, Joris Van Campenhout, Peter Verheyen, Stéphane Coen, Francois Leo, Roel Baets, et al. An octave-spanning mid-infrared frequency comb generated in a silicon nanophotonic wire waveguide. *Nat. Commun.*, 6, 2015.

[16] Albert Schliesser, Nathalie Picqué, and Theodor W Hänsch. Mid-infrared frequency combs. *Nat. Photonics*, 6(7):440, 2012.

[17] Marcelo Davanco, Jun Rong Ong, Andrea Bahgat Shehata, Alberto Tosi, Imad Agha, Solomon Assefa, Fengnian Xia, William MJ Green, Shayan Mookherjea, and Kartik Srinivasan. Telecommunications-band heralded single photons from a silicon nanophotonic chip. *Appl. Phys. Lett.*, 100(26):261104, 2012.

[18] Matthew D Eisaman, Jingyun Fan, Alan Migdall, and Sergey V Polyakov. Invited review article: Single-photon sources and detectors. *Review of scientific instruments*, 82(7):071101, 2011.

[19] Bryn A Bell, Jiakun He, Chunle Xiong, and Benjamin J Eggleton. Frequency conversion in silicon in the single photon regime. *Opt. Express*, 24(5):5235–5242, 2016.

[20] Ravi Pant, David Marpaung, Irina V. Kabakova, Blair Morrison, Christopher G. Poulton, and Benjamin J. Eggleton. On-chip stimulated Brillouin scattering for microwave signal processing and generation. *Laser Photon. Rev.*, 8(5):653–666, 2014.

[21] Shai Gertler, Eric A Kittlaus, Nils T Otterstrom, Prashanta Kharel, and Peter T Rakich. Microwave filtering using forward Brillouin scattering in photonic-phononic emit-receive devices. *J. Lightwave Technol.*, 2020.

[22] Shai Gertler, Eric A Kittlaus, Nils T Otterstrom, and Peter T Rakich. Tunable RF-photonic filtering with high out-of-band rejection in silicon. *arXiv preprint arXiv:2003.05480*, 2020.

[23] Eric A. Kittlaus, Heedeuk Shin, and Peter T. Rakich. Large Brillouin amplification in silicon. *Nat. Photon.*, 10(7):463–467, 2016.

[24] Heedeuk Shin, Jonathan A Cox, Robert Jarecki, Andrew Starbuck, Zheng Wang, and Peter T Rakich. Control of coherent information via on-chip photonic–phononic emitter–receivers. *Nat. Commum.*, 6, 2015.

[25] Eric A Kittlaus, Prashanta Kharel, Nils T Otterstrom, Zheng Wang, and Peter T Rakich. RF-photonic filters via on-chip photonic–phononic emit–receive operations. *J. Light. Technol.*, 36(13):2803–2809, 2018.

[26] Shai Gertler, Prashanta Kharel, Eric A Kittlaus, Nils T Otterstrom, and Peter T Rakich. Shaping nonlinear optical response using nonlocal forward Brillouin interactions. *arXiv preprint arXiv:1909.08129*, 2019.

[27] Yair Antman, Alex Clain, Yosef London, and Avi Zadok. Optomechanical sensing of liquids outside standard fibers using forward stimulated brillouin scattering. *Optica*, 3(5):510–516, 2016.

[28] Gil Bashan, Hilel Hagai Diamandi, Yosef London, Eyal Preter, and Avi Zadok. Optomechanical time-domain reflectometry. *Nat. Commun.*, 9(1):1–9, 2018.

[29] Eric A. Kittlaus, Nils T. Otterstrom, and Peter T. Rakich. On-chip inter-modal Brillouin scattering. *Nat. Commun.*, 8:15819, Jul 2017.

[30] Heedeuk Shin, Wenjun Qiu, Robert Jarecki, Jonathan A. Cox, Roy H. Olsson, Andrew Starbuck, Zheng Wang, and Peter T. Rakich. Tailorable stimulated Brillouin scattering in nanoscale silicon waveguides. *Nat. Commun.*, 4:1944, 2013.

[31] M. S. Kang, A. Butsch, and P. St J. Russell. Reconfigurable light-driven opto-acoustic isolators in photonic crystal fibre. *Nat. Photonics*, 5(9):549–553, 2011.

[32] Xinpeng Huang and Shanhui Fan. Complete all-optical silica fiber isolator via stimulated Brillouin scattering. *J. Lightwave Technol.*, 29(15):2267–2275, Aug 2011.

[33] Christopher G Poulton, Ravi Pant, Adam Byrnes, Shanhui Fan, MJ Steel, and Benjamin J Eggleton. Design for broadband on-chip isolator using stimulated Brillouin scattering in dispersion-engineered chalcogenide waveguides. *Opt. Express*, 20(19):21235–21246, 2012.

[34] Blair Morrison, Alvaro Casas-Bedoya, Guanghui Ren, Khu Vu, Yang Liu, Atiyeh Zarifi, Thach G Nguyen, Duk-Yong Choi, David Marpaung, Stephen J Madden, et al. Compact brillouin devices through hybrid integration on silicon. *Optica*, 4(8):847–854, 2017.

[35] Luc Thévenaz, Marc Niklès, Alexandre Fellay, Massimo Facchini, and Philippe A Robert. Applications of distributed Brillouin fiber sensing. In *International Conference on Applied Optical Metrology*, volume 3407, pages 374–382. International Society for Optics and Photonics, 1998.

[36] Elsa Garmire. Perspectives on stimulated Brillouin scattering. *New J. Phys.*, 19(1):011003, 2017.

[37] John Tyndall. On the blue color of the sky, the polarization of skylight, and polarization of light by cloudy matter generally. *Journal of the Franklin Institute*, 88(1):34–40, 1869.

[38] John W Strutt. Xv. on the light from the sky, its polarization and colour. *The London, Edinburgh, and Dublin Philosophical Magazine and Journal of Science*, 41(271):107–120, 1871.

[39] Joseph Larmor. The principle of molecular scattering of radiation. *Philos. Mag.*, 37(217):161–163, 1919.

[40] C. V. Raman. The Doppler effect in the molecular scattering of radiation. *Nature*, 103(2583):165, 1919.

[41] León Brillouin. Scattering of light rays in a transparent homogeneous body: influence of thermal agitation. *Ann. De Phys*, 17(88), 1922.

[42] E. F. Gross. Change of wave-length of light due to elastic heat waves at scattering in liquids. *Nature*, 126(3171):201, 1930.

[43] R. S. Krishnan. Elastic constants of crystals from light scattering measurements. *Proc. Indian Acad. Sci. - Sect. A*, 41(3):91–97, 1955.

[44] T. H. Maiman. Stimulated optical radiation in ruby. *Nature*, 187:493, 1960.

[45] RY Chiao, CH Townes, and BP Stoicheff. Stimulated Brillouin scattering and coherent generation of intense hypersonic waves. *Phys. Rev. Lett.*, 12(21):592, 1964.

[46] E Garmire and C H Townes. Stimulated Brillouin scattering in liquids. *Appl. Phys. Lett*, 5(4):84–86, 1964.

[47] R. Y. Chiao and B. P. Stoicheff. Brillouin scattering in Liquids excited by the He–Ne maser. *J. Opt. Soc. Am.*, 54(10):1286–1287, 1964.

[48] Richard G Brewer and Klaus E Rieckhoff. Stimulated Brillouin scattering in liquids. *Phys. Rev. Lett.*, 13(11):334, 1964.

[49] EE Hagenlocker, RW Minck, and WG Rado. Effects of phonon lifetime on stimulated optical scattering in gases. *Phys. Rev.*, 154(2):226, 1967.

[50] Hans Meixner, Paul Leiderer, Paul Berberich, and Edgar Lüscher. The elastic constants of solid argon determined by stimulated brillouin scattering. *Phys. Lett. A*, 40(3):257–258, 1972.

[51] WH Renninger, P Kharel, RO Behunin, and PT Rakich. Bulk crystalline optomechanics. *Nat. Phys.*, 14(6):601, 2018.

[52] H Takuma and D A Jennings. Stimulated Brillouin scattering in the off-axis resonator. *Appl. Phys. Lett.*, 5(12):239–241, 1964.

[53] E P Ippen and R H Stolen. Stimulated Brillouin scattering in optical fibers. *Appl. Phys. Lett.*, 21(11):539–541, 1972.

[54] Richard G Smith. Optical power handling capacity of low loss optical fibers as determined by stimulated Raman and Brillouin scattering. *Appl. Opt.*, 11(11):2489–2494, 1972.

[55] KO Hill, BS Kawasaki, and DC Johnson. Cw brillouin laser. *Appl. Phys. Lett*, 28(10):608–609, 1976.

[56] N Olsson and J Van Der Ziel. Characteristics of a semiconductor laser pumped brillouin amplifier with electronically controlled bandwidth. *J. Lightwave Technol.*, 5(1):147–153, 1987.

[57] Kwang Yong Song, Sanghoon Chin, Nikolay Primerov, and Luc Thévenaz. Time-domain distributed fiber sensor with 1 cm spatial resolution based on Brillouin dynamic grating. *J. Lightwave Technol.*, 28(14):2062–2067, 2010.

[58] Paulo Dainese, P St J Russell, N Joly, JC Knight, GS Wiederhecker, Hugo L Fragnito, Vincent Laude, and Abdelkrim Khelif. Stimulated Brillouin scattering from multi-

GHz-guided acoustic phonons in nanostructured photonic crystal fibres. *Nat. Phys.*, 2(6):388, 2006.

[59] RK Kadiwar and IP Giles. Optical fibre Brillouin ring laser gyroscope. *Electron. Lett.*, 25:1729–1731, 1989.

[60] Jiang Li, Myoung-Gyun Suh, and Kerry Vahala. Microresonator Brillouin gyroscope. *Optica*, 4(3):346–348, 2017.

[61] Jiang Li, Hansuek Lee, and Kerry J. Vahala. Microwave synthesizer using an on-chip Brillouin oscillator. *Nat. Commun.*, 4:2097, 2013.

[62] Jiang Li, Hansuek Lee, and Kerry J. Vahala. Low-noise brillouin laser on a chip at 1064 nm. *Opt. Lett.*, 39(2):287–290, 2014.

[63] Benjamin J Eggleton, Christopher G Poulton, Peter T Rakich, Michael J Steel, and Gaurav Bahl. Brillouin integrated photonics. *Nat. Photonics*, 13(10):664–677, 2019.

[64] Ricardo Claps, Dimitri Dimitropoulos, Varun Raghunathan, Y Han, and B Jalali. Observation of stimulated Raman amplification in silicon waveguides. *Opt. Express*, 11(15):1731–1739, 2003.

[65] Ansheng Liu, Haisheng Rong, Mario Paniccia, Oded Cohen, and Dani Hak. Net optical gain in a low loss silicon-on-insulator waveguide by stimulated Raman scattering. *Opt. Express*, 12(18):4261–4268, 2004.

[66] TK Liang and HK Tsang. Efficient Raman amplification in silicon-on-insulator waveguides. *Appl. Phys. Lett.*, 85(16):3343–3345, 2004.

[67] Hiroshi Fukuda, Koji Yamada, Tetsufumi Shoji, Mitsutoshi Takahashi, Tai Tsuchizawa, Toshifumi Watanabe, Jun-ichi Takahashi, and Sei-ichi Itabashi. Four-wave mixing in silicon wire waveguides. *Optics express*, 13(12):4629–4637, 2005.

[68] Mark A. Foster, Amy C. Turner, Jay E. Sharping, Bradley S. Schmidt, Michal Lipson, and Alexander L. Gaeta. Broad-band optical parametric gain on a silicon photonic chip. *Nature*, 441(7096):960–963, 2006.

[69] Peter T. Rakich, Charles Reinke, Ryan Camacho, Paul Davids, and Zheng Wang. Giant enhancement of stimulated Brillouin scattering in the subwavelength limit. *Phys. Rev. X*, 2:011008, 2012.

[70] David K. Biegelsen. Photoelastic tensor of silicon and the volume dependence of the average gap. *Phys. Rev. Lett.*, 32:1196–1199, 1974.

[71] R. M. Shelby, M. D. Levenson, S. H. Perlmutter, R. G. DeVoe, and D. F. Walls. Broad-band parametric deamplification of quantum noise in an optical fiber. *Phys. Rev. Lett.*, 57:691–694, 1986.

[72] M. S. Kang, A. Nazarkin, A. Brenn, and P. St J. Russell. Tightly trapped acoustic phonons in photonic crystal fibres as highly nonlinear artificial Raman oscillators. *Nat. Phys.*, 5(4):276–280, 2009.

[73] Raphaël Van Laer, Bart Kuyken, Dries Van Thourhout, and Roel Baets. Interaction between light and highly confined hypersound in a silicon photonic nanowire. *Nat. Photon.*, 9(3):199–203, 2015.

[74] Raphaël Van Laer, Alexandre Bazin, Bart Kuyken, Roel Baets, and Dries Van Thourhout. Net on-chip Brillouin gain based on suspended silicon nanowires. *New J. Phys.*, 17(11):115005, 2015.

[75] Prashanta Kharel, RO Behunin, WH Renninger, and PT Rakich. Noise and dynamics in forward Brillouin interactions. *Phys. Rev. A*, 93(6):063806, 2016.

[76] Nobuyuki Imoto, John R Jeffers, and Rodney Loudon. Quantum mechanical treatment of a propagating optical beam. In *Quantum Measurements in Optics*, pages 295–311. Springer, 1992.

[77] JE Sipe and MJ Steel. A Hamiltonian treatment of stimulated Brillouin scattering in nanoscale integrated waveguides. *New J. Phys.*, 18(4):045004, 2016.

[78] Markus Aspelmeyer, Tobias J Kippenberg, and Florian Marquardt. Cavity optomechanics. *Rev. Mod. Phys.*, 86(4):1391, 2014.

[79] HERMANN A Haus. Steady-state quantum analysis of linear systems. *Proceedings of the IEEE*, 58(10):1599–1611, 1970.

[80] Steven G Johnson, Mihai Ibanescu, MA Skorobogatiy, Ori Weisberg, JD Joannopoulos, and Yoel Fink. Perturbation theory for maxwell's equations with shifting material boundaries. *Physical review E*, 65(6):066611, 2002.

[81] Jiang Li, Hansuek Lee, Tong Chen, and Kerry J Vahala. Characterization of a high coherence, Brillouin microcavity laser on silicon. *Opt. Express*, 20(18):20170–20180, 2012.

[82] William Loh, Adam A S Green, Fred N Baynes, Daniel C Cole, Franklyn J Quinlan, Hansuek Lee, Kerry J Vahala, Scott B Papp, and Scott A Diddams. Dual-microcavity narrow-linewidth Brillouin laser. *Optica*, 2(3):225–232, 2015.

[83] William Loh, Siva Yegnanarayanan, Frederick O'Donnell, and Paul W Juodawlkis. Ultra-narrow linewidth Brillouin laser with nanokelvin temperature self-referencing. *Optica*, 6(2):152–159, 2019.

[84] Sarat Gundavarapu, Grant M Brodnik, Matthew Puckett, Taran Huffman, Debapam Bose, Ryan Behunin, JF Wu, TQ Qiu, Catia Pinho, Nitesh Chauhan, et al. Sub-hertz fundamental linewidth photonic integrated Brillouin laser. *Nat. Photonics*, 13:60–67, 2019.

[85] N.A. Olsson and J.P. van der Ziel. Fibre Brillouin amplifier with electronically controlled bandwidth. *Electron. Lett.*, 22(9):488–490, 1986.

[86] D Culverhouse, F Farahi, C N Pannell, and D A Jackson. Potential of stimulated Brillouin scattering as sensing mechanism for distributed temperature sensors. *Electron. Lett.*, 25(14):913–915, 1989.

[87] Nobuyuki Yoshizawa and Takeshi Imai. Stimulated Brillouin scattering suppression by means of applying strain distribution to fiber with cabling. *J. Lightwave Technol.*, 11(10):1518–1522, 1993.

[88] Takuo Tanemura, Yuichi Takushima, and Kazuro Kikuchi. Narrowband optical filter, with a variable transmission spectrum, using stimulated Brillouin scattering in optical fiber. *Opt. Lett.*, 27(17):1552–1554, 2002.

[89] Amol Choudhary, Blair Morrison, Iman Aryanfar, Shayan Shahnia, Mattia Pagani, Yang Liu, Khu Vu, Stephen Madden, David Marpaung, and Benjamin J Eggleton. Advanced integrated microwave signal processing with giant on-chip Brillouin gain. *J. Lightwave Technol.*, 35(4):846–854, 2017.

[90] P. Kharel, R. O. Behunin, W. H. Renninger, and P. T. Rakich. Noise and dynamics in forward Brillouin interactions. *Phys. Rev. A*, 93:063806, 2016.

[91] P. St J. Russell, D. Culverhouse, and F. Farahi. Experimental observation of forward stimulated Brillouin scattering in dual-mode single-core fibre. *Electron. Lett.*, 26(15):1195–1196, 1990.

[92] P. St J. Russell, D. Culverhouse, and F. Farahi. Theory of forward stimulated Brillouin scattering in dual-mode single-core fibers. *IEEE J. Quant. Electron*, 27(3):836–842, 1991.

[93] M. S. Kang, A. Brenn, and P. St J. Russell. All-optical control of gigahertz acoustic resonances by forward stimulated interpolarization scattering in a photonic crystal fiber. *Phys. Rev. Lett.*, 105:153901, 2010.

[94] J. R. Koehler, R. E. Noskov, A. A. Sukhorukov, A. Butsch, D. Novoa, and P. St J. Russell. Resolving the mystery of milliwatt-threshold opto-mechanical self-oscillation in dual-nanoweb fiber. *APL Photonics*, 1(5):056101, 2016.

[95] Nils T Otterstrom, Ryan O Behunin, Eric A Kittlaus, Zheng Wang, and Peter T Rakich. A silicon Brillouin laser. *Science*, 360(6393):1113–1116, 2018.

[96] Nils T. Otterstrom, Ryan O. Behunin, Eric A. Kittlaus, Zheng Wang, and Peter T. Rakich. A silicon brillouin laser. *Science*, 360(6393):1113–1116, 2018.

[97] Nils T Otterstrom, Eric A Kittlaus, Shai Gertler, Ryan O Behunin, Anthony L Lentine, and Peter T Rakich. Resonantly enhanced nonreciprocal silicon Brillouin amplifier. *Optica*, 6(9):1117–1123, 2019.

[98] Nils T. Otterstrom, Shai Gertler, Yishu Zhou, Eric A. Kittlaus, Ryan O. Behunin, Michael Gehl, Andrew L. Starbuck, Christina M. Dallo, Andrew T. Pomerene, Douglas C. Trotter, Anthony L. Lentine, and Peter T. Rakich. Backscatter-Immune Injection-Locked Brillouin Laser in Silicon. *Phys. Rev. Applied*, 14:044042, Oct 2020.

[99] Nils T. Otterstrom, Ryan O. Behunin, Eric A. Kittlaus, and Peter T. Rakich. Optomechanical Cooling in a Continuous System. *Phys. Rev. X*, 8:041034, 2018.

[100] Daoxin Dai, Jian Wang, and Yaocheng Shi. Silicon mode (de)multiplexer enabling high capacity photonic networks-on-chip with a single-wavelength-carrier light. *Opt. Lett.*, 38(9):1422–1424, May 2013.

[101] LianWee Luo, Noam Ophir, Christine P. Chen, Lucas H. Gabrielli, Carl B. Poitras, Keren Bergmen, and Michal Lipson. WDM-compatible mode-division multiplexing on a silicon chip. *Nat. Commun.*, 5:3069, Jan 2014.

[102] Christopher G. Poulton, Ravi Pant, Adam Byrnes, Shanhui Fan, M. J. Steel, and Benjamin J. Eggleton. Design for broadband on-chip isolator using stimulated Brillouin scattering in dispersion-engineered chalcogenide waveguides. *Opt. Express*, 20(19):21235–21246, 2012.

[103] Stephen E Harris. Tunable optical parametric oscillators. *Proceedings of the IEEE*, 57(12):2096–2113, 1969.

[104] Xu Yi, Qi-Fan Yang, Ki Youl Yang, Myoung-Gyun Suh, and Kerry Vahala. Soliton frequency comb at microwave rates in a high-Q silica microresonator. *Optica*, 2(12):1078–1085, 2015.

[105] A Berrou, M Raybaut, A Godard, and M Lefebvre. High-resolution photoacoustic and direct absorption spectroscopy of main greenhouse gases by use of a pulsed entangled cavity doubly resonant OPO. *Appl. Phys. B*, 98(1):217, 2010.

[106] I Ricciardi, E De Tommasi, P Maddaloni, S Mosca, A Rocco, J-J Zondy, M De Rosa, and P De Natale. Frequency-comb-referenced singly-resonant OPO for sub-Doppler spectroscopy. *Opt. Express*, 20(8):9178–9186, 2012.

[107] Zachary L Newman, Vincent Maurice, Tara Drake, Jordan R Stone, Travis C Briles, Daryl T Spencer, Connor Fredrick, Qing Li, Daron Westly, Bojan R Ilic, et al. Architecture for the photonic integration of an optical atomic clock. *Optica*, 6(5):680–685, 2019.

[108] V Lecoeuche, David J Webb, Christopher N Pannell, and David A Jackson. Brillouin based distributed fibre sensor incorporating a mode-locked brillouin fibre ring laser. *Optics communications*, 152(4):263–268, 1998.

[109] Myoung-Gyun Suh, Qi-Fan Yang, and Kerry J Vahala. Phonon-limited-linewidth of brillouin lasers at cryogenic temperatures. *Phys. Rev. Lett.*, 119(14):143901, 2017.

[110] Ryan O. Behunin, Nils T. Otterstrom, Peter T. Rakich, Sarat Gundavarapu, and Daniel J. Blumenthal. Fundamental noise dynamics in cascaded-order brillouin lasers. *Phys. Rev. A*, 98:023832, 2018.

[111] Raphaël Van Laer, Bart Kuyken, Dries Van Thourhout, and Roel Baets. Interaction between light and highly confined hypersound in a silicon photonic nanowire. *Nat. Photonics*, 9(3):199–203, Mar 2015.

[112] Li Ge, Yi D Chong, and A Douglas Stone. Steady-state ab initio laser theory: generalizations and analytic results. *Physical Review A*, 82(6):063824, 2010.

[113] JP Hurault and K Maki. Breakdown of the mean field theory in the superconducting transition region. *Phys. Rev. B*, 2(7):2560, 1970.

[114] HE Stanley. Mean field theory of magnetic phase transitions. *Introduction to Phase Transitions and Critical Phenomena*, 1971.

[115] Ganapathy Baskaran, Z Zou, and Philip W Anderson. The resonating valence bond state and high-T_c superconductivity—a mean field theory. *Solid State Commun.*, 63(11):973–976, 1987.

[116] R Bonifacio and LA Lugiato. Optical bistability and cooperative effects in resonance fluorescence. *Phys. Rev. A*, 18(3):1129, 1978.

[117] Pierre Meystre. On the use of the mean-field theory in optical bistability. *Opt. Commun.*, 26(2):277–280, 1978.

[118] V DeGiorgio and Marlan O Scully. Analogy between the laser threshold region and a second-order phase transition. *Phys. Rev. A*, 2(4):1170, 1970.

[119] Amnon Yariv. Quantum electronics, 3rd. *Edn.(John WieLy & Sons, New York, 1988) p*, 389, 1989.

[120] Kerry J Vahala. Back-action limit of linewidth in an optomechanical oscillator. *Phys. Rev. A*, 78(2):023832, 2008.

[121] L Richter, H Mandelberg, M Kruger, and P McGrath. Linewidth determination from self-heterodyne measurements with subcoherence delay times. *IEEE J. Quantum Electron.*, 22(11):2070–2074, 1986.

[122] MP Van Exter, SJM Kuppens, and JP Woerdman. Excess phase noise in self-heterodyne detection. *IEEE J. Quantum Electron.*, 28(3):580–584, 1992.

[123] Wei C Jiang, Xiyuan Lu, Jidong Zhang, and Qiang Lin. High-frequency silicon optomechanical oscillator with an ultralow threshold. *Opt. Express*, 20(14):15991–15996, 2012.

[124] Xiaoyi Bao, Jabulani Dhliwayo, Nicol Heron, David J Webb, and David A Jackson. Experimental and theoretical studies on a distributed temperature sensor based on Brillouin scattering. *J. Lightwave Technol.*, 13(7):1340–1348, 1995.

[125] Atiyeh Zarifi, Birgit Stiller, Moritz Merklein, Neuton Li, Khu Vu, Duk-Yong Choi, Pan Ma, Stephen J Madden, and Benjamin J Eggleton. Highly localized distributed Brillouin scattering response in a photonic integrated circuit. *APL Photonics*, 3(3):036101, 2018.

[126] Kwang Yong Song, Miguel González Herráez, and Luc Thévenaz. Observation of pulse delaying and advancement in optical fibers using stimulated Brillouin scattering. *Opt. Express*, 13(1):82–88, 2005.

[127] Ravi Pant, David Marpaung, Irina V Kabakova, Blair Morrison, Christopher G Poulton, and Benjamin J Eggleton. On-chip stimulated Brillouin scattering for microwave signal processing and generation. *Laser Photonics Rev.*, 8(5):653–666, 2014.

[128] Yahia Souidi, Fethallah Taleb, Junbo Zheng, Min Won Lee, Frédéric Du Burck, and Vincent Roncin. Low-noise and high-gain Brillouin optical amplifier for narrowband active optical filtering based on a pump-to-signal optoelectronic tracking. *Appl. Opt.*, 55(2):248–253, 2016.

[129] Blair Morrison, Alvaro Casas-Bedoya, Guanghui Ren, Khu Vu, Yang Liu, Atiyeh Zarifi, Thach G. Nguyen, Duk-Yong Choi, David Marpaung, Stephen J. Madden, Arnan Mitchell, and Benjamin J. Eggleton. Compact Brillouin devices through hybrid integration on silicon. *Optica*, 4(8):847–854, 2017.

[130] Christian Wolff, Philipp Gutsche, Michael J Steel, Benjamin J Eggleton, and Christopher G Poulton. Power limits and a figure of merit for stimulated Brillouin scattering in the presence of third and fifth order loss. *Opt. Express*, 23(20):26628–26638, 2015.

[131] Christian Wolff, Raphael Van Laer, Michael J Steel, Benjamin J Eggleton, and Christopher G Poulton. Brillouin resonance broadening due to structural variations in nanoscale waveguides. *arXiv preprint arXiv:1510.00079*, 2015.

[132] Brent E Little, Sai T Chu, Hermann A Haus, J Foresi, and J-P Laine. Microring resonator channel dropping filters. *J. Lightwave Technol.*, 15(6):998–1005, 1997.

[133] Amir H Safavi-Naeini, TP Mayer Alegre, Jasper Chan, Matt Eichenfield, Martin Winger, Qiang Lin, Jeff T Hill, Darrick E Chang, and Oskar Painter. Electromagnetically induced transparency and slow light with optomechanics. *Nature*, 472(7341):69, 2011.

[134] Myeong Soo Kang, A Butsch, and P St J Russell. Reconfigurable light-driven opto-acoustic isolators in photonic crystal fibre. *Nat. Photonics*, 5(9):549, 2011.

[135] Ewold Verhagen and Andrea Alu. Optomechanical nonreciprocity. *Nat. Phys.*, 13:922, 2017.

[136] Elias Giacoumidis, Amol Choudhary, Eric Magi, David Marpaung, Khu Vu, Pan Ma, Duk-Yong Choi, Steve Madden, Bill Corcoran, Mark Pelusi, et al. Chip-based Brillouin processing for carrier recovery in self-coherent optical communications. *Optica*, 5(10):1191–1199, 2018.

[137] Yoshitomo Okawachi, Matthew S Bigelow, Jay E Sharping, Zhaoming Zhu, Aaron Schweinsberg, Daniel J Gauthier, Robert W Boyd, and Alexander L Gaeta. Tunable all-optical delays via brillouin slow light in an optical fiber. *Phys. Rev. Lett.*, 94(15):153902, 2005.

[138] Ravi Pant, Adam Byrnes, Christopher G Poulton, Enbang Li, Duk-Yong Choi, Steve Madden, Barry Luther-Davies, and Benjamin J Eggleton. Photonic-chip-based tunable slow and fast light via stimulated Brillouin scattering. *Opt. Lett.*, 37(5):969–971, 2012.

[139] L. Pavesi and D.J. Lockwood. *Silicon Photonics*, volume 1 of *Physics and astronomy online library*. Springer, 2004.

[140] Eric A Kittlaus, Prashanta Kharel, Nils T Otterstrom, Zheng Wang, and Peter T Rakich. RF-photonic filters via on-chip photonic-phononic emit-receive operations. *J. Lightwave Technol.*, 36(13):2803–2809, 2018.

[141] A Kodigala, M Gehl, CT DeRose, D Hood, AT Pomerene, C Dallo, D Trotter, P Moore, AL Starbuck, J Lee, et al. Silicon photonic single-sideband generation with dual-parallel mach-zehnder modulators. In *CLEO: Science and Innovations*, pages STh4N–6. Optical Society of America, 2019.

[142] Adil Masood, Marianna Pantouvaki, Guy Lepage, Peter Verheyen, Joris Van Campenhout, Philippe Absil, Dries Van Thourhout, and Wim Bogaerts. Comparison of

heater architectures for thermal control of silicon photonic circuits. In *10th International Conference on Group IV Photonics*, pages 83–84. IEEE, 2013.

[143] Amy C Turner-Foster, Mark A Foster, Jacob S Levy, Carl B Poitras, Reza Salem, Alexander L Gaeta, and Michal Lipson. Ultrashort free-carrier lifetime in low-loss silicon nanowaveguides. *Opt. Express*, 18(4):3582–3591, 2010.

[144] J Komma, C Schwarz, G Hofmann, D Heinert, and R Nawrodt. Thermo-optic coefficient of silicon at 1550 nm and cryogenic temperatures. *Appl. Phys. Lett.*, 101(4):041905, 2012.

[145] Mi Wang, Antonio Ribero, Yufei Xing, and Wim Bogaerts. Tolerant, broadband tunable 2× 2 coupler circuit. *Opt. Express*, 28(4):5555–5566, 2020.

[146] Arkady Pikovsky, Michael Rosenblum, and Jürgen Kurths. *Synchronization: a universal concept in nonlinear sciences*, volume 12. Cambridge university press, 2003.

[147] Mian Zhang, Gustavo S Wiederhecker, Sasikanth Manipatruni, Arthur Barnard, Paul McEuen, and Michal Lipson. Synchronization of micromechanical oscillators using light. *Phys. Rev. Lett.*, 109(23):233906, 2012.

[148] HL Stover and WH Steier. Locking of laser oscillators by light injection. *Appl. Phys. Lett.*, 8(4):91–93, 1966.

[149] M Sasnett. Injection-locked laser stabilizer, July 17 1973. US Patent 3,747,004.

[150] Kaneyuki Kurokawa. Injection locking of microwave solid-state oscillators. *Proc. IEEE*, 61(10):1386–1410, 1973.

[151] Zujie Fang, Haiwen Cai, Gaoting Chen, and Ronghui Qu. *Single Frequency Semiconductor Lasers*, volume 1. John Wiley & Sons, 2017.

[152] Katarzyna Balakier, Martyn J Fice, Lalitha Ponnampalam, Alwyn J Seeds, and Cyril C Renaud. Monolithically integrated optical phase lock loop for microwave photonics. *J. Lightwave Technol.*, 32(20):3893–3900, 2014.

[153] Katarzyna Balakier, Lalitha Ponnampalam, Martyn J Fice, Cyril C Renaud, and Alwyn J Seeds. Integrated semiconductor laser optical phase lock loops. *IEEE J. Sel. Topics Quantum Electron.*, 24(1):1–12, 2017.

[154] RWP Drever, John L Hall, FV Kowalski, J_ Hough, GM Ford, AJ Munley, and H Ward. Laser phase and frequency stabilization using an optical resonator. *Appl. Phys. B*, 31(2):97–105, 1983.

[155] Roy Lang. Injection locking properties of a semiconductor laser. *IEEE J. Quantum Electron.*, 18(6):976–983, 1982.

[156] Todd Lyndell Gustavson. *Precision rotation sensing using atom interferometry.* PhD thesis, PhD Thesis, 2000.

[157] Sang Eon Park, Taeg Yong Kwon, and Ho Seong Lee. Production of Raman laser beams using injection-locking technique. *IEEE Trans. Instrum. Meas.*, 52(2):277–279, 2003.

[158] Tara M Fortier, Y Le Coq, JE Stalnaker, Davi Ortega, Scott A Diddams, Christopher W Oates, and L Hollberg. Kilohertz-resolution spectroscopy of cold atoms with an optical frequency comb. *Phys. Rev. Lett.*, 97(16):163905, 2006.

[159] BK Mathason and PJ Delfyett. Pulsed injection locking dynamics of passively mode-locked external-cavity semiconductor laser systems for all-optical clock recovery. *J. Lightwave Technol.*, 18(8):1111, 2000.

[160] Radan Slavík, Zhixin Liu, and David J Richardson. Optical injection locking for carrier phase recovery and regeneration. In *Optical Fiber Communication Conference*, pages Th4I–3. Optical Society of America, 2017.

[161] Gregory E. Obarski and Jolene D. Splett. Transfer standard for the spectral density of relative intensity noise of optical fiber sources near 1550 nm. *J. Opt. Soc. Am. B*, 18(6):750–761, Jun 2001.

[162] Peter W. Millonni. *An introduction to quantum optics and quantum fluctuations.* Oxford University Press, 2019.

[163] Behzad Razavi. A study of injection locking and pulling in oscillators. *IEEE J. Solid-State Circuits*, 39(9):1415–1424, 2004.

[164] L Richter, H Mandelberg, M Kruger, and P McGrath. Linewidth determination from self-heterodyne measurements with subcoherence delay times. *IEEE J. Quantum Electron.*, 22(11):2070–2074, 1986.

[165] Eric A Kittlaus, Heedeuk Shin, and Peter T Rakich. Large Brillouin amplification in silicon. *Nat. Photonics*, 10(7):463, 2016.

[166] A. Chraplyvy, D. Marcuse, and R. Tkach. Effect of rayleigh backscattering from optical fibers on dfb laser wavelength. *J. Lightwave Technol.*, 4(5):555–559, 1986.

[167] K. Petermann. External optical feedback phenomena in semiconductor lasers. *IEEE J. Sel. Top. Quantum Electron.*, 1(2):480–489, 1995.

[168] HA Haus. The noise figure of optical amplifiers. *IEEE Photonic Tech L.*, 10(11):1602–1604, 1998.

[169] Xiaojun Xie, Yitang Dai, Yu Ji, Kun Xu, Yan Li, Jian Wu, and Jintong Lin. Broadband photonic radio-frequency channelization based on a 39-gHz optical frequency comb. *IEEE Photonics Tech. L.*, 24(8):661–663, 2012.

[170] Camille-Sophie Bres, Sanja Zlatanovic, Andreas OJ Wiberg, James R Adleman, Christopher K Huynh, EW Jacobs, Joshua M Kvavle, and Stojan Radic. Parametric photonic channelized RF receiver. *IEEE Photonics Technology Letters*, 23(6):344–346, 2011.

[171] Hermann A Haus. *Waves and fields in optoelectronics.* Prentice-Hall,, 1984.

[172] Emmanuel Desurvire, Dominique Bayart, Bertrand Desthieux, and Sébastien Bigo. *Erbium-doped fiber amplifiers: Device and System Developments*, volume 2. Wiley-Interscience New York, NY, 2002.

[173] V.J. Urick, J.D. McKinney, and K.J. Williams. *Fundamentals of Microwave Photonics.* Wiley series in microwave and optical engineering. John Wiley & Sons, Inc., 2015.

[174] RF Kalman, JC Fan, and LG Kazovsky. Dynamic range of coherent analog fiber-optic links. *J. Lightwave Technol.*, 12(7):1263–1277, 1994.

[175] Albert Schliesser, Olivier Arcizet, Rémi Rivière, Georg Anetsberger, and Tobias J Kippenberg. Resolved-sideband cooling and position measurement of a micromechanical oscillator close to the heisenberg uncertainty limit. *Nat. Phys.*, 5(7):509–514, 2009.

[176] Aaron D O'Connell, Max Hofheinz, Markus Ansmann, Radoslaw C Bialczak, Mike Lenander, Erik Lucero, Matthew Neeley, Daniel Sank, H Wang, M Weides, et al. Quantum ground state and single-phonon control of a mechanical resonator. *Nature*, 464(7289):697, 2010.

[177] Ewold Verhagen, Samuel Deléglise, Stefan Weis, Albert Schliesser, and Tobias J Kippenberg. Quantum-coherent coupling of a mechanical oscillator to an optical cavity mode. *Nature*, 482(7383):63–67, 2012.

[178] TA Palomaki, JD Teufel, RW Simmonds, and KW Lehnert. Entangling mechanical motion with microwave fields. *Science*, 342(6159):710–713, 2013.

[179] William Marshall, Christoph Simon, Roger Penrose, and Dik Bouwmeester. Towards quantum superpositions of a mirror. *Phys. Rev. Lett.*, 91(13):130401, 2003.

[180] Florian Marquardt and Peter Thomas Rakich. Quantum theory of continuum optomechanics. *New J. Phys.*, 2018.

[181] Birgit Stiller, Moritz Merklein, Khu Vu, Pan Ma, Stephen J Madden, Christopher G Poulton, and Benjamin J Eggleton. Crosstalk-free multi-wavelength coherent light storage via Brillouin interaction. *arXiv preprint arXiv:1803.08626*, 2018.

[182] Yin-Chung Chen, Seunghwi Kim, and Gaurav Bahl. Brillouin cooling in a linear waveguide. *New J. Phys.*, 18(11):115004, 2016.

[183] Raphaël Van Laer, Christopher J Sarabalis, Roel Baets, Dries Van Thourhout, and Amir H Safavi-Naeini. Thermal Brillouin noise observed in silicon optomechanical waveguide. *J. Opt.*, 19(4):044002, 2017.

[184] SJM Habraken, K Stannigel, Mikhail D Lukin, P Zoller, and P Rabl. Continuous mode cooling and phonon routers for phononic quantum networks. *New J. Phys.*, 14(11):115004, 2012.

[185] Rishi N Patel, Zhaoyou Wang, Wentao Jiang, Christopher J Sarabalis, Jeff T Hill, and Amir H Safavi-Naeini. A single-mode phononic wire. *arXiv preprint arXiv:1711.00847*, 2017.

[186] Laszlo Daniel T'oth, Nathan Rafaël Bernier, Andreas Nunnenkamp, AK Feofanov, and TJ Kippenberg. A dissipative quantum reservoir for microwave light using a mechanical oscillator. *Nat. Phys.*, 13(8):787, 2017.

[187] Eric A Kittlaus, Nils T Otterstrom, Prashanta Kharel, Shai Gertler, and Peter Rakich. Nonreciprocal inter-band Brillouin modulation. *Nat. Photonics*, 12(10):613, 2018.

[188] C. Wolff, P. Gutsche, M. J. Steel, B. J. Eggleton, and C. G. Poulton. Impact of nonlinear loss on stimulated Brillouin scattering. *J. Opt. Soc. Am. B*, 32(9):1968–1978, 2015.

[189] Shaul Pearl, Nir Rotenberg, and Henry M van Driel. Three photon absorption in silicon for 2300–3300 nm. *Appl. Phys. Lett.*, 93(13):131102, 2008.

[190] Lawrence M Rosenfeld, Dominic A Sulway, Gary F Sinclair, Vikas Anant, Mark G Thompson, John G Rarity, and Joshua W Silverstone. Mid-infrared quantum optics in silicon. *arXiv preprint arXiv:1906.10158*, 2019.

[191] Richard Soref. Mid-infrared photonics in silicon and germanium. *Nat. Photonics*, 4(8):495–497, 2010.

[192] AL Gentile, M Braunstein, DA Pinnow, JA Harrington, DM Henderson, LM Hobrock, J Myer, RC Pastor, and RR Turk. Infrared fiber optical materials. In *Fiber Optics*, pages 105–118. Springer, 1979.

[193] Xiaoping Liu, Bart Kuyken, Gunther Roelkens, Roel Baets, Richard M Osgood Jr, and William MJ Green. Bridging the mid-infrared-to-telecom gap with silicon nanophotonic spectral translation. *Nat. Photonics*, 6(10):667–671, 2012.

[194] Cornelia Fischer and Markus W Sigrist. Mid-IR difference frequency generation. In *Solid-state mid-infrared laser sources*, pages 99–143. Springer, 2003.

[195] Xiushan Zhu and Ravi Jain. Watt-level er-doped and er-pr-codoped zblan fiber amplifiers at the 2.7-2.8 μm wavelength range. *Opt. Lett.*, 33(14):1578–1580, 2008.

[196] Simon Duval, Martin Bernier, Vincent Fortin, Jérôme Genest, Michel Piché, and Réal Vallée. Femtosecond fiber lasers reach the mid-infrared. *Optica*, 2(7):623–626, 2015.

[197] Ori Henderson-Sapir, Stuart D Jackson, and David J Ottaway. Versatile and widely tunable mid-infrared erbium doped zblan fiber laser. *Opt. Lett.*, 41(7):1676–1679, 2016.

[198] Jean-Christophe Gauthier, Vincent Fortin, Simon Duval, Réal Vallée, and Martin Bernier. In-amplifier mid-infrared supercontinuum generation. *Opt. Lett.*, 40(22):5247–5250, 2015.

[199] Behsan Behzadi, Maryam Aliannezhadi, Mani Hossein-Zadeh, and Ravinder K Jain. Design of a new family of narrow-linewidth mid-infrared lasers. *JOSA B*, 34(12):2501–2513, 2017.

[200] Xiaoping Liu, Bart Kuyken, William MJ Green, Richard M Osgood Jr, Roel Baets, and Gunther Roelkens. Mid-infrared nonlinear silicon photonics. In *Silicon Photonics IX*, volume 8990, page 89900O. International Society for Optics and Photonics, 2014.

[201] Varun Raghunathan, David Borlaug, Robert R Rice, and Bahram Jalali. Demonstration of a mid-infrared silicon Raman amplifier. *Opt. Express*, 15(22):14355–14362, 2007.

[202] B. Jalali, V. Raghunathan, R. Shori, S. Fathpour, D. Dimitropoulos, and Oscar Stafsudd. Prospects for silicon mid-ir raman lasers. *IEEE J. Sel. Top. Quantum Electron.*, 12(6):1618–1627, Nov 2006.

[203] Xiaoping Liu, Richard M Osgood, Yurii A Vlasov, and William MJ Green. Mid-infrared optical parametric amplifier using silicon nanophotonic waveguides. *Nat. Photonics*, 4(8):557–560, 2010.

[204] Bart Kuyken, Xiaoping Liu, Günther Roelkens, Roel Baets, Richard M Osgood Jr, and William MJ Green. 50 dB parametric on-chip gain in silicon photonic wires. *Opt. Lett.*, 36(22):4401–4403, 2011.

[205] Shiyue Hua, Jianming Wen, Xiaoshun Jiang, Qian Hua, Liang Jiang, and Min Xiao. Demonstration of a chip-based optical isolator with parametric amplification. *Nat. Commun.*, 7, 2016.

[206] Chung L Tang, Walter R Bosenberg, Takashi Ukachi, Randall J Lane, and L Kevin Cheng. Optical parametric oscillators. *Proceedings of the IEEE*, 80(3):365–374, 1992.

[207] VD Vaidya, B Morrison, LG Helt, R Shahrokhshahi, DH Mahler, MJ Collins, K Tan, J Lavoie, A Repingon, M Menotti, et al. Broadband quadrature-squeezed vacuum and nonclassical photon number correlations from a nanophotonic device. *arXiv preprint arXiv:1904.07833*, 2019.

[208] Qing Li, Marcelo Davanço, and Kartik Srinivasan. Efficient and low-noise single-photon-level frequency conversion interfaces using silicon nanophotonics. *Nat. Photonics*, 10(6):406, 2016.